MODELLING AND PREDICTION OF FOAM STRUCTURE

A THESIS SUBMITTED TO

IMPERIAL COLLEGE LONDON

FOR THE DEGREE OF

DOCTOR OF PHILOSOPHY

BY

YINGJIE WANG

Department of Earth Science and Engineering

March 2009

ACKNOWLEDGEMENT

I wish to express my gratitude to:

My supervisor, Dr. Stephen Neethling, for his tremendous academic and financial support, patience and encouragement.

Professor Jan Cilliers, for his financial support and insightful instructions during my study.

My colleagues, Dr. Kathryn Hadler, Dr. Nicolas Barbian, Dr. Kristian Waters, Dr. Mark Pursell, Dr. Christopher Smith, Mr. Gareth Morris, Miss Caitlin Rogers, Miss Kathryn Cole, Mr. Pablo Brito Parada, Mr. Andrew Pattison, and Mr. Rafal Zietara, for providing not only help but also enjoyment during my study.

My parents for their love and encouragement.

ABSTRACT

The primary objective of this thesis is to explore the relationship between the surface and underlying structure of dry foams. This relationship is important for both research and industry because the surface film size distribution is typically the only information available in opaque foams when referring to the underlying bubble size distribution. This study is carried out by simulating foams with free surfaces.

Firstly, the method of simulating 3D dry foams with free surfaces is presented. The simulation method is verified for foams with uniform bubble sizes by comparing their simulation results to experimental values reported in literature. The validity of the method and its ability to accurately model the structure of both surface and internal bubbles is demonstrated by the excellent agreement between the experimental study and the simulation results.

Secondly, the simulation results are shown for the relationship between the surface film size distribution and the surface bubble size distribution. The results show that, for a given surface bubble size, there is a distribution of possible surface film sizes. However, for the range of polydispersity used in this thesis, the distribution of the ratio of film size to the size of bubble to which it is attached is found to be independent of the underlying bubble size distribution. A functional form of this relationship is obtained by nonlinear regression. Based on the functions obtained, the surface film size distributions can be computed using the underlying surface bubble size distribution. This is the inverse of what is acquired and therefore a numerical procedure for obtaining the surface bubble size distributions using the corresponding surface film size distribution is developed. This method is demonstrated to accurately reproduce the results from the full structural foam simulations.

TABLE OF CONTENTS

LIST OF FIGURES

LIST OF TABLES

NOMENCLATURE

Roman Symbols

$\overrightarrow{ab}$	vector pointing from *a* to *b*
$\overrightarrow{ad}$	vector pointing from *a* to *d*
A	coefficient matrix of a simultaneous equation
$A_{i,j}$	entry of matrix *A* (the *i*th row and the *j*th column)
$A(i)$	facet area *i*
A_p	cross-sectional area of Plateau border
B_t	total number of bubbles
C	shape coefficient
D_{ave}	average distance between bubbles in a foam
D_d	diameter of a distorted bubble
$D_{\min}$	minimum distance between seed points
D_s	spherical diameter of a bubble
D_u	diameter of a undistorted bubble
E	number of edges of a convex polyhedron
$E(x_{i,j})$	pair potential energy between point *i* and *j*
$E(x_{i,j})_x$	the first derivative of $E(x_{i,j})$
$E(x_{i,j})_{xx}$	the second derivative of $E(x_{i,j})$
E_{convex}	energy of convex constraint
E_{edge}	energy of edge
$E_S(i)$	surface energy of face *i*
E_{total}	system energy

$E_{total}^{(0)}$	initial system energy
ΔE_{total}	change of system energy
E_t	total number of nominal edges
$E_t^{'}$	total number of real edges
EF_i	expected frequency of data point *i*
f	number of faces per bubble
$f(r)$	size frequency distribution function of bubble radius, *r*
$f_u(r)$	uncorrected size frequency distribution function of bubble radius, *r*
$f_c(r)$	corrected size frequency distribution function of bubble radius, *r*
F	number of faces of a convex polyhedron
$\overline{F}$	force on an oriented edge of a face
F_t	total number of nominal faces
$F_t^{'}$	total number of real faces
$F(r_S)$	size frequency distribution function of surface film radius, r_S
$F(r_S)_{est}$	estimated value for the frequency of surface film radius, r_S
h	positive constant that controls the magnitude of the equilibrium distance relative to the average distance between points.
H	mean curvature
H_0	null hypothesis
H_{Potts}	Hamiltonian of a system
ΔH	energy change in Q-Potts simulation
$J_{i,j}$	interaction energy between two neighbouring sites *(i, j)*
k	Boltzmann constant
$l_{\max}$	maximum length of an edge
$l_{\min}$	minimum length of an edge

L_k	the Onsager kinetic coefficient;
m	number of non-empty frequencies
n_{ij}	normal unit vector of the straight cell boundary segment <*i, j*>
$\vec{n}$	outward normal direction of a facet
N_{ave}	average number of edges per polygon
N_b	number of available samples
N_L	number of large bubbles
N_P	number of points in the system
N_S	number of small bubbles
$\overrightarrow{oa}$	vector pointing from *o* to *a*
OF_i	observed frequency of data point *i*
p	pressure in liquid film
Δp	pressure difference across a liquid-gas interface
$p(f)$	frequency of a bubble with f faces
$P(\omega \rightarrow \omega')$	probability of bubble ω' displacing bubble ω by one lattice site
$\vec{Q}$	projection of the edge on the tangent plane
r	normalised radius of a bubble
Δr	increment of r
r_1	principal radius of an interface
r_2	principal radius of an interface
$r_{\max}$	maximum normalised radius of a bubble
$r_{\min}$	minimum normalised radius of a bubble
$\overline{r_i}$	position of the *i*th vertex

$\overline{r_{ij}}$	vector pointing from $\bar{r}_i$ to $\bar{r}_j$;
$r_{j,k}$	unbiased mean radius by the *j*th and the *k*th moments of the observation
$r'_{j,k}$	biased mean radius by the *j*th and *k*th moments of the observation
r_S	normalised radius of a surface film
$r_{S,\min}$	minimum normalised film radius
Δr_S	increment of r_S
R^2	coefficient of determination
R_{32}	Sauter mean radius
R_b	equivalent spherical radius of a bubble
R_f	equivalent circular radius of a film
$S(r)$	size frequency distribution of bubble radius, r
S_f	projected area of a film
S_{fac}	space factor
$S_{\min}$	minimum area of a bubble face
S_k	current surface area of the *k*th bubble
S_k^t	target surface area of the *k*th bubble
$\vec{S}$	edge vector
SS_E	residual sum of squared errors
SS_T	total sum of squared errors
T	system temperature
$T(r_S)$	surface film size distribution
$T(r_S)_{est}$	estimated surface film size distribution
v	degree of freedom
v_i	velocity of the *i*th vertex

V	number of vertices of a convex polyhedron
V_b	volume of a bubble
V_{large}	volume of a large bubble in a bi-disperse foam
V_{small}	volume of a small bubble in a bi-disperse foam
V_t	total number of nominal vertices
$V_{tetra,\,i}$	volume of the *i*th tetrahedron
V_{total}	total volume of all the tetrahera
W_{bin}	optimal bin width of a histogram
x	coordinate of *x*-axis
$x_{E\min}$	minimum-energy distance
$x_{i,\,j}$	distance between point *i* and *j*
$X_{\max}$	maximum value of *x*-coordinate
y	coordinate of *y*-axis
y_i	the *i*th observed value
$\hat{y}_i$	the *i*th predicted value
$Y_{\max}$	maximum value of *y*- coordinate
z	coordinate of *y*-axis
$Z_{\max}$	maximum value of *z*-coordinate

Greek Symbols

α	significance level of chi-square test
$\delta_{i,\,j}$	Kronecker delta function
γ	surface tension
ε	unit of energy

θ	angle between the outward normal of a face of a polyhedron and the vector pointing out from a point within the polyhedron
γ_{line}	line tension energy
λ	length of Plateau border per volume
σ	standard deviation of bubble sizes
φ	angle between force and constraint plane
Φ	tetrahedral angle between two edges
Φ_l	liquid fraction of foam
χ^2	chi-square statistic
$\chi^2_{critical}$	critical value of a chi-square distribution
ω	value of a 2D grid site
ω'	value of a 2D grid site
ω_{LJ}	equilibrium distance between seed points
$\wp$	free energy in a vertex model
$\Re$	Rayleigh dissipation function

CHAPTER I

INTRODUCTION

1.1 Background

Drinking a glass of beers, taking a fragrant bath, or just blowing some colourful bubbles to amuse your kids, foams pervade every corner of the world, and their existence enhances the enjoyments of our lives. Foams are found in a wide variety of industrial products such as packaging padding, metal or food foams and aquatic foam filters. The particular application of this work is froth flotation, which is a widely used separation process in water purification and mineral processing.

In recent years, a considerable amount of research has focused on the manner in which foam structure impacts the overall performance of flotation systems, especially with respect to water drainage and the recovery of the products. This study, involving modelling foam structure and relating it to performance, is therefore the latest chapter in a long history of study in this field.

Foam structure, usually characterized by bubble size and bubble size distributions, is one of the key factors in determining the functionality and mechanical properties of foam and froth, such as its stability, rheology and drainage (Weaire and Hutzler, 1999). Therefore, the structure of foam can consequently have a strong impact on the performance of many industrial processes, including flotation. How to obtain, analyse and predict bubble size distribution constitutes the main body of this work.

In the mining industry, bubble size distributions are commonly obtained by optical measurements of the foam surface together with image analysis. Unfortunately in most cases, the direct measurement of the internal structure is severely restricted by the opaque and transient nature of most foams (Figure 1.1). Non-optical measurements, such as x-ray tomography (Lambert et al., 2005) or NMR (Kose, 1995) tend to be expensive, time-consuming and sometimes too complicated to set up in an industrial environment. In industry, the measured surface film size distribution is typically assumed to be identical to the underlying bubble size distribution, or with simple statistical corrections (Cheng and Lemlich, 1983). This assumption will be challenged in this work by demonstrating the existence of a systematic bias between the 2D film size distribution on the surface and the corresponding 3D bubble size distribution under the surface.

Figure 1.1: A photo of industrial foam surface.

To overcome the difficulties in experimentally measuring the internal foam structure, this project employs a novel simulation approach to reproduce and study foam structures. Modelling and simulation technology has greatly enhanced the studies of

foam, particularly in a field where direct measurements are mostly intricate and expensive. Therefore simulation can be significantly cheaper and more convenient, and applied to a wide variety of foam structures.

In this work, two crucial questions will be addressed and finally solved by producing realistic foam structures with free surfaces:

1. Is there any quantitative correlation between the 2D surface film size distribution and the underlying 3D bubble size distribution?

2. How can the internal bubble size distribution be predicted with only surface information available?

Question 1 attempts to quantitatively relate the foam surface, which is optically measured, with the internal structure of foam, which is usually difficult to obtain. Question 2 reflects the ultimate objective of this research: to predict the internal foam structure based on a known surface structure. Successful solutions to these questions will be of great benefit to both research and industry.

1.2 The objectives of the research

There are two principal objectives of this research: to discover the relationship between the 2D surface film size distribution and the underlying 3D distribution and to predict the internal bubble size distribution based on a 2D film size distribution visible at the foam surface.

The above objectives were achieved in a number of distinct steps. First of all, a simulation approach based on 3D Voronoi tessellation was implemented and validated by published experimental results (Matzke, 1946). Secondly, a statistical approach was applied to investigate the relationship between the surface and internal structure. Thirdly, the internal structures of a variety of foams were predicted by applying the relationship discovered in the simulations. The foam model was tested for both robustness and accuracy. Finally, the model developed in this work was compared with the methods previously reported to evaluate its performance.

1.3 Structure of the thesis

The report is arranged into 7 chapters; below is a summary of the contents in each chapter:

- Chapter I – INTRODUCTION. This provides the background information on this study, the specific objectives of this project, and a brief summary of the organisation of the report.

- Chapter II – LITERATURE REVIEW. This chapter outlines early and current studies on foam structure and simulation. A brief introduction to techniques of image analysis, method of Voronoi tessellation and Surface Evolver are also presented.

- Chapter III – METHODOLOGY. This presents two different methods of generating foams with free surfaces. The processes for implementing topological and structural transformations are also discussed.

- Chapter IV – BUBBLE SHAPE AND THE TOPOLOGY OF FOAM. This chapter presents the preliminary results of foam modelling and visual simulation, which are compared with the experimental and simulation works published previously.

- Chapter V – BUBBLE SIZE DISTRIBUTION. The distributions of the surface film size and internal bubble size are studied here. An empirical formula is proposed to quantitatively describe the relationship between the two distributions.

- Chapter VI – PREDICTING BUBBLE SIZE DISTRIBUTION. Predictions

of the internal bubble size distribution are evaluated and examined for validity and robustness in a variety of foams. The model developed in this work is also compared with the statistical method reported in literature.

- Chapter VII – CONCLUSIONS AND FUTURE WORK. The conclusions drawn from this work are presented, with recommendations for future study.

CHAPTER II

LITERATURE REVIEW

Introduction

There is extensive literature on many aspects of foam behaviours. This chapter presents a review of the relevant literature, with particular emphasis on the following 3 topics:

1. An overview of foam structure and glossary of some foam specific terms. In particular, the rules of Plateau and Laplace will be described as they are the theoretical basis for the modelling and simulation in this work.

2. The technology of image analysis, specially with its application in measuring bubble size and limitations in foam research.

3. Voronoi tessellations and Surface Evolver, which are the main simulation tools of this work. The key steps for carrying out Voronoi tessellations will be described in details. The framework and functionality of Surface Evolver will be reviewed, especially how it can be applied to produce a realistic foam structure and to implement topological and structural transitions.

2.1 Foam Structure

Bubbles and foams are familiar to most people, however, they still contain many mysteries. To expose the relationship of their multiple components, the first step is to describe foam structure.

Foam is a disperse system, consisting of gas bubbles which are separated by liquid films. Visually, a foam can be defined as an aggregate of gas bubbles held in a continuous aqueous matrix (Sadoc and Rivier, 1999). The components of foam are: lamellae, vertex, Plateau border and the air encapsulated in the bubble lamellae (Figure 2.1). Lamellae are the thin films separating two contacting bubbles. Plateau borders are the conjunction area where three lamellae meet. Vertices are the conjunction of a group of Plateau borders. The method used to produce the foam, the extent of drainage and the coarsening due to diffusion or coalescence will all contribute to determine the structure of a foam, though the basic structural components remain the same.

Surface tension plays an important role in shaping foam structure. Surface tension is an attractive property of the surface of a liquid, which is caused by the cohesive forces between liquid molecules (Weaire and Hutzler, 1999). At the liquid-gas interface, liquid molecules are pulled inwards by other molecules deeper inside the liquid and are not attracted as intensely by the gas molecules. Therefore, all of the molecules at the surface are subject to an inward force of molecular attraction which is balanced only by the liquid's resistance to compression. The liquid squeezes itself together until it has the locally lowest surface area possible. Therefore the surface tension serves as the driving force to decrease the surface area and shape the foam.

Most foams owe their existence to the presence of surfactants, which are materials that generally decrease the surface tension by absorbing at the liquid-gas interface.

With the introduction of surfactant molecules at the liquid-gas interface, the surface tension is reduced (Weaire and Hutzler, 1999), which decreases the rate of liquid being sucked into Plateau borders. Therefore surfactants provide a stabilising role for thin films against rupture.

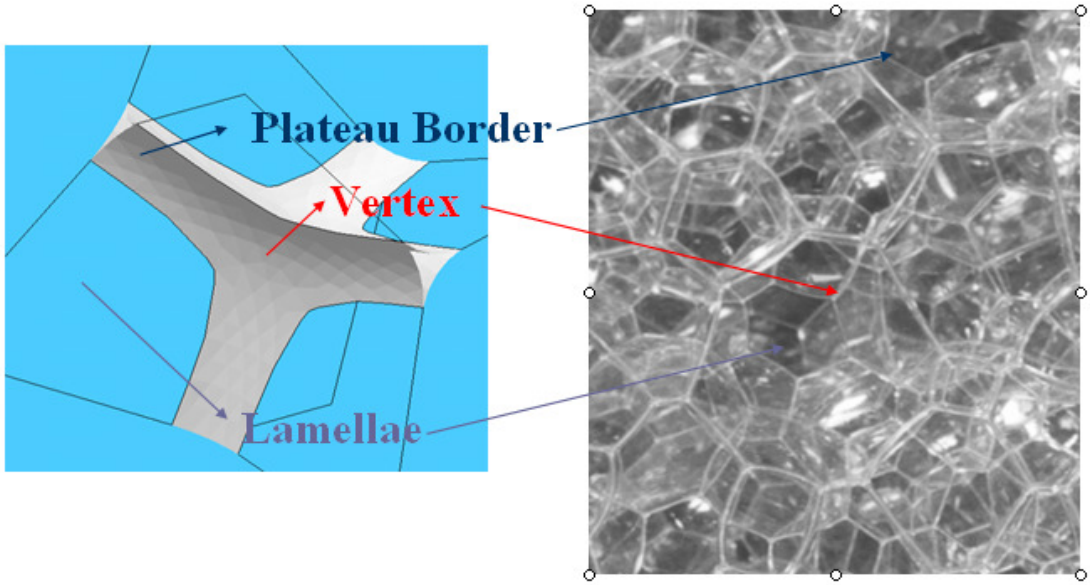

Figure 2.1: The 3D structure of a foam.

2.2 The Rules of Plateau

The study of foam structure under various conditions has been progressing for more than a century. Plateau (1873) was the first scientist to study the equilibrium structure of dry foams. With the assumption that surface tension is uniform everywhere in films, Plateau's two rules for dry foams are stated as follows:

Equilibrium rule 1: The bubble faces in 3D, or bubble sides in 2D, can not adjoin in arbitrary arrangements. Only three films can intersect at a time, and the dihedral angles are always 120°.

Although rule 1 is summarised from experience, it can be demonstrated theoretically within simplified and idealised models by considering a forbidden four-fold intersection. A small dissociation happens to split the initial intersection into two threefold vertices in order to lower the total energy. Just such a deformation occurs spontaneously whenever a fourfold vertex forms (Figure 2.2).

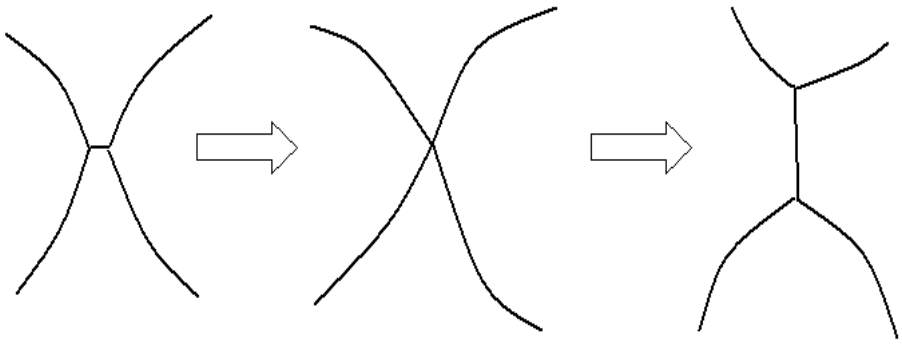

Figure 2.2: The dynamic deformation process of a fourfold vertex dissociating into two stable threefold vertices.

Equilibrium rule 2: For three-dimensional dry foams, no more than four Plateau

borders (or six lamellae) may meet at the vertices of the structure, with all the value of the angles having $\Phi = \cos^{-1}(-1/3)$. The tetrahedral vertices are symmetric.

Rule 2 is partially derived from rule 1 as the symmetric tetrahedral vertex is dictated by the symmetric adjoining intersection of films. In the case of wet foams, the above laws do not always hold. In a 3D dry foam, the liquid is incorporated in the Plateau borders. As the liquid fraction increases, these Plateau borders expand and the films shrink accordingly and eventually disappear. This wetting process results in bubble separation and the round-off of the tetrahedral vertices in order to hold high percentage of liquid (Sadoc and Rivier, 1999).

2.3 The law of Laplace

Another basic law that governs equilibrium foam systems is the law of Laplace. It describes the equilibrium pressure difference sustained across the interface between two different phases: typically liquid and gas. It relates the pressure difference to the shape of a surface.

Laplace's law states that the pressure difference is proportional to the mean curvature of the interface, H, with twice the surface tension (or surface energy per unit area) of the interface as the proportionality:

$$\Delta p = 2H\gamma \tag{2.1}$$

A film within a foam consists of two interfaces. Since the films are very thin compared to their curvatures, both interfaces can be assumed to have the same curvature and therefore the total pressure difference is:

$$\Delta p = 4H\gamma \tag{2.2}$$

For a 3D foam, the mean curvature is equal to the average of the inverse of the two principal radii of curvature, r_1 and r_2:

$$H = \frac{1}{2}\left(\frac{1}{r_1} + \frac{1}{r_2}\right) \tag{2.3}$$

In 2D the second radius of curvature is infinite and therefore:

$$H = \frac{1}{r} \qquad \text{(2D)} \tag{2.4}$$

Figure 2.3 shows an example of the 2D structure of a dry foam.

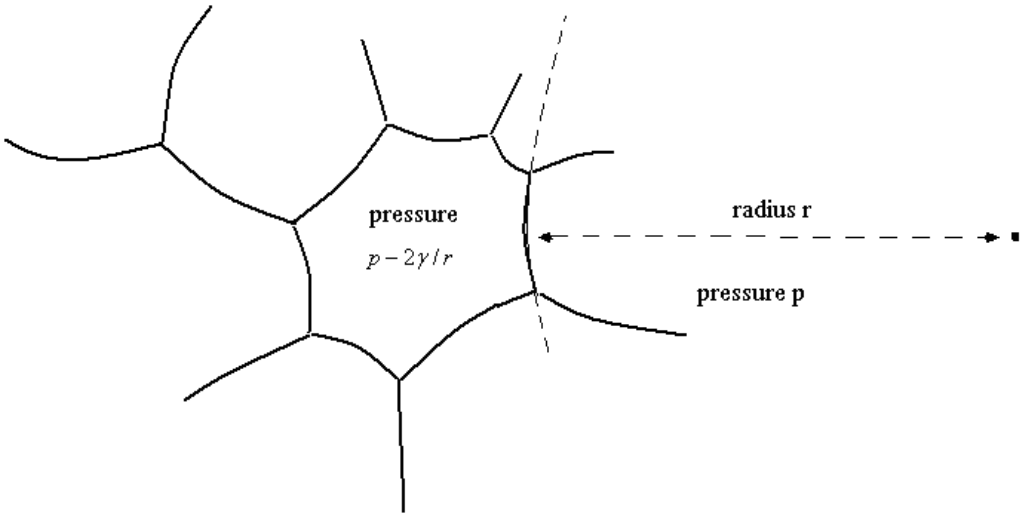

Figure 2.3: The internal structure of a 2D dry foam.

2.4 The shape of bubbles

A long standing mathematical problem relating to the idealised structure of foams is how to partition space into equal volume cells such that they have the lowest surface area. Kelvin (1887) proposed the tetrakaidecahedron as a candidate structure. The tetrakaidecahedron has 14 sides consisting of 8 hexagonal and 6 quadrilateral faces. Weaire and Phelan found a better solution of the Kelvin problem by using computer simulations of foam (Weaire and Phelan, 1994). The Weaire-Phelan structure consists of two kinds of cells with equal volume: a pentagonal dodecahedron and a tetrakaidecahedron with 2 hexagons and 12 pentagons (Figure 2.4). The simulation results show that the surface area of Weaire-Phelan structure is 0.3% less than the Kelvin structure.

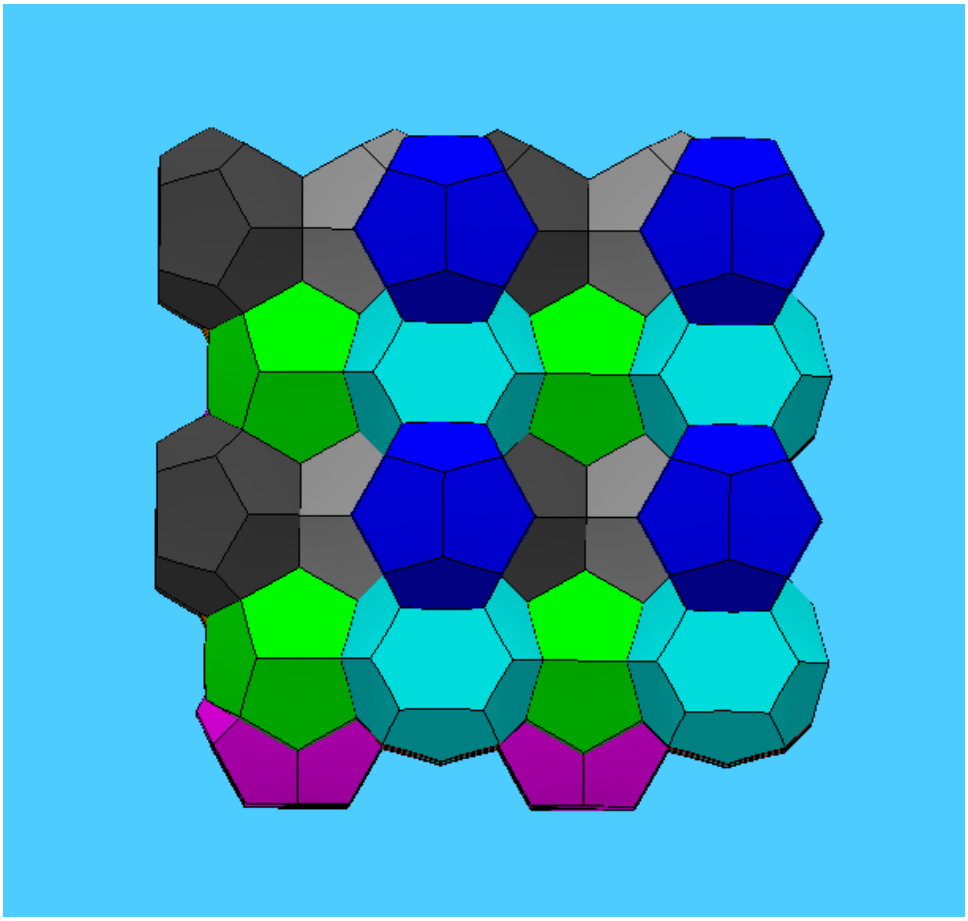

Figure 2.4: The Weaire-Phelan structure of foam simulated by Surface Evolver.

Matzke (1946) studied the topology of foam with uniform bubble sizes experimentally. He used a syringe and dipped it into a soap solution to produce equal volume bubbles. The bubbles were taken into a glass container one by one to produce a randomly packed foam. Matzke investigated the topology of six hundred bubbles in the interior of the foam and four hundred bubbles on the surface using a binocular dissecting microscope. The average number of faces per bubble which was reported in Matzke's experiment is less than Kelvin's theoretical prediction. No Kelvin cell was found in the random foam produced by Matzke. He showed that pentagonal faces were the most common type instead of the quadrilateral and hexagonal sides found in the Kelvin structure. His study also demonstrated that foams exhibit topological disorder even when there is no volumetric disorder.

In this work, uniformly sized foam is always denoted as monodisperse foam and non-uniformly sized is polydisperse foam. Foams encountered in daily-use and industries are virtually always polydisperse and disordered. Producing random foam structures with a controllable polydispersity was very difficult. Only recently, with the help of Surface Evolver and more powerful computers, has it become possible to successfully simulate random foams with a wide range of cell-volumes (Kraynik et al., 2003). It is an important milestone and key step to a further understanding of real foam. Figure 2.5 shows some examples of 3D foam simulated using Surface Evolver.

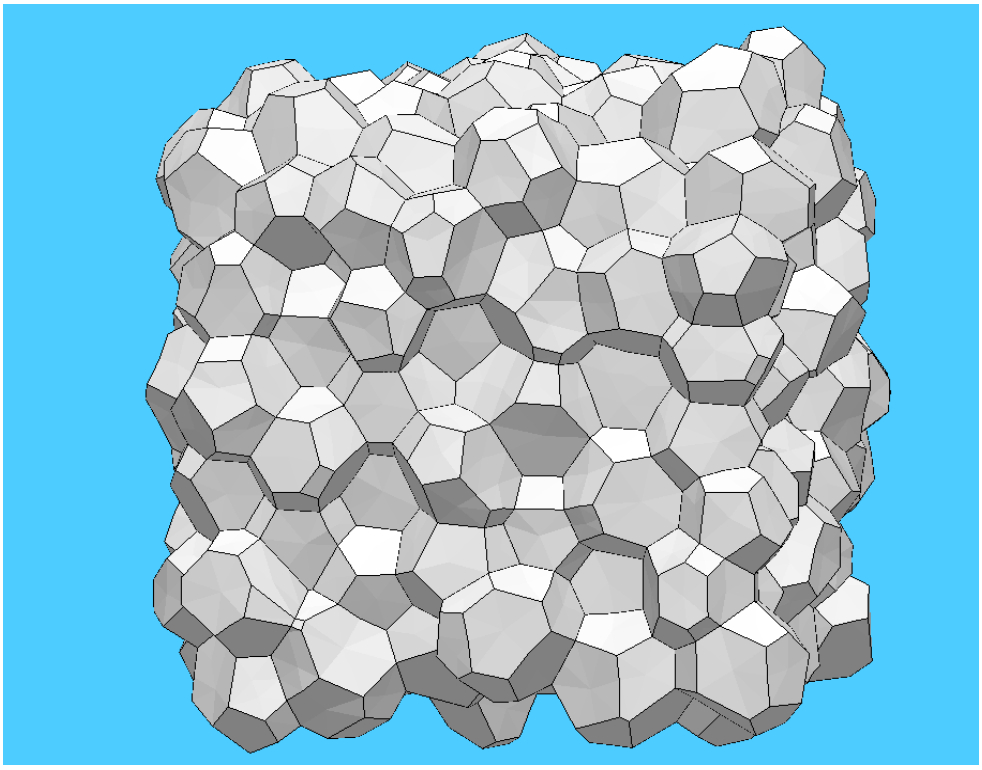

Figure 2.5A: fully periodic Voronoi foam produced by Surface Evolver.

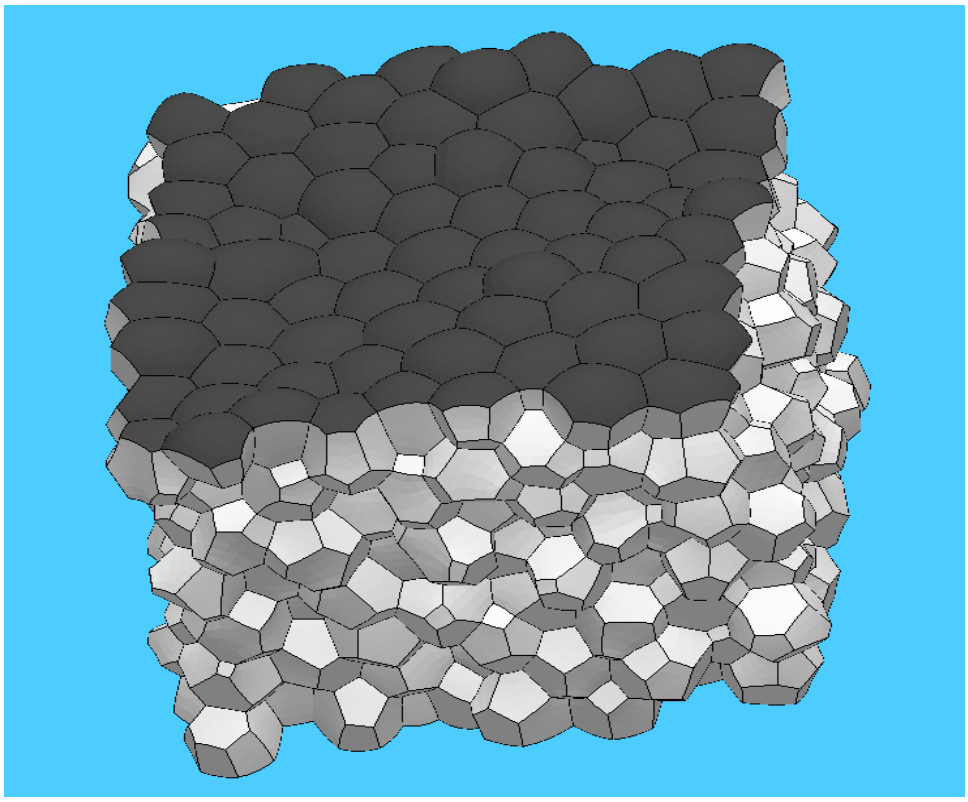

Figure 2.5B: A Voronoi foam with free surfaces in Z direction.

For monodisperse foam, Kraynik et al. (2003) used several different bubble packing algorithms to generate initial foam structures, which were then adjusted and relaxed by Surface Evolver. The results obtained by Kraynik et al. are in good agreement with those of Matzke' experiments (Figure 2.6). His simulation results also show that the average number of faces per bubble increases when the bubble size distribution becomes more polydisperse. Furthermore, when the polydispersity of foam increases, both of the distributions, the number of faces per cell and the number of edges per face, broaden.

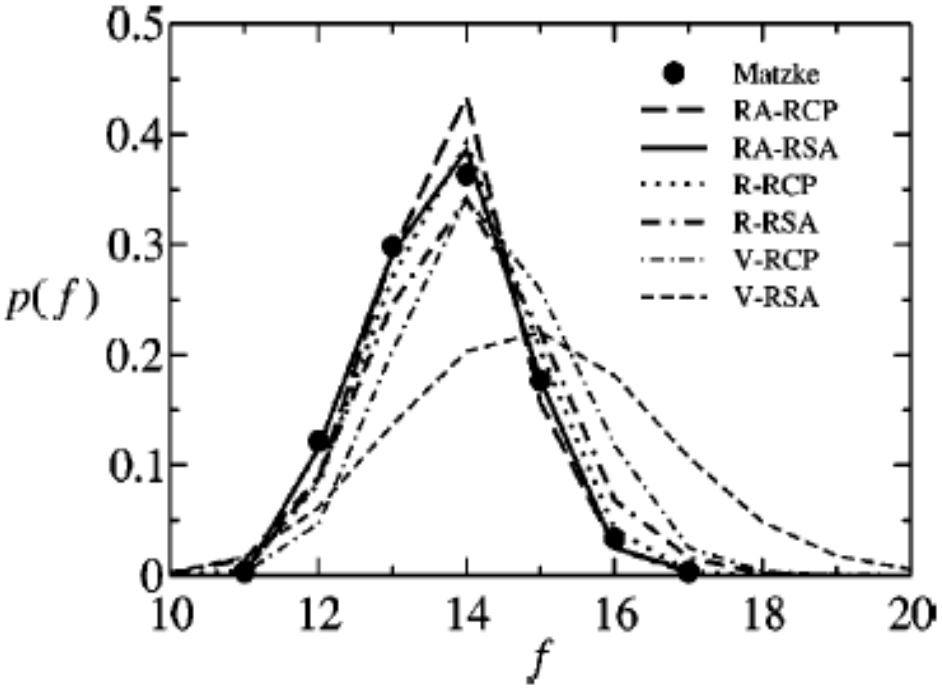

Figure 2.6: The distribution of cells with faces (Kraynik, 2003).

2.5 Measurement of bubble size distribution

In recent years, many studies have been carried out to measure the bubble size and its distribution within foams. For the economy and operational convenience, direct visual or photographical measurements, such as tomography and image analysis, are still the mainstream methods in both laboratory and industry because they are economic and convenient. However, experiments have demonstrated that there are systematic errors presenting in the visual measuring process, which diminishes the usefulness of these methods (Bisperink et al., 1992). Fortunately, a few viable correction methods have been proposed to rectify the data.

2.5.1 Tomography

Recently, optical tomography has been employed as a non-destructive method for reproducing foam structure and estimating bubble size distribution. The set-up of a typical optical tomography system is shown in Figure 2.7. A CCD camera with a narrow opening is used to detect shadows as light is scattered inside the foam. The shadows highlight the Plateau borders. The imaging takes place while the foam sample is rotated slowly on a turntable. The two dimensional optical slices of the foam structure can be obtained by using a very small depth-of-field objective lens. These two dimensional slices are then processed numerically by tomography software to reconstruct the corresponding 3D foam structure (Monnereau and Vignes-Adler, 1998). This can also be used to calculate individual bubble sizes.

Computer-aided optical tomography methods have an acceptable performance in several laboratory scale experiments. However, in practice, it has been unsuitable, so far, for application on industrial foams as the dynamic and opaque nature of the foam restricts the depth of optical observation. Even with transparent films, light scattering makes accurate internal measurements difficult.

X-ray tomography gained popularity for its easy penetration of opaque foam structures and the capacity of dealing with a very large number of bubbles. However, it requires stable foams to obtain good quality images (Lambert et al, 2005). Furthermore, any significant transition of the foam structure will cause severe errors in the reconstruction process. This had limited the widespread application of this technique, particularly for dynamic industrial foams.

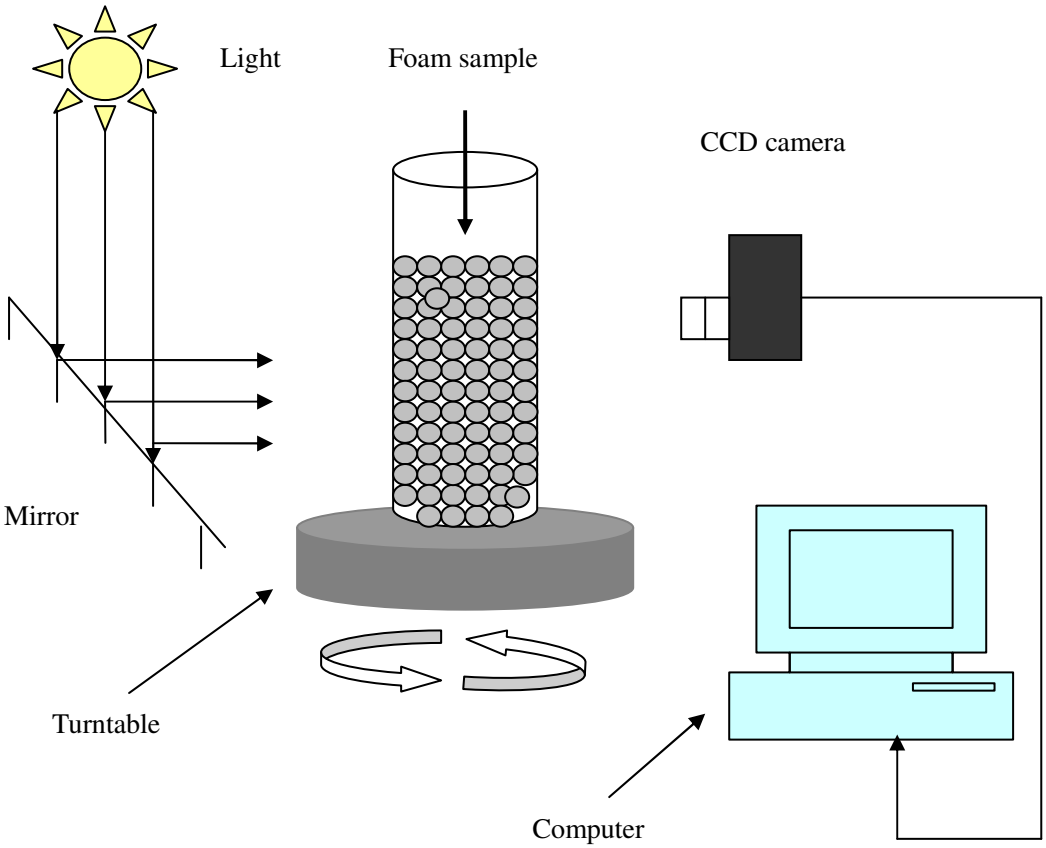

Figure 2.7: Experimental set-up for computerised optical tomography.

2.5.2 Image analysis

In the mining industry, the bubble sizes and their distribution are usually obtained by image processing techniques, which only measures the surface bubbles. Typically, image analysis extracts 2D surface bubble sizes from digitized images taken at a flotation plant. The bubbles are identified by partitioning the digital frame along the lines with lower light intensity (Aldrich et al., 1997). The bubble size is denoted by the equivalent circular diameter of the partitioned area. There has since been much research implemented on designing efficient software to automatically record and analyse the digital frames taken above the froth surface (Ozbayoglu, 2007). This has provided the basis for online monitoring at industrial flotation plants. *Smartfroth* is one such package, which is jointly developed by University of Cape Town, Anglo Platinum and Stone Three. Smartfroth has been used for the analysis of flotation froth surfaces to obtain bubble size in several studies (Hadler et al., 2006). An example of a frame being analysed by Smartfroth is given in Figure 2.8.

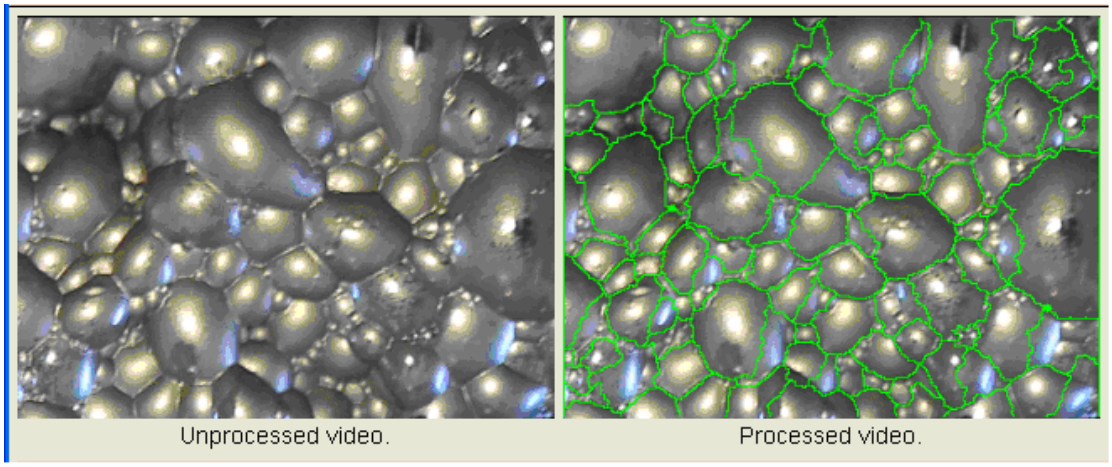

Figure 2.8: The image analysis of foam surface (as used in Hadler et al., 2006).

2.5.3 Errors in measuring bubble size distributions

As bubble size and its distribution are two of the key parameters for representing foam structures, both scientists and engineers are concerned with the accuracy of measured bubble size distributions. However, only a few studies have been reported regarding bubble size correction.

In experiments the measurement of bubble size distributions is subject to a few sources of errors, which are explicitly outlined below.

Firstly, a statistical sampling bias exists in most of the measuring process as small bubbles are preferentially missed out when a sampling plane slices through a foam. De Vries (1957, 1972) proposed a theoretical method (Equation 2.5) to correct the sampling bias.

$$f_c(r) = [\int_0^\infty \frac{f_u(r)dr}{r}]^{-1} \frac{f_u(r)}{r} \tag{2.5}$$

Where:

r = bubble radius (normalised radius is used in this work)

$f_c(r)$ = corrected size frequency distribution function,

$f_u(r)$ = uncorrected size frequency distribution function.

For Equation 2.5, it is assumed that the probability of a bubble being touched by a sampling plane is proportional to its radius when a sampling plane is horizontally placed through a foam. Therefore large bubbles have higher probability of being counted than smaller bubbles in the measuring process, which creates a statistical bias in $f_u(r)$. This bias can be corrected by dividing $f_u(r)$ by its radius, *r*. The total frequency after correcting the statistical bias is given by $\int_0^\infty \frac{f_u(r)dr}{r}]$.

Equation 2.6 presents a useful statistical relationship for the mean radius by the *j*th and the *k*th moments of the observation:

$$r_{j,k} = r'_{j-1,k-1} \tag{2.6}$$

Where:

$$r_{j,k} = [\int_0^\infty r^j f_c(r)dr / \int_0^\infty r^k f_c(r)dr]^{1/(j-k)} \quad \text{(without bias)}$$

$$r'_{j-1,k-1} = [\int_0^\infty r^{j-1} f_u(r)dr / \int_0^\infty r^{k-1} f_u(r)dr]^{1/(j-k)} \quad \text{(with bias)}$$

Secondly, at the bounding wall of a liquid foam, such as a glass wall, the peripheral bubbles are distorted subject to both the boundary restriction and extrusion from inner bubbles. The bubble distortion effect should be taken into account in the calculation of bubble diameter, especially in heterogeneous bubble systems. Figure 2.9 depicts the distinct distorting effect of a retaining wall to the attached bubble.

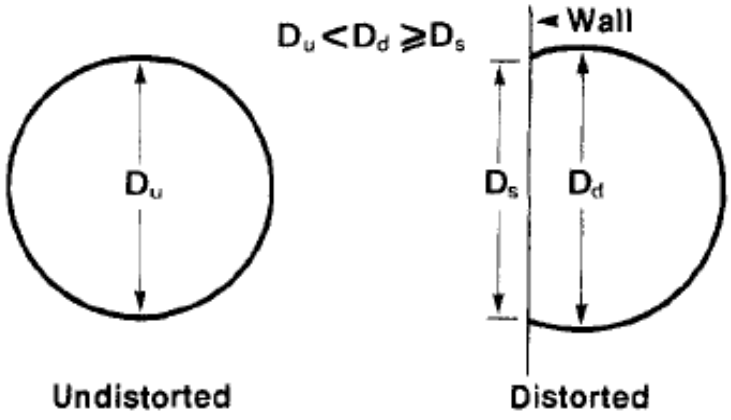

Figure 2.9: Distortion of a spherical bubble by a retaining wall (Cheng and Lemlich, 1983).

Thirdly, large bubbles tend to be wedged away from bounding walls by small bubbles. As a result, a slight difference between peripheral and internal bubbles, in terms of

bubble size distribution, can be reasonably expected.

Finally, as gas diffuses within a bubble system, large bubbles grow at the expense of small bubbles (de Vries, 1957). The rate of diffusion at the foam surface is likely to be different from that of underlying bubbles. Similarly, boundary effects might also influence these bubble coalescences. Therefore, with the aging of foam, further errors could be introduced into the measuring process.

2.6 Simulation and modelling of foam structure

Although a number of studies have been carried out to measure foam structure experimentally, unfortunately, most of them require complicated set-ups and strict control of operational parameters. The measuring process tends to be expensive, time-consuming and prone to changes in the environment. It is especially difficult to gain fine control of the parameters of foam structure. These problems can be avoided through a simulation approach, in which the properties of foam are easily controlled and changed. In addition, simulation can provide very detailed information about the topology and structure of foam (Wang and Neethling, 2006). These strengths make simulation an attractive alternative, though it must be demonstrated that the simulation can accurately mimic real foams.

Since the 1990s, significant breakthroughs have been seen in foam simulations. In this section, both 2D and 3D foam simulations will be introduced.

2.6.1 Simulation of two-dimensional foam

Much simulation work has concentrated on modelling 2D foams. This is because they need fewer parameters and thus less computational power, to define the system and retain many of the essential and interesting properties of 3D foams. The structure of foams under static conditions is governed by energy minimisation (Sadoc and Rivier, 1997). Plateau's laws in 2D determine the geometry of the film-network. Some conditions must be satisfied in order to define an equilibrium 2D foam structure (Figure 2.10):

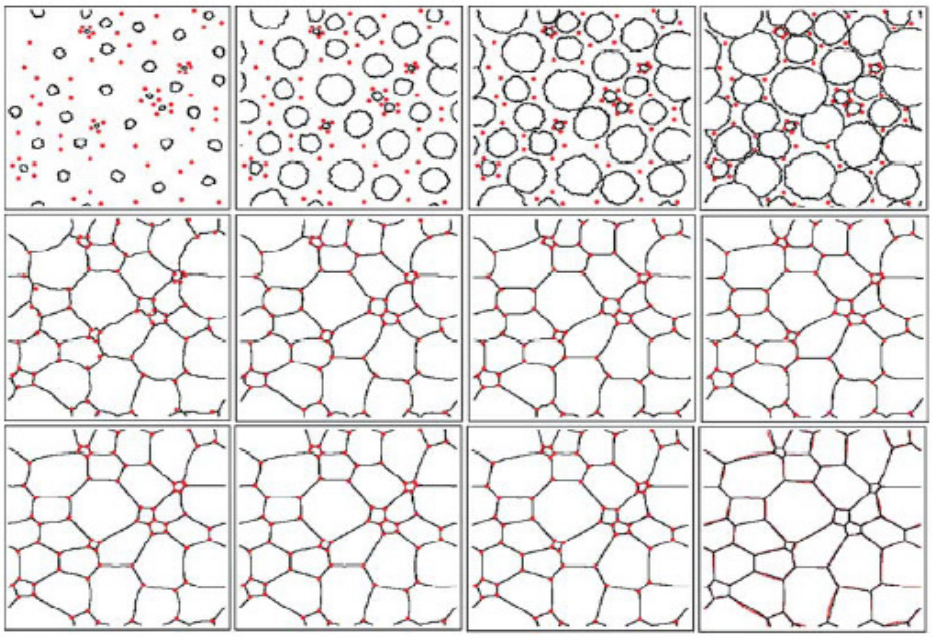

Figure 2.10: The simulation of the growth of 2D foam (Vasconcelos et al., 2003).

a) Polygonal cells separated by circular lines which define the cell boundaries must meet at an angle of 120º.

b) The curvature of the film is determined by the pressure difference across the interface of gas and liquid.

Previous studies using the simulation of 2D foams can be categorized through their different mechanisms to produce foam structure, such as the Q-Potts model which produces foam structure by dynamic approaches and the Voronoi tessellation with energy minimisation which starts from an initial structure produced by Voronoi tessellation and adjusts it subject to Plateau's rules and surface energy minimisation.

Among various 2D models developed so far, Q-Potts model is the most popular one, because it not only successfully models dry foam structure, foam coarsening, and drainage (Jiang. et al., 1996 and 1999), but also captures much of the physics of foam. The Q-Potts model is a generalization of the Ising model to more than two spin

components, which allows large numbers of bubbles, fixed bubble areas, and large foam distortions. A Q-Potts model consists of spins, with Q different values, on a lattice, which is usually a 2D rectangular Euclidean lattice. The value of Q is usually equal to the number of bubbles to be produced in the simulation. The model treats a foam on a 2D lattice by assigning an integer index to each lattice point. The value at a known grid site is ω if the site lies inside bubble ω. Each bubble in the foam is thus a connected set of grids with the same index ω. Each bubble is thus labelled by this index ω and occupies many grid sites. Each pair of neighbours with different indices determines a bubble wall and the surface energy of the bubble wall. Bubble areas are the sum of the lattice sites for each index. The Hamiltonian is given by Equation 2.7 (Vasconcelos et al., 2003):

$$H_{Potts} = J_{\omega,\omega'} \sum_{i,\, j\,(sites)} (1 - \delta_{\omega_i \omega_j}) + \lambda_{Potts} \sum_{k\,(bubbles)} (S_k - S_k^t)^2 \qquad (2.7)$$

$J_{\omega,\omega'}$ denotes the interaction energy between the neighboring sites. λ_{Potts} is a parameter specifying the strength of the area constraint, S_k is the current surface area of the *k*th bubble, and S_k^t the target area of the *k*th bubble. $\delta_{\omega,\omega'}$ is Kronecker delta function which takes the following form (Equation 2.8):

$$\delta_{i,j} = \begin{cases} 1, & if\ i = j \\ 0, & if\ i \neq j \end{cases} \qquad (2.8)$$

Energy minimisation is implemented through iteratively reducing the total wall energy (sum of the 2D bubble perimeters). During the simulation process, a grid site (*i*, *j*) is picked randomly by a Monte Carlo method. Then an attempt to change its index from ω to ω' is performed with the probability (Equation 2.9):

$$P(\omega \to \omega') = \begin{cases} 1, & if\ \Delta H < 0 \\ \exp(-\Delta H / kT), & if\ \Delta H \geq 0 \end{cases} \qquad (2.9)$$

where ΔH is the energy gain the change produces. Each such move corresponds to bubble ω' displacing bubble ω by one lattice site. Figure 2.10 shows the results of the Q-Potts simulation implemented by Vasconcelos et al (2003).

Another approach, which has been successful in 2D foam simulation, is Voronoi tessellation with energy minimisation method. Different from the dynamic approach of Q-Potts model, this method consists of two steps. Firstly, a topologically similar initial structure is produced by 2D Voronoi tessellation. Then the energy of the initial structure is minimised by Surface Evolver, with topological transformations and surface refinement. Cox and Whittick (2006) simulated disordered foam structures with Surface Evolver. In their simulations, Surface Evolver is set in a circular arc mode in order to accurately represent the curved edges in a 2D foam. The initial foam structure is created from a 2D Voronoi tessellation process based upon randomly placed points. The system energy is proportional to the total length of the edges in the foam if the surface tension is uniform. Firstly, a minimum of the total edge length is found. Then the 2D foam structure is annealed to a deeper energy minima by a large number of topological transitions, such as T1 process, in order to better represent the real foam structure. Two of the distinct strengths of Cox and Whittick's work are that it is able to roughly control the range of bubble sizes in a random foam structure and the simulated structure satisfies the topological requirements of Plateau's laws.

2.6.2 Simulation of three-dimensional foam

In contrast to 2D simulation, the 3D equivalent is much more complicated due to the great difficulty in using a simple mathematical form to describe an arbitrary non-spherical surface. Although in the 3D case, the local equilibrium conditions and Laplace's law remain as simple as in two dimensional cases, the number of geometrical and topological variables increases dramatically, especially when there are large numbers of disordered cells involved. The numerical study of 3D foams has

been made tractable through increases in computer power and the development of software.

A number of papers using computer simulations of 3D foams have recently appeared. Kawasaki et al (1995) employed a vertex model to reproduce foam structures. Vertex model has great similarity with the dynamic models of grain growth which are based on the idea of curvature-driven evolution of a cellular structure (Weaire and Hutzler, 1999). In a vertex model, the configuration of a bubble is determined by the state and assignment of its vertices. The total energy is the sum of all the vertex energies. The equation of motion for the *i*th vertex, which has the position $\bar{r}_i$ and the velocity v_i, is given by:

$$\frac{\partial \wp}{\partial \bar{r}_i} + \frac{\partial \Re}{\partial v_i} = 0, \qquad i = 1, 2, \ldots, N \tag{2.10}$$

In equation (2.10), $\wp$ and $\Re$ denotes the free energy and the Rayleigh dissipation function respectively, and *N* is the number of vertices in the system. In a 3D case, $\wp$ and $\Re$ can be expressed as follows (Nakashima et al., 1989):

$$\wp = \gamma_{line} \sum_{<i,j>} | \overline{r_{ij}} | \tag{2.11}$$

$$\Re = \frac{\gamma_{line}}{6L_k} [\sum_i \sum_i {}^{(i)} | \overline{r_{ij}} | (v_i \cdot n_{ij})^2 + \sum_{<i,j>} (v_i \cdot n_{ij})(v_j \cdot n_{ij})] \tag{2.12}$$

where:

γ_{line} = the line tension energy;

L_k = the Onsager kinetic coefficient;

$\overline{r_{ij}} = \bar{r}_i - \bar{r}_j$;

n_{ij} = the normal unit vector of the straight cell boundary segment <*i, j*>;

Furthermore, the sum $\sum_{<i\ j>}$ is over all the connected vertex pairs <*ij*> and the sum $\sum_{i}^{(i)}$ over three vertices *j*, connecting to the vertex *i*.

Equations (2.10)–(2.12) define the motion of vertices and approximately describe the evolution of 3D foam structure (Nakashima et al., 1989). Figure 2.11 shows a three-dimensional foam structure produced by the vertex model (Kazuhiro et al, 1994).

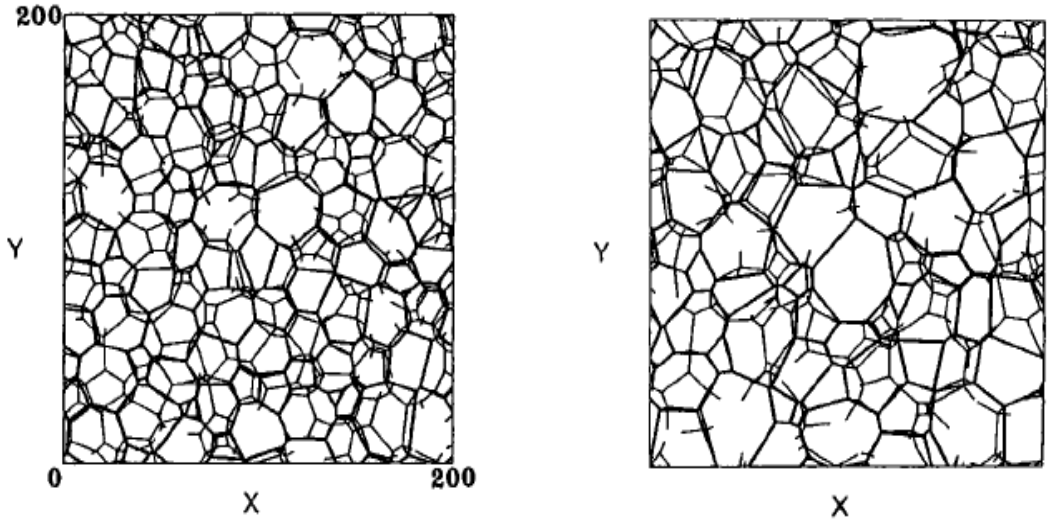

Figure 2.11: 3D foam structure produced by vertex model, given as a X-Y view (Kazuhiro et al, 1994).

In recent years, 3D Voronoi tessellation with energy minimisation by Surface Evolver has become the most popular method used to reproduce 3D foam structure because of Surface Evolver' ability to handle arbitrary surfaces with user-defined refinement. Similar to 2D cases, the initial foam structure is produced by 3D Voronoi tessellation, which meets the topological requirements of Plateau's rules. It is then adjusted,

together with surface area minimisation, by Surface Evolver through topological transformations. The key points of a 3D foam simulation are described below (Weaire and Hutzler, 1999):

a) Use a series of plane-faced convex polyhedra to set up a periodic space-filling structure;

b) Triangulate through every face of the bodies, partitioning the face into a mesh of flat triangles, which are the logical components of faces;

c) Minimise the surface energy by iteratively reducing the total surface area using gradient descent methods;

d) Refine the mesh produced in step (b) to further minimise the surface energy until satisfying convergence has been reached.

A large number of simulations have been reported using Surface Evolver. Kraynik et al. (2001, 2003) studied the bubble shapes of random monodisperse and bi-disperse foams by 3D Voronoi tessellation followed by energy minimisation. Both geometric and topological properties of random foams were studied and compared with Matzke's experimental study. Kraynik reported an average of 13.7 faces per bubble and a similar distribution for the number of edges per face in his simulation, which are in remarkable agreement with Matzke's observation. Kraynik (2004) also simulated polydisperse foams employing a variety of methods to study the transition of foam topology and structure with the increasing polydispersity. In particular, Kraynik discovered the relationship between the length of Plateau border per volume and the foam polydispersity, which is of paramount importance to quantitatively investigate the impact of foam structure on foam drainage. Wang and Neethling (2006) employed a similar approach to investigate the topological and structural properties of polydisperse foams. Figure 2.12 shows the internal structure of foam produced by

Surface Evolver.

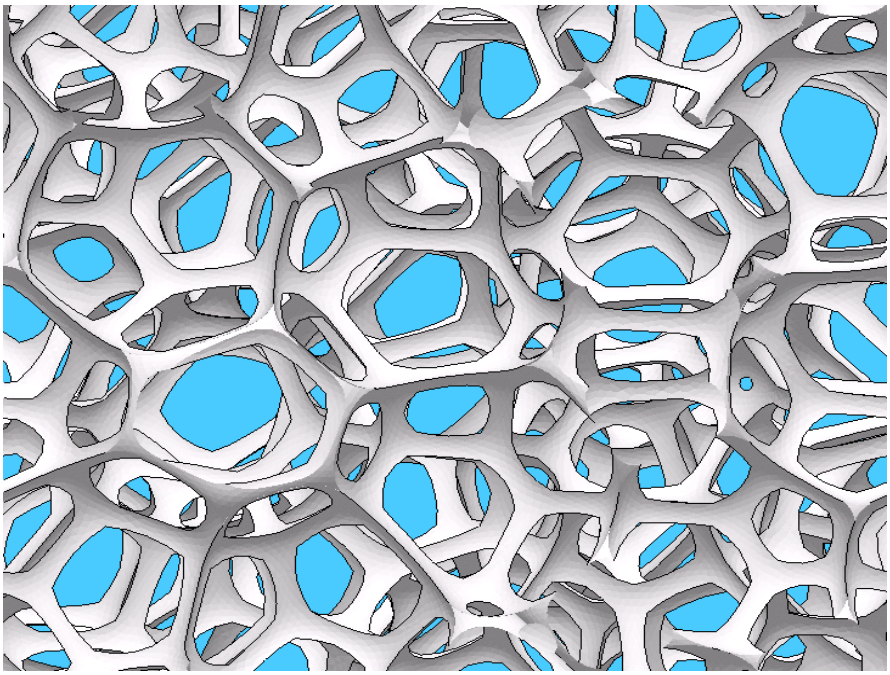

Figure 2.12: The internal structure of foam.

Another model has been developed, the 'bubble model'. However, it is not very successful in reproducing 3D foam structures. It is based on bubble-bubble interactions, is a different approach to modelling a foam with high liquid fraction. In a bubble model, equations of motion for individual bubble centres are developed by introducing interactions between neighbouring bubbles. The only structural parameters are their radii and the time-dependent positions of their centres (Durian, 1996). No explicit parameters are introduced to describe bubble shapes. For a wet foam, the shape of gas bubbles transforms from a polyhedron to a sphere as a result of the rounding-off effect of the increasing liquid fraction. Thus the structure is not necessarily subject to the topological and geometric constraints of Plateau's laws. This work only considers foams in dry limit, which strictly obey Plateau's law. Therefore the bubble model is not relevant to this work.

2.7 Surface Evolver and Voronoi tessellation

2.7.1 An introduction to Surface Evolver

Surface Evolver, designed by Kenneth A. Brakke, is an interactive program for the study of arbitrary surfaces. One of the most distinct strengths of Surface Evolver is the breadth of surface problems that covers, rather than finding optimal treatment for some specific problems (Brakke, 1996 and Phelan et al., 1995). A simulation with Surface Evolver usually involves two separate processes. One is producing the initial data file. Since Surface Evolver only provides a general framework to handle surface problems, the properties and characteristics of targeted surfaces need to be defined by the users themselves. The other is to produce the operational process and commands for evolving the surfaces. Users have freedom to define any movement, transformation and deletion of surface components or the surface as a whole.

The software employs a vertex-edge-facet element model of the surfaces. Surfaces can be associated with bodies, but there are no volume elements defined. Energy is solely calculated by associating quantities of the facets, edges and vertices. Usually the dominant contribution to the system energy is due to surface tension. In this case energy depends only on the facet area. The basic geometric elements used to represent a surface are vertices, edges, facets and bodies. These elements are defined as follow:

1) Vertices are points in Euclidean space. The coordinates of vertices are the parameters that determine the location of a surface. During the simulation, it is the vertex coordinates that are changed by Surface Evolver rather than the edges, faces and bodies.

2) Edges are oriented line segments joining pairs of vertices: a head vertex and a tail vertex.

3) Facets are the logical elements of a surface. In fact, no separate surface entity is defined in Surface Evolver. Every face of a bubble is approximated by a series of triangular facets. In the surface minimising process, the rearrangement and smoothening of the mesh of triangular facets result in a smaller surface area.

4) Bodies are three-dimensional regions enclosed by a set of oriented facets. All facets in the body must have its normal direction outward.

In Surface Evolver, facets always have a triangular shape. Any facet which has four or more edges must get divided into triangles. Edges are defined as vectors which have a head and a tail vertex. Edges are assembled onto facets and their directions are determined by the right-hand rule.

Once a model has been set up, the targeted surfaces evolve towards a minimum in energy by methods which can be selected by the user. Vertices are moved along the direction of the gradient in which energy is associated only with the vertex coordinates. Alternatively, one can define variants of conjugate gradient schemes. The mesh can be refined at any time; the simplest scheme divides each triangle into four by placing a vertex in the middle of each edge.

Probably the most useful feature of Surface Evolver is that it provides a programming interface whereby the user can observe and control virtually all aspects of the simulation procedure, which is very convenient for the study of foam topology. Figure 2.13 shows the operation windows and image viewer of Surface Evolver.

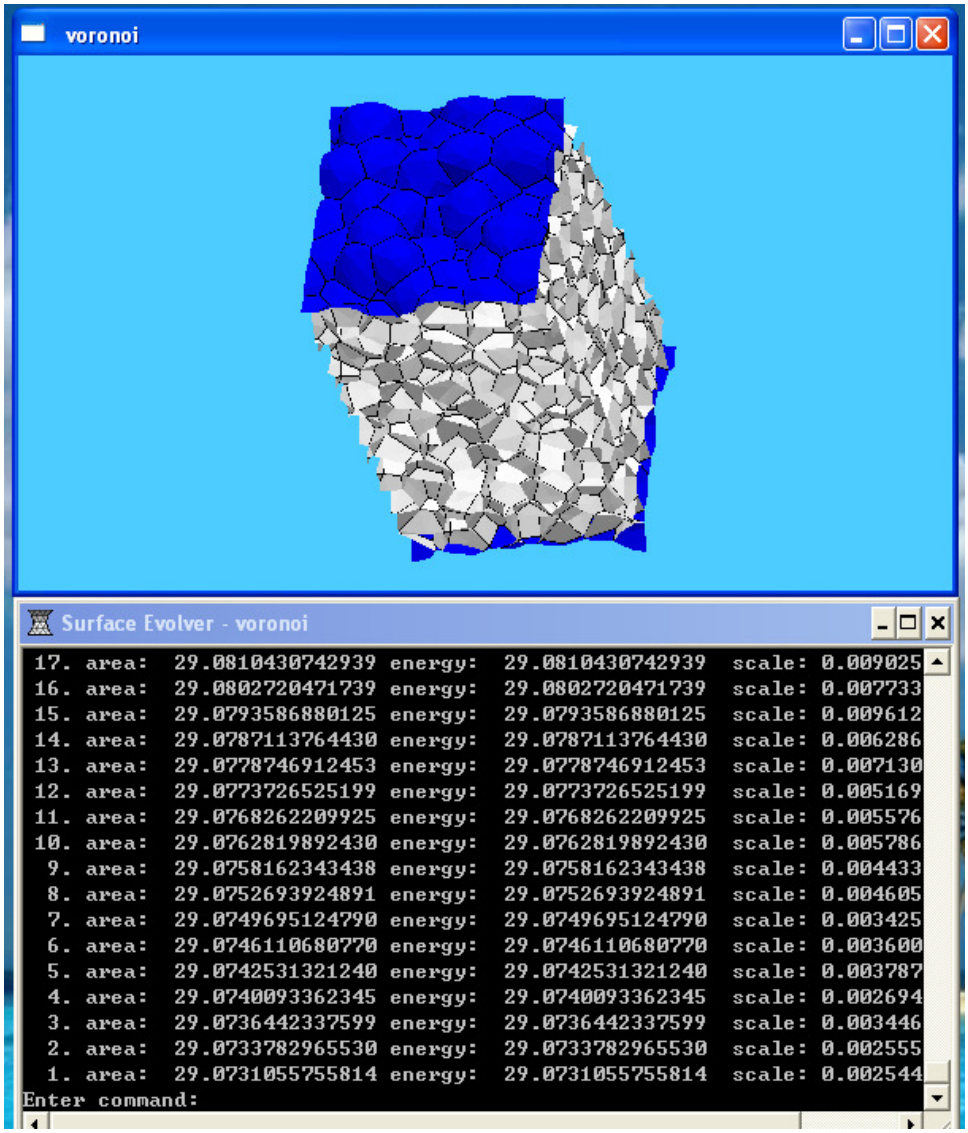

Figure 2.13: The main windows and image viewer of Surface Evolver.

2.7.2 Voronoi tessellation

As Surface Evolver only provides a general framework for foam simulation, Voronoi tessellation will be used to produce the initial foam structure for Surface Evolver.

A Voronoi tessellation is also called Voronoi decomposition, and was named after the Russian mathematician, G.F. Voronoi, who defined and studied the general *n*-dimensional case in 1908. The Voronoi tessellation is a very useful tool to investigate the mechanisms of geometrical frustration and assemble disordered

polyhedra (Montoro, 1993). In this work, the Voronoi tessellation is used to generate initial foam structure in which the sizes and positions of bubbles are random and disordered.

The methodology can be simply described as: a Voronoi tessellation partitions the volume into cells centered upon the individual sites in such a fashion that all points within a cell (including the boundary) are closer to that site than to any other site in the system. Simply put: given a set of *N* points in a space, Voronoi tessellation divides the domain into a set of polyhedral regions. Furthermore, each polyhedron only contains one of the *N* points. If both of the conditions are satisfied, the lines joining the neighboring points form a mesh known as a Delaunay triangle (Sadoc and Rivier, 1997).

A substantial number of algorithms have been developed to numerically compute 2D and 3D Voronoi tessellation. Sugihara (1992) developed an efficient algorithm for numerically computing the Voronoi tessellation, which dramatically reduced the computational errors in space partition. Kuhn (1998) employed a randomized parallel algorithm for computing planar Voronoi tessellation of *n*-point space. Several other scientists have also developed similar, but more complicated methods, to produce triangulation for Voronoi tessellation. A typical process of 2D Voronoi tessellation includes four steps, which are outlined in the following diagrams:

a) Assigning random points in the two-dimensional plane (Figure 2.14):

Figure 2.14: The first step for 2D Voronoi tessellation – placing random points.

b) Triangulating through the placed points in the plane, in the manner that no other points are enclosed in the circumcircle determined by the triangle (Figure 2.15):

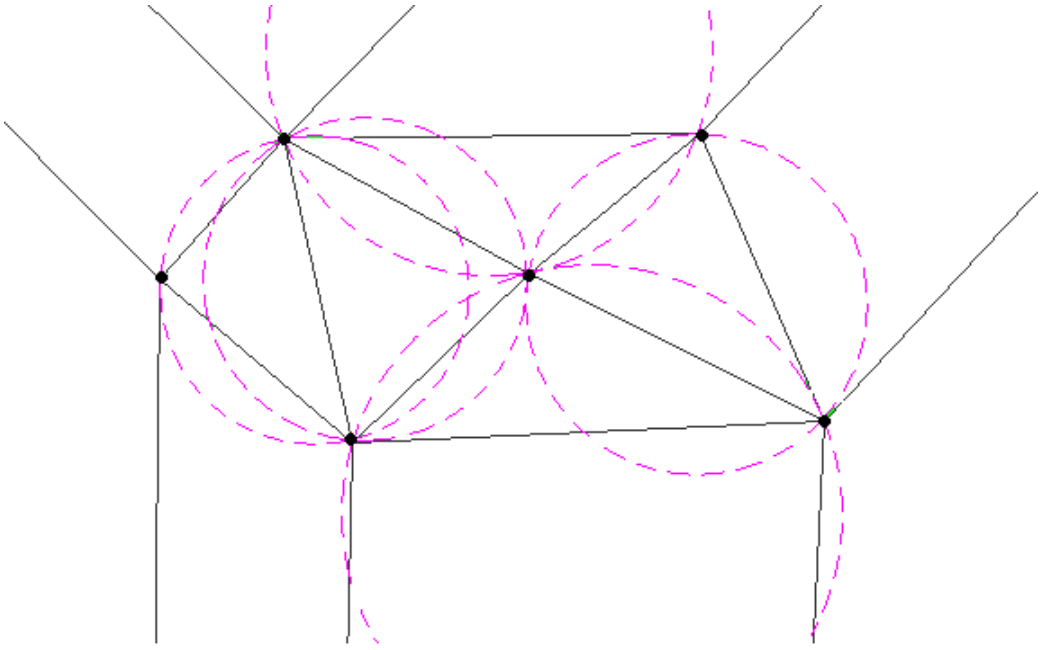

Figure 2.15: The second step for 2D Voronoi tessellation - triangulating.

c) Finding the perpendicular bisecting line on each edge of the triangle network and enclosing the random points within those perpendicular bisecting lines.

This is to tessellate the 2D space subject to the initial layout of random points. These bisectors join the centres of the circumcircles (Figure 2.16).

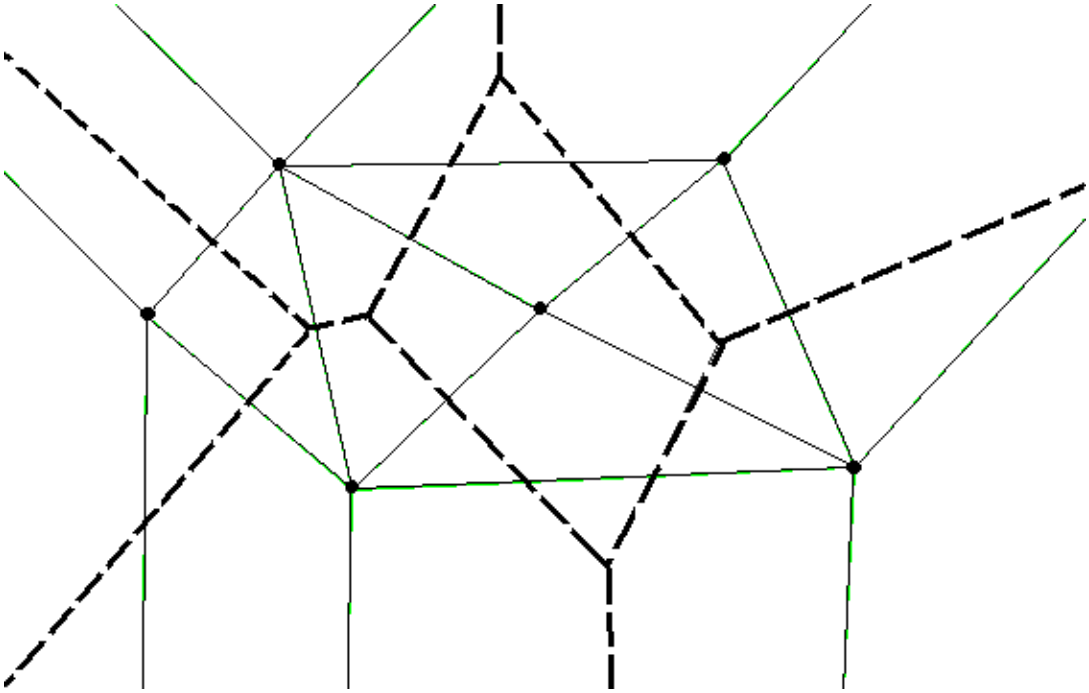

Figure 2.16: The third step for 2D Voronoi tessellation – tessellating.

d) The final layout of 2D Voronoi tessellation (Figure 2.17):

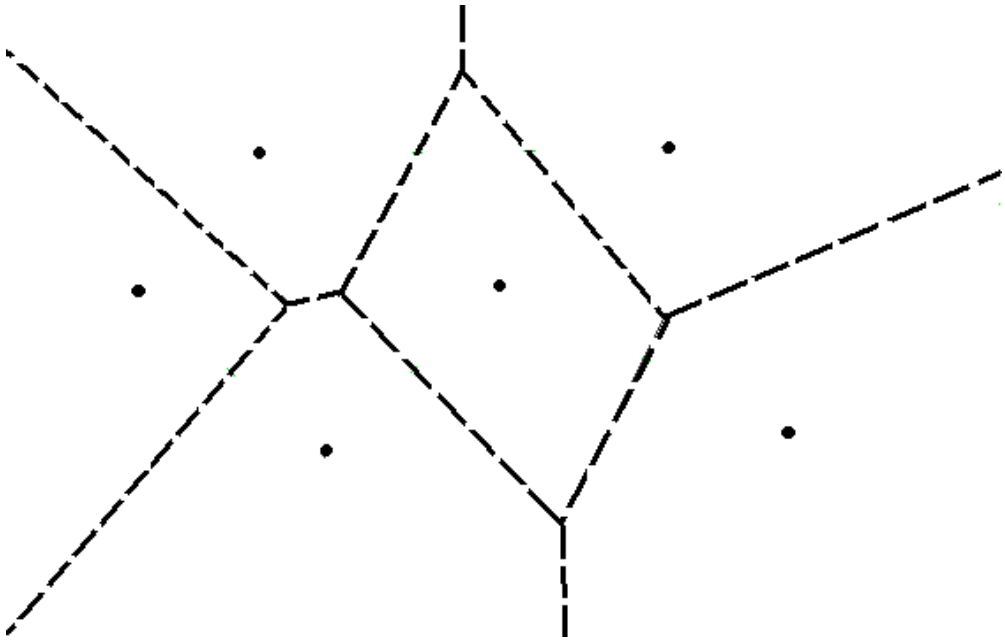

Figure 2.17: The final layout of a 2D Voronoi tessellation.

In this work, the 2D Voronoi tessellation method mentioned above is expanded into 3D space. In 3D Voronoi tessellation, the triangle network consists of tetrahedra. Thus the convex polygons are replaced by polyhedra in order to partition the space. The following steps are proposed for 3D Voronoi tessellation:

a) Generate a certain number of random points, which is subject to the given minimum distance between points, in a defined 3D space;

b) Produce tetrahedra in a way that no points placed in a) are enclosed inside the forming tetrahedrons;

c) Make triangulation through the generated random points under the prescribed rules;

d) Find the circumcentres of the tetrahedron produced in the previous step and connect the centres around a vertex shared by all the tetrahedra to produce

the polyhedra;

e) Delete redundant edges and very small faces; relax the Voronoi structure to satisfy Plateau's law and minimise the surface energy.

2.8 Foam drainage

Foam drainage is influenced by the structure of foam. In particular, it is closely associated with the length of Plateau border per volume. The length of Plateau border per volume is in turn determined by the bubble size distribution. Therefore, understanding the structure of foam is the starting point to predict foam drainage behaviours.

The flow of liquid relative to bubbles is typically called foam drainage (Stone et. al., 2002). Foam drainage is one of the key factors dictating the grade of the products in froth flotation. In the flotation process, the quantity of water recovered is closely correlated with the amount of gangue collected, which is sequentially related to the purity of the final products (Neethling et al, 2003). A number of studies have been carried out to investigate the impact of foam structure to foam (Vera and Durian, 2002).

Understanding the formation of foam drainage is the first step to study the impact of the foam structure on drainage behaviours. At the moment when a foam is formed, the liquid content is usually much larger than the equilibrium liquid fraction in the foam. Consequently, the excess liquid starts to drain out through the network of Plateau borders to reach an equilibrium state. During the flotation process, the liquid contained in the walls of foam cells is sucked into the Plateau borders by the pressure difference between films and Plateau borders. Then the liquid flows downwards along the gravitational gradient (di Meglio and Baglioni, 1994). This process is usually accompanied by film thinning, bubble rupture and growth. As a result, the drainage process not only changes the liquid fraction in a foam, but also causes rheological and topological changes (Figure 2.18).

From the perspective of micro-mechanisms, liquid drainage is the consequence of the

interaction of internal and external forces on the foam. Gravity is the main driving force for liquid drainage, while liquid phase viscosity and capillary pressure, which act in the opposite direction to liquid outflow, works as a resisting force.

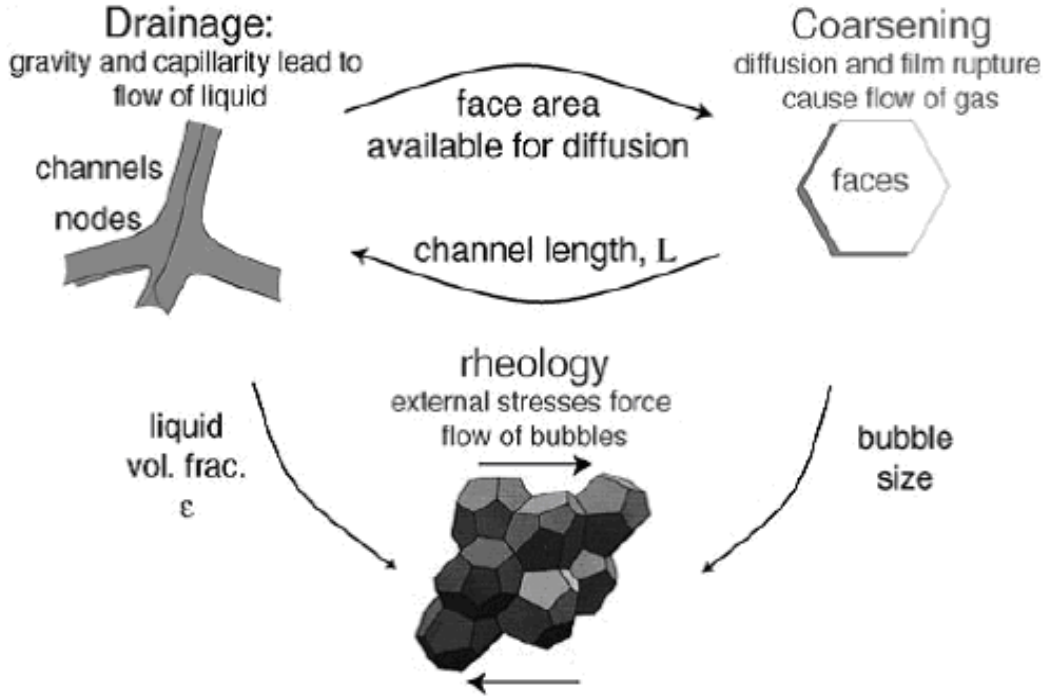

Figure 2.18: The drainage process (Stone et al., 2003).

Conclusion

It has been shown that considerable studies have already been undertaken on the physical aspects of foam theories, such as Plateau rules, quantitative description of foam structure, coarsening and liquid drainage. In recent years, scientists have been increasingly interested in modelling and simulation of foam structure and drainage behaviours. Several 2D and 3D models, such as Q-Potts model, vertex model and random packing model, have been developed. After the appearance of Surface Evolver, developed by Brakke (1996), there was a rapid progress in 3D foam simulation work based on Voronoi tessellation. In particular, the studies from Kraynik and Neethling constitute the basis of the modelling and simulation method in this thesis.

Even though both Neethling and Kraynik et al. succeeded in reproducing periodic foam structure, no work had been carried out to relate the surface and internal structure of foam. This was the primary task of this work.

CHAPTER III

METHODOLOGY

Introduction

Due to the great difficulty and high cost involved in experimentally measuring the internal structure of foam, computer simulations of foam structure are employed in this work. In this chapter, the method and techniques used to produce realistic foam structures will be described.

The three basic steps required to produce a realistic foam structure with a free surface are:

1) Create an initial fully periodic foam structure which is similar to that of a real foam and possesses the desired bubble size distribution. The initial structure should fulfil the topological, though not necessarily the geometric requirements of Plateau's Rules.

2) Slice through one of the periods to produce 2 free surfaces.

3) Minimise the surface energy of the foam, subject to the constraints that the bubble volumes must remain constant. Topological and geometric transitions will be carried out to systematically reduce the total surface energy.

In this work, 3D Voronoi tessellation is used to produce the initial foam structures. This is because they both fill space and display topological similarities to real foams. The distribution of bubble sizes within the foam can be controlled by varying the distribution of the seed points used to generate the Voronoi tessellation. Two different methods of placing random seed points, constrained random placement (CRP) and Monte Carlo (MC) method, are introduced.

Once the initial Voronoi tessellations have been implemented, these structures need to be modified and relaxed in order to meet the Plateau's rules and evolve into an energy minimum. The energy of foam is predominantly surface energy. The Surface Evolver package is used to carry out this energy-minimising task. A large number of topological and geometric transformations are triggered during the course of structure relaxation and energy reduction.

3.1 Producing Voronoi tessellations using constrained random placement method

In this work, Voronoi tessellation is used to generate the initial foam structure which displays sufficient randomness and disorder. Simply put, a Voronoi tessellation is the partition of the volume into cells centered upon the individual sites in such a pattern that all points within a cell are closer to that site than to any other sites in the system.

3.1.1 Basic definitions

A Voronoi tessellation is an arrangement of domains which fills space. In two dimensions, these domains are polygons and in three dimensions they are polyhedra. All the polygons or polyhedra generated in a Voronoi tessellation are convex. The Voronoi tessellation is topologically similar to a real foam (Kraynik et al., 2003), with 3 faces meeting at an edge and 4 edges at a vertex. Thus it is a convenient starting point for foam simulation.

Constrained random placement (CRP) means that the coordinates of the initial seed points are assigned randomly in the 3D space, subject to a minimum point-point distance constraint. Within a certain range, the range of bubble sizes produced by Voronoi tessellation increases with the decreasing minimum distance. This will be explained with more details in Section 3.2.

An empirical estimation of the minimum distance, $D_{\min}$, is given by Equation 3.1 (Neethling, 2004). Equation 3.1 is based on the calculation of the average distance between the centres of two adjacent cells in random close packing of spheres. The prefactor, 1.64, is an empirical coefficient for the approximate densest random packing by random placement method, which is larger than the figure for cubic close

packing of equal volume spheres, 1.12. This is because cubic close packing can not be achieved by randomly placing the points. S_{fac} is a space factor that controls how far the packing is from the densest random close packing. Therefore, in the simulation, S_{fac} should always be less than 1.0. Otherwise, the program will fail to place all the points in the system.

$$D_{\min} = 1.64(X_{\max} \cdot Y_{\max} \cdot Z_{\max} / N_P)^{1/3} \cdot S_{fac} \qquad (3.1)$$

where

$X_{\max}$, $Y_{\max}$, $Z_{\max}$ = maximum values of *x, y, z* coordinates;

N_P = number of points;

S_{fac} =space factor that controls how far the system is from the densest random close packing.

3.1.2 The steps of producing a foam structure

The initial conditions of simulation are described below:

a) The system is periodic, with length of period equal to 1.0 in each direction. Mathematically, this space is described as follows: for any point $A(x, y, z)$ in the prescribed space, its coordinates are subject to the constraints in Equation 3.2.

$$\begin{cases} 0 \le x \le 1.0; \\ 0 \le y \le 1.0; \\ 0 \le z \le 1.0; \end{cases} \qquad (3.2)$$

Equation 3.2 states boundary conditions for point assignment. The Voronoi

structure is initially fully periodic. It is subsequently sliced in one of the directions in order to produce two surfaces.

b) The polydispersity of foam is determined by the space factor, S_{fac}, in the CRP model.

The basic steps for producing an initial 3D Voronoi structure are:

Step I: Randomly assign the coordinates of the seed points, subject to the constraint of the minimum distance between points defined by Equation 3.1:

Step II: Make a 3D Delaunay triangulation. A Delaunay triangulation for a set of points is a collection of edges, for each of which we can find a circle containing the edge's endpoints but not containing any other points.

In the beginning, the program finds the nearest two points in the system. A third point is then found in the system so that it forms the smallest circumcircle, with no other points enclosed. A fourth point is chosen to form a circumsphere which contains no other points. Finally, the four points are connected to form an initial tetrahedron, with its four triangular facets being numbered. The second tetrahedron is set up by connecting the 3 points on one of the tetrahedron's facets to another point in the system such that there are no other points within the circumsphere passing through the four prescribed points. In a similar pattern, the program repetitively connects other available points to the existing tetrahedra. As a result, the space is filled with an intricate 3D triangle network, known as a 3D Delaunay Triangulation (Figure 3.1). Each triangular face and tetrahedron is assigned a unique ID.

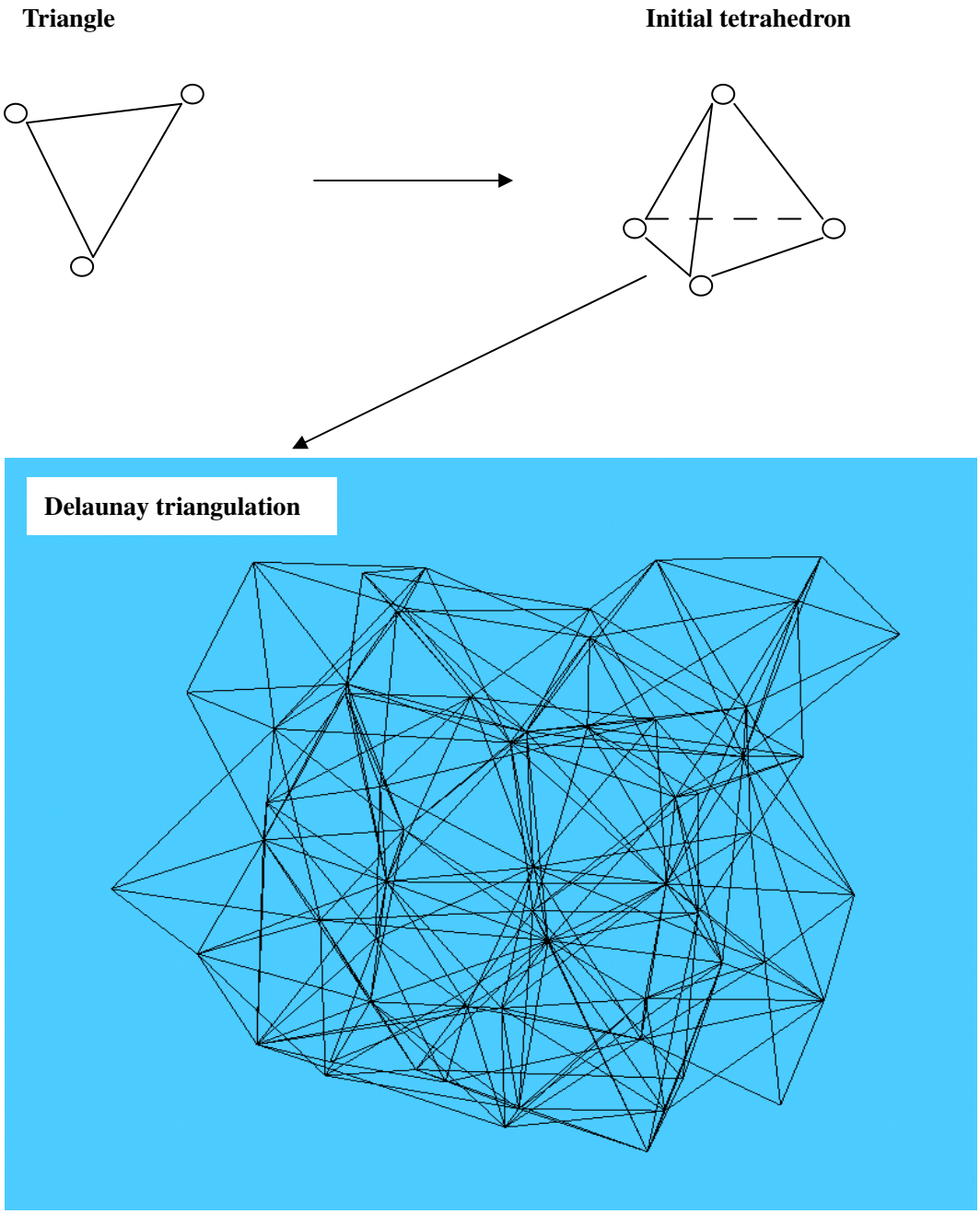

Figure 3.1: The steps of making a 3D Delaunay triangulation.

Step III: Create faces. Based on the tetrahedra produced in Step II, a face is created by connecting the circumcentres of all the tetrahedra that share a particular common tetrahedron edge. Each tetrahedron edge is actually shared by a number of triangular faces which are shared by two adjacent tetrahedra. The edges of the faces are created by connecting the circumcentres of two tetrahedra that share a common triangular

face. This step is finished when all the circumcentres of the tetrahedra that share a common tetrahedron edge are connected and form a polygon.

Step IV: Create bodies. Bodies are the volumes enclosed by all the faces that are created from tetrahedra sharing a particular common seed point. This seed point is thus within the body.

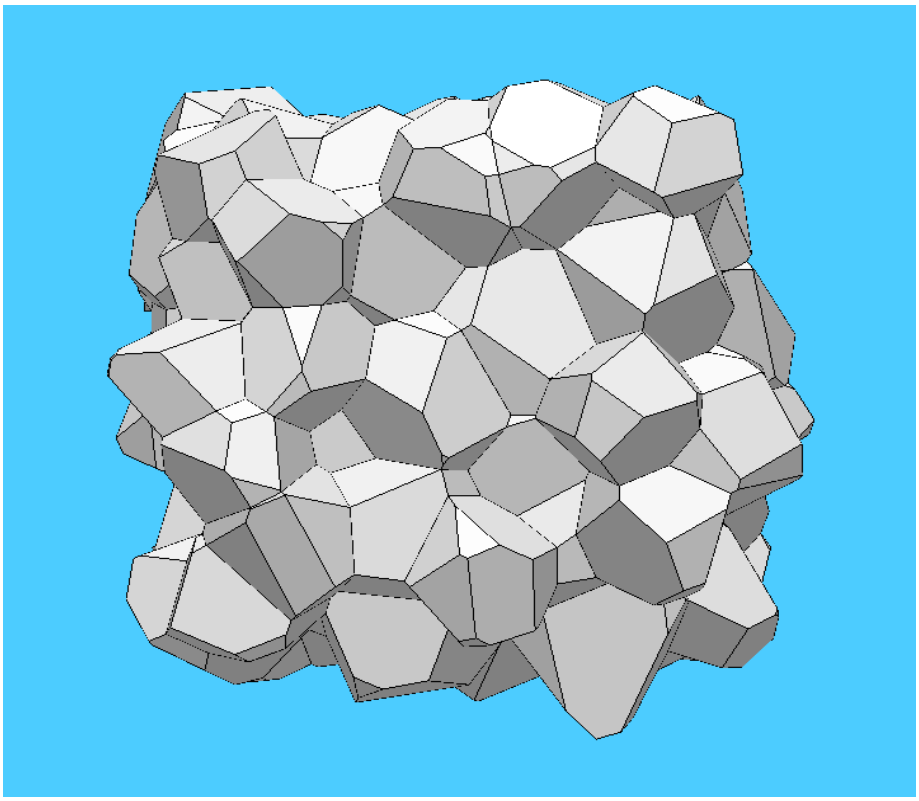

Figure 3.2: The 3D Voronoi tessellation used as the initial input structure for the foam simulation.

Step V: Identify the normal direction of a face. In Surface Evolver, the bodies are defined by the enclosure of a series of faces (Figure 3.2). An individual bubble is created by connecting all of its logical faces. Each face has either inward or outward normal directions. As the faces are flat and convex, the cross product between the vectors connecting subsequent points on the face gives the direction of the outward normal. If the dot product of this normal vector and a vector connecting a point within

the bubble and the point used to calculate the normal vector is positive, the face has an outward normal. Otherwise, the normal direction is inward. Figure 3.3 shows the determination of the outward normal of a facet. Vector $\vec{n}$ is the outward normal direction of the facet, $\overline{abcd}$, which is defined by the cross product of vector $\overrightarrow{ab}$ and $\overrightarrow{ad}$. Point o denotes an arbitrary point inside the bubble. θ is the angle between $\vec{n}$ and $\overrightarrow{oa}$. If $\cos\theta > 0$, face $\overline{abcd}$ has an outward normal. In this work, all the foam faces must have an outward normal direction.

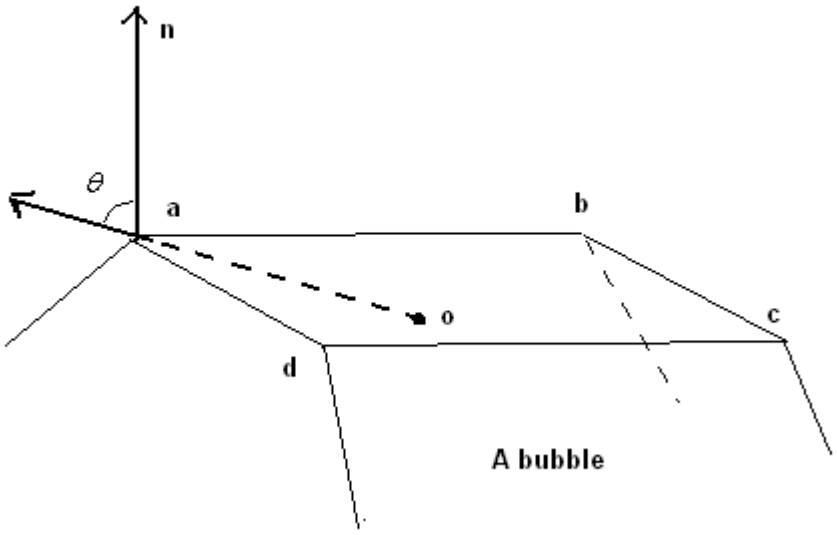

Figure 3.3: The outward normal of a facet of a bubble.

Step VI: Calculate the volume of a bubble. The volume of an arbitrary convex polyhedron can be calculated as follows: divide the polyhedron into a collection of tetrahedra; then sum up the volumes of all the tetrahedra. For a tetrahedron with vertices $A=(a_1,a_2,a_3)$, $B=(b_1,b_2,b_3)$, $C=(c_1,c_2,c_3)$ and $D=(d_1,d_2,d_3)$, the volume, $V_{tetra,i}$, is given by Equation 3.3.

$$V_{tetra,i}=\frac{|(A-D)\cdot(B-D)\times(C-D)|}{6} \tag{3.3}$$

Due to the great difficulty in graphically interpreting this method for an arbitrary convex polyhedron, the corresponding calculating procedure for a cube is used as an example to simplify the description (Figure 3.4).

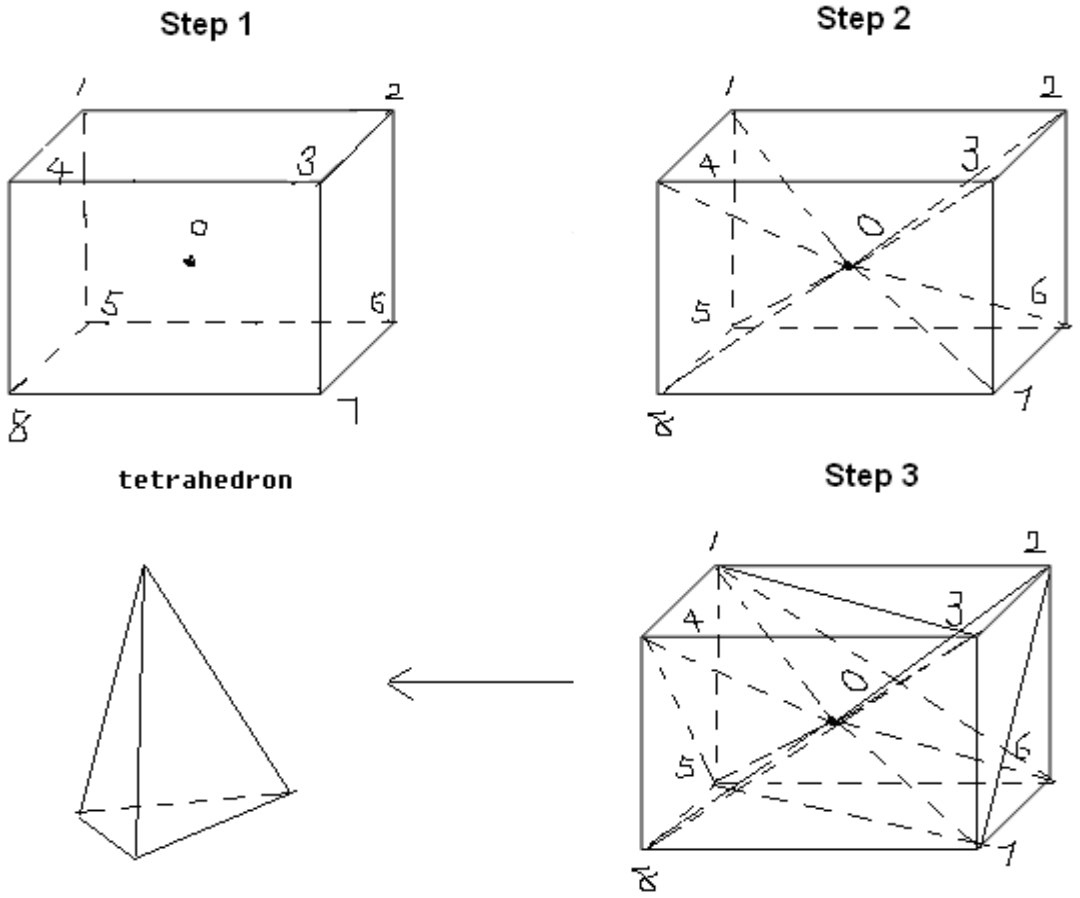

Figure 3.4: The process of calculating the volume of an arbitrary convex polyhedron.

For the given convex polyhedron 1-2-3-4-5-6-7-8 (Figure 3.4), an arbitrary point O is found inside it. Then point O is connected with all the vertices of the polyhedron. As a result, the original polyhedron is partitioned into several 'pyramids' which share a common vertex, O. The pyramids are further divided into a number of tetrahedra by connecting the vertices of the polyhedron. The total volume of the given arbitrary

convex polyhedron, $V_{tetra,\,i}$, is given by Equation 3.4:

$$V_{total} = \sum_{i=1}^{n} V_{tetra,\,i} \tag{3.4}$$

Step VII: Produce a free surface. The initial foam created in the previous steps is fully periodic. For the purpose of studying the bubble size distribution on the foam surface, the periods need to be cut in one or two, or even three directions, in order to produce free surfaces. The free surface is created by considering a virtual plane sliced through one of the periods. Any bubble that intersects this plane is removed. This is achieved by finding every edge that has a point on either side of the plane. This edge is removed together with any faces connected to the edge and any bubbles connected to the faces.

Figure 3.5 and 3.6 show the foams before and after boundary-cutting along the *Z* axis, with a free surface along the *Z* direction.

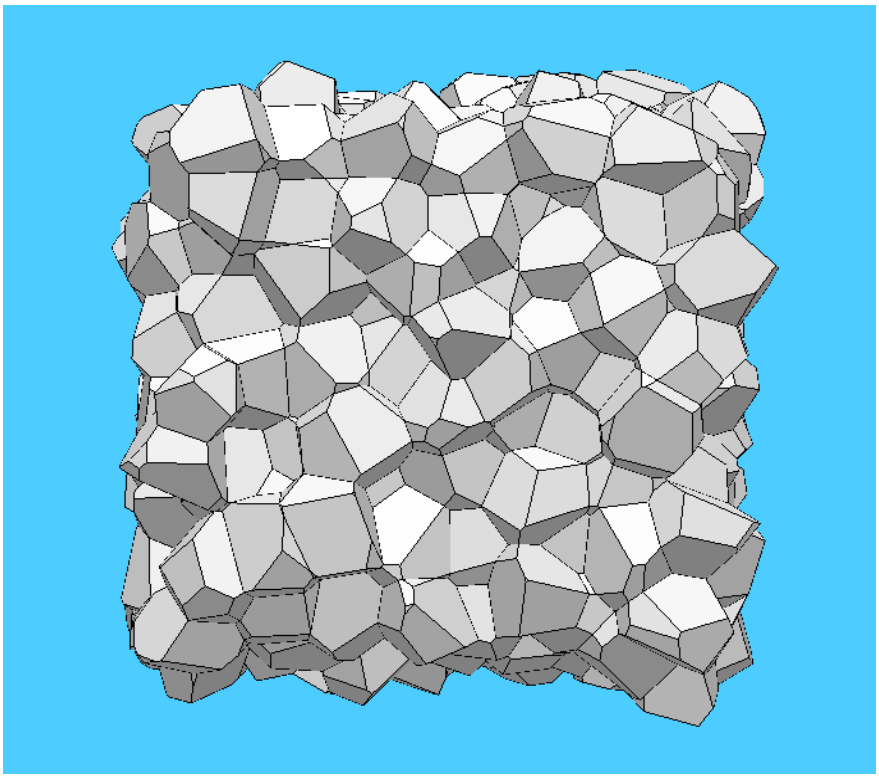

Figure 3.5: An example of a fully periodic Voronoi tessellation.

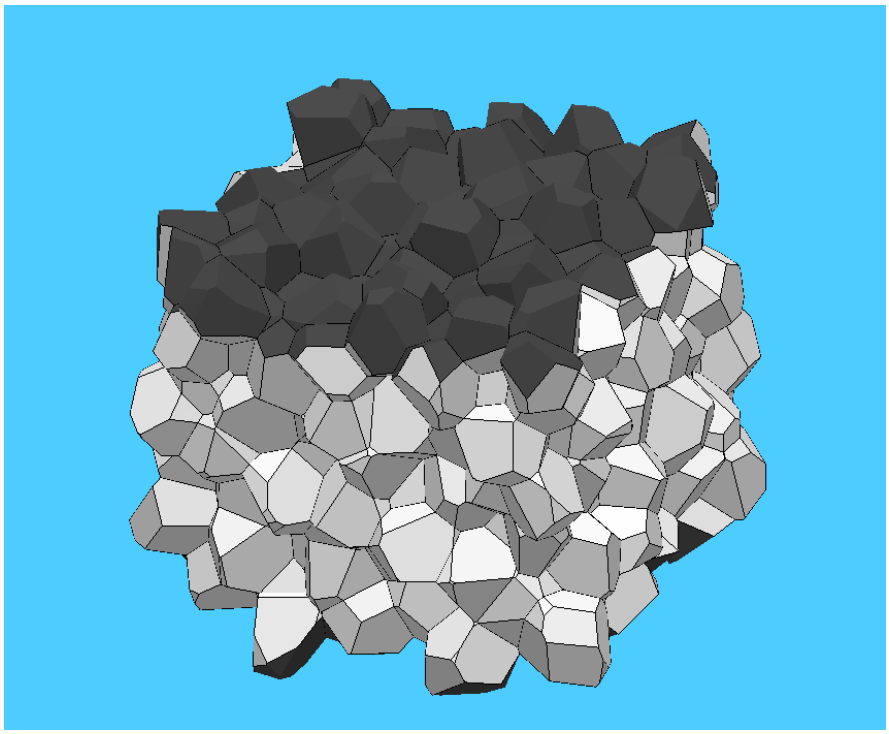

Figure 3.6: The Voronoi tessellation from Figure 3.6, but with a free surface along the *Z* axis.

3.2 Producing Voronoi tessellations using Monte Carlo method

The constrained random placement (CRP) method, together with Voronoi tessellation, is a good starting point for producing random foam structures. However, the volumetric disorder of foams produced using this method is not sufficiently high. Although no theoretical explanation for this limitation has been reported, Xu and Li (2009) have demonstrated that, for a given number of points, a upper limit of volumetric disorder of the cells (measured by normalised standard deviation of cell volumes) produced by Voronoi tessellation exists for complete random placement method ($S_{fac} = 0$). In this work, a large number of simulations have established that, for 500 points, the approximate upper limit of the normalised standard deviation (NSD) of bubble radius is 0.16. For 1500 points, this upper limit can increase to 0.18, which is rarely obtained. Table 3.1 gives an approximate correlation between the value of S_{fac} and the obtained normalised standard deviation. In Table 3.1 the value of NSD will show small variance if the simulations with the same S_{fac} are repeated because points are randomly placed. Using a random number generator with a certain distribution will risk of creating foam structures without sufficient randomness.

S_{fac}	0.5	0.25	0.1	0.01	0.001	< 0.0001
NSD	≈ 0.03	≈ 0.08	≈ 0.12	≈ 0.16	≈ 0.16	≈ 0.16

Table 3.1: The approximate correlation between the value of S_{fac} and the obtained normalized standard deviation (NSD) of bubble sizes.

In this section, the factors constraining Voronoi tessellation based on CRP method will be identified and analysed. A new method, based on point-point interaction, is proposed to enhance the model's capacity to produce foams with much wider bubble

size distributions.

3.2.1 The limitations of the constrained random placement method

To investigate the mechanism which limits the CRP model from producing wider bubble size distributions, we first need to recall the step in which the initial seed points are randomly assigned. The pattern of assigning points plays a vital role in determining the width of the bubble size distribution.

The initial points placed in this step are the common vertices shared by the tetrahedra whose centres are defined as the vertices of a bubble. Due to this description, it can be reasonably concluded that, although the initially placed sphere centres do not necessarily represent the geometric centres of bubbles, they do roughly reflect the relative positions of the bubbles in the system. A 2D Voronoi tessellation graph is used to demonstrate the problem due to the difficulty in drawing and visualising a 3D structure.

Figure 3.7 shows the 2D Voronoi tessellation with 88 reasonably evenly-distributed initial seed points. In this graph, the initial seeds are placed approximately evenly in the 2D plane. The plane is then tessellated into a collection of area-filling polygons. Any point within a polygon is closer to the enclosed initial seed than to any other seeds. It is not difficult to observe that the area distribution of the grids is very narrow in the current layout of the initial points. In Figure 3.8, the distribution of the initial seed points becomes more uneven than that in Figure 3.7. As shown in Figure 3.8, the largest area is approximately 15 times larger than that of the smallest one. In a highly polydisperse foam, the ratio of the volume of the largest bubble over that of the smallest one can be a few hundreds. The reason is that, in the areas with high density of points, the radius of the circle is expected to be small in order to form a circumcircle around a given centre without other points inside. In the sparse areas in which the distance between points is relatively large, it is possible to partition the area

into relatively larger polygons. Therefore, creating an imbalanced and random distribution of the circle centres is crucial to broaden the 2D area distribution.

However, ordered structures should be avoided in simulations in order to preserve sufficient randomness in the foam structure. Figure 3.9 and 3.10 exhibit samples of extreme distributions of points, with all the points clumping into 3 and 1 clusters respectively. In these two unfavourable scenarios, the subsequent Voronoi tessellation, based on the layout in Figure 3.9 and 3.10, will not produce an ideally random foam structure. In this work, these cases are avoided by running the Monte Carlo simulation at very high temperature, which effectively prevents the points from aggregating into an ordered structure.

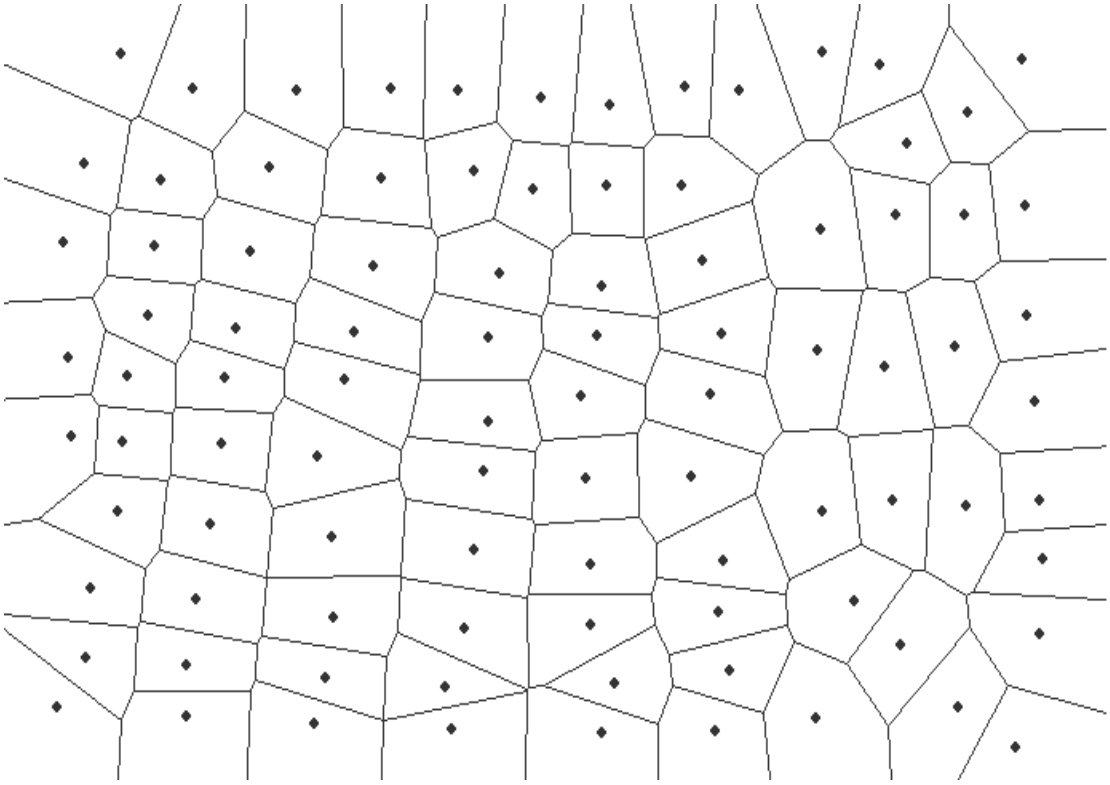

Figure 3.7: The 2D Voronoi tessellation with 88 evenly distributed initial points.

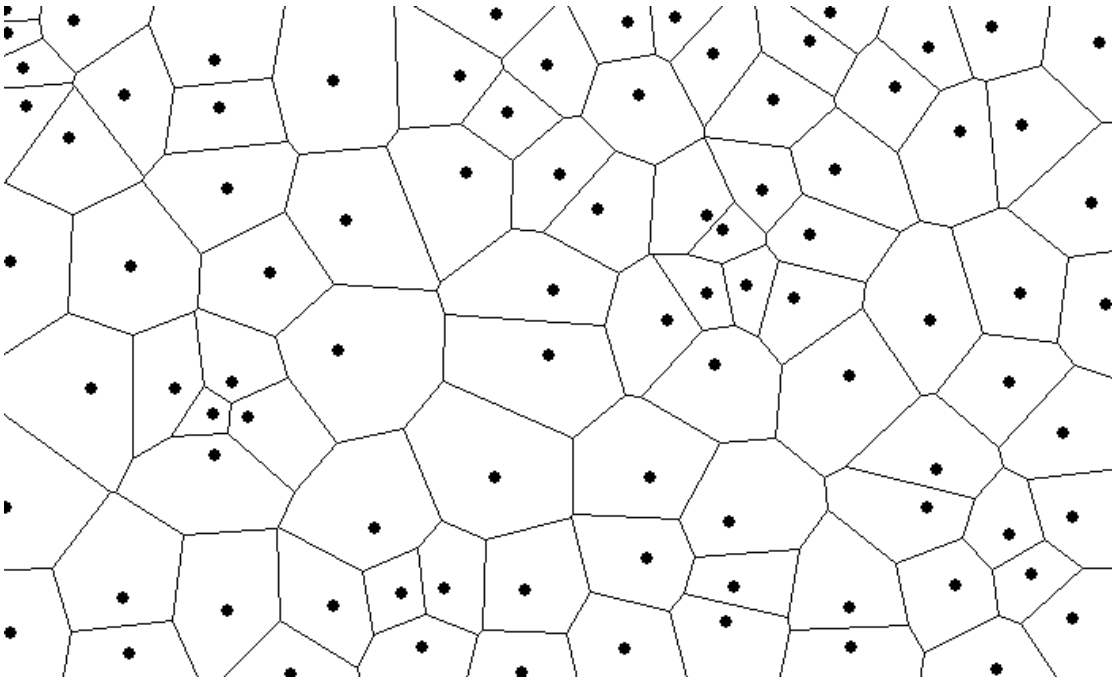

Figure 3.8: The 2D Voronoi tessellation with 88 unevenly distributed initial points

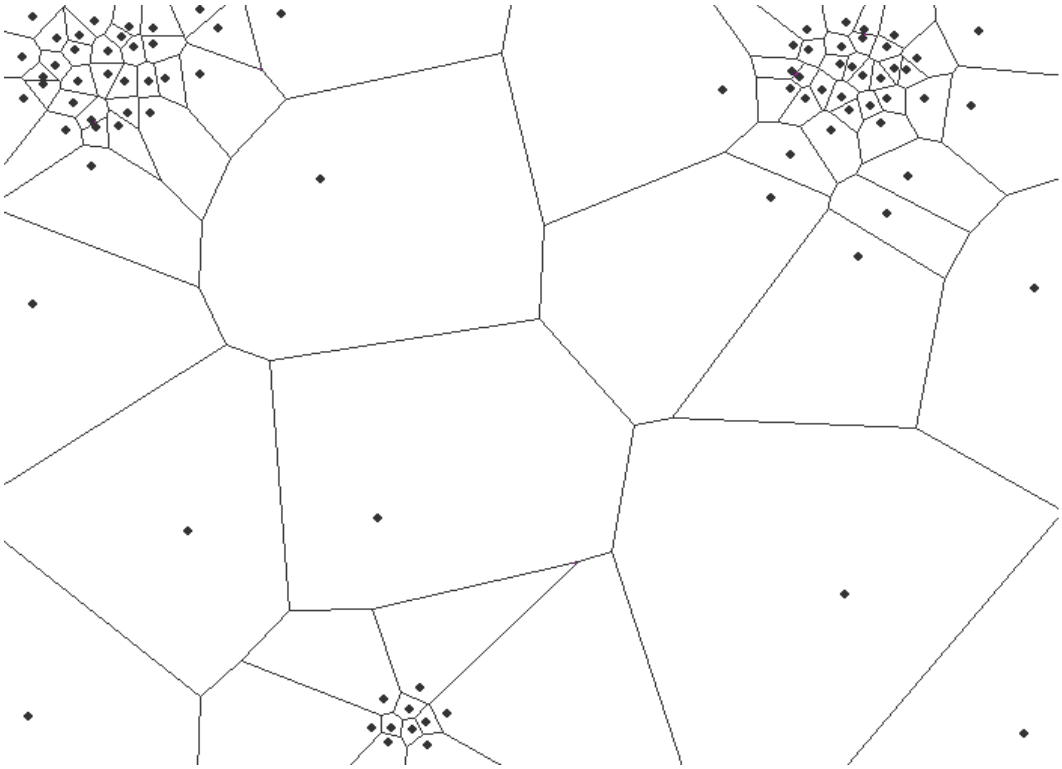

Figure 3.9: An extremely imbalanced distribution of 88 points. (3 point clusters are formed)

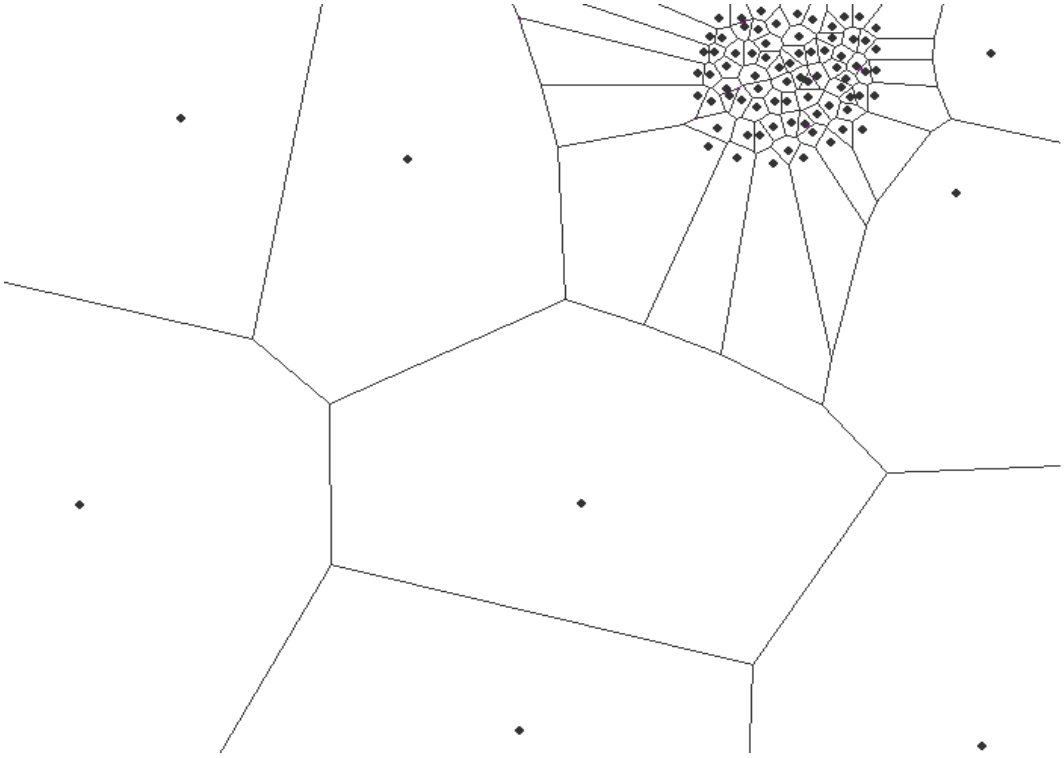

Figure 3.10: An extremely imbalanced distribution of 88 points. (1 point clusters is formed)

3.2.2 The Monte Carlo method

Extending the above analysis from a 2D case to a 3D case, it can be reasonably expected that the uneven distribution of seed points will result in a wider bubble size distribution. Small bubbles forms in the regions with high density of points, while, large bubbles are produced in the relatively sparse domains. That is the main mechanism proposed to increase foam polydispersity. In this work, normalised standard deviation (NSD), σ, is used to represent the level of foam polydispersity. NSD is the standard deviation of the dimensionless radii of the internal bubbles (normalised by the Sauter mean of the internal bubbles).

The Monte Carlo (MC) method used in this work is similar to the Monte Carlo simulation for molecular system which is effective in controlling 3D point distribution by introducing pairwise interaction between points (Landau and Binder, 2005). By this method, the positions of the initially randomly placed seeds are adjusted by

allowing interactions between them. These interactions are attractive at long range, promoting clumping, but repulsive at short range in order to stop the seed points collapsing onto a single location in space. This therefore has the desirable property of inducing a controllable degree of clumping and thus a controllable degree of polydispersity in the bubbles produced.

As the initial points are assigned in a fully periodic space, any molecule–environment interaction will not be considered. In addition, a few further simplifications and assumptions should be made:

1.) The points in the defined space are infinitely small isotropic molecules.

2.) Any movement of the points happens instantaneously. It means that the velocity of movement is not considered in the model.

3.) Intermolecular force is the only form of interaction between points. The intermolecular potential energy (pair potential) is the only component of the system energy. Pair potentials only exist during the interaction between two points and are determined by the distance between the two points. In this work, the energy of the pair potential, $E(x_{i,j})$, is defined by Equation 3.5 (Figure 3.11):

$$E(x_{i,j}) = 4.0\varepsilon[(\frac{x_{i,j}}{\omega_{LJ}})^{-8} - (\frac{x_{i,j}}{\omega_{LJ}})^{-4}] \quad (3.5)$$

Where:

$x_{i,j}$ = distance between points *i* and *j*;

ε = natural unit of energy;

ω_{LJ} = equilibrium distance.

In this work, ω_{LJ} is estimated by Equation 3.6 in which $x_{\max}, y_{\max}, z_{\max}$ denotes the maximum value of *x, y, z* coordinates respectively.

$$\omega_{LJ} = hD_{ave} \tag{3.6}$$

where $D_{ave} = (x_{\max} \cdot y_{\max} \cdot z_{\max} / N_p)^{\frac{1}{3}}$

h = a positive constant that controls the magnitude of the equilibrium distance relative to the average distance between points.

In Equation 3.6, D_{ave} denotes the average distance between points in the system. When $\omega_{LJ} << D_{ave}$ (or $h << 1$), the range of point-point interaction is much shorter than the average distance between points. The point system shows a disordered property. It is important to correlate ω_{LJ} with D_{ave} in the simulation as different number of points in the system will result in different average distance. The value of *h* is 0.01 in this thesis, which is determined empirically by balancing the maximum polydispersity obtained and the time cost of the simulations. If *h* is smaller than 0.008, higher polydispersity is achieved, but the simulation time is formidably long. If *h* is larger than 0.04, the maximum polydispersity obtained shows a noticeable decrease.

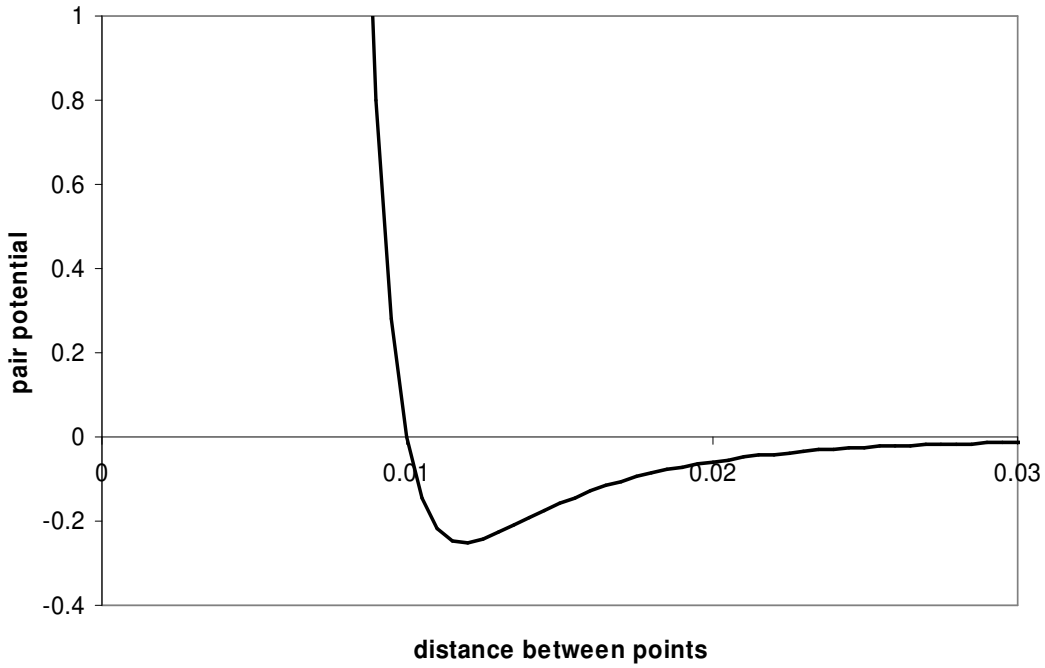

Figure 3.11: The relationship between the distance between points and the pair potential energy. (based on Equation 3.5, $\omega_{LJ} = 0.01 D_{ave}$)

Equation 3.5 is an empirical formula transformed from Lennard-Jones potential formula (Equation 3.7), which was proposed by John Lennard-Jones (1924):

$$\frac{E(x_{i,j})}{\varepsilon} = 4.0[(\frac{x_{i,j}}{\omega_{LJ}})^{-12} - (\frac{x_{i,j}}{\omega_{LJ}})^{-6}] \qquad (3.7)$$

Lennard-Jones potential (also referred to as the 6-12 potential) is an empirical mathematical model that represents intermolecular behaviors. The $(\frac{x_{i,j}}{\omega_{LJ}})^{-12}$ term denotes the repulsion and $(\frac{x_{i,j}}{\omega_{LJ}})^{-6}$ term describes the attraction. The ω_{LJ} term reflects the equilibrium distance between points (where $E(x_{i,j}) = 0$).

Many other modified Lennard-Jones potentials were proposed for different molecular

systems, such as '6-8' and '4-6-12' potentials (Kaplan, 2006). In this work, '4-8' potential is used in order to extend the 'cut-off' distance between points, which results in a slower transition between repulsive and attractive forces. A slow force transition usually results in a slower rate of convergence of simulations. A large number of simulations with different power combinations have established that Monte Carlo simulations with '4-8' potential has a 'desirable rate' of convergence. A 'desirable rate' in this context means that the Monte Carlo simulation runs slow enough for us to obtain different levels of polydispersity approximately every half hour in the course of simulation, instead of reaching an equilibrium status in a few minutes. In the meanwhile, it has reasonable CPU time (typically less than eight hours). In this sense, the purpose of introducing '4-8' pair potential between points is to obtain a 'controllable' numerical procedure rather than implement accurate molecular dynamic simulations.

The total intermolecular potential energy is taken to be a sum of all the isolated pair interactions. Hence,

$$E_{total} = \sum_{i} \sum_{j} E(x_{i,j}) \quad (i < j \text{ and } i, j = 1, 2, 3 \ldots N) \tag{3.8}$$

The basic steps for producing polydisperse foams by Monte Carlo method can be described as follows:

Step I: The coordinates of the initial seed points are assigned by a random number generator with uniform distribution. The initial system energy, $E_{total}^{(0)}$, is calculated.

Step II: Point *i* is selected randomly and moved by a random displacement in the periodic system.

Step III: The change of the system energy, ΔE_{total}, corresponding to the random

displacement, is calculated. If $\Delta E_{total} < 0$, the new coordinates of point i is accepted and go to step II. Otherwise, it has the probability of $e^{-\frac{\Delta E_{total}}{kT}}$ being permitted. k is a Boltzmann constant, T denotes the absolute temperature of the system, which is treated as a constant in this work. However, if the number of points in the simulation increases, T should increase correspondingly. This is because the density of the system increases when more points being added into the system. This results in a higher probability of a point being placed into the effective range of pair interaction which usually results in a decrease in total energy. Therefore, the rate of convergence is likely to be higher. To maintain the approximate same rate of convergence, temperature should be increased. This impact can be neglected in this work because the number of points in the simulation is always constant.

Repeat step II and III (defined as one Monte Carlo step) for a sufficient number of times (15,000 – 50,000 in this work) in order to obtain a favourable 3D layout of seed points for the Voronoi tessellation.

It is very important to implement this Monte Carlo simulation at very high temperature (> 3000). This is to run the simulation in a disordered phase (Landau et al., 2005 and Valleau, 2005). Due to Equation 3.6, the range of force defined by Equation 3.5 is approximately 1% of the average distance between points. This can be approximated as a gas system which has a relatively low critical temperature for the order-disorder phase transition. Estimating the critical temperature of this system is out of the scope of this work. However, extensive Monte Carlo simulations in this work have shown that point distributions are disordered at temperature above 3000. In fact, high temperature results in a large value of $e^{-\frac{\Delta E_{total}}{kT}}$, which allows a large number of molecular movements causing energy increase. As a result, a large portion of molecules 'diffuse' from high density region to low density region. When temperature

is infinitely high ($T \to \infty$), $e^{-\frac{\Delta E_{total}}{kT}}$ reaches to 1.0, which means any movement will be allowed. The Monte Carlo simulation will become a stochastic process, without converging to any featured configuration.

Figure 3.12, 3.13 and 3.14 demonstrates the importance of running the MC simulations at high temperature. Figure 3.12 (viewed from X-Y plane) exhibits the 500 initial seed points assigned by the random placement method. The configurations viewed from Y-Z and X-Z planes appear to be very similar. The corresponding normalised standard deviation for the resultant random foam is 0.15 (moderately polydisperse). The Monte Carlo simulation is employed at very low temperature (T = 1.0, $\omega_{LJ} = 0.01 D_{ave}$) to change the 3D distribution of the 500 seed points displayed in Figure 3.12. As shown in Figure 3.13, after 50,000 MC steps, all the points have collapsed into a few regions, whilst the other regions are almost empty. This shows that at low temperature the system will 'condense', which is undesirable as an initial point distribution for a random foam.

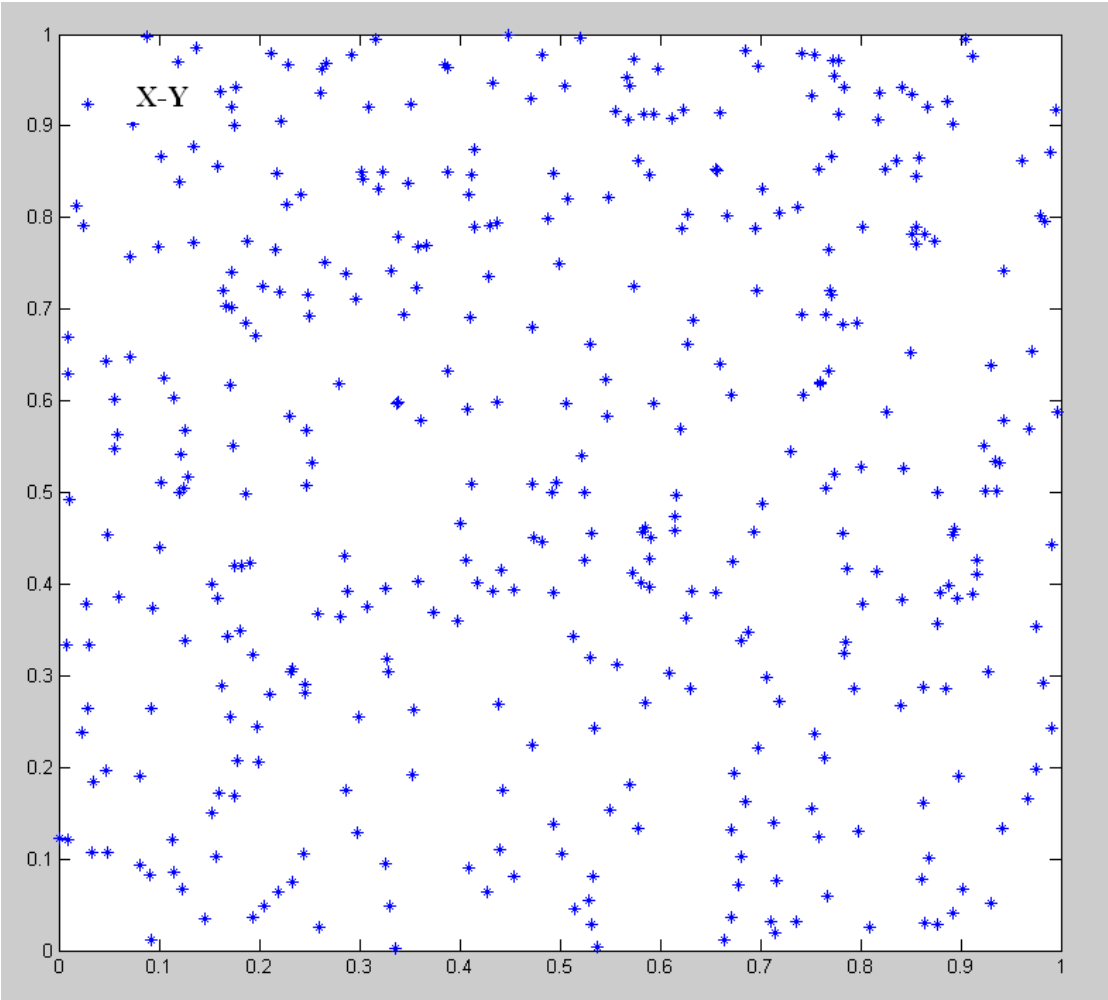

Figure 3.12: The 3D layout of 500 randomly assigned seed points (viewed from X-Y plane). The corresponding NSD is 0.15. Point distributions viewed from Y-Z and X-Z planes exhibit a similar configuration.

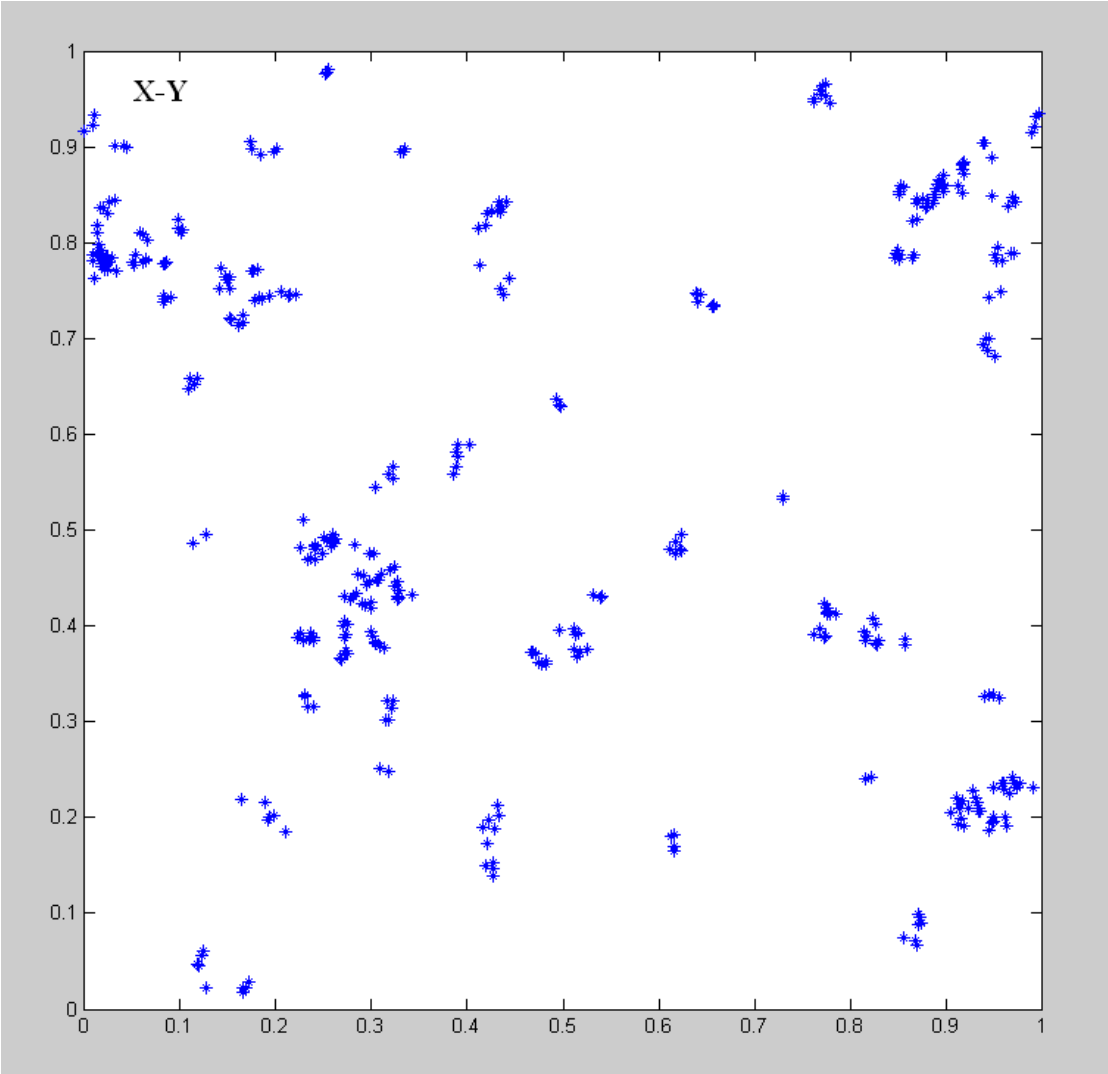

Figure 3.13: The layout of 500 seed points after 50,000 MC steps with T = 1.0 and $\omega_{LJ} = 0.01D_{ave}$ (viewed from X-Y plane). Point distributions viewed from Y-Z and X-Z planes exhibit a similar configuration.

Figure 3.14 shows the layout of the same 500 initial seed points resulted from the Monte Carlo simulation at very high temperature (T = 3500 and $\omega_{LJ} = 0.01D_{ave}$) with the same number of MC steps (50,000 MC steps). As shown in Figure 3.14, the seed points are disorderedly and randomly distributed in the 3D space, with some regions having relatively higher level of clumping. The maximum number of MC steps that have ever been tried in this work is 1,000,000 (T = 3500 and $\omega_{LJ} = 0.01D_{ave}$) (Figure 3.15). No 'point condense' has ever been observed from simulations at temperature

larger than 3000. The number of MC steps adopted in this work ranges from 15,000 to 50,000. Simulations running within these 'safety zones' (T > 3000 and MC steps are 15,000–50,000) can avoid unfavourable point-clumping and effectively produce highly polydisperse foams.

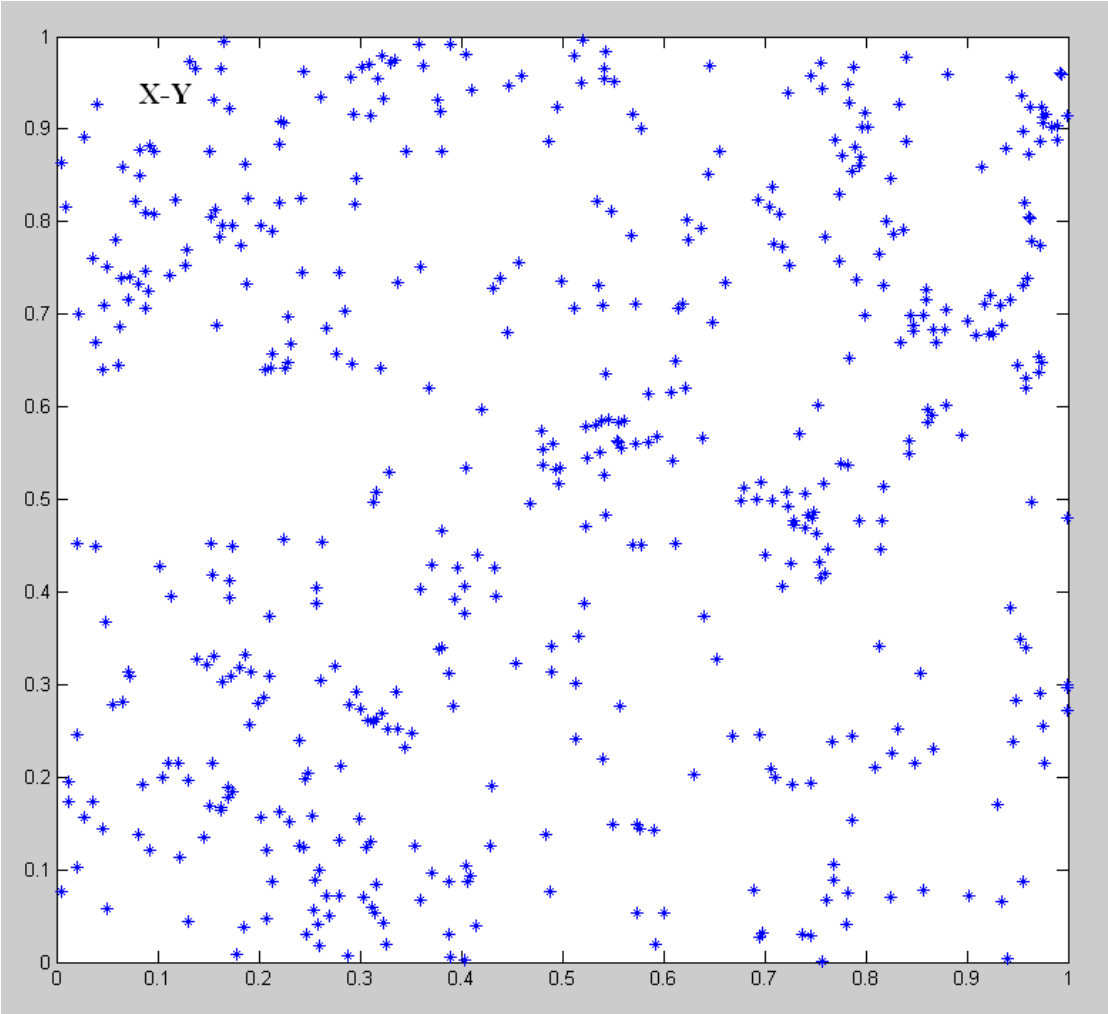

Figure 3.14: The layout of 500 seed points after 50,000 MC steps with T = 3500 and $\omega_{LJ} = 0.01 D_{ave}$ (viewed from X-Y plane). The corresponding NSD = 0.31. Point distributions viewed from Y-Z and X-Z planes exhibit a similar configuration.

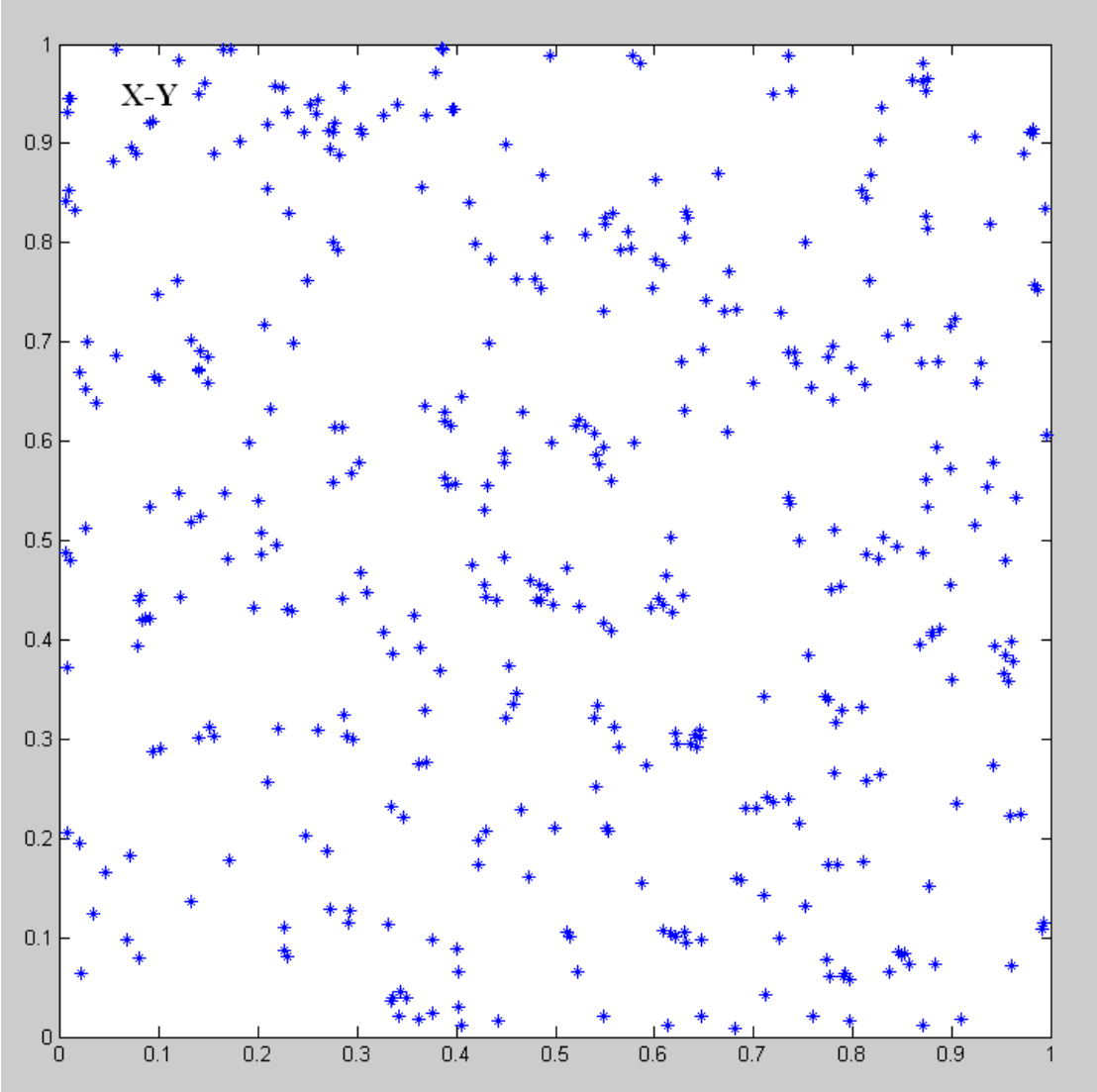

Figure 3.15: The layout of 500 seed points after 1,000,000 MC steps with T = 3500 and $\omega_{LJ} = 0.01 D_{ave}$ (viewed from X-Y plane). The corresponding NSD = 0.32. Point distributions viewed from Y-Z and X-Z planes exhibit a similar configuration.

The procedure for producing the foam structure by the Monte Carlo method is the same as that described in section 3.1, including: producing tetrahedra, creating bubbles with tetrahedra and cutting foam periods.

Figure 3.16 shows that the comparison between the bubble size distribution produced with the Monte Carlo method and the broadest distribution obtained from the constrained random placement method (NSD = 0.16). The bubble size distributions of

foams produced by the Monte Carlo method are significantly wider than that produced by constrained random placement method.

Table 3.2 compares the ranges of polydispersity produced by the two different methods. The normalized standard deviation of the bubble sizes of a foam produced by the MC method is twice as large as that created from the traditional CRP method. This evidence gives us the confidence that 'implementing' a Monte Carlo molecular simulation at high temperature will significantly improve the capacity of the model to produce highly polydisperse foams.

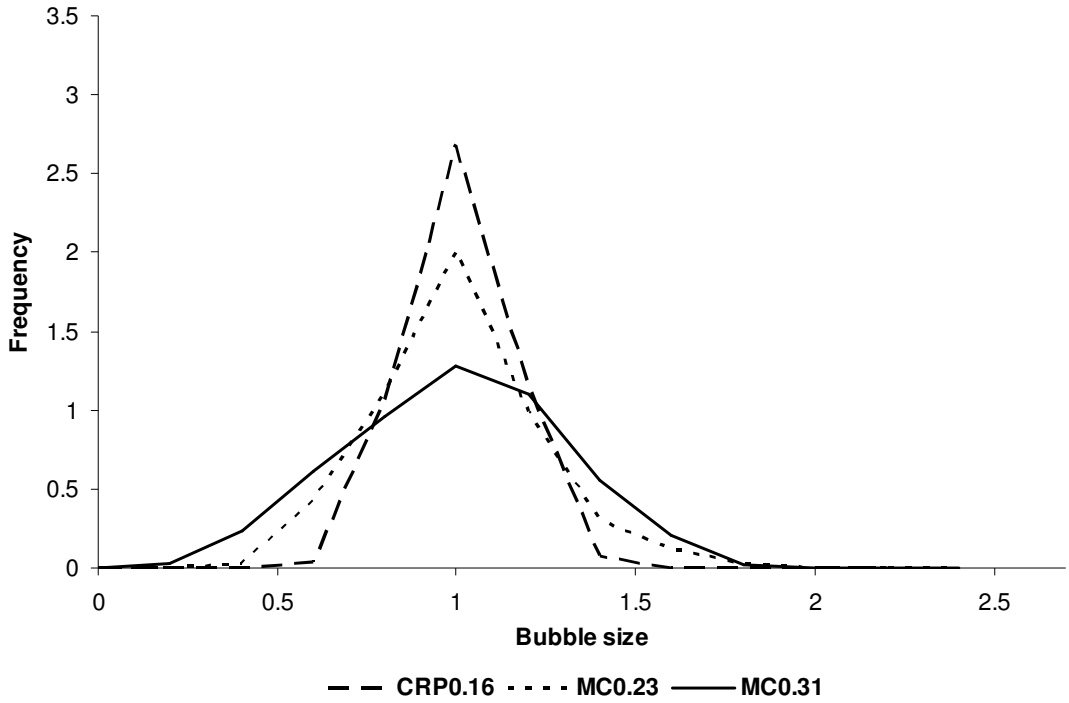

Figure 3.16: The bubble size distributions produced by Monte Carlo (MC) method and Constrained Random Placing (CRP) method. (CRP0.16 = produced by Constrained Random Placement method with NSD = 0.16; MC0.23 = produced by Monte Carlo method with NSD = 0.23; MC0.31 = produced by Monte Carlo method with NSD = 0.31.)

Method	Monte Carlo	Random placement
The range of NSD	0.0 – 0.31 (The standard deviation may be increased slightly by increasing the number of Monte Carlo steps.)	0.0 – 0.16 (0.16 is the highest polydispersity that has ever been produced in this work)

Table 3.2: The levels of foam polydispersity produced by the Monte Carlo method and the constrained random placement method.

3.3 The control of the bubble size distribution

It has been ascertained above that highly polydisperse foams can be effectively produced by the Monte Carlo method. Another challenge is that we often need to produce foams with certain range of normalized standard deviation in order to study the impact of polydispersity to the foam properties. This requires controlling the bubble size distributions in the simulation, which is essentially determined by the 3D distribution of the seed points. Thus it is important to explore the impact of the parameters of Monte Carlo molecular simulation on the final bubble size distribution.

Recall Equation 3.5 and Monte Carlo simulations, three parameters may influence the 3D layout of the seed points: the number of MC steps, the equilibrium distance between points, ω_{LJ} and the temperature of the system.

3.3.1 The number of Monte Carlo steps

In a Monte Carlo molecular simulation at a constant high temperature, a certain level of imbalance in point distribution will form after a sufficient number of MC steps. In practice, it is important to know the approximate correlation between the number of MC steps and the resultant normalized standard deviation. This aims to produce foams with controllable bubble size distributions. Figure 3.17 shows this relationship for simulations with T = 3500 and $\omega_{LJ} = 0.01D_{ave}$. Each NSD shown in Figure 3.17 is the mean of 3 runs, with error bars less than 10%. It is worth mentioning that, for a given number of MC steps, it is impossible to obtain exactly the same NSD in each run because of the stochastic nature of Monte Carlo simulation and the random layout of the initial points. Figure 3.17 is used as a reference graph for estimating the approximate number of MC steps (T = 3500) for a given level of polydispersity. Without explicit notification, all the Monte Carlo molecular simulations in this work

are implemented at T = 3500. To produce a foam with NSD = 0.31, roughly 50,000 MC steps need to be carried out. And, for foam with NSD = 0.20, approximately 3,000-4,000 MC steps will be enough.

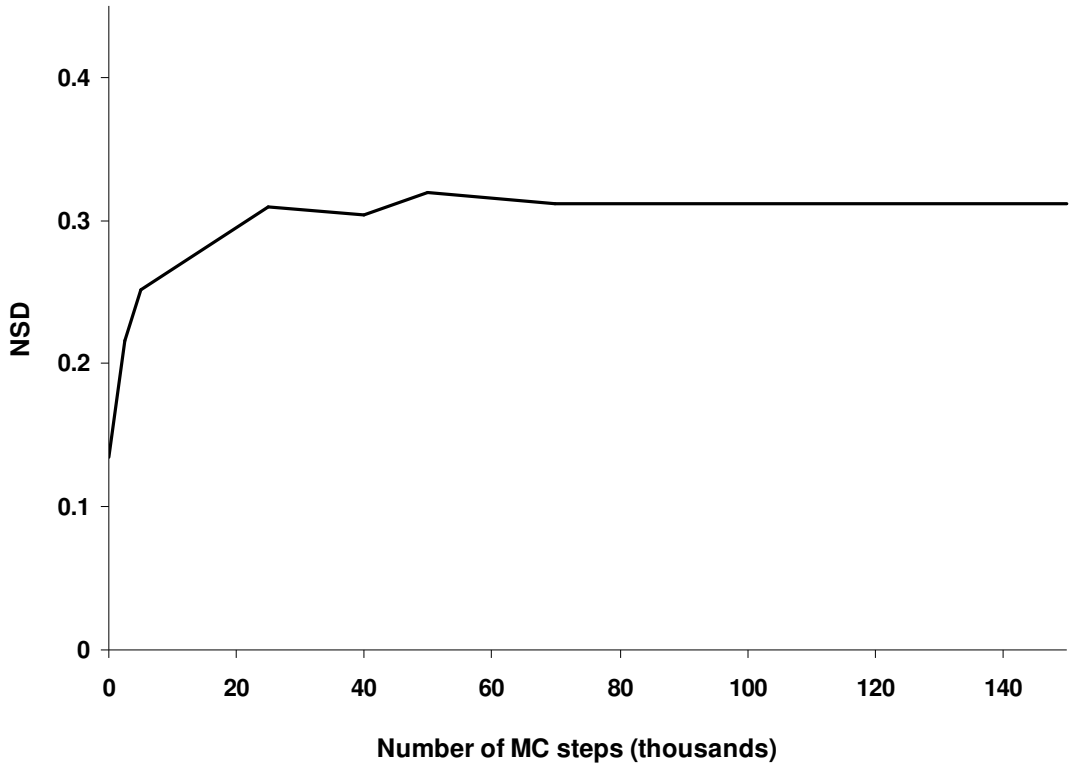

Figure 3.17: The impact of the number of MC steps to foam polydispersity. (T = 3500 and $\omega_{LJ} = 0.01 D_{ave}$).

As shown in Figure 3.17, after 50,000 MC iterations, the system is approaching its equilibrium state. Continuing to increase the number of MC steps does not raise the value of NSD further, instead, a very slight fluctuation is observed. This is the reason that a maximum of 50,000 MC steps is adopted in most of the simulations.

3.3.2 The equilibrium distance between seed points

The equilibrium distance between seed points, ω_{LJ}, determines the distance at which

points have zero pair potential. In the simulation, the equilibrium distance is related to two important parameters: the approximate minimum distance between seed points and the minimum-energy distance. Although there is no restriction on the minimum distance between two points, points are not likely to be placed nearer than ω because the pair potential energy shoots up sharply when the distance is less than ω (Figure 3.11), which means this attempt has very low probability to be permitted. Therefore, the value of the equilibrium distance in Lennard-Jones model strongly influences the maximum density of points in the simulation. Recalling Equation 3.5, the minimum-energy distance $x_{E\min}$ can be derived from the following two conditions: $E(x_{i,j})_x = 0$ and $E(x_{i,j})_{xx} > 0$, where $E(x_{i,j})_x$ is the first derivative of $E(x_{i,j})$ and $E(x_{ij})_{xx}$ is the second derivative of $E(x_{i,j})$. Applying the above two conditions, the following relationship can be obtained (Equation 3.9):

$$x_{E\min} = \sqrt[4]{2}\,\omega \approx 1.19\,\omega_{LJ} \tag{3.9}$$

This quantitative relationship has been graphically coupled by Figure 3.11 in which the location of $x_{E\min}$ is approximately $0.2\,\omega_{LJ}$ larger than the x coordinate of zero $E(x_{i,j})$.

Figure 3.18 shows the relationship between the equilibrium distance and the NSD of the foam (500 seed points, T = 3500). Foams under different numbers of MC iterations display a similar trend: all drops monotonically with the increasing equilibrium distance. This is because that, when the equilibrium distance increases, the minimum distance between points increases. As a result, the density of points in high density region decreases and the level of imbalance of the distribution drops. As a result, a narrower bubble size distribution will be achieved during the Voronoi tessellation process.

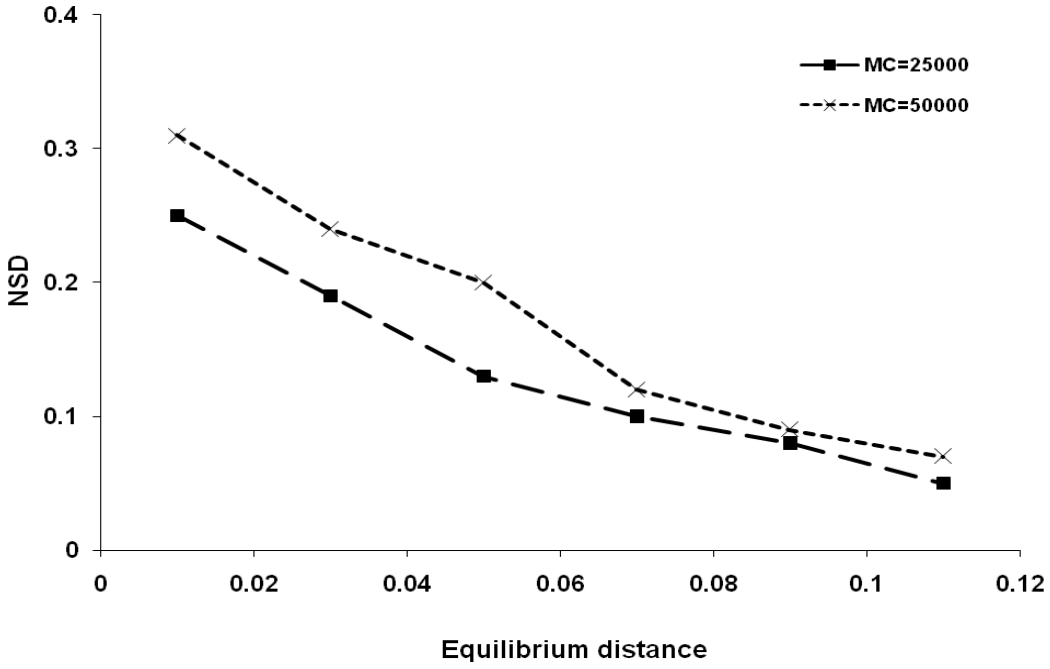

Figure 3.18: The impacts of the equilibrium distance to the polydispersity of foams. (500 points, T = 3500). MC = 25,000 and 50,000 means 25,000 and 50,000 MC steps are adopted respectively.

3.3.3 The temperature of the system

Temperature describes the thermodynamic state of a system. It is the result of motions of all the atoms or molecules which make up the system. In Monte Carlo molecular simulation, temperature reflects the internal energy of the system and influences the probability of the transition of a microscopic state if that transition triggers an increase of the total energy.

As elaborated in the previous section, both zero and infinite temperature is undesirable in the simulation. In this work, high temperature is carefully chosen (T = 3500) so that the point system has the desirable randomness and disorder. All the Monte Carlo molecular simulations are carried out at a constant temperature. Thus detailed study of the temperature is not of particular interest of this research project.

3.4 The Application of Surface Evolver

The initial foam structure generated by 3D Voronoi tessellation is far from equilibrium. Surface minimization and structure relaxation are thus required in order to obtain an ideal foam structure. Surface Evolver (Brakke, 1996) is applied in the simulation to achieve the minimum surface area structure based on the initial structure. The energy-reduction process is accomplished by defining a series of transformations which are realised by the command language of Surface Evolver. During the surface minimising process, a large number of topological changes are implemented. In the meantime, foam surface are refined and further minimised accordingly. Since the underlying structure also has contribution to the system energy, an annealing process is carried out to release the energy trapped in the internal structure.

3.4.1 System Energy

The Surface Evolver works by minimizing the total energy of the surface. Strictly speaking, in a foam system, the total energy can be decomposed into a few main sources: surface tension, gravitational energy and energy originated from geometric constraints on bubbles. In this work, gravitational potential energy is neglected in order to reduce the complexity of the model and the amount of computations involved. The only energy in the simulation is surface energy which is proportional to the total surface area since surface tension (or surface energy per unit area) is constant.

In Surface Evolver, each facet is considered to have a surface tension of 1.0 by default. Different facets may have different surface tensions, which can be defined by the initial data file. In this work the default value of surface tension, 1.0, is adopted. The value of surface tension does not influence the foam structure as it is constant and merely used to calculate the normalised surface energy. In a discrete form, the total surface energy is equal to the sum of all the facet areas times their respective surface

tensions. Letting γ be the surface tension and $A(i)$ be the area of facet. The surface energy of an individual facet, $E_S(i)$, can be defined as:

$$E_S(i) = \int_{S(i)} \gamma \cdot dA(i) \tag{3.10}$$

Thus the total surface energy, E_{total}, can be obtained by summing up the surface energy of all the facets:

$$E_{total} = \sum_{i=1}^{n} E_S(i) \tag{3.11}$$

3.4.2 Energy minimising process

The surface energy is understood to be affected by both the total foam surface area and the foam structure. This is because the shape and level of surface exposure of the top-layer bubbles are affected by the bubbles below the surface. The changes of the internal structure are highly likely to trigger transitions of surface features, such as the layout of surface bubbles and the distribution of surface films. Therefore, both the surface and the internal structure should be taken into account in order to evolve the system to an energy minima.

The energy minimising procedure comprises of two intertwined processes: a) topological transformation, such as refining surface, T1 transformation and minimising the total surface area. The density of surface energy is assumed to be uniform at any position on foam surface. Therefore minimising the surface energy is equivalent to minimising the total surface area of foam; b) geometric transformation, such as structure relaxation which is to eliminate the geometric frustration and foam annealing. These processes are unavoidably accompanied by a large number of

topological transitions. The details of the above processes are described as follows:

Topological transformation: When the initial data file is read in Surface Evolver, all the non-triangular faces in the foam model are automatically divided into triangles. The surface in Surface Evolver is approximated by a triangle mesh. In order to ensure uniform refinement and trigger appropriate topological changes, three operational parameters are used in the process of topological rearrangements: $l_{\max}$, $l_{\min}$ and $S_{\min}$. These three parameters are correlated. $l_{\max}$ is the maximum length of an edge, which is defined as follow:

$$l_{\max} = C_S \cdot (x_{\max} \cdot y_{\max} \cdot z_{\max})^{\frac{1}{3}} / N_P \tag{3.14}$$

$x_{\max}$, $y_{\max}$ and $z_{\max}$ are the maximum values of *x, y, z* coordinates respectively which dictating the boundaries of the cube space. N_P is the number of bubbles in the foam. C_S is a shape coefficient, ranging from 0.2 to 0.7 in this work. $l_{\min}$ is usually equal to $l_{\max}/10$. And $S_{\min}$ is set to $l_{\min}^2$.

If an edge is longer than $l_{\max}$, it is divided into 2 edges. If an edge is shorter than $l_{\min}$, one of the two procedures will happen: 1) if it is either an edge within a face or only a part of a Plateau border it will be deleted; 2) if it is the entire Plateau border (connecting 2 foam vertices), a topological transformation will be triggered (T1 process). Similarly, if a facet has an area less than $S_{\min}$, it will be deleted if it is only a portion of a larger face; it will trigger topological changes if it represent an entire face. In the simulation, the actual values of $l_{\min}$, $l_{\max}$ and $S_{\min}$ can be changed by users, subject to the level of refinement required.

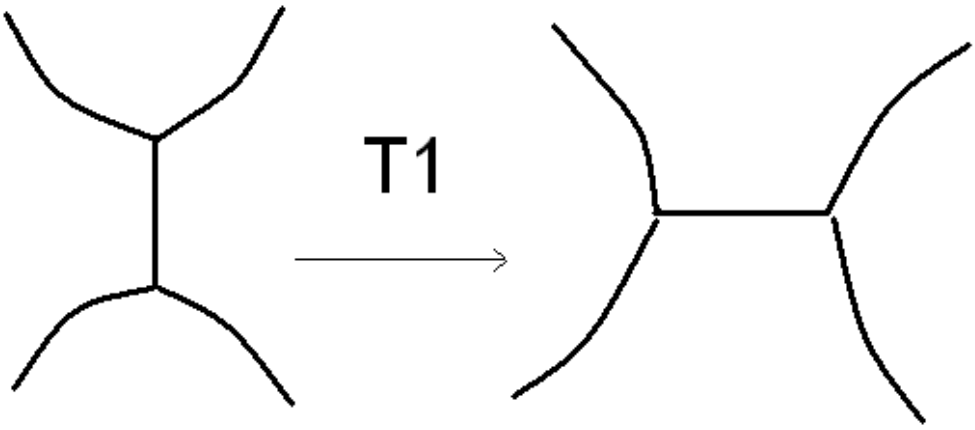

Figure 3.19: A schematic description of a 2D T1 process. (A 2D T1 process is an exchange of neighbouring bubbles which indicates the topological changes of four bubbles.).

T1 process is the only form of topological transformation implemented in this simulation. Figure 3.19 shows a typical T1 transformation in a 2D foam. The bubbles on the top and bottom 'squeeze apart' the two bubbles that are in contact to form a new edge after the short edge shrinks to zero length. In a 3D foam, the T1 process becomes more complicated as an edge is formed by three bubbles. In a 3D T1 process, a small triangular facet is formed, rather than a new edge, when the short edge shrinks to zero length.

Due to the difficulty in showing the internal structure of contacting bubbles, a series of simplified schematic figures are used to describe the T1 process in a 3D foam. In Figure 3.20, a short edge ($< l_{\min}$) is identified. The short edge connects with both the top bubble and the bottom one. The top and bottom bubbles will move together during the course of edge shrinking. The three bubbles in the middle that are in contact with each other will consequently be 'squeezed apart' (Figure 3.21).

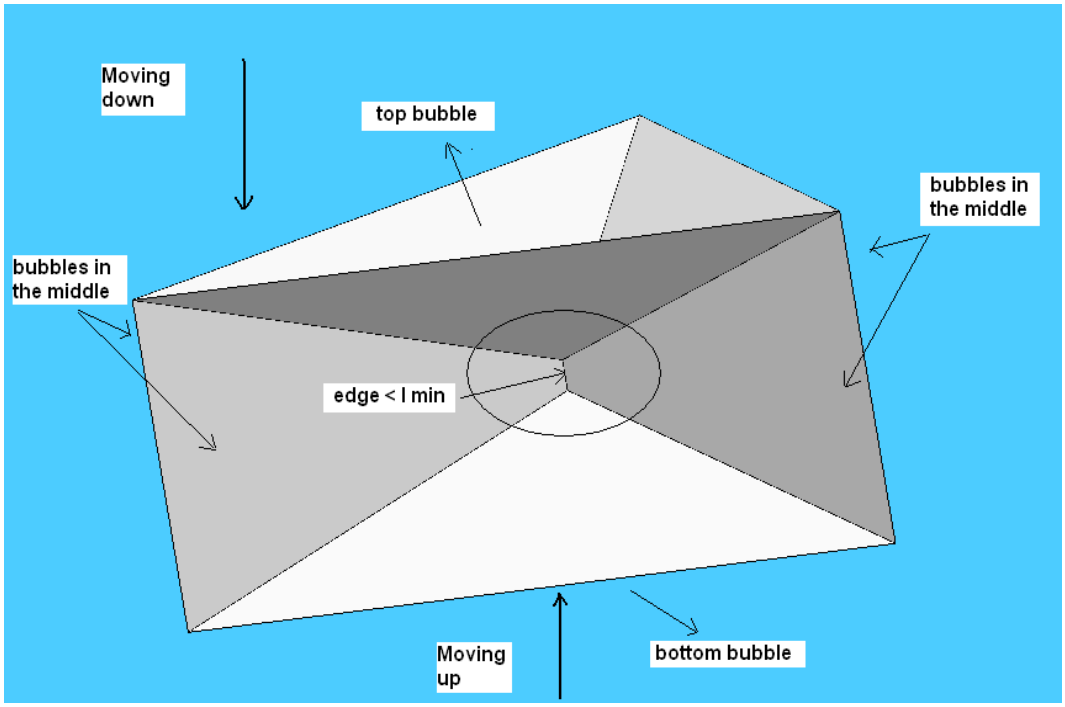

Figure 3.20: The schematic description of the internal structure of contacting bubbles in a T1 process.

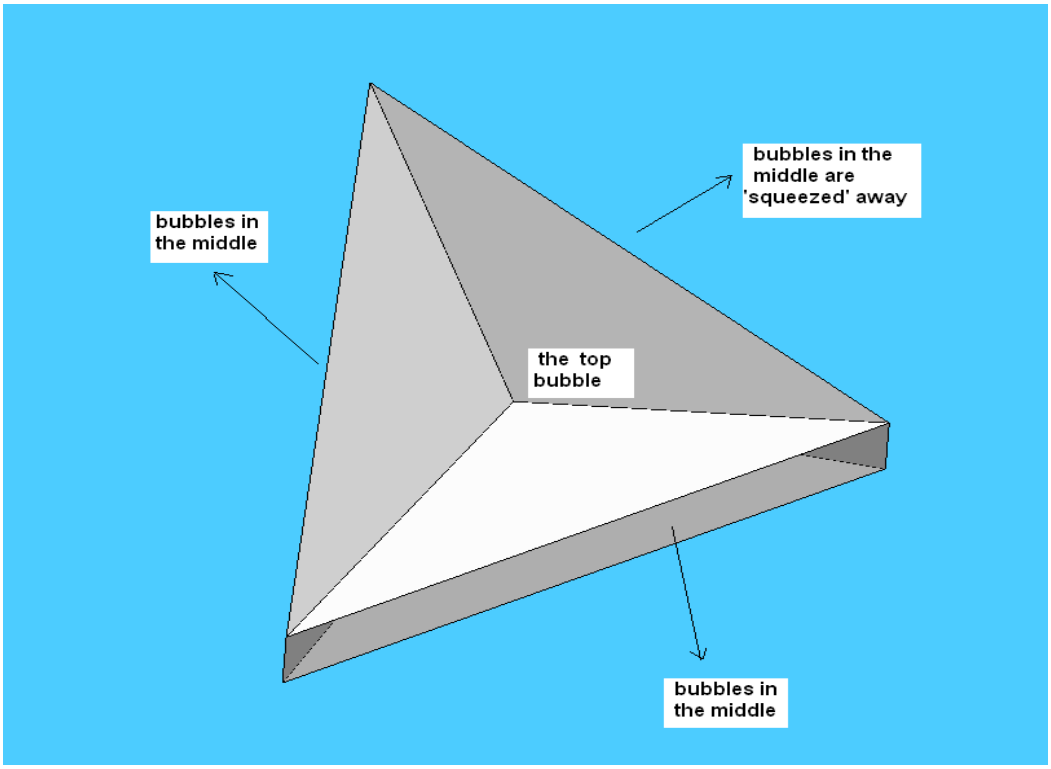

Figure 3.21: The movements of the bubbles in a T1 process (observe from top).

As a result of the above process, the top and bottom bubbles finally come into contact with each other. A small triangular facet is created when the two meet. As shown in Figure 3.22 and 3.23, the short edge has transformed into a small triangular facet. Every edge of the new triangular facet is formed by the conjunction of three bubbles, which satisfies the geometric requirements of Plateau Rules. In most cases, this is a quasi-static state. The reverse of the above process can also occur, with a triangular facet shrinking to zero and being replaced by an edge.

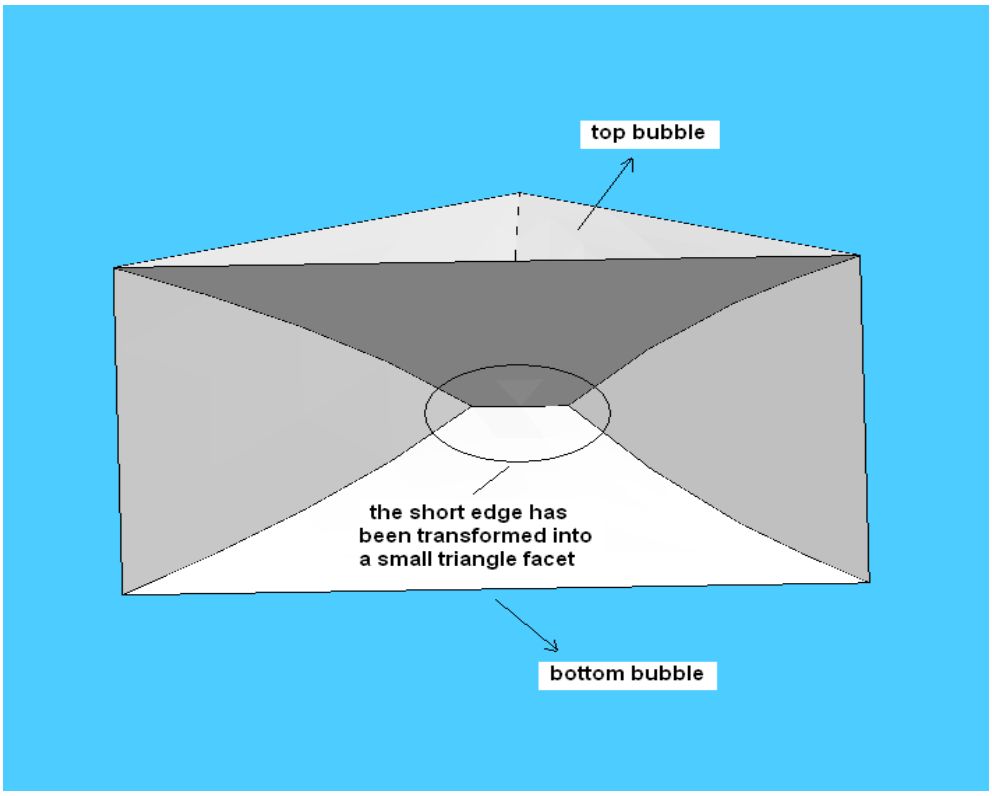

Figure 3.22: The quasi-static state of the bubbles in a T1 process.

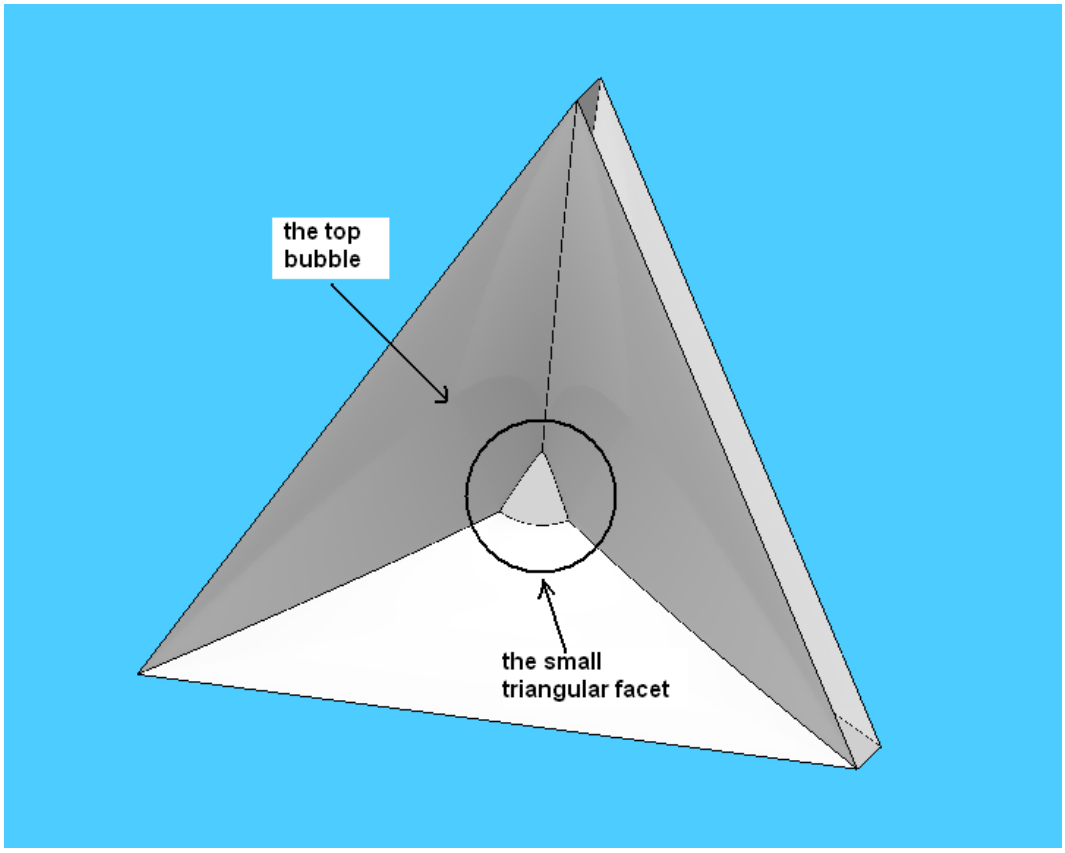

Figure 3.23: The quasi-static state of the bubbles in a T1 process (observe from top).

In this transition, it is important to define the minimum area of the face, $S_{\min}$. This is because, during the energy-decreasing procedure, a number of very small facets appear as a result of the geometric and topological rearrangements. These ultra small facets can become troublesome as they slow down the convergence dramatically. For a facet which is smaller than $S_{\min}$ and bounded by four edges (Figure 3.24), it will be transformed into a new quadrilateral facet. The shortest pair of the opposite edges contracts to zero length, then they are expanded in the opposite direction to form a new quadrilateral. In this sense, the quad-quad transition shows a similar mechanism with the edge-triangle transition. Both of them are triggered by the critical length or area defined by the user. Figure 3.25 shows the new quadrilateral facet formed through the topological transformation. These topological transformations are implemented when required in the simulation in order to gradually evolve the system into an equilibrium and low-energy state.

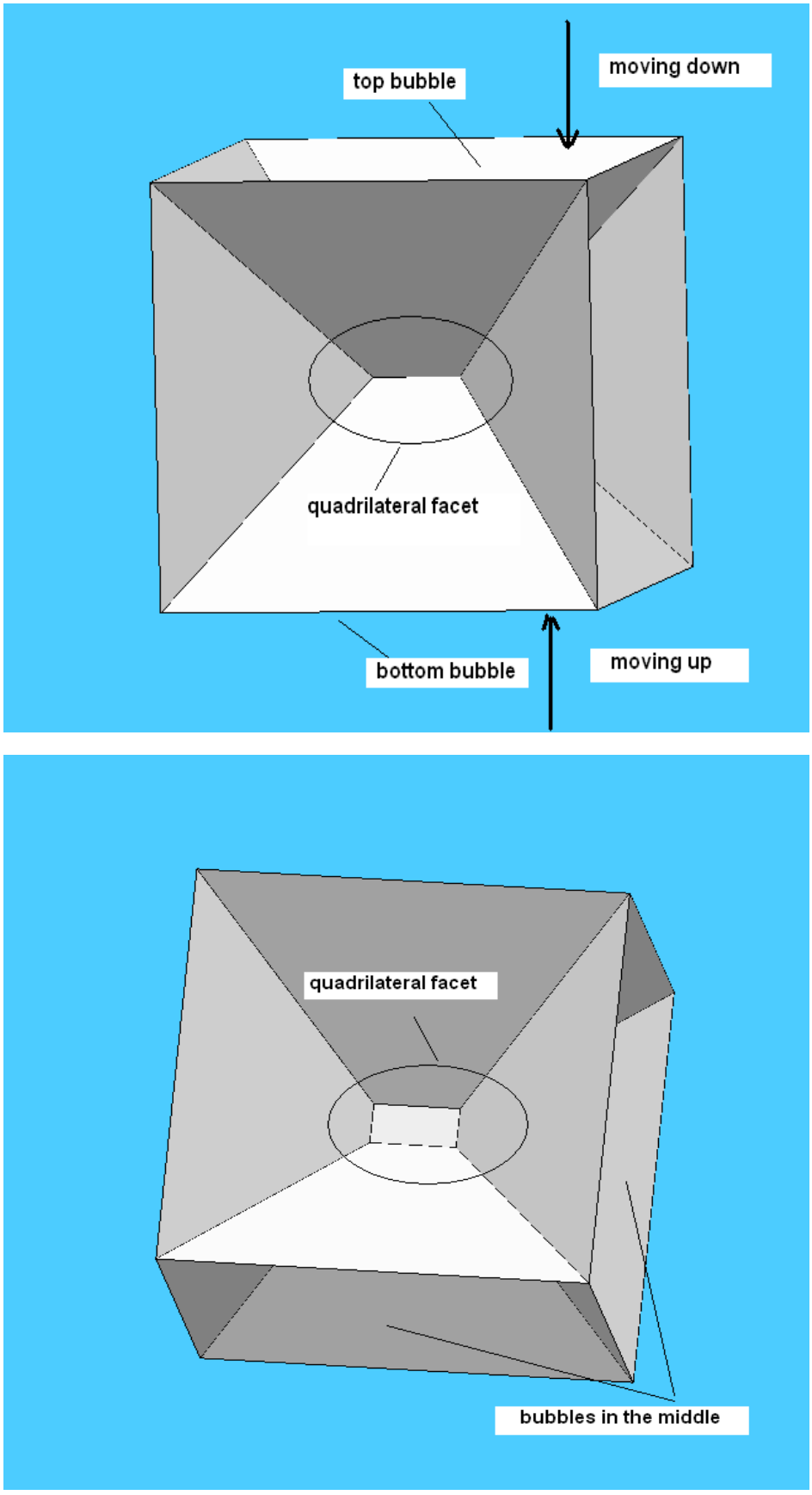

Figure 3.24: The transformation of small quadrilateral facets.

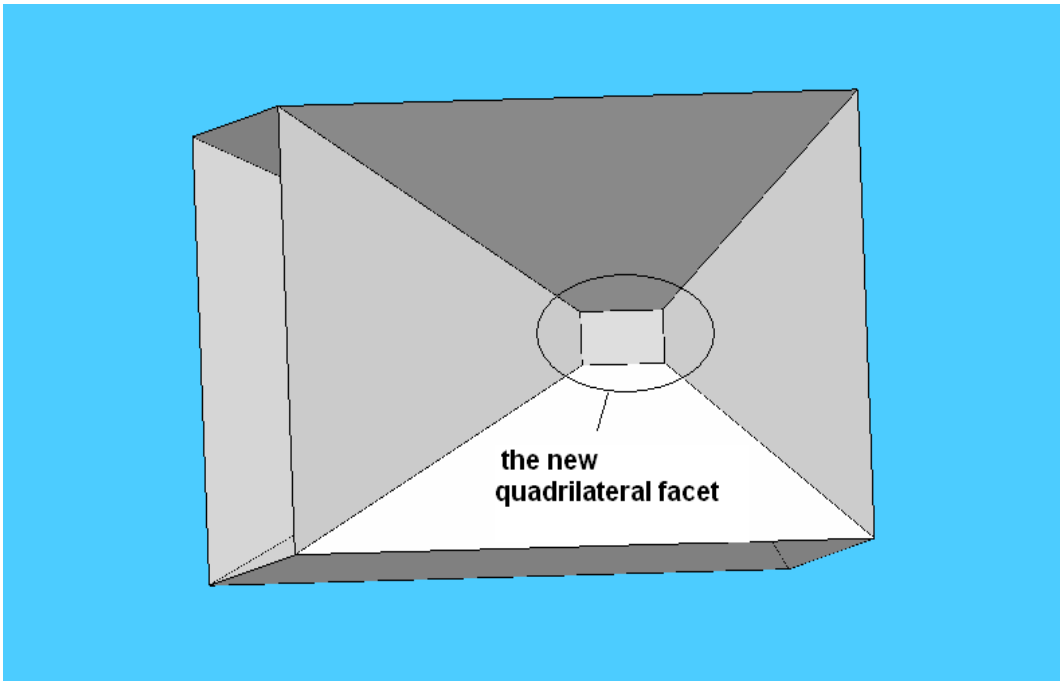

Figure 3.25: A new quadrilateral facet created by the quad-quad transformation.

In the simulation, a series of operations have been defined and implemented through the command language of Surface Evolver in order to realise the topological transformations described above. Usually, the topology transformation process starts with a few surface relaxations, to prepare a smooth foam surface. During the course of the iterative relaxation, the flat initial foam faces change to relatively smoother curved faces which are approximated by a mesh of small triangles. A small percentage drop of surface energy can be observed as a result of the decreasing surface area. The operations in this step neither change the triangulation mesh nor the topology of the foam.

The surface can be compulsorily refined by implementing the refine command. 'Refinement' of triangulation means producing a new triangle network by subdividing each triangle of the original triangulation. In Surface Evolver, this scheme can be accomplished by creating new vertices at the midpoints of all edges and use these to subdivide the original facet into four new triangle facets. Picture 3 in Figure 3.26 shows the surface after being refined once. It is worth mentioning that this

triangulation refinement does not change the topology of a surface and the surface energy.

The triangulation can be polished up by equiangulation operation. This is to examine whether changing the diagonal of a quadrilateral face, which is bounded by four triple edges, would make the original triangles more equiangular. It is helpful to repeat the above process a few times to get an optimal equiangulation.

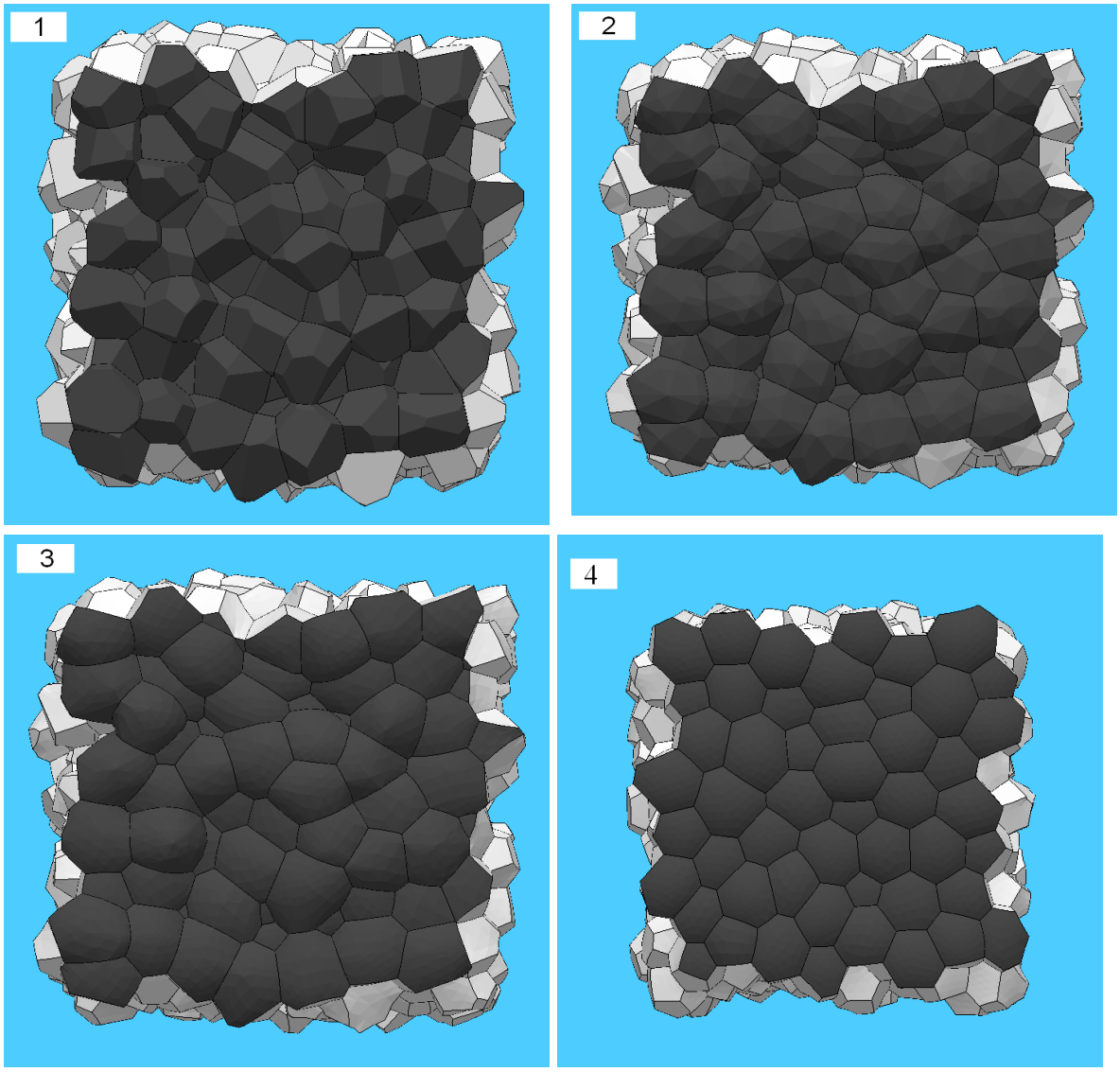

Figure 3.26: The evolution of the foam surface simulation. (1 = the initial surface; 2 = the surface without being refined; 3 = the surface being refined once; 4 = the surface of a fully relaxed foam.)

A series of topological checks are necessarily implemented to ensure that the foam structure still satisfies the requirements of Plateau Rules; the length of the each facet edge is between $l_{\min}$ and $l_{\max}$; and the area of any face is larger than $S_{\min}$.

Repeating the above process several times until the energy no longer decreases and the eigenvalues for the energy minimisation are all positive. It means that the foam has reached an equilibrium state. Figure 3.27 shows the foam surfaces before and after topological transformations. In Figure 3.27, the picture on the left displays the initial foam surface without undergoing topological transitions. Some small triangular and quadrilateral facets can be observed. However, after a large number of topological transformations, as shown in the picture on the right, these 'odd' facets disappear and an equilibrium surface structure appears. The topological transition process stops where no further topological transformations occur.

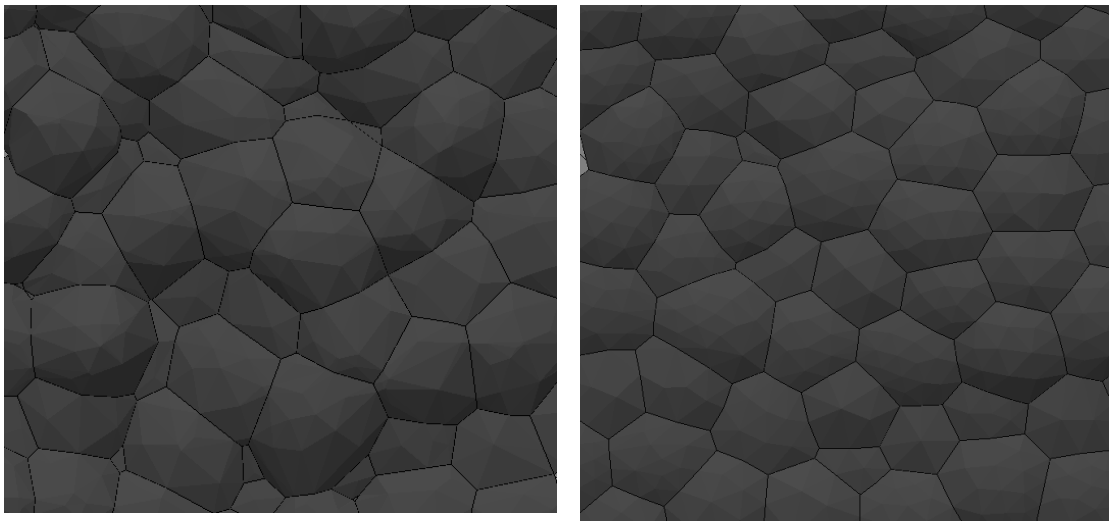

Figure 3.27: The foam surfaces before and after topological transformations. (left: before topological rearrangements; right: after topological rearrangements)

Annealing process: As previously mentioned, the layout of surface films is influenced by the interaction between the surface bubbles and the underlying bubbles. The twisting effect of shear forces among bubbles also affects foam topology. It

means that the internal structure of foam accounts for shaping the foam surface and thus influencing the surface energy.

In order to ensure that the foam structure does not represent a relatively high energy point, a procedure for structural transformation is implemented. This procedure is similar to that adopted by Kraynik et al. (2003). This process consists of annealing the structure by stretching and compressing the structure in each principal axis in turn. A typical annealing process contains the following steps:

1. The foam is fully relaxed and adjusted to reach an equilibrium state in which surface energy no longer decreases.

2. The period is stretched a small amount, typically multiplying a stretching factor 1.05-1.1, in one direction and compressed in the other two, divided by the square root of the stretching factor. This operation will not change the volumes of the bubbles.

3. The stretched foam is again relaxed and any required topological changes are implemented.

4. Repeat step 2 and 3 for a few times, typically 3 times in this work. The total stretch ranges from 10% to 30%.

5. Compress the stretched foam in step 4 by simply dividing the same stretching factor in step 2 in one direction and multiply the square root of it in the other two directions. In each step of compression, foam structure is relaxed. This step stops until the foam restores its original shape. It is worth mentioning that this process is irreversible because a large number of topological changes happen during the relaxation process.

6. Repeat the above stretching-compressing process along each of the three principal axes for a few times until no topological transformations happen and the eigenvalues for the energy minimisation are all positive.

Figure 3.28 shows the changes of foam structure in the annealing process.

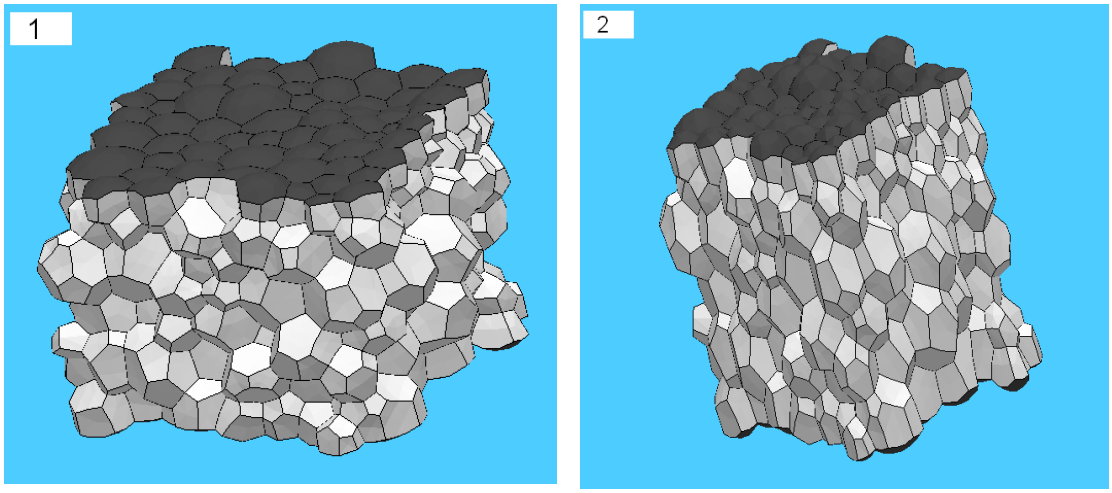

Figure 3.28: The foam structures in the annealing process. (1 = the original foam; 2= the stretched foam along one principal axis)

Conclusion

Due to the great difficulty in experimentally obtaining the information on the internal structure of foams, a simulation approach is employed to generate realistic foam structures from which the relevant topological and geometric data can be conveniently extracted.

The simulations use 3D Voronoi tessellation as initial structures. Two different methods of placing initial seed points for Voronoi tessellation, CRP and MC method, are described. The initial foam produced by the Voronoi tessellation is randomly packed and fully periodic. In order to produce free surfaces, a virtual plane is sliced through one of the periods and the bubbles intersected by the plane removed. The initial foam structure produced by the Voronoi tessellation is topologically similar to that of a real foam, having 3 films meeting at an edge and 4 edges at a vertex, but it is not a minimum energy structure. The Surface Evolver software package is used to minimise the foam surface area in order to produce an equilibrium structure. Topological transformations are carried out as required.

In order to further reduce the energy of the structure, an annealing process similar to that employed by Kraynik et al (2003) is adopted. This involves applying extensional and compressional strains to the foam along each of the principal axes.

CHAPTER IV

BUBBLE SHAPE AND THE TOPOLOGY OF FOAM

Introduction

The primary aim of this chapter is to test the validity and accuracy of the modelling method described in the previous chapter. The simulated structures are compared to both experimental results and previously reported simulations.

Firstly, a number of visual results are presented to qualitatively demonstrate that the simulated foam structure satisfies the geometric and topological requirements of Plateau's laws and agree with previous studies. Secondly, the results of monodisperse foams are compared to the results reported from Matzke's experiment (1946) which meticulously studied the topology of bubbles. After being validated by the experimental results, the simulated structure is compared to Kraynik's simulation (2003). Although Kraynik has done considerable amount of work on periodic foams, no simulation studies on foam surfaces have been carried out. In this section, bubbles at surface will be studied separately. Finally, the impact of the bubble size distribution on the topology of foam is investigated.

4.1 Surface of foam

To investigate the relationship between the foam surface and the internal structure, a fully periodic foam is not appropriate. In order to generate a surface, the foam is sliced through one of the periods. This produces what is in effect an infinitely large slab of foam with a free surface at the top and bottom. By having a foam which has periods in 2 directions and free surfaces in a third direction, the only edge effects are those associated with the free surfaces. Since gravity is not considered when the structure is determined, the effect of having two free surfaces is that there is an increase in the accuracy of the statistics by doubling the number of surface bubbles. Figure 4.1A and 4.1B show a fully periodic foam and a foam with free surfaces respectively.

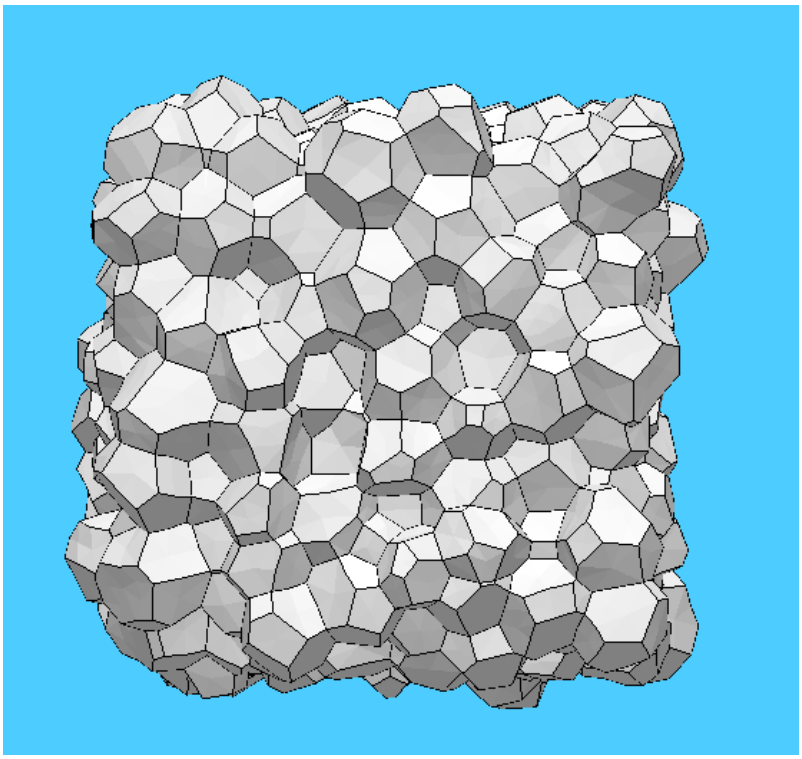

Figure 4.1A: A fully periodic foam.

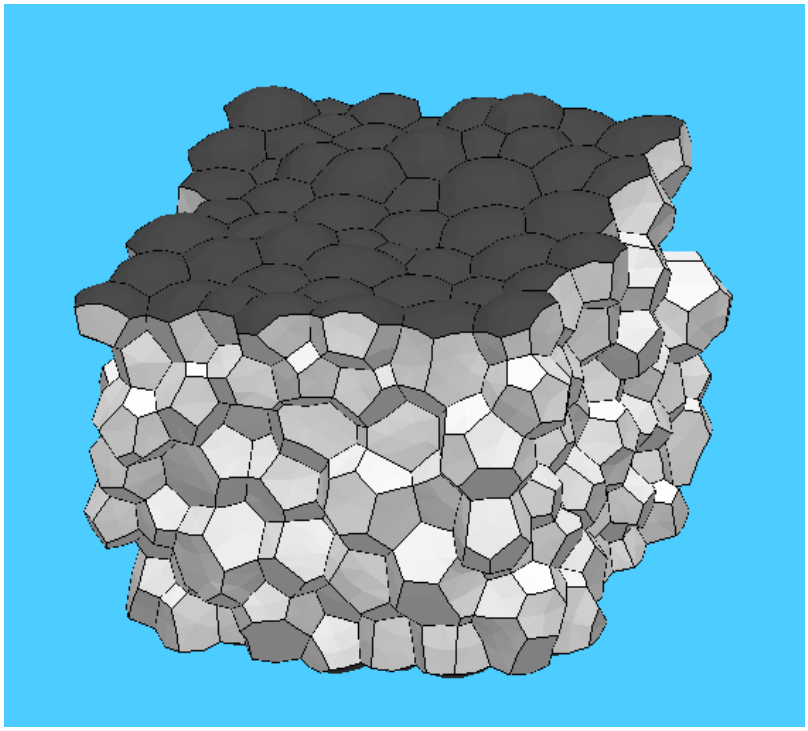

Figure 4.1B: A foam with free surfaces.

In some cases, the surface of foam is subject to geometric constraint, such as the walls of a container. In these circumstances, the free surface deforms in line with the shape of the constraining plane. Figure 4.2B shows a foam with constrained surfaces. In the simulation, exerting constraints on the foam surface neither changes the volume of the bubbles nor triggers considerable topological and geometric transformations. Figure 4.3A and 4.3B show the comparison between an unconstrained surface and a constrained one respectively. On a constrained surface, the films of the constrained bubbles must meet the constraining plane at 90°. This is the result of forces balancing at the interface. As shown in Figure 4.4, the counterforce from the constraining plane is along the tangent of the film at the interface. If the angle between the tangent and the constraining plane is φ (initially $< 90^\circ$), there must be a component of the counterforce along that plane. This component of the counterforce tangential to the plane will move the film along its direction. As a result, the contacting angle, φ increases. The movement stops until φ is equal to 90°, an angle

with zero component of the counterforce along the constraining plane.

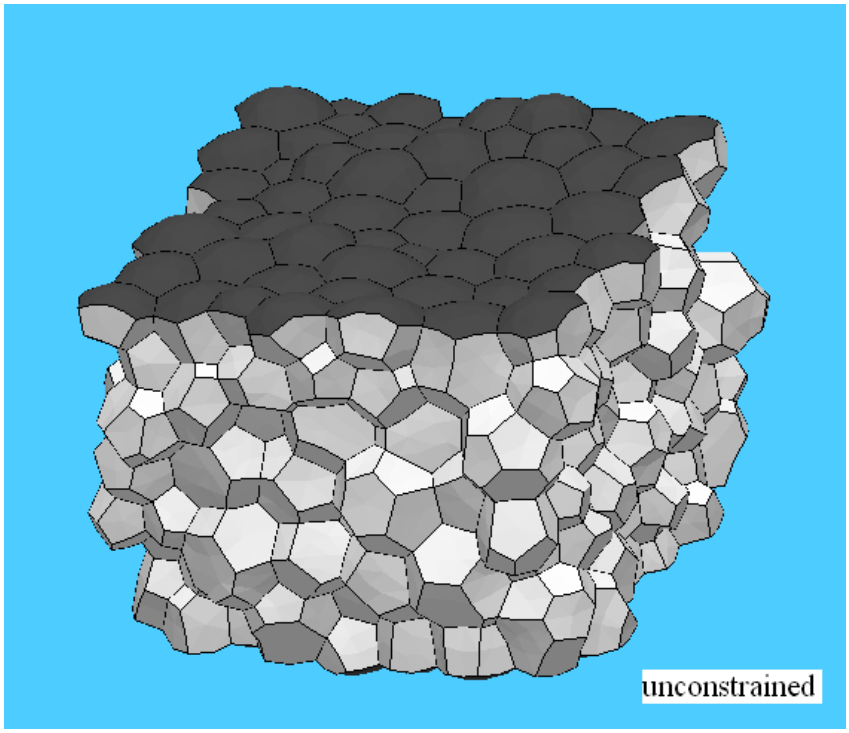

Figure 4.2A: Foams with unconstrained surfaces.

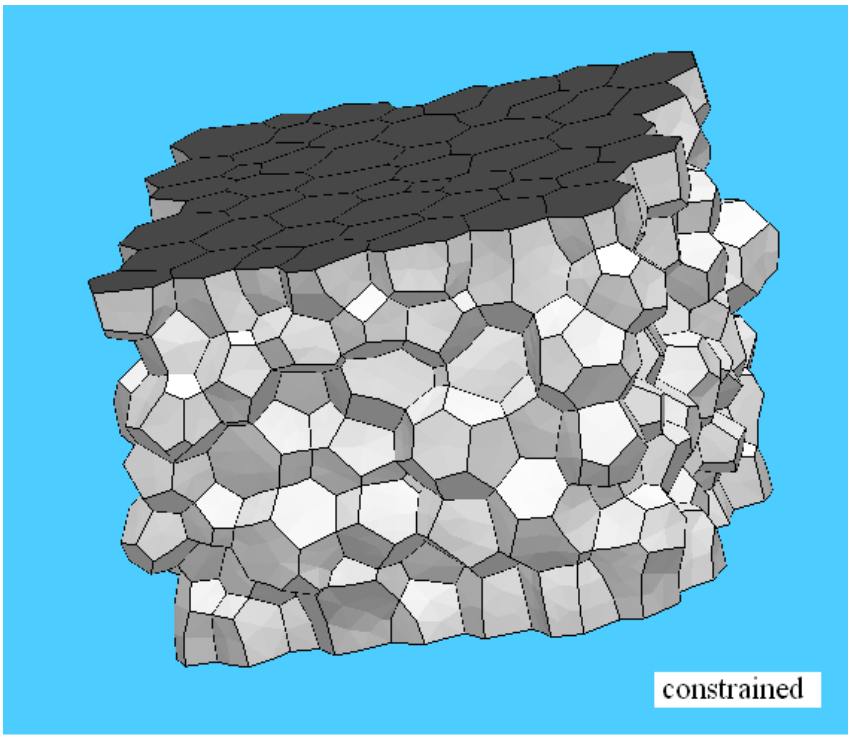

Figure 4.2B: Foams with constrained surfaces.

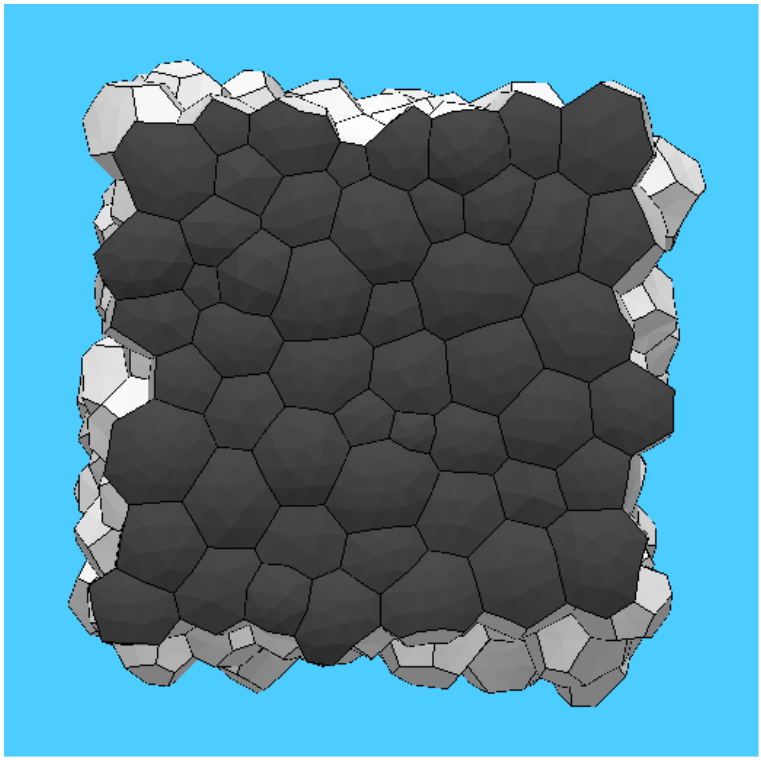

Unconstrained surface

Figure 4.3A: An unconstrained foam surface.

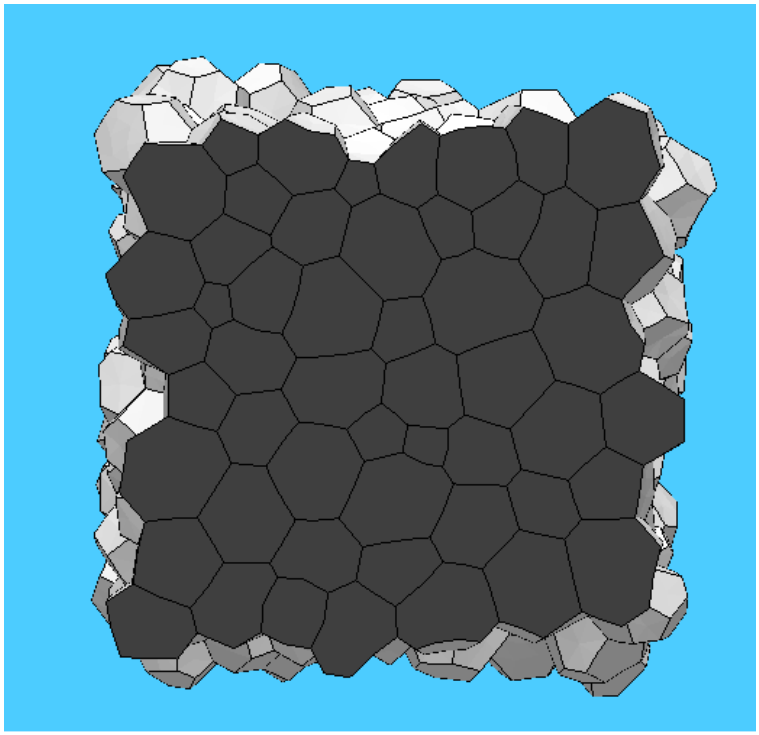

Constrained surface

Figure 4.3B: A constrained foam surface.

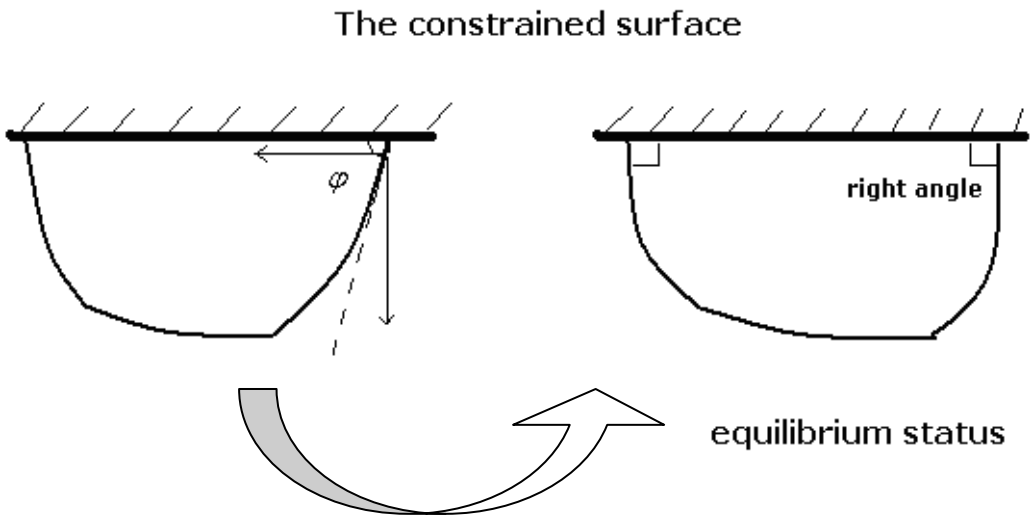

Figure 4.4: The contacting angle between a constraining plane and films of a bubble.

4.2 Topology of bubbles

4.2.1 An overview of the topology of bubbles

Before quantitatively studying the topology of bubbles, it would be advisable to have a general view on the shape of bubbles.

Figure 4.5 shows a periodic monodisperse foam which consists of 400 randomly packed bubbles. As mentioned previously in Chapter II, monodisperse foam refers to a foam with equally sized bubbles and polydisperse foam refers to a foam with a range of bubble sizes. These two terms will be frequently used in this thesis.

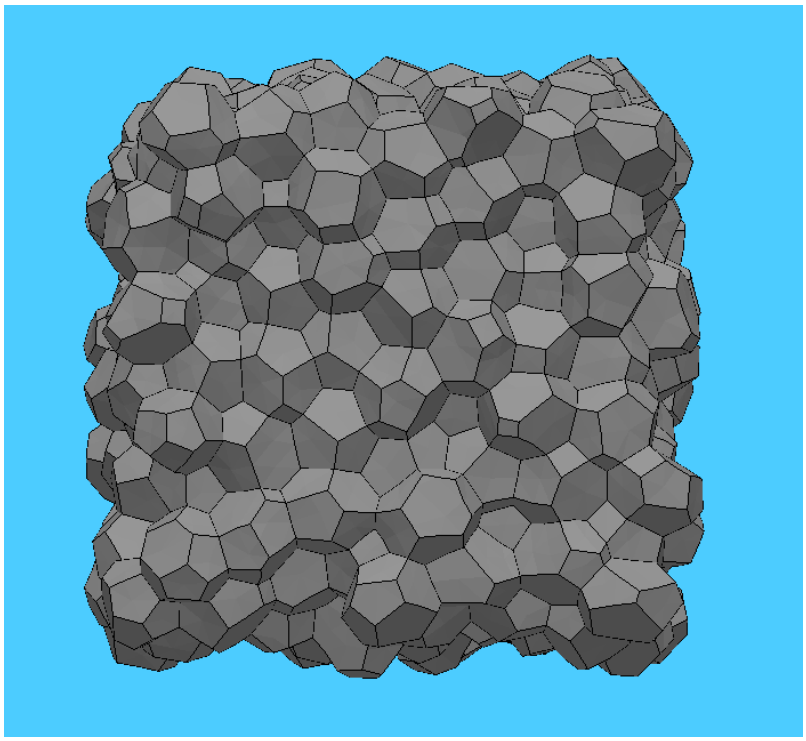

Figure 4.5: A periodic foam with 400 bubbles.

Figure 4.6 shows examples of the individual bubbles produced in the simulation. The bubbles are packed in a random and disordered manner by which the space is fully occupied.

The numbers marked on each picture represent the number of faces of each sample bubble. It can be observed that bubbles produced in the simulation may have 5 to 24 faces. Most of the faces are pentagonal, with the remaining ones being mostly in quadrilateral and hexagonal forms. The number of faces reflects the number of surrounding bubbles. The topology of bubbles found in this work is different to the ordered foam structure predicted by both Kevin (1887) and Lewis (1944), both of whom claim tetrakaidecahedron, with 8 hexagonal and 6 square faces (or its approximations), to be the most ideal form. However, the results of this work show close agreement with the experimental works by Matzke (1946) who meticulously measured 400 disordered uniformly sized bubbles, without finding typical Kevin cells. Detailed comparisons between this work and Matzke's experiment will be shown in the next two sections.

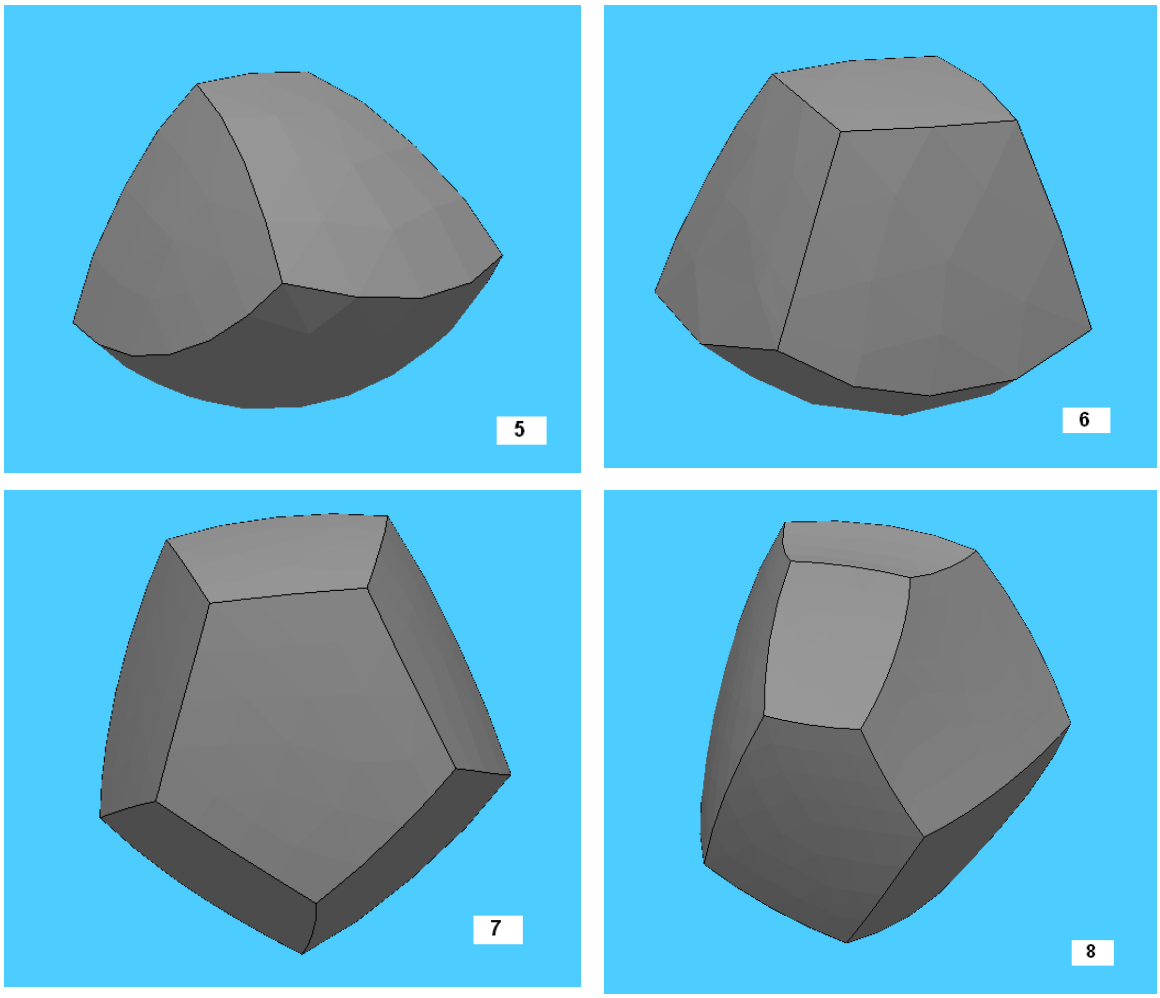

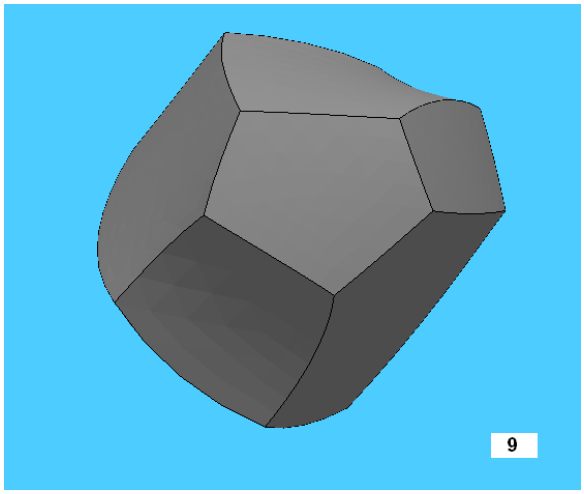
9

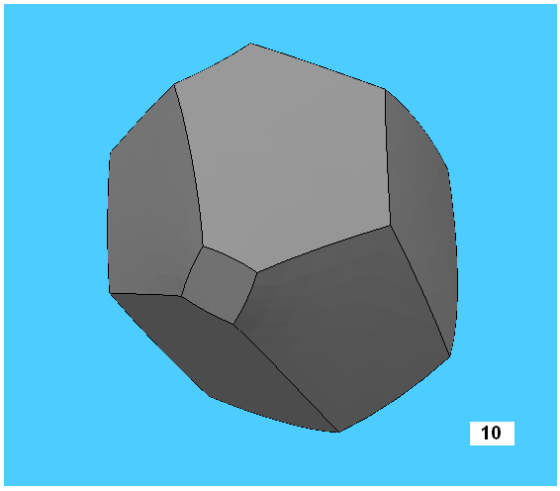
10

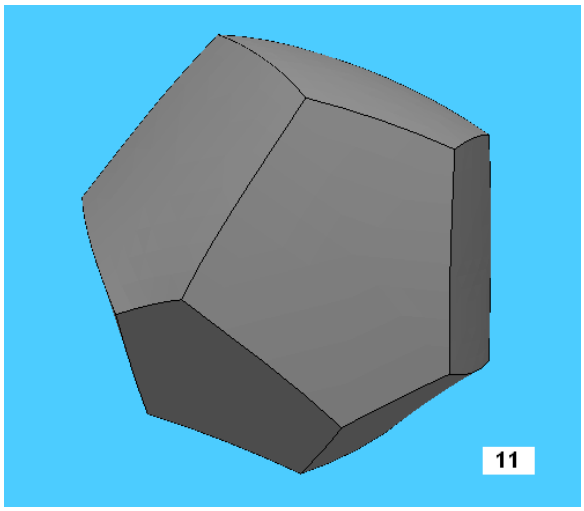
11

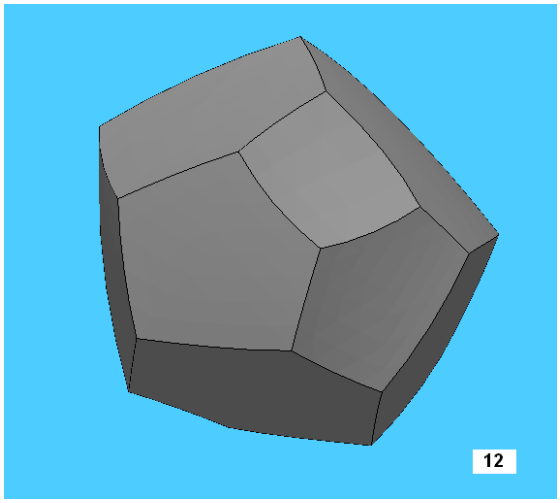
12

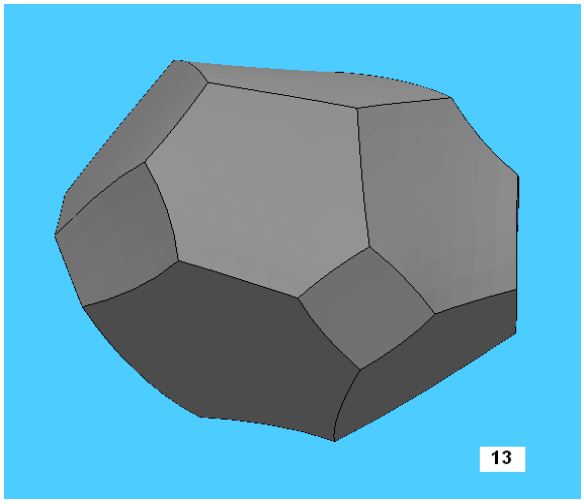
13

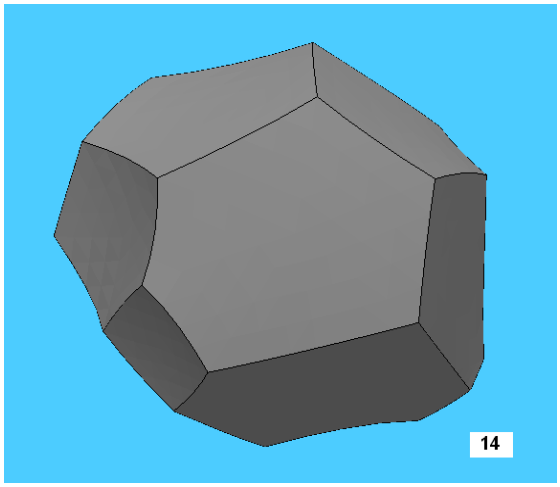
14

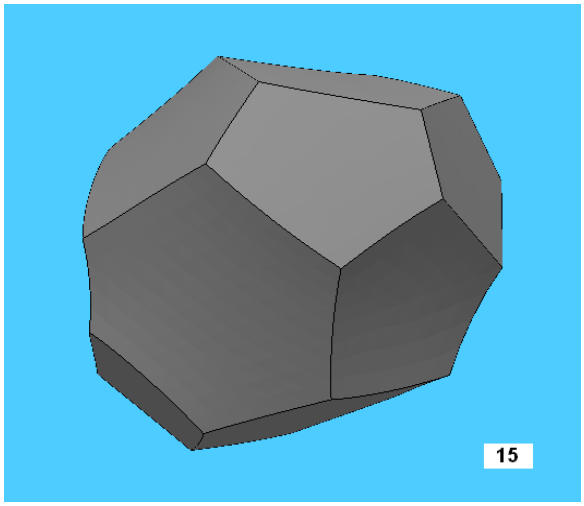
15

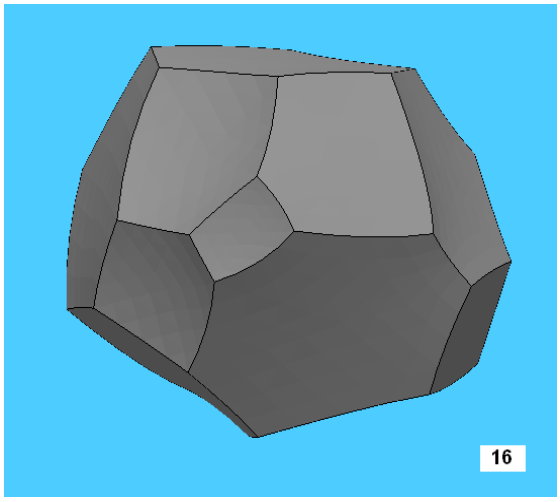
16

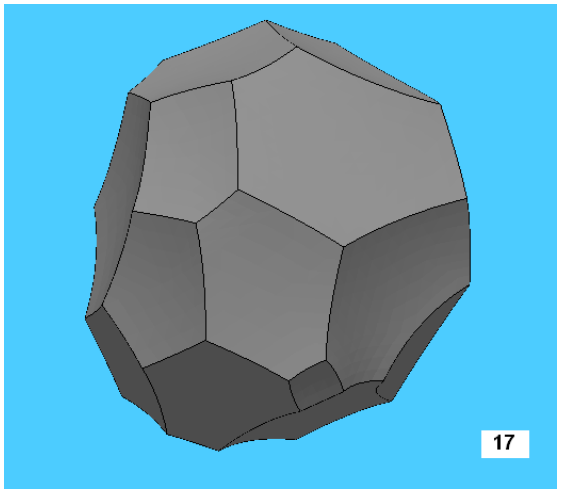
17

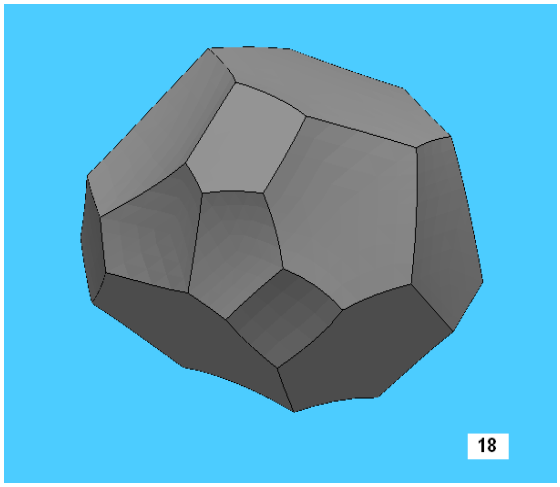
18

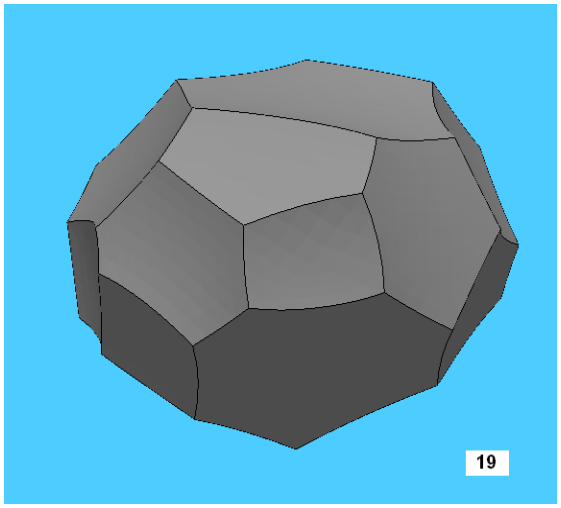
19

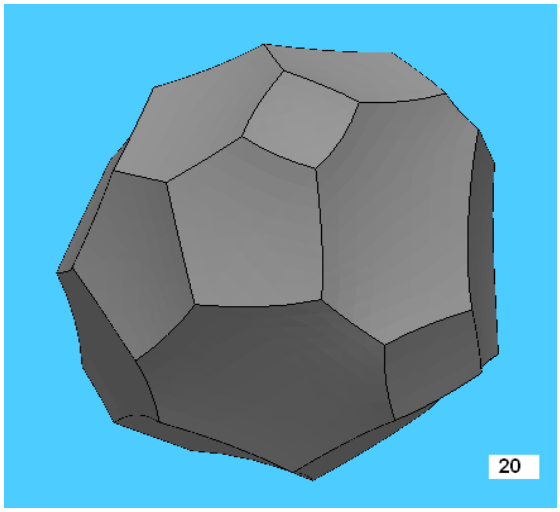
20

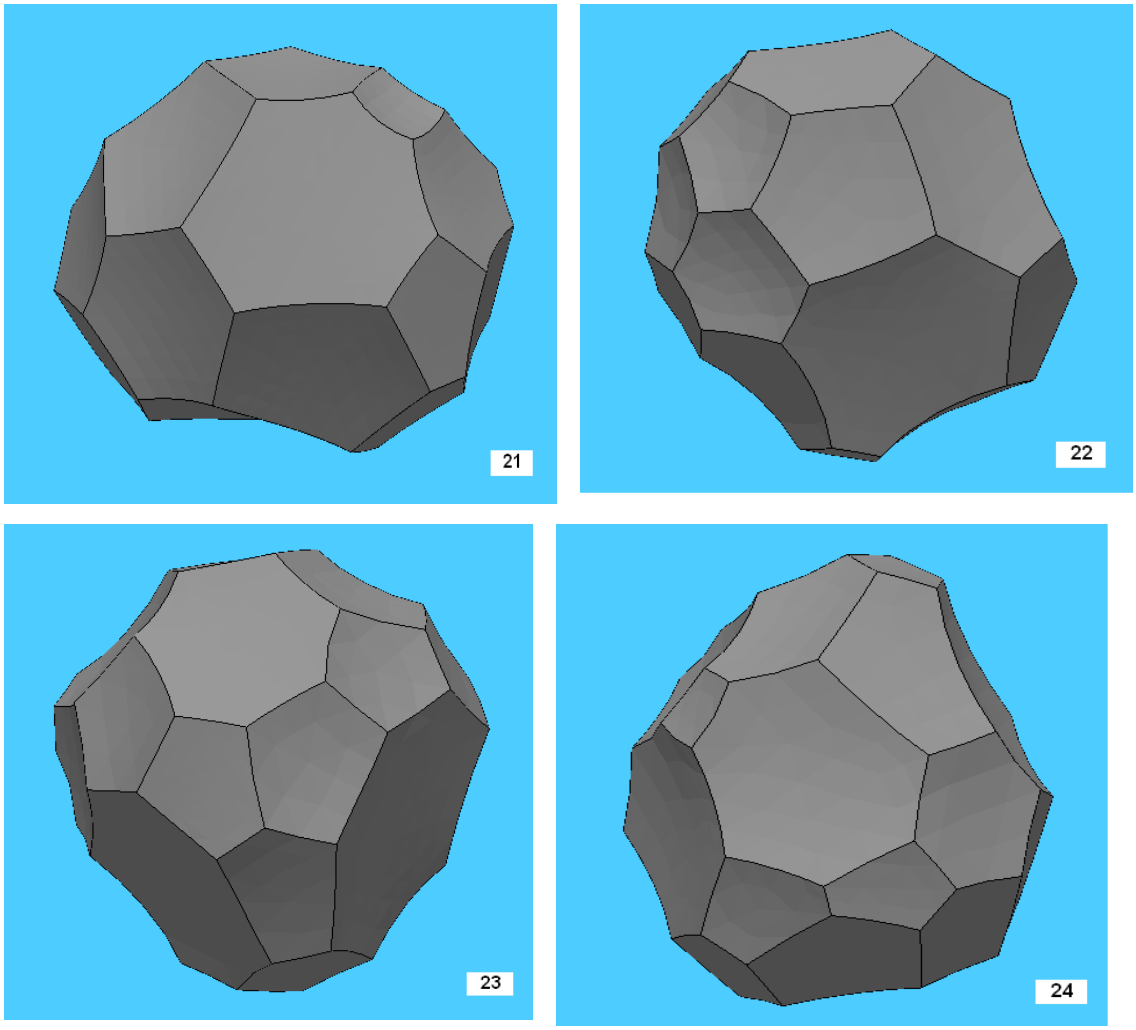

Figure 4.6: The 3D shape of bubbles obtained in the simulation.

As shown in Figure 4.6, in a polyhedron-approximated bubble, the edges with a common vertex have equal angles between each other, at approximately 109°. This topological feature is consistent with Plateau's laws, which requires no more than four edges can share a vertex with an angle of $\cos^{-1}(-1/3)$ (Weaire and Hutzler, 1999).

Figure 4.7 shows foam clusters consisting of 2 and 3 bubbles. This indicates how the bubbles contact each other in the simulated foams. It can be observed that the edges of all underlying bubbles are formed by the conjunction of three bubbles, meeting at 120°. These edges constitute the network of Plateau borders.

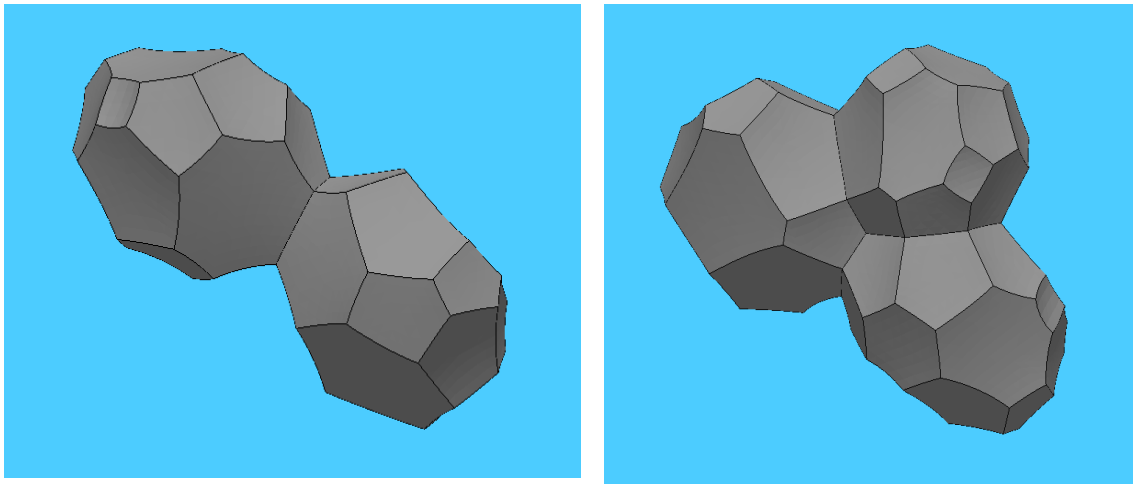

Figure 4.7: Bubble clusters consisting of 2 and 3 bubbles.

4.2.2 Number of faces per bubble of monodisperse foam

The number of faces per bubble (NFPB) reflects the number of surrounding bubbles. The number of faces per bubble obtained in this work is compared to the figures reported by Matzke. In 1946, Matzke carried out his famous and painstaking experiment to study the 3D shape of bubbles. He manually produced a monodisperse foam within a cylinder, by carrying each bubble separately with a syringe and placing them into a cylindrical dish one by one. A binocular dissecting microscope was used to investigate the topology of the foam, including the number of faces per bubble and the number of edges per face.

In Matzke's experiment, the bubbles are divided into three categories, namely the bubbles that are in contact with the walls of the container and the bubbles at the free surface and the internal bubbles. In this work, the monodisperse foam produced using a Voronoi tessellation has periodical boundaries in two directions and free surfaces in the third direction. Accordingly, the bubbles are divided into two categories: surface bubbles and internal bubbles. Since the effect of gravity is neglected, bubbles at both surfaces are considered indistinguishable in terms of topology. The difference between Matzke's two types of surface bubbles can be investigated by either having

the surface films unconstrained or constrained to lie on a plane.

The objective of simulating monodisperse foam is to make comparison with Matzke's experiment and validate the model developed in this work. The simulation is repeated three times. In each run, a foam with 500 ± 5 uniformly sized bubbles is used. All the foams are fully relaxed and annealed according to the procedure described in Chapter 3. The average number of faces per bubble is shown in Table 4.1:

	Internal NFPB	**Surface NFPB**
This work	**13.7 ± 0.1**	**11.0 ± 0.1**
Matzke's	**13.7**	**11.0**

Table 4.1: The average NFPB of the monodisperse foams in this work and data from Matzke's experiment.

As shown in Table 4.1, the average NFPB of the monodisperse foam ranges from 10.9 to 11.1 over the 3 runs, averaged at 11.0. The corresponding figure for the internal bubbles ranges from 13.6 to 13.8, averaged at 13.7. The above figures show very close agreement with those reported by Matzke, which are 11.0 and 13.7 respectively.

Figure 4.8 shows the distributions of the number of faces per bubble, with the solid line indicating the distribution for surface bubbles and the dashed line representing that for the internal bubbles. The displacement between the two peaks (11 for surface bubbles and 14 for internal bubbles) is significant. The average number of faces per internal bubble is larger than that of surface bubble. This means that, on average, the internal bubbles have more neighbouring bubbles than those on the surface, and, the surface bubbles display a wider distribution of NFPB than that of the internal bubbles. Over the 3 runs, the standard deviation of NFPB for surface bubbles and internal bubbles are 1.59 ± 0.07 and 1.10 ± 0.04 respectively. This means that the shape of the

underlying bubbles is more regular than those attached to the surface.

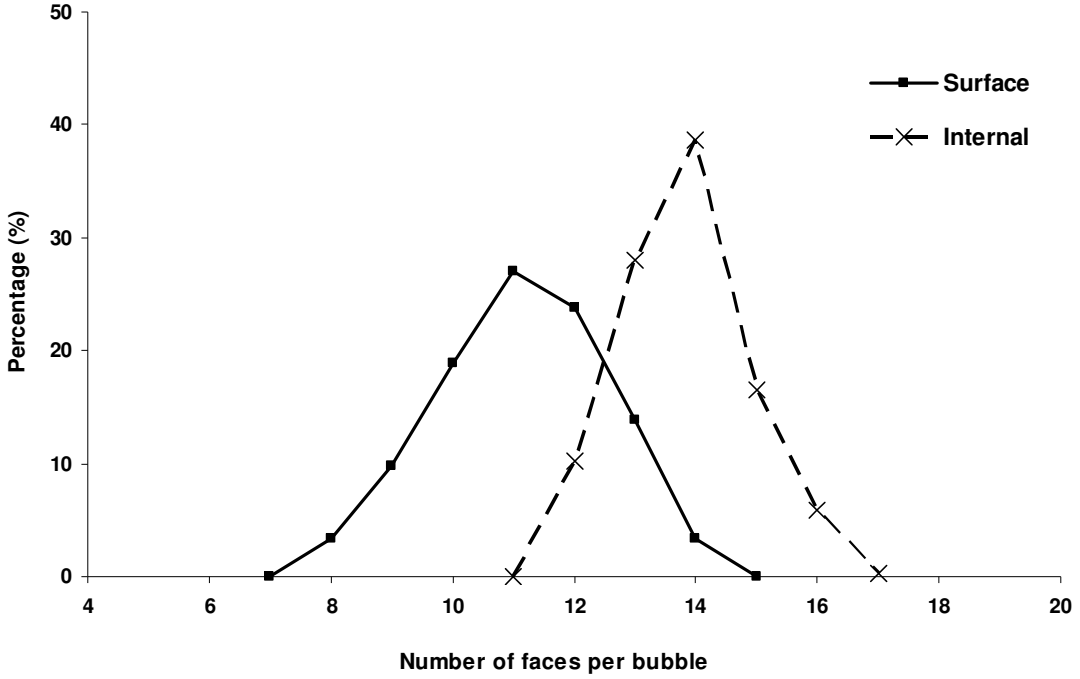

Figure 4.8: The distribution of NFPB of monodisperse foam.

Figure 4.9 shows that the majority of the internal bubbles have 12 to 16 faces, with a distribution that is in close agreement with both Matzke's experiment and Kraynik's simulations (2003). Each frequency in Figure 4.9 is the mean of the 3 runs, with an error bar less than 3.0% of the corresponding mean. For the surface bubbles (Figure 4.10), bubbles with 8 to 14 faces are most common, which is in good agreement with the experimental results. Each frequency is the mean over the 3 runs, with an error bar less than 6.5% of the corresponding mean. The above results demonstrate that the agreement between this work and Matzke's experiment is excellent. The reason for the slight discrepancy between these distributions is most likely due to the limited sample size available especially for the surface bubbles.

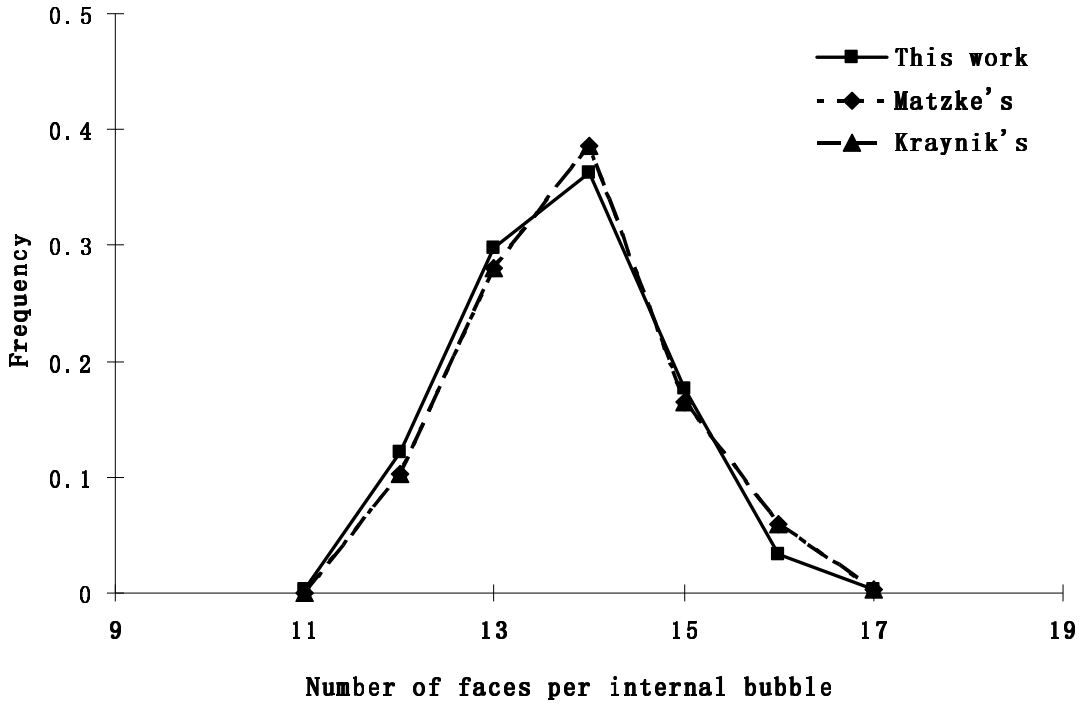

Figure 4.9: The number of faces per internal bubble of the monodisperse foam, Matzke's and Kraynik's work.

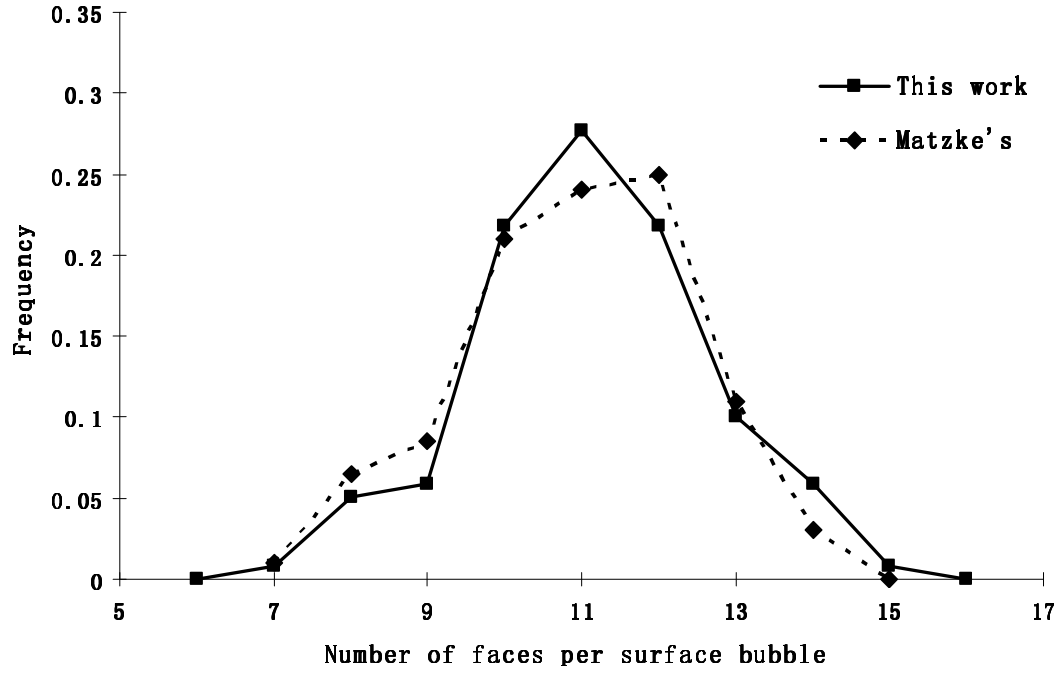

Figure 4.10: The number of faces per surface bubble of the simulated foam and Matzke's work.

The consistency between this work and that of Matzke's experiment, in terms of the

NFPB distribution, is quantitatively evaluated using the chi-square test. In this work, the chi-square test was employed to investigate whether an observed frequency distribution differs from a specific expected frequency distribution. The frequency distribution obtained from Matzke's is denoted as the expected frequency and the frequency distribution obtained from the simulations is the observed frequency. The null hypothesis (H_0) states that the two distributions are the same. The chi-square statistic, χ^2, is given by Equation 4.1:

$$\chi^2 = \sum [\frac{(EF_i - OF_i)^2}{EF_i}] \quad (i = 1, 2, \ldots, N) \tag{4.1}$$

Where:

EF_i = the ith non-empty expected frequency;

OF_i = the ith non-empty observed frequency.

The chi-square test is implemented under certain significance level, α, and degrees of freedom, υ. The degrees of freedom, υ, is given by m-1, where m is the total number of non-empty frequencies in the statistics. For a given significance level and degree of freedom, if the critical value of the chi-square distribution, $\chi^2_{critical}$, is larger than χ^2, the null hypothesis (H_0) is accepted. It means that the observed distribution shows no significant difference with the expected distribution under the given significance level and degrees of freedom. Table 4.2 shows the results of the chi-square test for the distributions in Figure 4.9 and 4.10. The significance level in both tests is 0.995. The chi-square statistics of both tests are much less than the corresponding critical values. Therefore, the null hypothesis is accepted with probability at least 0.995. This means that the distribution of NFPB in this work is in excellent agreement with that obtained from Matzke's experiment.

NFPB distribution	χ^2	$\chi^2_{critical}$
Internal	0.028	0.207 ($\upsilon = 4$, α =0.995)
Surface	0.050	0.989 ($\upsilon = 7$, α =0.995)

Table 4.2: The chi-square test for the level of consistency between the calculated NFPB distribution and the distribution obtained from Matzke's experiment.

The excellent agreement between the simulation results and Matzke's experiment provides confidence in this simulation method's ability to reproduce the structure of real foams.

4.2.3 Number of faces per bubble of polydisperse foam

In this section, the effect of increasing polydispersity on the number of faces per bubble is shown.

To track the above trend, foams with different bubble size distributions (normalised standard deviation being 0.07, 0.14, 0.20, 0.31) are produced, in addition to the previously studied monodisperse foams. Each sample of foam contains 500 ± 5 bubbles. The simulation for each sample is repeated 3 times. Table 4.3 shows the comparison of the average NFPB of foams with different levels of polydispersity:

NSD	Method for producing the foams	Average NFPB (internal bubbles)	Average NFPB (surface bubbles)
0.0	CRP	13.7 ± 0.1	11.0 ± 0.1
0.07	CRP	13.7 ± 0.1	11.0 ± 0.1
0.14	CRP	13.7 ± 0.1	11.1 ± 0.1
0.20	MC	13.3 ± 0.1	11.2 ± 0.1
0.31	MC	12.4 ± 0.1	11.2 ± 0.1

Table 4.3: The average number of faces per bubble. CRP means that foam is produced by constrained random placement method; MC means that foam is produced by Monte Carlo method. NSD is the normalised standard deviation of the internal bubble sizes.

For Table 4.3, it can be seen that the mean of the NFPB for the internal bubbles displays a clear trend decreasing in value with an increase in foam polydispersity, whereas the corresponding values for the surface bubbles show a very slight increasing trend. Figures 4.11 and 4.12 shows the frequency distribution of the NFPB for the surface and internal bubbles respectively. Both distributions become broader when the bubble size distributions become wider (NSD becomes larger). It means that the variance of both distributions increases when the foam polydispersity rises. For the internal bubbles, uniformly sized foam has the narrowest distribution, with most of the bubbles having 12-16 faces. While, for highly polydisperse foams (NSD = 0.31), this range increases to 5-21. For the surface bubbles, Monodisperse foam has the narrowest range, 7 – 15. And foam with NSD = 0.31 displays the widest distribution, 5-19. This indicates that polydisperse foams tend to have a larger variety of topology. This is because, in a highly polydisperse foam, some large bubbles are surrounded by a few small or medium sized bubbles. As a result, the large bubbles tend to have more neighbouring bubbles attached. Conversely, small bubbles are likely to have fewer than average neighbours.

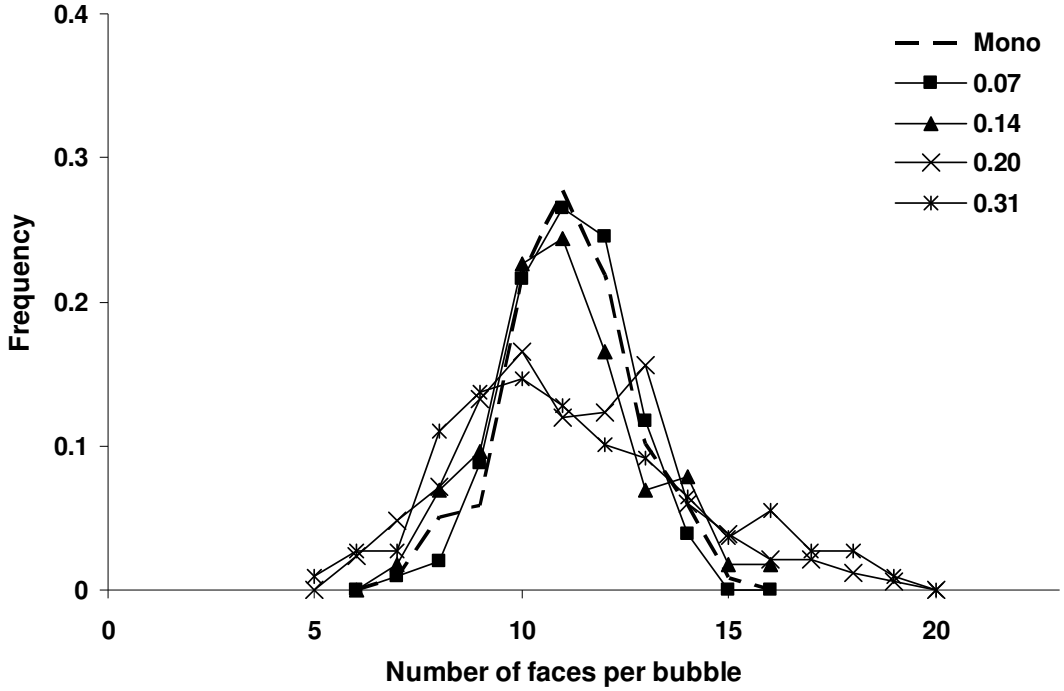

Figure 4.11: NFPB for the surface bubbles (NSD = 0.0, 0.07, 0.14, 0.20, 0.31 respectively).

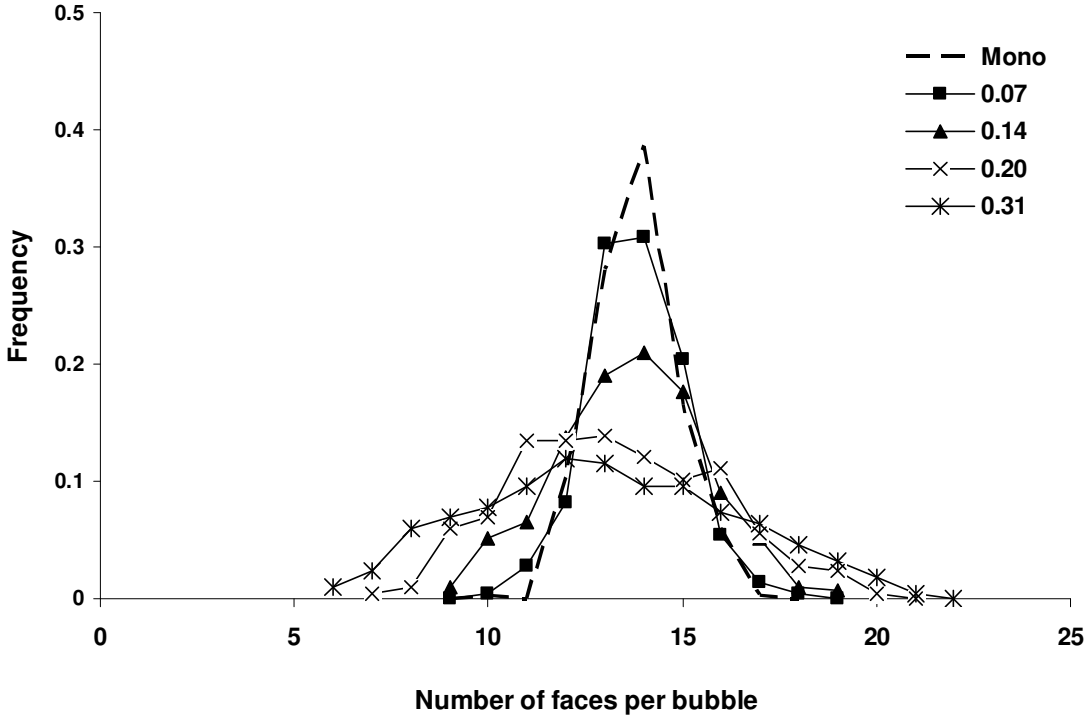

Figure 4.12: NFPB for the internal bubbles (NSD = 0.0, 0.07, 0.14, 0.20, 0.31 respectively).

4.2.4 Number of edges per face

Another important parameter used to describe the topology of bubble is number of edges per face (NEPF). In dry foams, the angles of vertices are dictated by Plateau's Rules. Some of the edges have to curve slightly in order to satisfy the topological requirements of Plateau's rules. As the number of edges on a face increases, the edges switch from being concave to convex on average. Figure 4.13 shows the types of foam faces observed in the simulations.

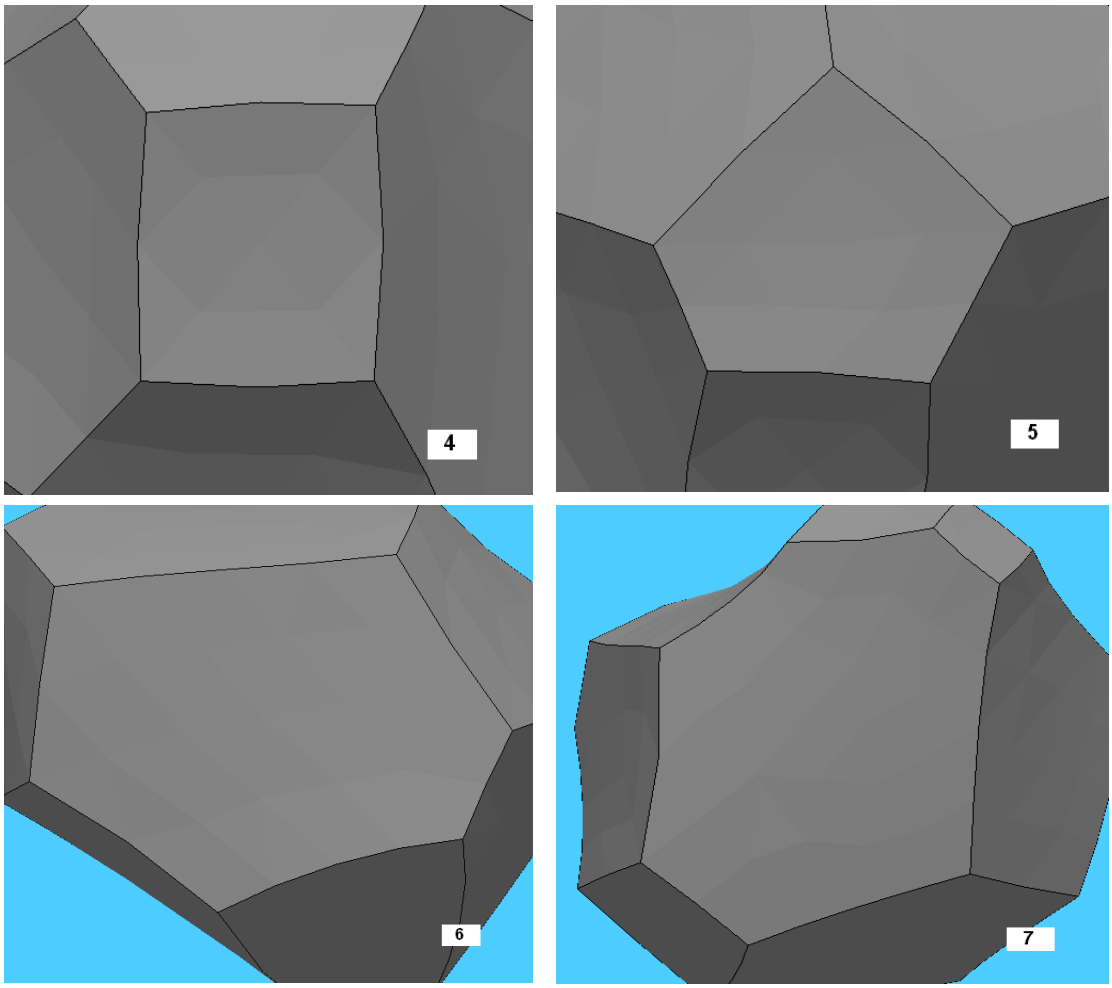

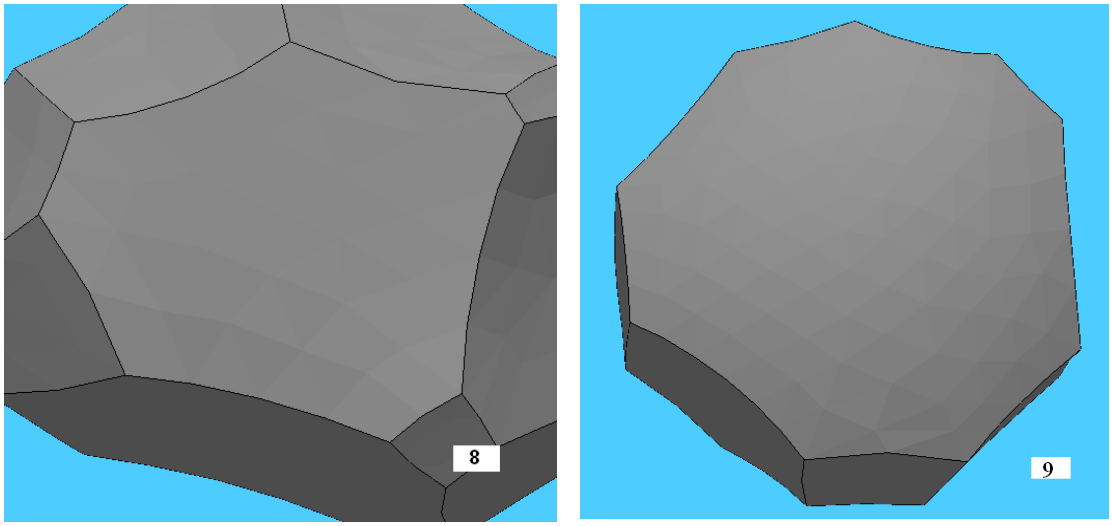

Figure 4.13: The types of foam faces observed in the simulation. (The numbers marked on the pictures represent the number of edges of the polygon). Faces with 9 edges are very rare in this work.

For an equilibrium structure of dry foam, NEPF may range from 4 to 9, with pentagons being the most typical shape, accounting for 55%-65% of all the faces. This phenomena may be attributed to the impact of Plateau's rules. Recalling Plateau's rules, the angle between two edges must be $\cos^{-1}(1/3)$ (approximately 109°). The internal angles in a regular pentagon are 108°, therefore they require only a small curvature to meet the laws of Plateau.

Figure 4.14 shows the distributions of the NEPF for the monodisperse foams in this work, Matzke's experiment and Kraynik's similar simulation (2003). Each frequency of 'This work' in Fig 4.14 is the average value over 3 runs. The frequencies in each run have random fluctuations of less than 8% of their average values. The results obtained in this work are consistent with both Matzke's and Kraynik's studies. The chi-square test was employed to evaluate the likeness between the distributions of this work and Matzke's. The null hypothesis states that the distribution obtained in this work (observed distribution) and Matzke's distribution (expected distribution) are the same. For the observed NEPF distribution, the degrees of freedom (υ) are 3 and the

chi-square statistic, χ^2, is 0.072. If the significance level (α) is set to 0.99, the critical value, $\chi^2_{critical}$, is 0.115. Therefore, $\chi^2 < \chi^2_{critical}$. The null hypothesis is therefore accepted. It means that there is no significant difference between the distributions obtained from this work and that from Matzke's experiment (for $\alpha =$ 0.99). All of the experimental and theoretical works consistently show that quadrilateral, pentagonal and hexagonal faces are the dominant types among bubbles, approximately weighting at 10%, 60% and 28% respectively. Triangular faces and faces with more than 7 edges account for less than 2% of total faces in an equilibrium foam.

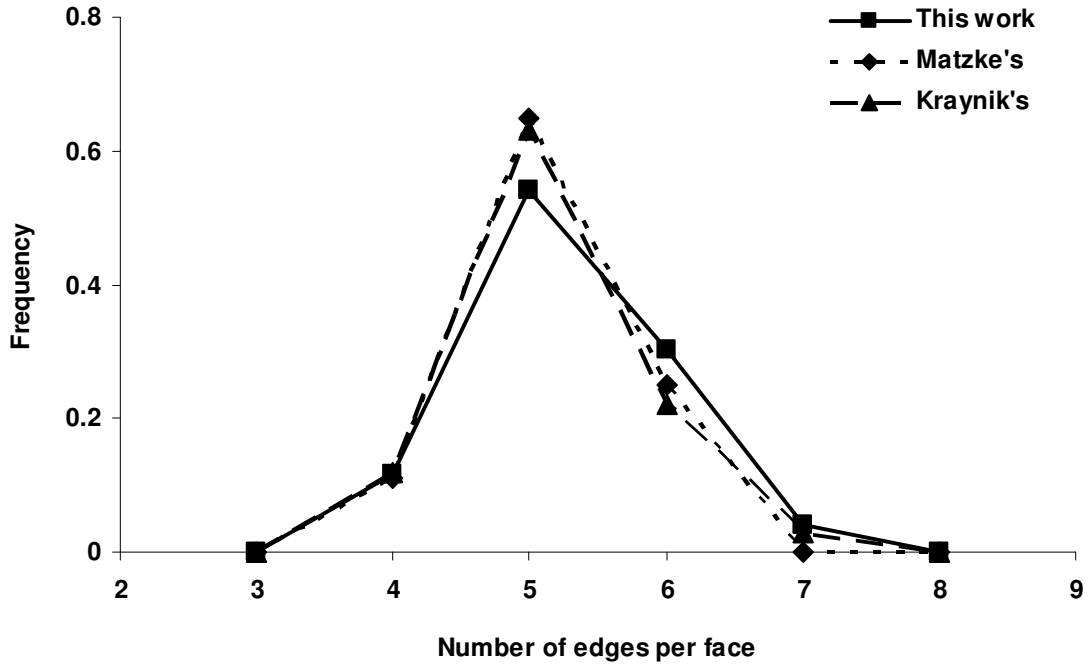

Figure 4.14: NEPF of the monodisperse foams.

The distributions of NEPF of the polydisperse foams (NSD = 0.14, 0.20 and 0.31) are also studied in a similar way. Figure 4.15 and 4.16 show the corresponding distributions for the surface and internal bubbles respectively.

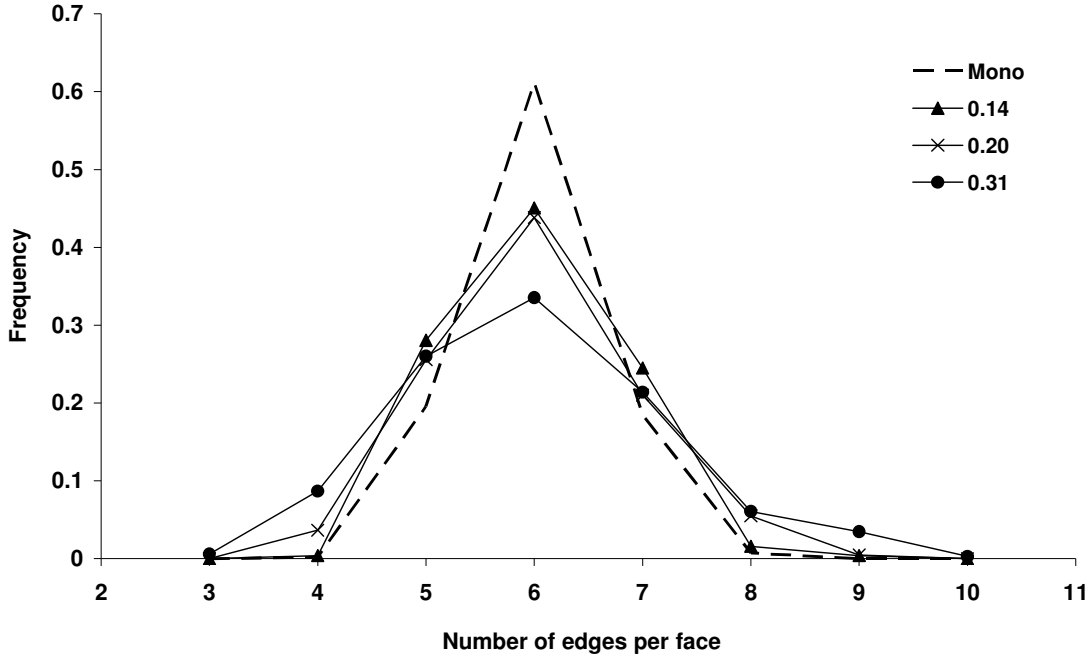

Figure 4.15: NEPF of the surface bubbles in foams with different levels of polydispersity.

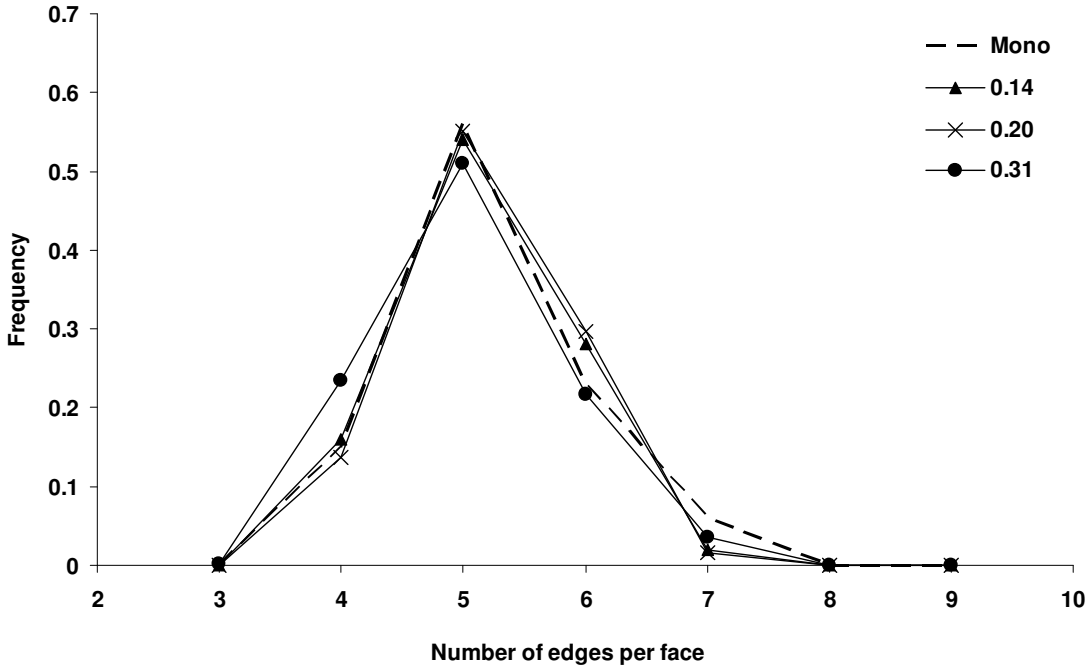

Figure 4.16: NEPF of the internal bubbles in foams with different levels of polydispersity.

The NEPF distributions of the internal bubbles appear to be insensitive to the increase

in foam polydispersity, with all the samples having a similar and consistent form of distribution. The internal distributions show approximately 55% of the faces are pentagonal, whilst 44% of the surface bubbles have a NEPF value equal to 5. The average value of NEPF for all the simulations is 5.1 ± 0.03 in this work. That observation is very similar to the one previously obtained from the monodisperse foams. Unlike the internal films, the surface films are topologically two-dimensional and periodic. According to Euler, there must be 6 edges per face on average. Unlike the internal faces, there is a marked increase in the variability of the number of edges per face as the polydispersity increases.

Due to Plateau's laws, the angles between any pair of edges which share a common vertex are equal to $\cos^{-1}(-1/3)$. Assume that all the faces are flat convex polygons and have N_{ave} edges in average. As the sum of the external angles is equal to 2π, the following relationship can be obtained:

$$(\pi - \cos^{-1}(-1/3)) \times N_{ave} = 2\pi \tag{4.1}$$

Therefore, the average number of edges per face can be estimated by Equation 4.2:

$$N_{ave} = 2/(1 - \cos^{-1}(-\frac{1}{3})/\pi) \approx 5.1 \tag{4.2}$$

The corresponding figure obtained from the simulations is 5.1 ± 0.03, which is very close to the theoretical value.

Euler's rule (Equation 4.3), governing the correlation among number of faces, edges and vertices in a convex regular polyhedron (Weaire and Hutzler, 1999), is used as the basis for deriving the relationship between the average number of faces per bubble and the average number of edges per face for internal bubbles.

$$F - E + V = 2 \tag{4.3}$$

Where:

F = number of faces of a convex polyhedron;

E = number of edges of a convex polyhedron;

V = number of vertices of a convex polyhedron.

To derive the relationship between the number of faces per bubble and the number of edges per face, a few assumptions are made:

1. Plateau' laws are satisfied among all the bubbles. This means that each vertex is shared by four edges, each edge is shared by 3 bubbles and each face is shared by two bubbles.

2. There are no edge effects in the foam.

For all the internal bubbles, F_t, E_t and V_t denotes the total number of nominal faces, edges and vertices respectively. The number of nominal faces, edges and vertices is not equal to the number of real faces, edges and vertices. Within a foam, each face is shared by two bubbles, each edge is shared by 3 faces and each vertex is shared by 4 edges. Therefore, faces are counted twice, edges are three times and vertices are counted four times when counting these structural elements bubble by bubble. By summing up all the bubbles in the foam, we have Equation 4.4:

$$F_t - E_t + V_t = 2B_t \tag{4.4}$$

Where:

B_t = total number of bubbles;

E_t = total number of nominal edges;

F_t = total number of nominal faces;

V_t = total number of nominal vertices.

Examining around a vertex, each vertex is shared by 4 edges. For each 'real' edge, there are actually two 'real' $1/4$ vertices ($1/2$ in total) connected. And each edge is shared by 3 bubbles. Therefore, we can have Equation 4.5:

$$\frac{2v_t}{4} = \frac{E_t}{3} \tag{4.5}$$

Correlating 4.4 and 4.5 to form Equation 4.6:

$$\frac{F_t}{B_t} - \frac{E_t}{3B_t} = 2 \tag{4.6}$$

As $\frac{E_t}{3B_t} = \frac{1}{3}\frac{E_t}{F_t}\frac{F_t}{B_t}$, Equation 4.6 can be transformed to:

$$\frac{F_t}{B_t}(1 - \frac{E_t}{3F_t}) = 2 \tag{4.7}$$

By definition, $\frac{F_t}{B_t}$ denotes the average number of faces per bubble. $\frac{E_t}{F_t}$ represents the fraction of the total number of nominal edges over the total number of nominal faces. In this work, each face is actually counted twice as it is shared by two bubbles in the internal structure. Therefore, the following relationship can be obtained: $F_t = 2F_t^{'}$ and $E_t = E_t^{'}.F_t^{'}$ is the total number of real faces. By definition, $\frac{E_t^{'}}{F_t^{'}}$ denotes the average number of edges per face in a foam. Equation 4.7 can thus be rewritten as

Equation 4.8:

$$\frac{F_t}{B_t}(1-\frac{E_t^{'}}{6F_t^{'}})=2 \tag{4.8}$$

After a number of simple manipulations, a neater form of the relationship can be expressed as:

$$\frac{F_t}{B_t}=12/(6-\frac{E_t^{'}}{F_t^{'}}) \tag{4.9}$$

Equation 4.9 is used to estimate the theoretical value of the average number of faces per bubble which is 13.4 in this work. It is close to the results from both Matzke's and this work. The minor difference can be attributed to edge effects which can not be eliminated among the peripheral bubbles in the simulation.

Conclusion

The preliminary results presented in this chapter demonstrate that the simulation of random foams based on Voronoi tessellation is successful in reproducing real foam structure and topology. Foams with both unconstrained and constrained surfaces are able to be effectively produced.

The topology of bubbles generated by this simulation method is in excellent agreement with the real random foam made by Matzke. The number of faces per bubble of the surface and underlying bubbles of monodisperse foam is 13.7 ± 0.1 and 11.0 ± 0.1 respectively, very close to Matzke's 13.7 and 11.0. The distribution of the number of faces per bubble, for both the internal and surface bubbles, broadens with the increase of polydispersity.

The results of the number of edges per face also shows excellent agreement with both Matzke's and Kraynik's studies. Pentagonal faces are found to be the most common type for foams over all levels of polydispersity. The number of edges per face of the internal bubbles is found to be approximately independent of the bubble size distribution. For the surface films, a marked increase in the variability of the number of edges per face has been observed when the polydispersity increases.

CHAPTER V

BUBBLE SIZE DISTRIBUTION

Introduction

In this chapter, the results on the surface film size distribution and the surface bubble size distribution are presented and analysed.

The aim of this chapter is to provide fundamental understanding of the relationship between the two distributions and how this relationship is influenced by the bubble size distribution of foam. An empirical formula will be developed to quantitatively relate the surface film size distribution and the internal bubble size distribution. This important formula constitutes the theoretical basis for predicting bubble size distributions in this work.

The empirical formula is tested in different foams with both unconstrained and constrained surfaces in order to examine its validity and robustness.

5.1 Definition of bubble size and film size

In order to be able to compare and relate the surface film size distribution and the corresponding bulk distribution, both of them need to be represented using equivalent radii. The equivalent spherical radius is used to represent the size of the bubble. If the

volume of a bubble is V_b, and the equivalent spherical radius is R_b, then the relationship between V_b and R_b is:

$$R_b = \sqrt[3]{\frac{3}{4\pi}} V_b^{1/3} \tag{5.1}$$

In the process of image analysis, the surface information is recorded by a camera set vertically above the foam surface. Then the surface photo is partitioned into several closed areas (Figure 5.1). This means that the area of surface film recorded is not the actual area of the film, but rather the vertically projected area.

The size of the projected area is represented using an equivalent circular radius of the film. If the projected area of the targeted film is S_f, and the equivalent circular radius, R_f, is given by Equation 5.2:

$$R_f = \frac{1}{\sqrt{\pi}} S_f^{\frac{1}{2}} \tag{5.2}$$

In this work, both R_b and R_f are normalised by the Sauter mean of the internal bubble radii of the foam. The Sauter mean, R_{32}, is given by Equation 5.3, where $< \cdot >$ denotes the average function.

$$R_{32} = < R_b^3 > / < R_b^2 > \tag{5.3}$$

The Sauter mean, also called surface-volume mean, is defined as the radius of a sphere that has the same volume/surface area ratio as a particle of interest. The Sauter mean is usually the most relevant estimation of average particle size in cases where

surface force is dominant, such as in a liquid foam (Grau and Heiskanen, 2005). All the radii used in this and later chapters are normalised by the Sauter mean radius.

In order to avoid confusion, in the following sections, the normalised bubble size and film size are denoted as r and r_S respectively, which are given by $r = R_b / R_{32}$ and $r_S = R_f / R_{32}$.

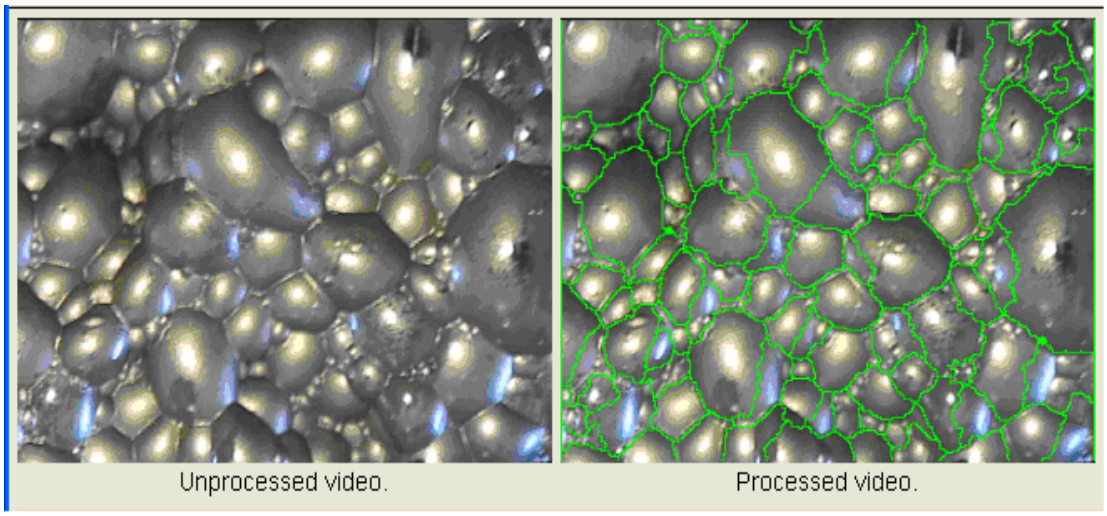

Figure 5.1: Image processing on the surface of industrial froth (used in Hadler et al., 2006).

5.2 The distribution of bubble size and film size

Depending on the property of the foam being predicted, the representative average bubble size requires different weighting when being calculated. For instance, when calculating the surface area of the foam, the average required is the area weighted, or Sauter mean. When the length of Plateau Border per volume (a critical parameter in drainage) is required, a combination of the area weighted and volume average means are required (Kraynik, 2005). The only way to be able to calculate all these different averages is to have an accurate bubble size distribution. As it is typically only the surface film size distribution that is conveniently known, its relationship to the actual internal bubble size distribution will be examined.

Figure 5.2 displays the internal bubble size distributions of a series of foams, with normalised standard deviation (NSD) equal to 0.0, 0.14 and 0.31 respectively. The distribution curves broaden with the increase of NSD, which displays a very regular and expected transition.

The bin width of the histograms plotted in the following sections of this thesis is determined by Equation 5.4 (Scott, 1979):

$$W_{bin} = 3.49 \cdot \sigma \cdot N_b^{-1/3} \tag{5.4}$$

In Equation 5.4, W_{bin} denotes the optimal bin width of a histogram, σ is the standard deviation of the sample population and N_b is the number of available samples which refers to the number of surface bubbles or films in this work. Scott's equation is applicable for obtaining an unbiased optimal estimation of the probability density function defined on a histogram with equally spaced bins.

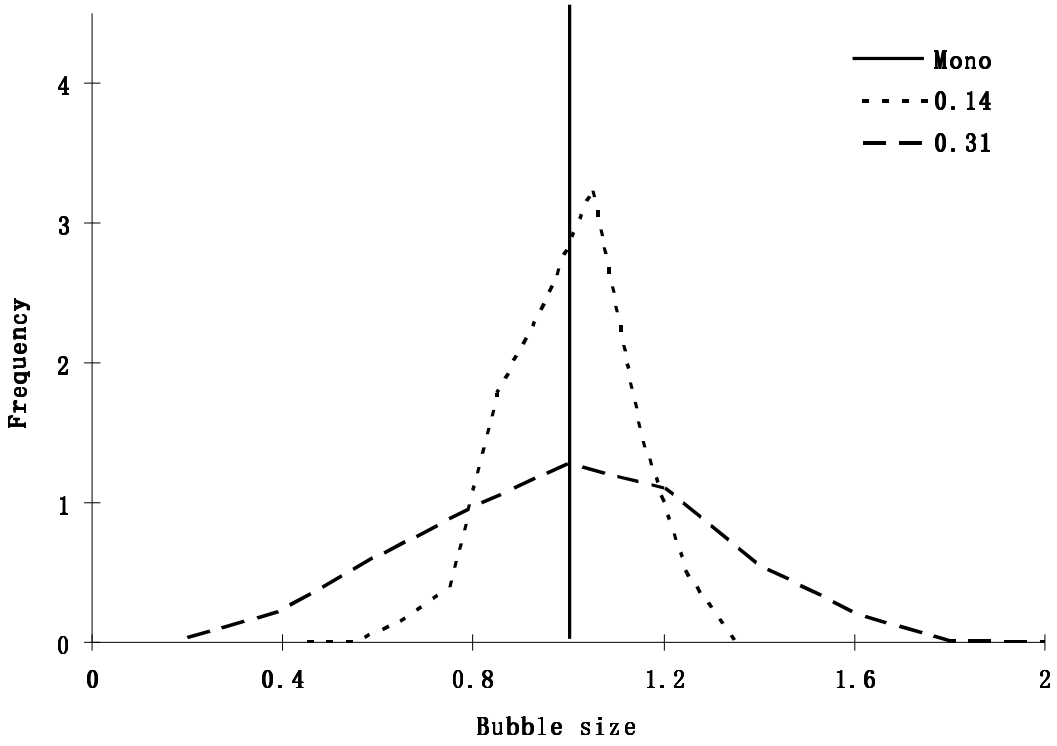

Figure 5.2: The internal bubble size (r) distributions (NSD = 0.0, 0.14 and 0.31.

Figure 5.3 shows the corresponding distributions of the surface film size, r_S. There is a marked difference between these film size distributions and the bubble size distributions. This is particularly noticeable for the monodisperse foam, which has a range of different surface film sizes. This can be understood by the comparison made in Figure 5.4. Even on the surface of a monodisperse foam, a range of bubble sizes can be observed (Figure 5.4). This is because there are a number of factors that determine the surface film size for a given surface bubble. The first and the most important factor is the radius of the bubble. The second is the position of a bubble relative to the neighbouring surface bubbles. If a surface bubble positions relatively lower than its neighbouring bubbles, it may have a lower level of exposure on the surface. A third, relatively trivial, factor is the distortion of the bubble within a foam. If viewed from a vertical perspective, the measured film size is slightly larger than the bulk size if a bubble is vertically squeezed and it appears to be smaller if vertically stretched.

The difference between the distributions in Figure 5.2 and 5.3 indicates that, at least for the spectrum of polydispersity studied in this work, the film size distribution is not a good proxy for the bulk distribution.

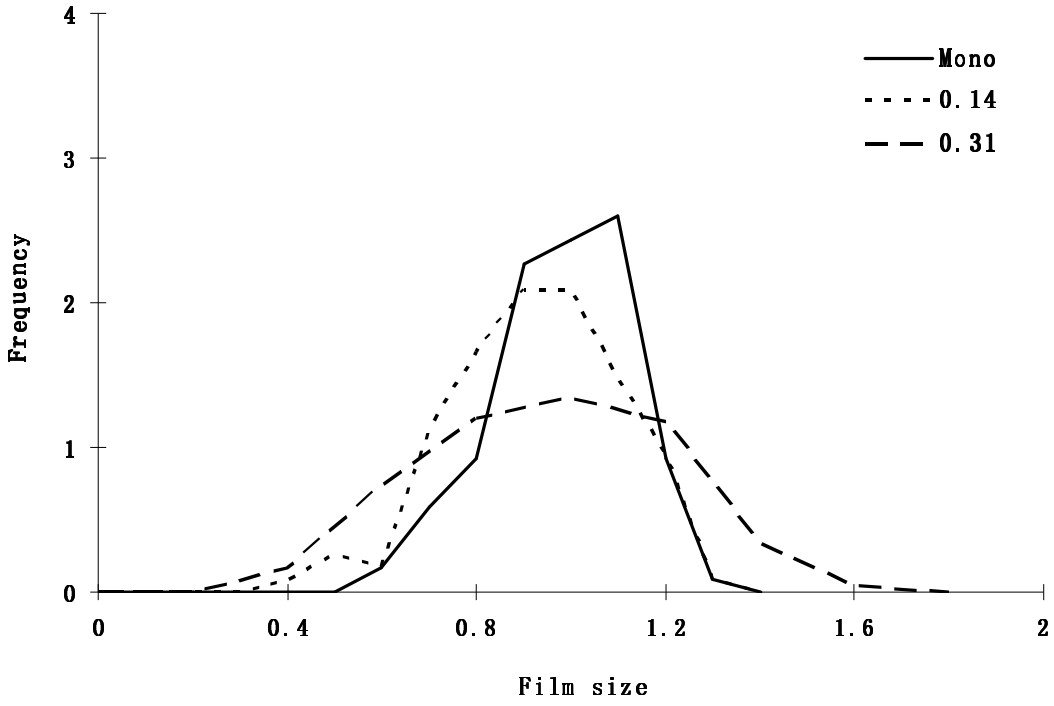

Figure 5.3: The surface film size (r_S) distributions (NSD = 0.0, 0.14 and 0.31.

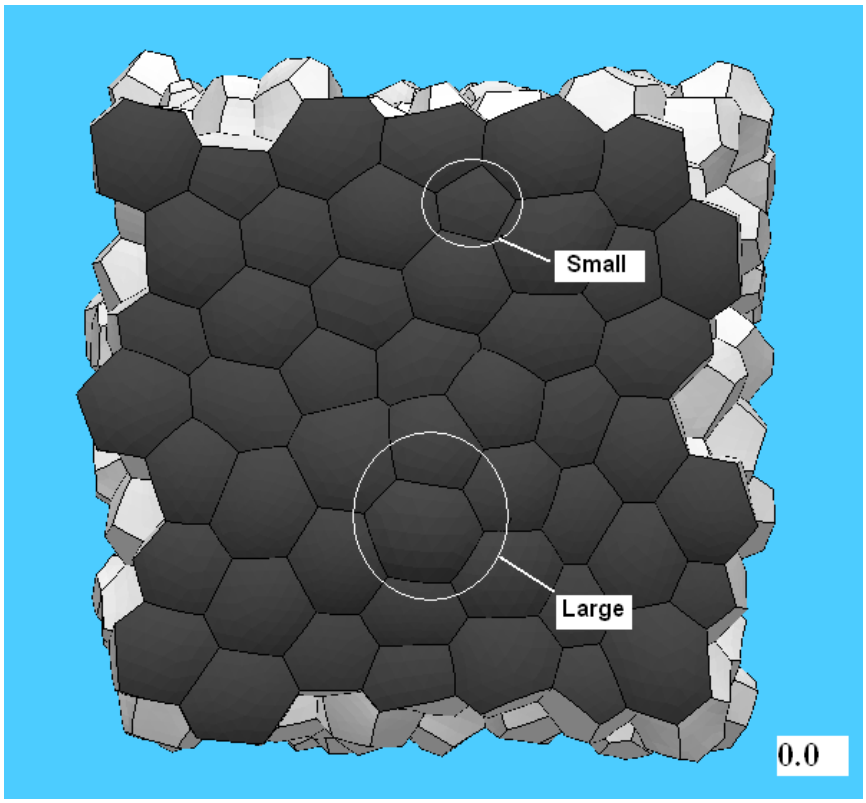
Small
Large
0.0

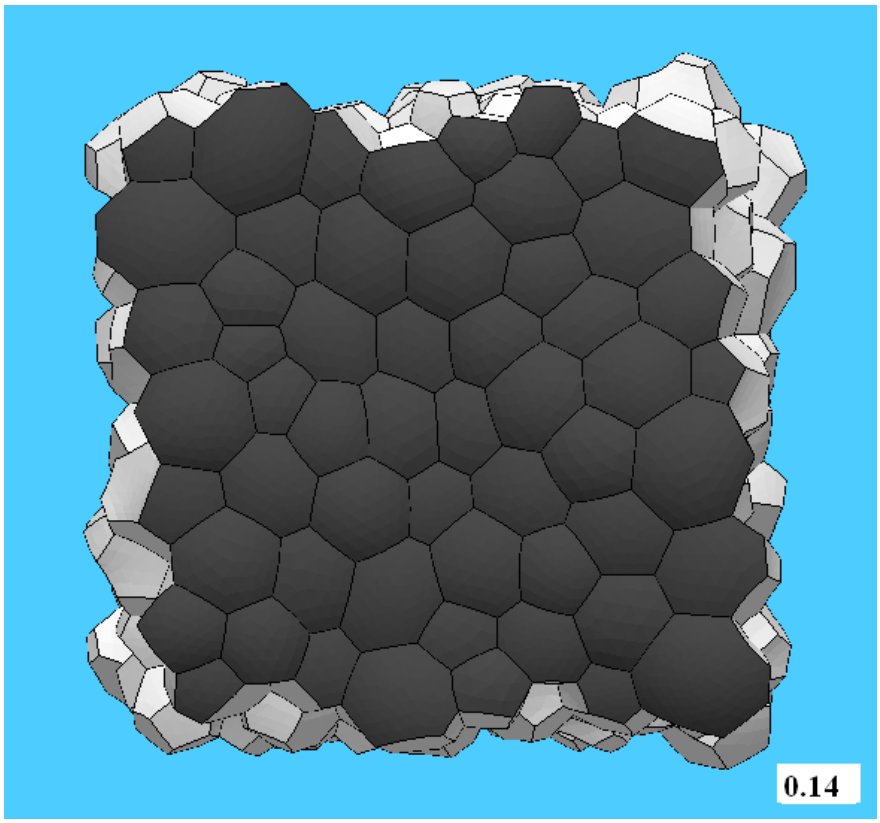
0.14

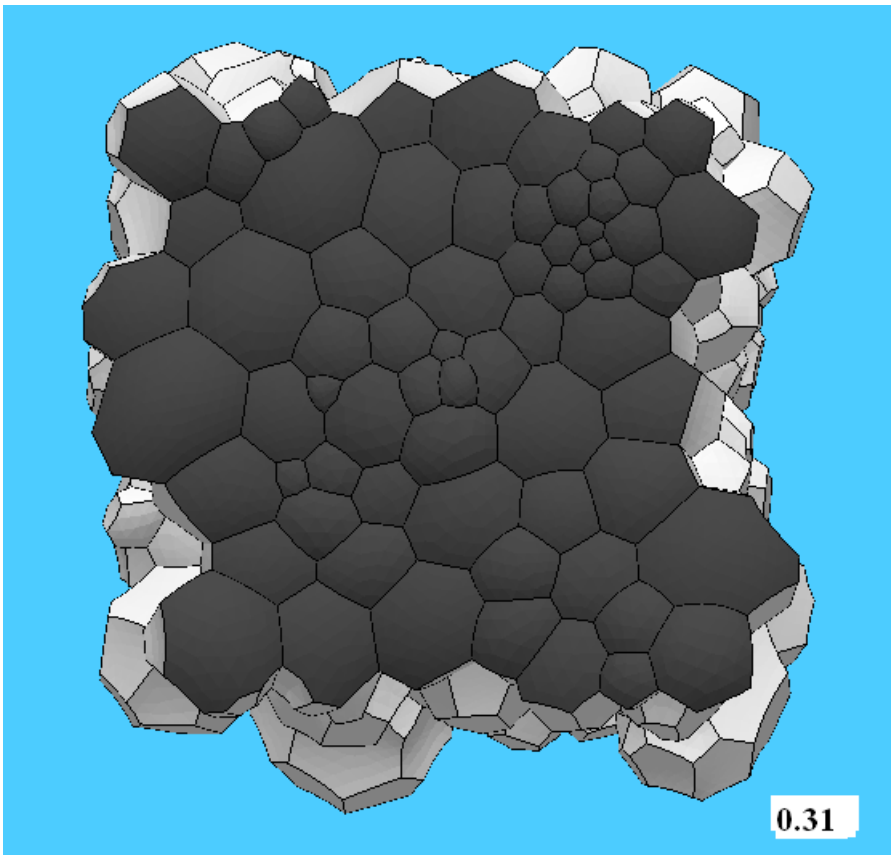

Figure 5.4: The surfaces of foams with different levels of polydispersity (NSD = 0.0, 0.14 and 0.31).

Figure 5.5 shows the film size, r_S, as a function of the radius of the bubble to which it is attached, r, and further illustrates the problem pointed out previously. There is no simple correlation between r_S and r. Even as the foam polydispersity increases, there is a range of possible r_S for a given r. What is also noticeable is that there are film sizes as small as approximately 90% of the radius of the bubble to which they are attached, but in these simulations no bubble has a film larger than approximately 1.2 times the radius of the bubble. This shows that large bubbles can have smaller films at the surface, but there is a limit to size of the film that can be attached to a bubble of a particular size. This means that, even though the relationship between surface topology and internal structure tends to be complex, the surface bubble can only have a limited range of exposures on the top of the foam.

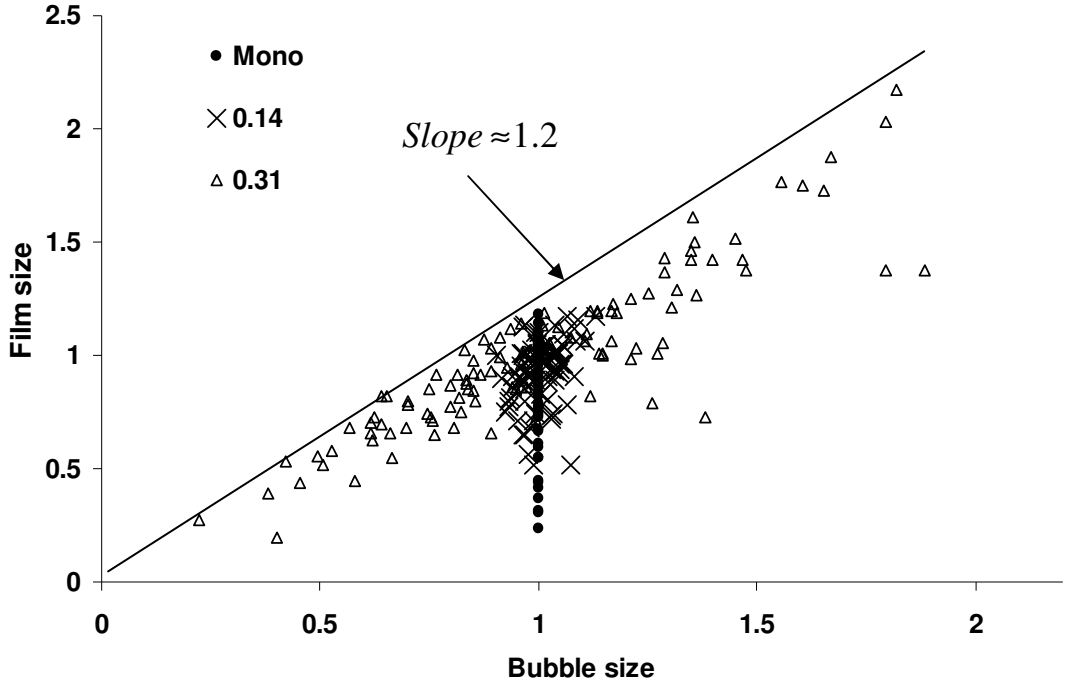

Figure 5.5: The relationship between the surface film size, r_S , and the size of the bubble to which it is attached, r .

In order to attempt to collapse the data from Figure 5.5 into a single distribution, we investigate the distribution of r / r_S, the ratio of the surface film radius to the radius of corresponding bubble. r / r_S can be intuitively understood as the level of surface exposure of a surface bubble. The frequency distribution in Figure 5.6 uses the same sets of data presented in Figure 5.5.

In this work, 500 ± 5 bubbles are produced in the 5 runs for each level of polydispersity. 130 ± 4 of them are surface bubbles. The normalised standard deviation of all the ratios is 0.148 ± 0.03 in all the runs. The narrow error bar of the sample standard deviation partially indicates the robustness of the underlying distribution. From Equation 5.4, the optimal width of histogram bin is 0.101 ± 0.002.

In Figure 5.6, the foams with different bubble size distribution have essentially the

same frequency distribution of the ratio. This indicates that the distribution of the ratio of film size to the radius of the bubble to which it is attached is independent of the polydispersity of the underlying bubbles. The independence of this statistical relationship from the polydispersity of the underlying bubbles provides an opportunity to relate the surface and the internal structure.

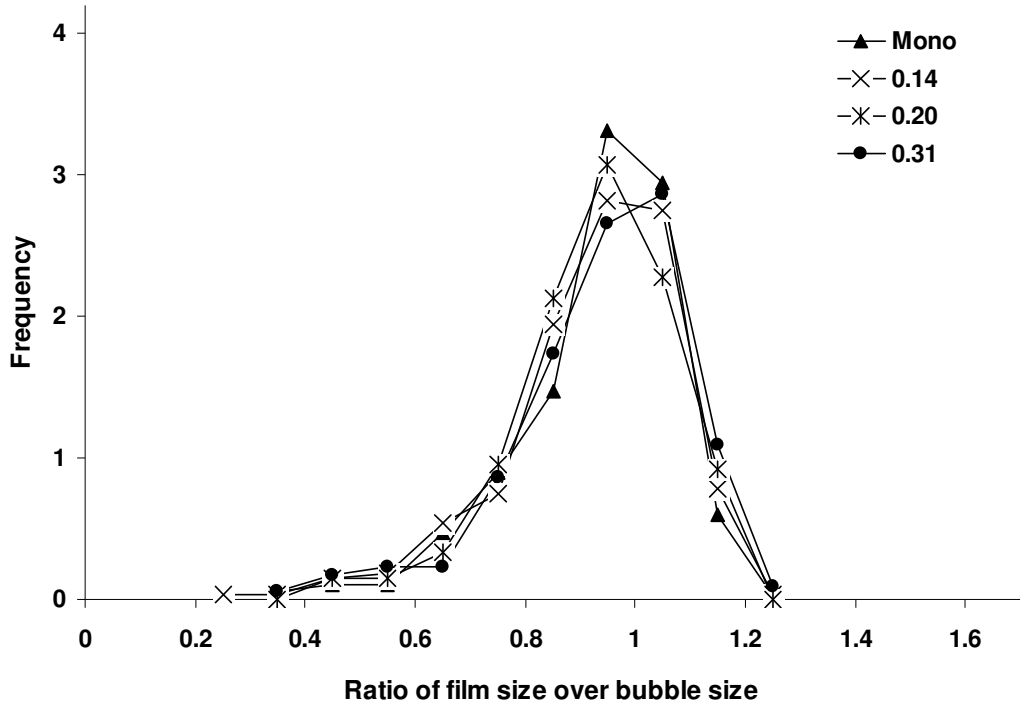

Figure 5.6: The frequency distributions of r / r_S for foams with unconstrained surfaces (NSD = 0.0, 0.14, 0.20 and 0.31). The bin width = 0.1.

In this work, foams with both unconstrained and constrained surfaces (Figure 4.3) are produced. Figure 5.7 shows the distribution of the ratio among constrained foams with different degrees of polydispersity (NSD = 0.0, 0.14, 0.20 and 0.31). The frequency distribution for the constrained surface appears to be very similar to that for the unconstrained surface. Figure 5.7 shows that the shapes of the distribution graphs are consistent and surface constraint has little impact on this distribution. From a statistical view of Figure 5.6 and 5.7, most of the surface film sizes are 0.8 - 1.0 times

of their corresponding surface bubble size. Only a small fraction (less than 15%) of films is noticeably less or larger than the radius of bubble to which it is attached. A thorough physical explanation of this phenomenon is still far from clear and requires much future study. Qualitatively speaking, at least three factors influence the surface film size distributions: bubble size which is obvious, bubble deformation and the packing effect of surface bubbles. Bubble deformation makes the 2D equivalent circular radius different from the corresponding 3D spherical radius. For example, if a bubble in the foam is stretched vertically, the 2D film size tends to be smaller than the 3D bubble size. On the contrary, if it deforms horizontally the 2D film size will be larger than the corresponding bubble size. In a randomly packed foam, the manner of packing also influences the relative position of surface bubbles. If the location of a surface bubble is relatively lower than its neighbours, it may have a smaller exposure on the surface.

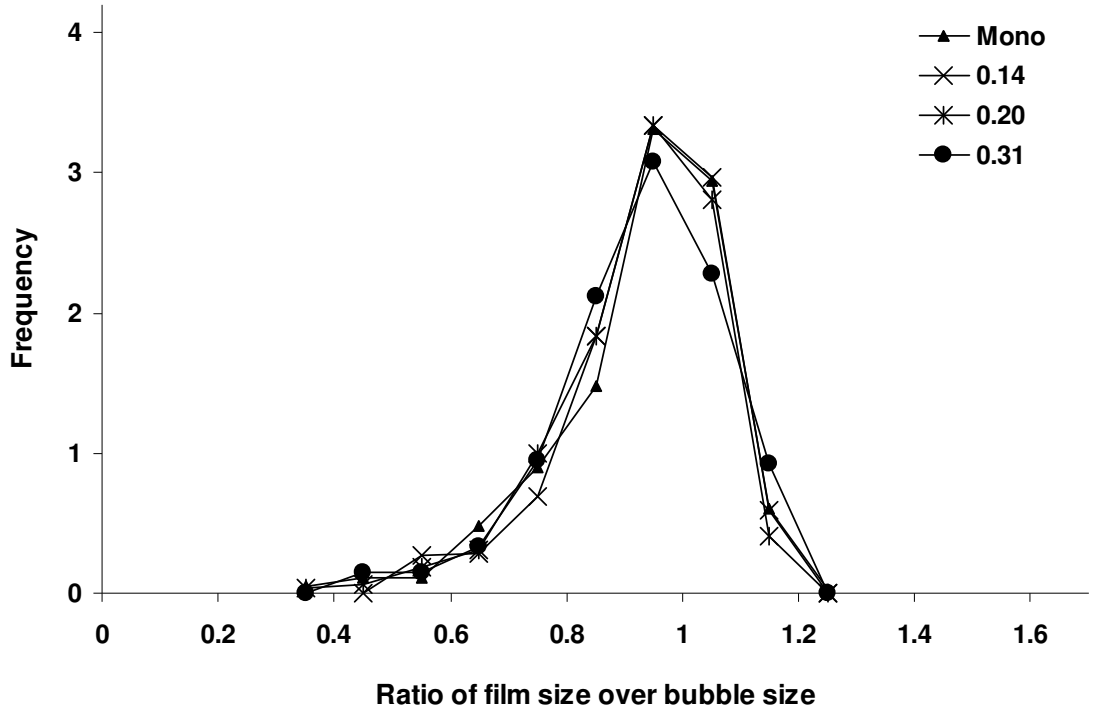

Figure 5.7: The frequency distributions of r / r_S for foams with constrained surfaces (NSD = 0.0, 0.14, 0.20 and 0.31). The bin width = 0.1.

Figure 5.8 shows the distributions for narrow bubble size intervals using data from the moderately polydisperse foam (NSD = 0.14). Surface bubbles from all of the 5 runs are used in order to have sufficient number of samples. The full range of bubbles is equally divided into a series of size fractions. The frequency distribution of the ratio within each fraction is studied and compared with the overall distribution. The averaged standard deviation of all the size fractions is 0.146 ± 0.005. But the number of samples in each fraction varies from approximately 50 (0.6 - 0.8 interval) to approximately 240 (1.0 – 1.2 interval). Figure 5.8 is plotted in order to demonstrate the robustness of the relationship. Therefore the average of the optimal bin sizes, 0.1, is used. All of the distributions are of a similar shape indicating that the distribution does not depend on the relative size of the bubbles involved. Although, the shapes of these graphs display great similarity, the distributions in Figure 5.8 show more variability than those in Figure 5.6 and 5.7 since they are based on sub-sets of the previous distributions and thus have relatively smaller sample sizes.

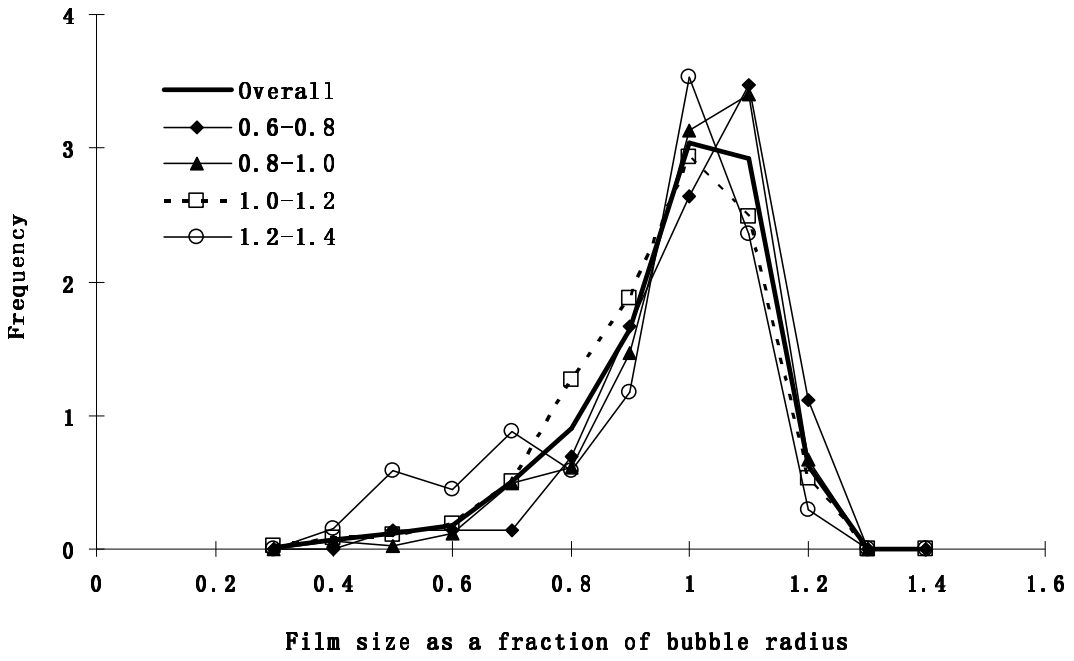

Figure 5.8: The frequency distributions of r / r_S for the individual bubble size fractions and the overall bubble radii. The bin width = 0.1.

5.3 An empirical relationship to describe the frequency distribution

The frequency distribution of the ratio shown in Figure 5.6 and 5.7 is the key to relating the surface film size distribution and the bulk distribution. If $f(r_S / r)$ denotes the distribution function of the ratio, the relationship between the film and bubble size distributions can be expressed as Equation 5.5. This indicates that the surface film size distribution, $F(r_S)$ can be obtained analytically, given an explicit expression of $f(r_S / r)$ and the bubble size distribution, $S(r)$.

$$F(r_S) = \int_{r=0}^{\infty} f\left(\frac{r_S}{r}\right) S(r)\, dr \tag{5.5}$$

Where:

r_S = normalised surface film radius;

r = normalised surface bubble radius;

$F(r_S)$ = frequency distribution of surface film size;

$S(r)$ = frequency distribution of surface bubble size;

In order to develop a functional form for Equation 5.5, the graphs are firstly transformed into a logarithmic coordinates system. Figure 5.9 shows that the frequency distribution appears to exhibit a power law relationship among the surface films which are smaller than the bubble radius to which they are attached. However, the frequency drops off rapidly when $\frac{r_S}{r} > 1.0$. As a result, the distribution skews to the right side. Equation 5.6 is proposed as an empirical formula that will display this behaviour. Equation 5.6 is obtained by the multiplication of a power law and a

sigmoid function.

$$f\left(\frac{r_S}{r}\right) = K \frac{\left(\frac{r_S}{r}\right)^n}{1 + \exp\left(C\left(\frac{r_S}{r} - l\right)\right)} \tag{5.6}$$

Where:

r_S = normalised surface film radius;

r = normalised surface bubble radius;

K, l, n and C are the fitting parameters

In Equation 5.6, n is the power law exponent for when the film size is smaller than the radius of the bubble to which it is attached. The value of n is obtained from the slope of the left tail of the distribution curve when plotted on log-log axes. The variability of n in different polydisperse foams is low, ranging from 4.0 to 5.0. C represents the steepness of the drop-off in the right hand tail, where the film sizes are larger than their surface bubble sizes. The apparent short right tail means that, observing optically from the top, most of the film sizes tend to be smaller than the size of the bubble to which they are attached, with a maximum of approximately 1.2 times the corresponding bubble size. l denotes the location of the drop-off. K functions as the scale factor of $f(\frac{r_S}{r})$. As the frequency distribution is a probability density function, the value of K can be determined by Equation 5.7.

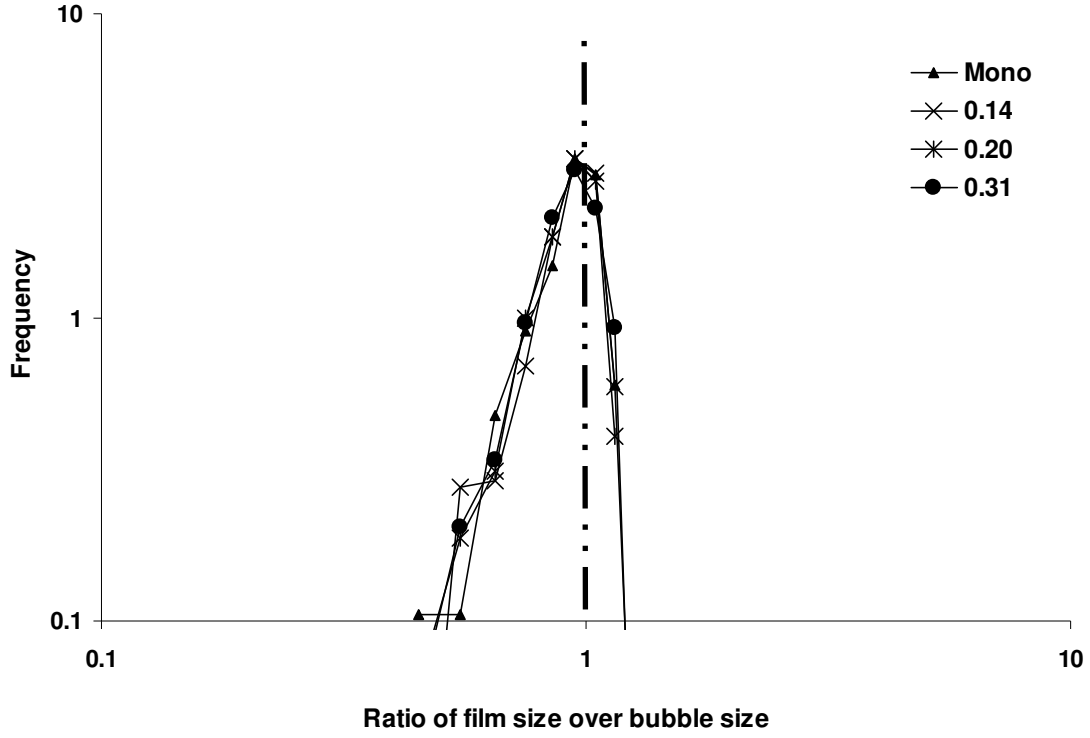

Figure 5.9: The logarithmic frequency distributions of foams with unconstrained surfaces (NSD = 0.0, 0.14, 0.20 and 0.31).

$$\int_0^{\infty} f\left(\frac{r_S}{r}\right) d\left(\frac{r_S}{r}\right) = 1 \tag{5.7}$$

In this work, the non-linear regression method is employed to compute the optimal values of the four equation parameters. As this regression needs to satisfy Equation 5.7, there are 3 degrees of freedom in the function fitting. *n, l, C* and *K* are obtained by fitting the cumulative distribution function, instead of the probability density function (Equation 5.6), to the data obtained from simulations. This is preferable because fitting to a histogram would have been influenced by the width of bin selected. The cumulative distribution, however, does not require bins.

Another reason for choosing cumulative distribution fitting is that each frequency in the histograms has different error variance which breaks the assumption used in the ordinary least squares method. Although we can use a weighted least squares method

to obtain unbiased estimation of the four parameters, an accurate and neat form of the weighting function is very difficult to obtain. In a cumulative distribution, however, all the data have constant error variance, which makes the ordinary least squares method valid. As no neat form of the integral for Equation 5.6 has been found, the fourth order Runge-Kutta method is employed to numerically integrate Equation 5.6 to obtain the cumulative values. The ordinary least squares method is then used to obtain optimal values of *n, l, C* and *K*. The optimal values of the 3 independent fitting parameters are iteratively obtained by minimising the squared errors between the empirical curve and the actual curve, while at the same time adjusting K to ensure that Equation 5.7 is satisfied for all of the time. The results for unconstrained and constrained distributions are below:

$$f\left(\frac{r_S}{r}\right) = \frac{3.55\left(\frac{r_S}{r}\right)^{4.62}}{1 + \exp\left(47.96\left(\frac{r_S}{r} - 1.08\right)\right)} \quad \text{(unconstrained)} \quad (5.8)$$

$$f\left(\frac{r_S}{r}\right) = \frac{3.51\left(\frac{r_S}{r}\right)^{4.67}}{1 + \exp\left(56.34\left(\frac{r_S}{r} - 1.08\right)\right)} \quad \text{(constrained)} \quad (5.9)$$

The coefficient of determination (COD) is used as a measurement of the goodness of fit of Equation 5.8 and 5.9. The coefficient of determination, R^2, is the proportion of the variability in the data set that is accounted for by a mathematical model or formula. The expression of R^2 employed in this work is as follow:

$$R^2 = 1.0 - \frac{SS_E}{SS_T} \quad (5.10)$$

In the above definition, $SS_E = \sum_{i=1}^{n}(y_i - \hat{y}_i)^2$ and $SS_T = \sum_{i=1}^{n}(y_i - \bar{y})^2$. y_i is the observed or actual values; $\hat{y}_i$ is the predicted value in the model or formula and $\bar{y}$ is the mean of all the observed values. Typically, if R^2 is 0.99, the formula can be regarded as an excellent fit. Table 5.1 shows the goodness of fit for both Equation 5.8 and 5.9. All the values of COD shown in Table 5.1 are above or very near to 0.99. This indicates that the equations derived in this work are a good fit to the simulation results. The cumulative distribution fitting for foams with unconstrained and constrained surfaces are also plotted on Figure 5.10 and 5.11 in order to demonstrate the excellent representation of the data obtained from simulation. In both of these graphs, the empirical distribution shows little variation from the curves obtained from the simulations.

NSD	R^2 **(unconstrained)**	R^2 **(constrained)**
Mono (0.0)	**0.995 ± 0.001**	**0.989 ± 0.002**
0.14	**0.992 ± 0.002**	**0.988 ± 0.002**
0.20	**0.994 ± 0.003**	**0.993 ± 0.003**
0.31	**0.991 ± 0.002**	**0.994 ± 0.002**

Table 5.1. The coefficient of determination, R^2, of the cumulative fitting for foams with both unconstrained and constrained surfaces (NSD = 0.0, 0.14, 0.20 and 0.31).

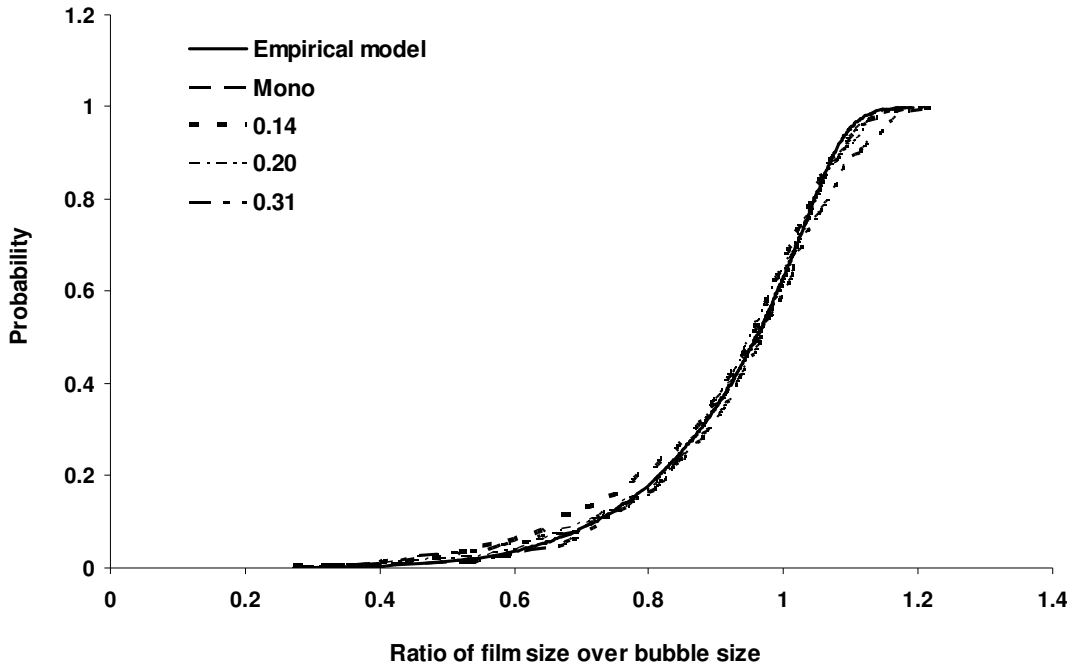

Figure 5.10: The cumulative frequency distributions of foams with unconstrained surfaces. The empirical distribution is based on Equation 5.8.

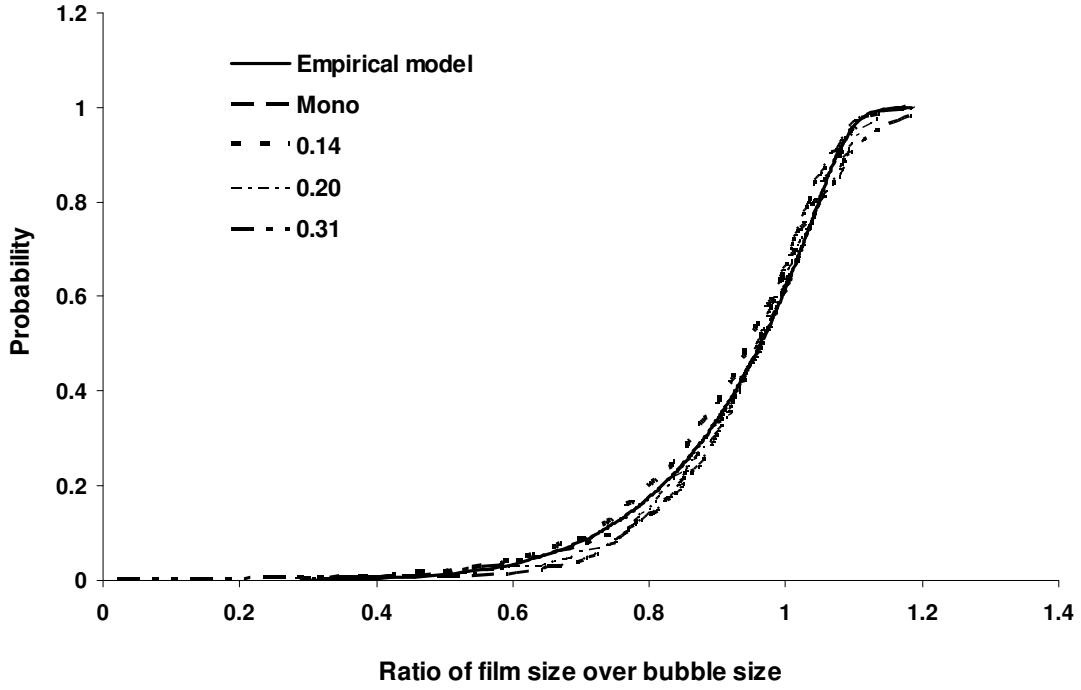

Figure 5.11: The cumulative frequency distributions of foams with constrained surfaces. The empirical distribution is based on Equation 5.9.

Conclusion

This chapter has demonstrated that the relationship between the size distribution of the films visible at the foam surface and the underlying bubble size distribution is complex, with a range of film sizes seen for a given surface bubble size. Even for foams with a uniform bubble size, a range of film sizes can be observed on the surface.

It is shown, though, that when the surface film size is normalized by the size of the bubble to which it is attached, the frequency distribution of this ratio collapses to a single curve that is independent of the underlying bubble size distribution over a wide range of polydispersity. A functional form for this frequency distribution has been proposed that accurately reflects the shape of the distribution.

CHAPTER VI

PREDICTING FILM AND BUBBLE SIZE DISTRIBUTIONS

Introduction

Based on the functional form obtained in Chapter V, both the 'forward problem' – predicting the surface film size distribution based on a given internal bubble size distribution and the 'backward problem' – predicting the internal bubble size distribution based on a given surface film size distribution, will be addressed in this chapter. Numerical procedures will be developed for computing the distributions for both problems. The robustness of the predicted distributions obtained from the numerical procedures will be examined using the chi-square test.

Furthermore, the performance of the distribution-prediction method developed in this work is compared with the relevant method proposed by de Vries, with a brief analysis of the weakness of de Vries' model.

6.1 Predicting the surface film size distribution

The statistical relationship between the surface film size distribution and the bulk distribution has successfully correlated the surface structure and the internal structure. In this sense, it provides the basis for predicting both the surface film size distribution from the bubble size distribution and vice versa. In this section, we are focusing on the former: predicting the surface film size distribution.

Recalling the theory of conditional expectation, the surface film size distribution, $F(r_S)$, can be expressed as a function of the distribution of the ratio of film size to bubble size, $f(\frac{r_S}{r})$, and the surface bubble size distribution, $S(r)$:

$$F(r_S) = \int_{r=0}^{\infty} f\left(\frac{r_S}{r}\right) S(r) dr \qquad (6.1)$$

r_S = normalised radius of surface film;

r = normalised radius of surface bubble;

Equation 6.1 is a continuous relationship between the surface film size distribution and the surface bubble size distribution. A discrete approximation is desirable for two reasons: 1) in both research and industry, $F(r_S)$ is commonly obtained from optical measurements, such as image analysis. The output data of the measuring process is likely to be discrete and sometimes difficult to be converted into a continuous relationship. 2) The ultimate objective of developing this formula is to predict the bulk distribution, thus an inverse of this relationship is required. It is more tractable to use discrete data when inverting an integral. Equation 6.2 is a discrete approximation of Equation 6.1:

$$F\left(r_S\right) \approx \sum_{r=0}^{r_{\max}} f\left(\frac{r_S}{r_i}\right) S\left(r_i\right) \Delta r_i \qquad (0 < r_i < r_{\max}) \tag{6.2}$$

In Equation 6.2, both $F(r_S)$ and $S(r)$ have the property of a vector, in which each element represents the frequency of a specific film size or bubble size. This can then be expanded as follows:

$$\begin{aligned} F(r_{S_1}) &= \sum_{r=0}^{r_{\max}} f(\frac{r_{S_1}}{r_i}) \cdot S(r_i) \cdot \Delta r_i \\ F(r_{S_2}) &= \sum_{r=0}^{r_{\max}} f(\frac{r_{S_2}}{r_i}) \cdot S(r_i) \cdot \Delta r_i \\ &\vdots \\ F(r_{S_n}) &= \sum_{r=0}^{r_{\max}} f(\frac{r_{S_n}}{r_i}) \cdot S(r_i) \cdot \Delta r_i \end{aligned} \tag{6.3}$$

Equation 6.3 can be rewritten in a matrix form:

$$F(r_S) = A \cdot S(r), \text{ where } \quad A_{i,j} = \Delta r \; f\left(\frac{i\Delta r_S + r_{S,\min}}{j\Delta r + r_{\min}}\right) \tag{6.4}$$

where

A = coefficient matrix of the simultaneous equations (Equation 6.5)

$A_{i,j}$ = entry of matrix A (the ith row and the jth column)

Δr_S = increment of r_S

Δr = increment of r

$r_{S,\min}$ and $r_{\min}$ = minimum values of r_S and r respectively

$$A = \begin{bmatrix} f(\frac{r_{S1}}{r_1}),\ f(\frac{r_{S1}}{r_2}),\cdots,\ f(\frac{r_{S1}}{r_i}),\ \cdots,\ f(\frac{r_{S1}}{r_n}) \\ f(\frac{r_{S2}}{r_1}),\ f(\frac{r_{S2}}{r_2}),\ \cdots,\ f(\frac{r_{S2}}{r_i}),\ \cdots,\ f(\frac{r_{S2}}{r_n}) \\ \vdots \\ f(\frac{r_{Sm}}{r_1}),\ f(\frac{r_{Sm}}{r_2}),\ \cdots,\ f(\frac{r_{Sm}}{r_i}),\ \cdots,\ f(\frac{r_{Sm}}{r_n}) \end{bmatrix}_{n\times m} \tag{6.5}$$

Using Equation 6.5 in conjunction with Equation 5.8 or 5.9 in Chapter V (depending on whether the surface is constrained or not), the surface film size distribution can be computed analytically using a known bubble size distribution. In order to test these formulae, a series of simulations have been implemented in a range of foams.

Figure 6.1 shows the predicted film size distribution of a monodisperse foam with unconstrained surfaces. In this case, the surface bubbles have uniform bubble size. The dashed line represents the film size distribution that might be obtained by optical measurement like image analysis. And the solid line denotes the predicted film size distribution based on Equation 6.4 and a known bubble size distribution, $S(r)$. The bin width of histogram is estimated by Scott's equation (Equation 5.4). The number of actual surface films and their standard deviation are used in the estimation of bin width since it is impossible to obtain those of the predicted distributions. In practice, that approximation works well as the difference between the predicted distribution and the actual distribution is usually quite small.

For Figure 6.1, 500 uniformly sized bubbles are produced, with 138 on the surface (N_b = 138) and the standard deviation of the actual surface film sizes equal to 0.12 (σ = 0.12), therefore the bin width is 0.08. The empirical prediction appears to be in excellent agreement with the actual distribution. The chi-square test is implemented in order to examine the goodness of fit of the predicted distribution to the actual distribution. In this case, the degrees of freedom (υ) are 9, the significance level (α)

is 0.99, the chi-square statistic (χ^2) is therefore 0.478, which is less than the corresponding critical value ($\chi^2_{critical}$), 2.088. All the test results are listed in Table 6.1 at the end of this section. As demonstrated in Figure 6.2, a range of film sizes are successfully predicted from a uniformly sized foam. This is coupled by Matzke's experiment (1946), in which a range of non-uniformly sized films can be observed from his manually produced monodisperse foam. This photo is not attached as the quality and resolution of it is too low to be displayed.

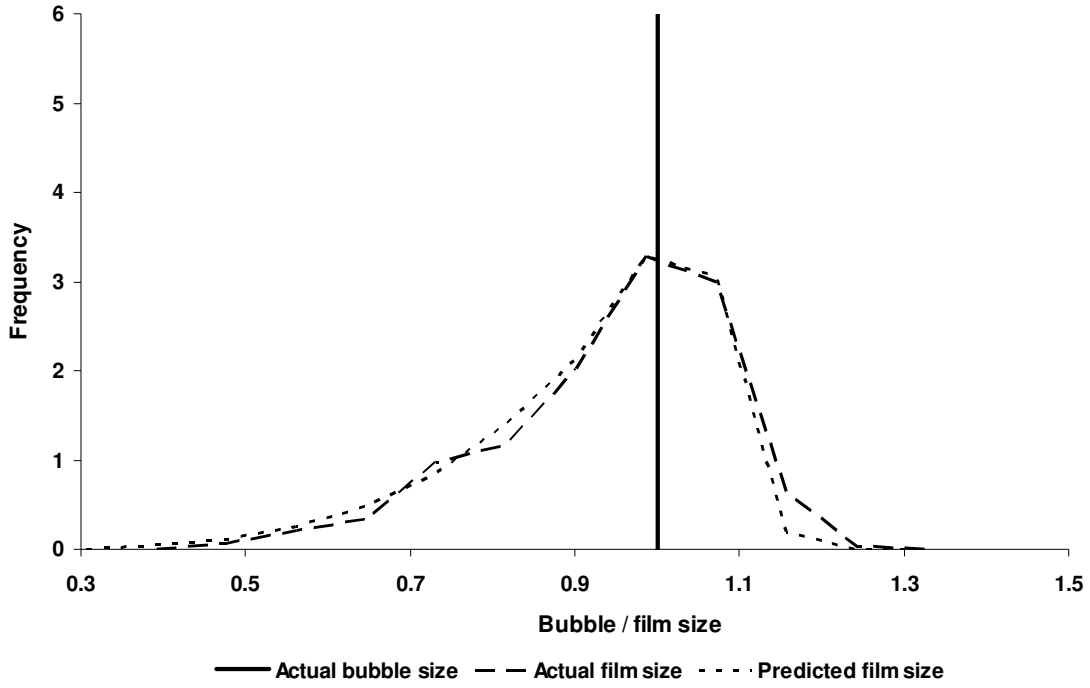

Figure 6.1: The predicted and the actual surface film size distributions of a monodisperse foam with unconstrained surfaces.

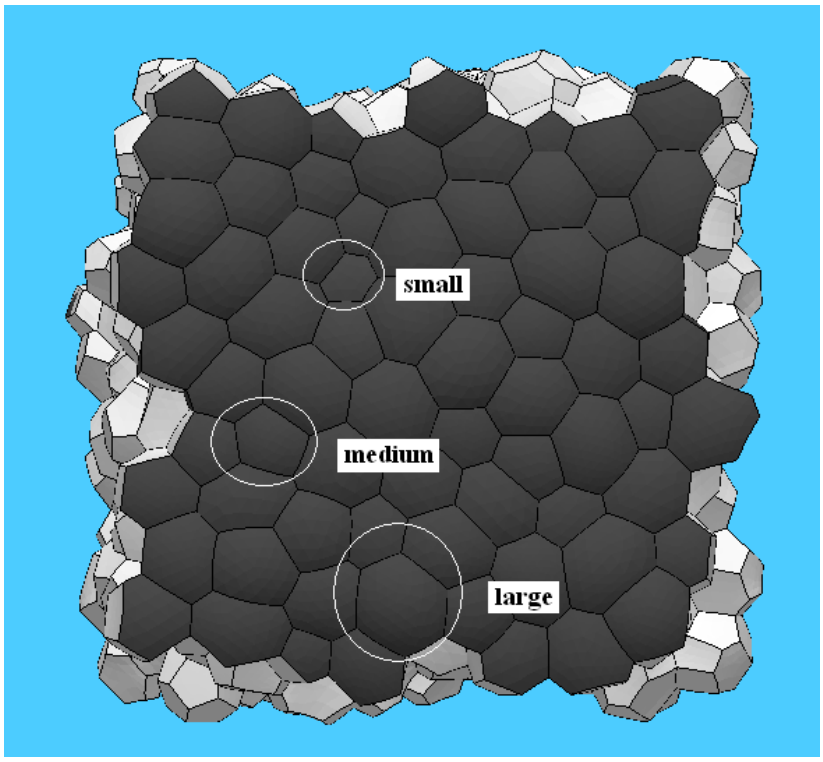

Figure 6.2: The surface of a monodisperse foam with unconstrained surfaces.

Figure 6.3 and 6.4 shows the predicted film size distribution when the surface of the monodisperse foam is constrained. In this case, Equation 6.4 is jointly used with Equation 5.9. The number of surface bubbles is still 138. The standard deviation of the surface film sizes, however, has slightly increased, rising to 0.13. The bin width accordingly increases to 0.09. Figure 6.4 shows the corresponding foam surfaces of this sample. For this constrained monodisperse foam, υ=7 and α = 0.99, χ^2 = 0.581, which is less than $\chi^2_{critical}$, 1.239.

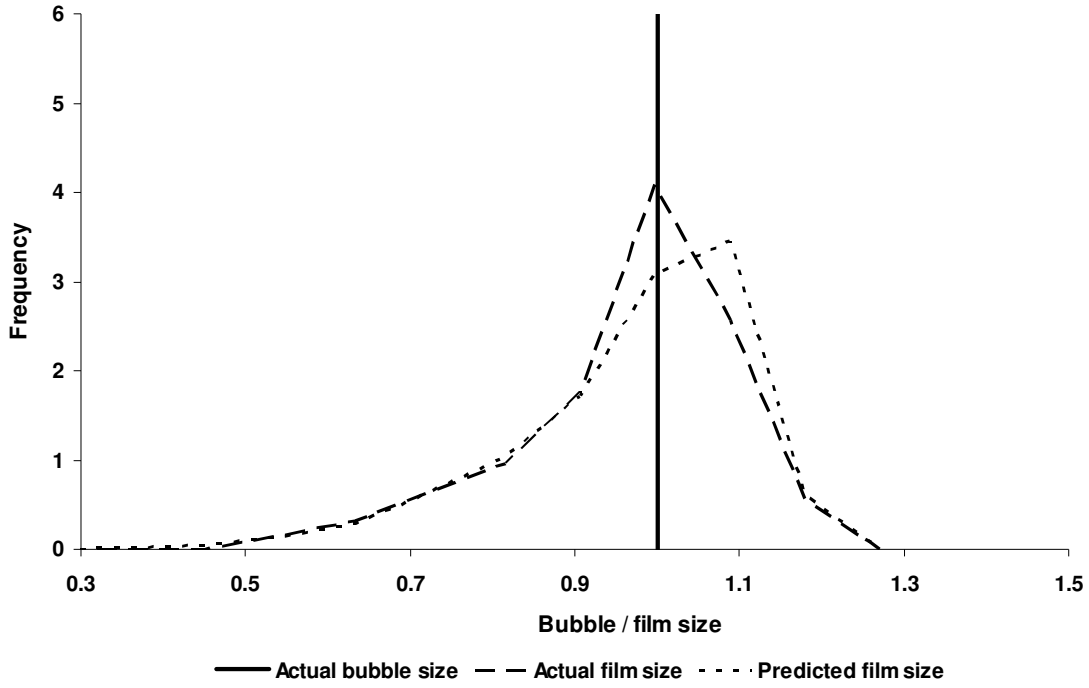

Figure 6.3: The predicted and the actual surface film size distributions of monodisperse foam with constrained surfaces.

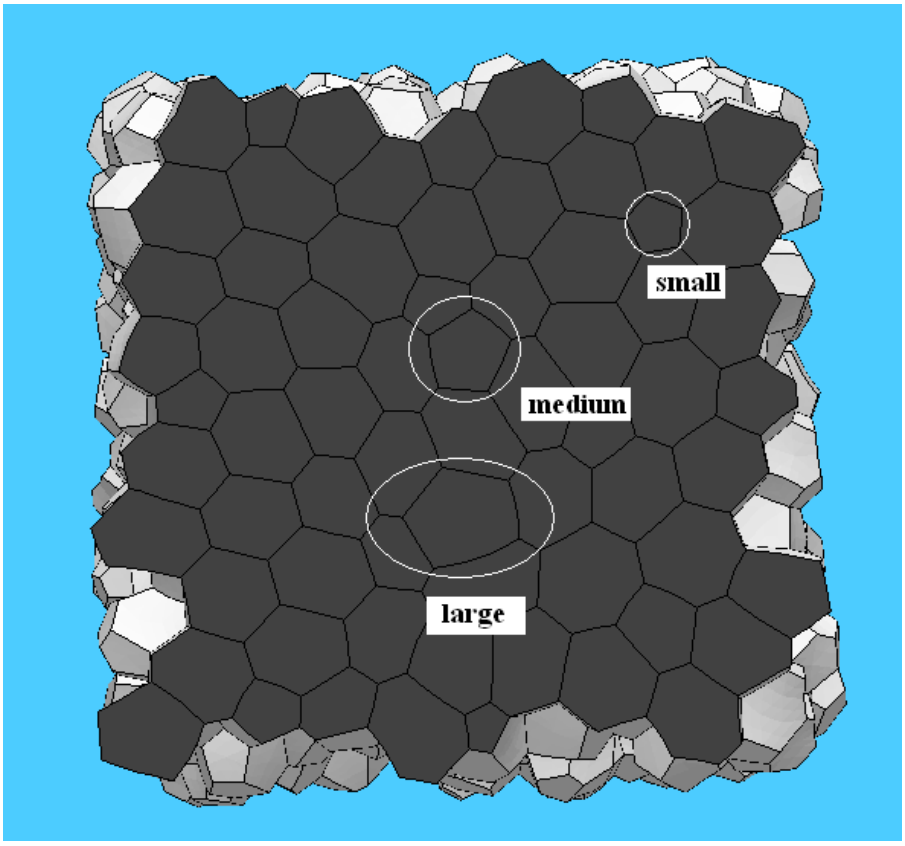

Figure 6.4: The surface of a monodisperse foam with constrained surfaces.

Figure 6.5 shows the application to a bi-disperse foam with unconstrained surfaces. 494 randomly packed bubbles are produced, with N_b = 132 and σ = 0.25 (bin width = 0.17). In a bi-disperse foam, there are only two bubble sizes and, in this particular case, the volume of the larger bubble is approximately 5.6 times the volume of the smaller one. Therefore, the equivalent spherical radius of the larger bubble is 1.76 times that of the smaller one. It can be seen from Figure 6.5 and 6.6 that, despite there only being two different bubble sizes within the system, there is a wide variation in the surface film sizes. In this case, υ=6 and α = 0.99, χ^2 is therefore equal to 0.150, which is less than $\chi^2_{critical}$, 0.872. Therefore the predicted film size distribution is in excellent agreement with the distribution obtained from the simulation. Both display a dual-peak shape, with a range of film sizes around each of the peaks. This demonstrates that a combination of Equation 5.8 and 6.4 is able to accurately model the distribution obtained from the detailed simulation.

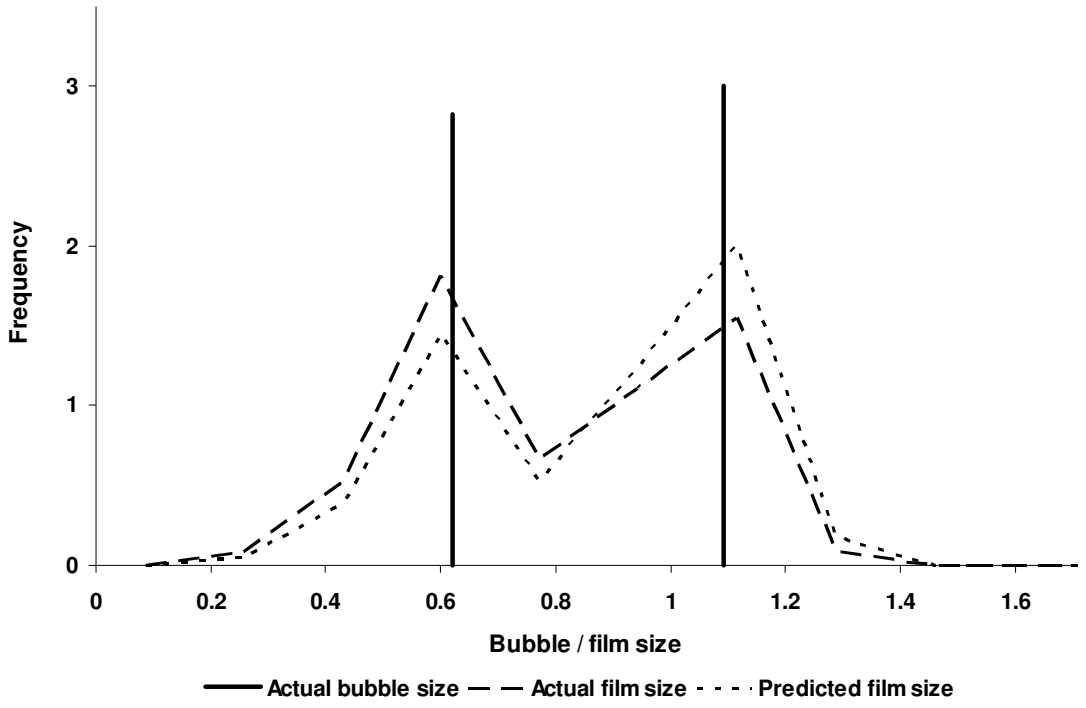

Figure 6.5: The predicted and the actual surface film size distributions in a bi-disperse foam with unconstrained surfaces.

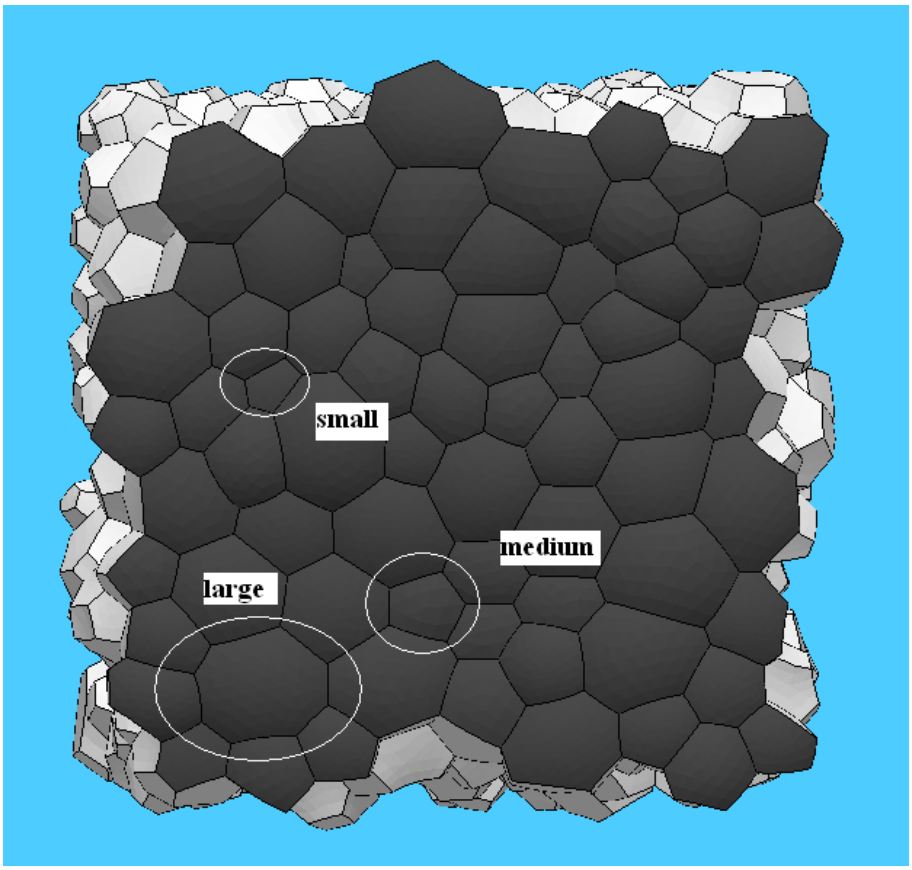

Figure 6.6: The surface of a bi-disperse foam with unconstrained surfaces.

A bi-disperse random foam with constrained surfaces has also been simulated. There are 495 bubbles in total, 130 of which are at the surface (σ = 0.19). Thus the bin width is equal to 0.13. The volume of the larger bubbles is approximately 3 times the volume of the smaller bubbles. The surface film size distribution can be predicted by jointly using Equation 5.9 and 6.4. In this case, υ=7 and α = 0.99, χ^2 is 0.417, which is less than $\chi^2_{critical}$, 1.239. As demonstrated in Figure 6.7, the predicted film size distribution appears to be very close to the corresponding distribution obtained from simulation. Figure 6.8 shows the surface of this constrained bi-disperse foam.

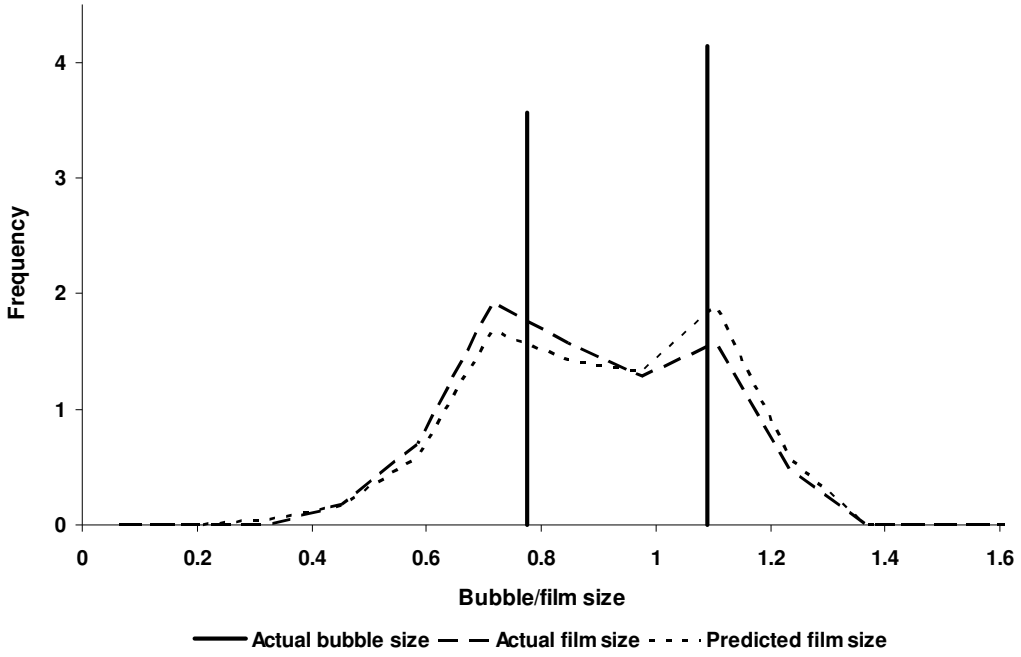

Figure 6.7: The predicted and the actual surface film size distributions in a bi-disperse foam with constrained surfaces.

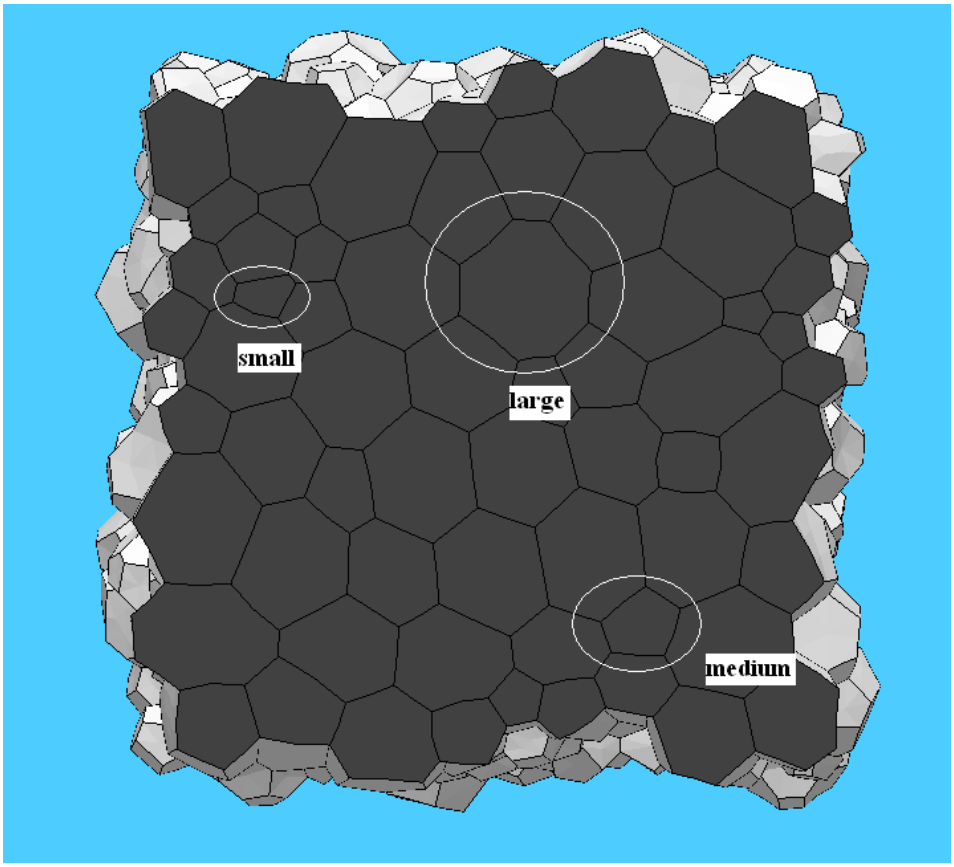

Figure 6.8: The surface of a bi-disperse foam with constrained surfaces.

Furthermore, the performance of the model in highly polydisperse foams is also presented. Figure 6.9 shows a foam (NSD = 0.31) with unconstrained surfaces. In this case, there are 495 bubbles in total, with N_b = 121 and σ = 0.27. The bin width is 0.19. In the chi-square test, χ^2 is equal to 0.140 (α = 6 and υ = 0.99), which is smaller than the corresponding $\chi^2_{critical}$, 0.872. Figure 6.10 shows the result of a constrained foam (NSD = 0.30, N_b = 121 and σ = 0.27), with a bin width of 0.19. For the constrained foam shown in Figure 6.10, χ^2 is equal to 1.007 (α = 8 and υ = 0.99), which is less than the corresponding $\chi^2_{critical}$, 1.647.

The above results at the 0.99 significance level suggest that the predicted distributions are in excellent agreement with the actual distributions. It is noticeable that, in the spectrum of high polydispersity, the difference between the actual film size distribution and the bulk distribution diminishes. This is because, in highly dispersed foams, bulk size becomes the dominant factor in determining the surface film size distribution, and the impact of bubble distortion and level of exposure on the surface play a relative less important role. This is different from the cases in which foams are uniformly sized or have a narrow range of bubble sizes.

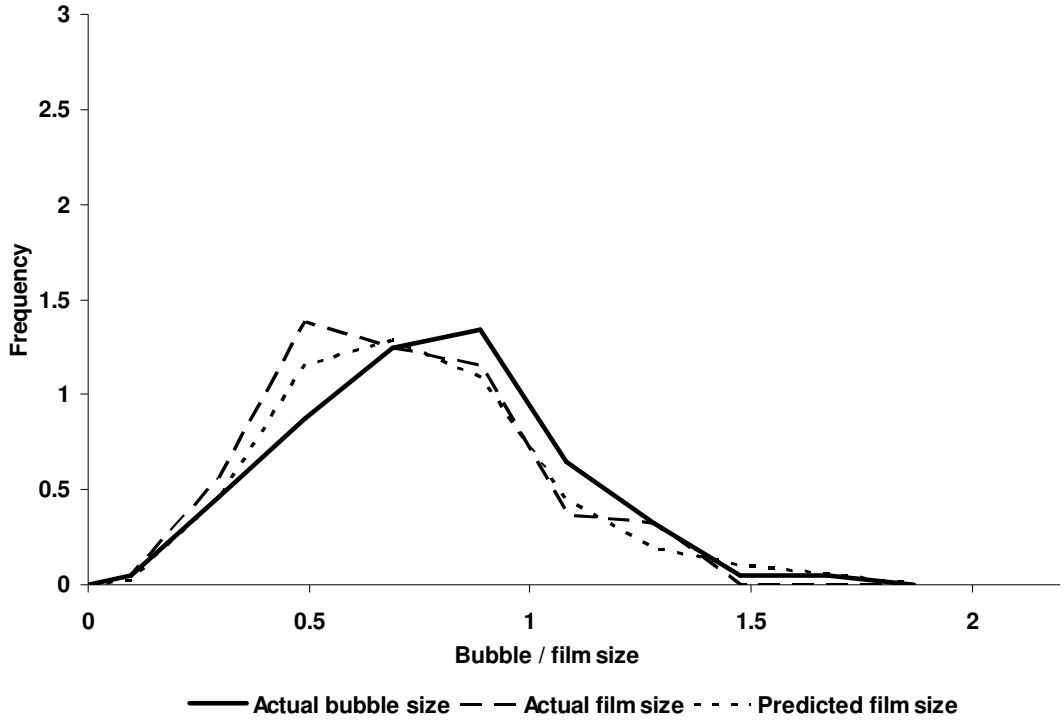

Figure 6.9: The predicted and the actual surface film size distributions in a highly polydisperse foam with unconstrained surfaces (NSD = 0.31).

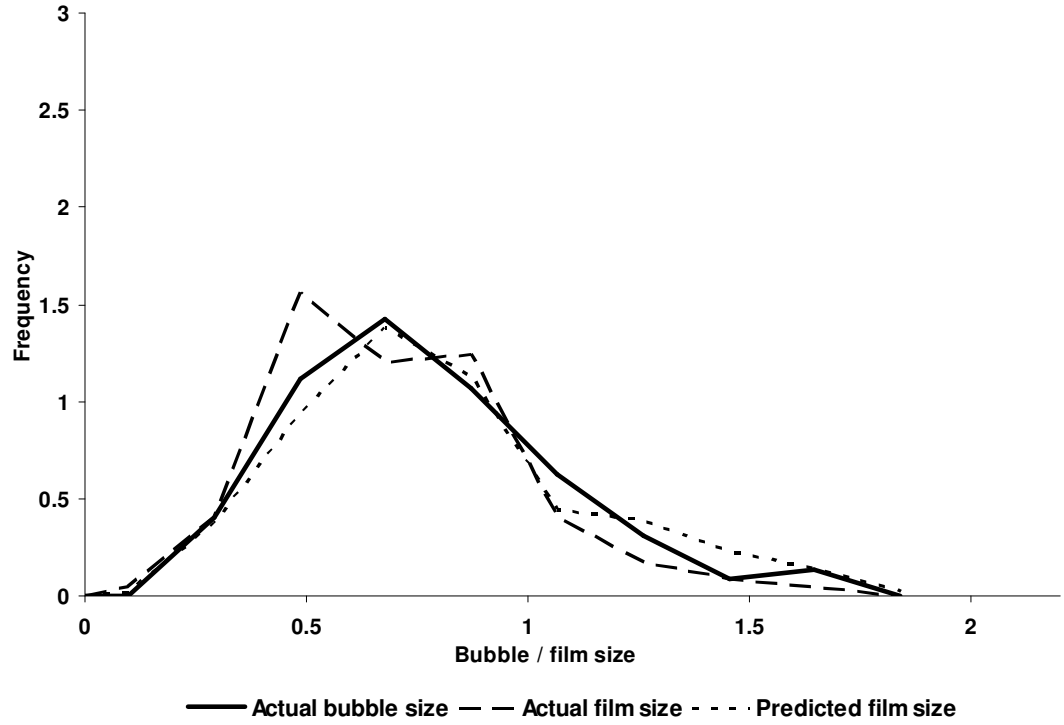

Figure 6.10: The predicted and the actual surface film size distributions in a highly polydisperse foam with constrained surfaces (NSD = 0.30).

Table 6.1 presents a summary of the results of all of the chi-square test in this section. In all the tests, the significance level is 0.99, which suggests high degree of agreement. The degrees of freedom are determined by subtracting 1 from the number of non-empty frequencies. The null hypothesis states that the actual film size distribution (expected distribution) and the predicted film size distribution (observed distribution) are the same. In all of the cases, χ^2 is less than $\chi^2_{critical}$ and the null hypothesis is accepted. This means that the model developed in this work is valid, robust and applicable to a range of dry foams.

NSD	**Degrees of freedom, υ (α = 0.99)**	$\chi^2_{critical}$	χ^2
Mono (uncons)	**9**	**2.088**	**0.468**
Mono (cons)	**7**	**1.239**	**0.581**
Bi-disp (uncons)	**6**	**0.872**	**0.150**
Bi-disp (cons)	**7**	**1.239**	**0.417**
0.31 (uncons)	**6**	**0.872**	**0.140**
0.30 (cons)	**8**	**1.647**	**1.007**

Table 6.1: The results of the chi-square test for all the predicted surface film size distributions. 'uncons' = unconstrained surfaces, 'cons' = constrained surfaces.

6.2. Predicting the surface bubble size distribution

Thus far we have succeeded in solving the forward problem; that is predicting the film size distribution from a known bubble size distribution. Our aim, though, is to solve the inverse of this problem: predicting the surface bubble size distribution based on a known film size distribution, as this is what is usually experimentally measured. The first approach attempted was to simply invert the matrix in Equation 6.5. There are two problems with inverting the matrix directly: the first is that the matrix in Equation 6.5 is often large and has a large fraction of the entries being nearly zero. Inverting it directly may incorporate a considerable amount of computational errors. Secondly, with all but the smoothest data, it gives some negative frequencies, caused by unconditionally fitting $S(r)$ to the actual data. Recalling Equation 6.2, the expected value of $F(r_S)$ is calculated with respect to the frequency distributions of $f(\frac{r_S}{r})$ and $S(r)$. If the slope in the actual data is steeper than the maximum slope in $f(\frac{r_S}{r})$, a negative value of $S(r)$ may be required to exactly fit the data. This type of noise in the data causes the predicted frequency to fluctuate wildly.

To overcome this problem, a numerical approach was adopted. By iteratively updating the values for $S(r)$ and recalculating the estimated values for $F(r_S)_{est}$, the square of the error, $(F(r_S)_{est} - F(r_S))^2$ could be minimized subject to the constraint that $S(r)$ remains positive for all r. Therefore the problem of inverting the matrix is transformed into a non-linear optimization problem: finding a set of $S(r_i)$ to obtain the minimum value of $\sum_{i=1}^{n}(F(r_{S_i})_{est} - F(r_{S\,i}))^2$, subject to the constraint that every $S(r_i) > 0$.

In this work, the numerical method described was tested using a series of random foams, such as bi-disperse, slightly polydisperse and highly polydisperse foam. In the following section, a few examples are presented in order to demonstrate the performance of this inversion method on foams over a wide range of polydispersity. The performance of this method is also compared with the method proposed by de Vries (1957).

De Vries proposed a universal theoretical method to reduce the statistical bias in the measured surface film size distribution. When exerting a sampling plane on the surface of a foam or measuring from a bound surface (constrained surface), small bubbles tend to be 'missed out' preferentially. The formula for correcting this bias can be expressed as follows:

$$f_c(r) = [\int_0^\infty \frac{f_u(r)dr}{r}]^{-1} \frac{f_u(r)}{r} \tag{6.6}$$

Where:

$f_c(r)$ = corrected size frequency distribution function of bubble radius, r.

$f_u(r)$ = uncorrected size frequency function obtained by a viewed plane (or constrained surface).

r = normalised bubble radius.

The results in constrained foams will be compared with the distributions obtained by Equation 6.6. The chi-square test is again used to evaluate the agreement between the predicted (or corrected) distributions and the actual distributions. The test results are listed in Table 6.2 at the end of this section.

Figure 6.11 shows a bi-disperse foam with unconstrained surfaces. The volume of the larger bubble is approximately 6 times that of the smaller one. The optimal bin width is estimated by Scott's equation. The sampling standard deviation, σ, is approximated

by the standard deviation of the actual bubble sizes since it is impossible to know the corresponding parameters of the predicted distributions. As shown in the graph, the measured surface 2D distribution is fundamentally different to the bulk distribution which displays a dual-peak shape initially. The predicted curve fits the actual distribution. In this case, the degree of freedom is 1 and the chi-square statistic is 0.76. The corresponding significance level for this test is therefore equal to 0.383. This indicates that the difference between the predicted distribution and the actual distribution is statistically reasonably large.

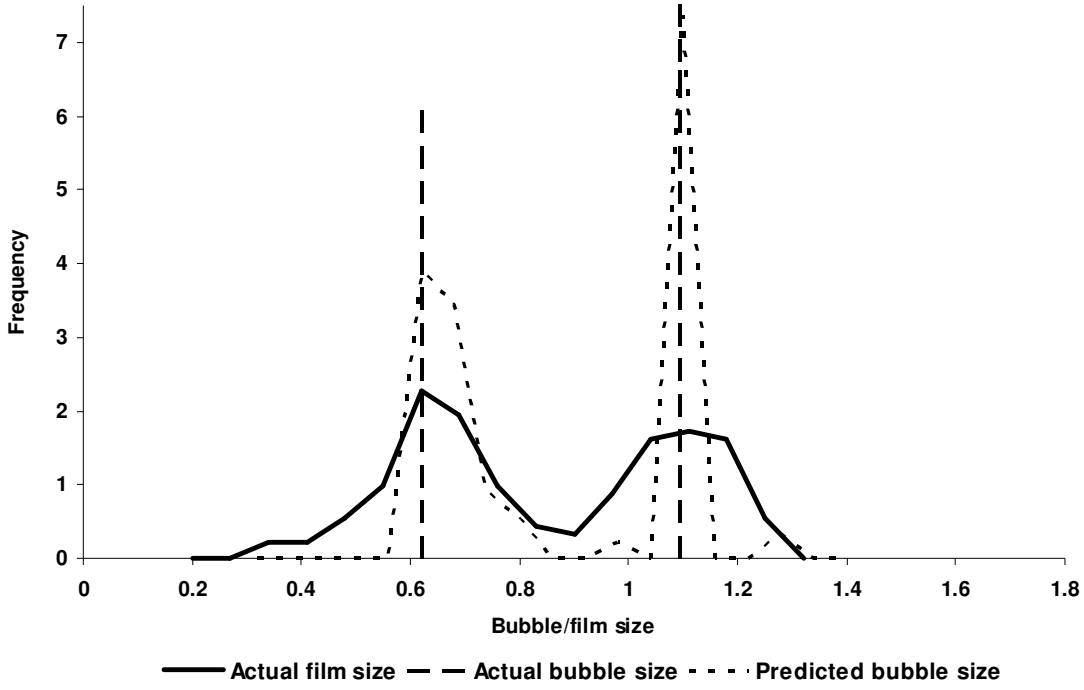

Figure 6.11: The predicted and the actual surface bubble size distributions of a bi-disperse foam with unconstrained surfaces. (V_{large} / V_{small} = 6.0, bin width = 0.13)

Figure 6.12 shows the results for the same foam but with constrained surfaces. This is to compare the predicted distribution of this work to that corrected by de Vries' method which applies to foams with constrained or bounding surfaces. The significance levels for this work and de Vries' are 0.228 and 0.003 respectively. This means that the corrected distribution is statistically more similar than the one

corrected by de Vries' method. A significance level of 0.003 means that the predicted distribution is almost sure different from the actual distribution. This has been demonstrated in Figure 6.12 in which the distribution corrected by de Vries' statistical method appears to be significantly different from the bulk distribution.

For the bi-disperse foams, although the shape of the bi-disperse distribution predicted by this work is very clear, the level of significance is low. This mainly results from the computational errors accumulated in the 'distribution converging' process. There are only two non-empty frequencies, thus 1 degree of freedom. In the computing process, a small fraction of bubble sizes may fail in converging into one of the two 'expected frequencies' which results in a slight increase in the chi-square statistic. For the chi-square distribution ($v = 1$), even a minor increase in the chi-square statistic will cause a dramatic drop in the significance level.

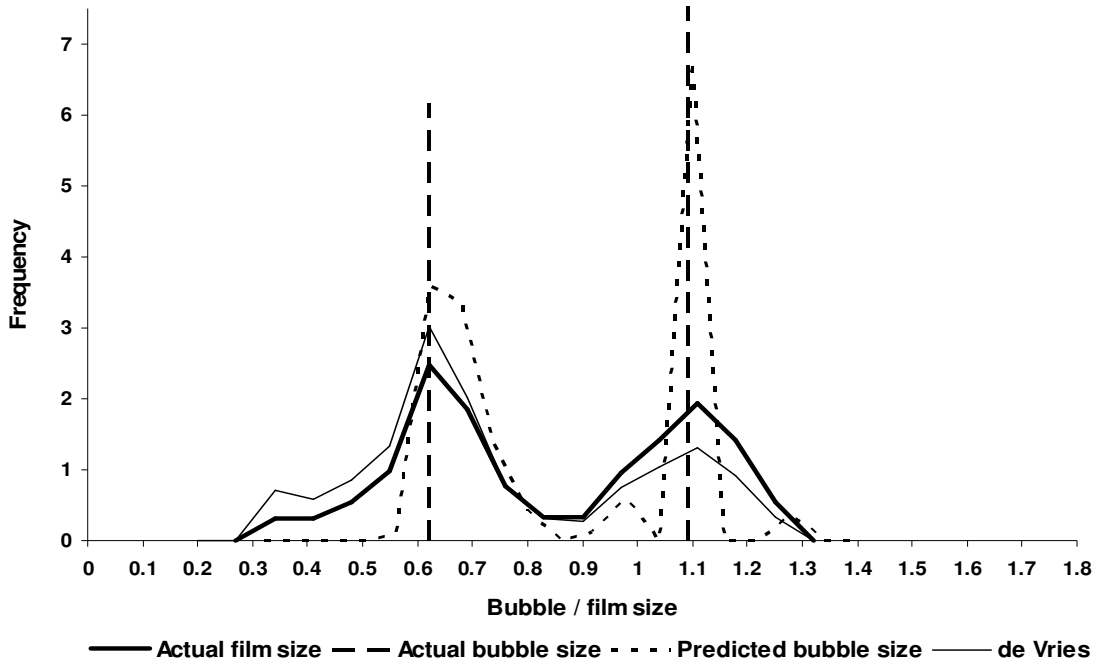

Figure 6.12: The comparison between the predicted bulk distribution of this work and that corrected by de Vries' method. The surface of foam is constrained (V_{large} / V_{small} = 6.0, bin width = 0.13).

Figure 6.13 and 6.14 show the reconstruction of bulk distributions in a slightly polydisperse foam (NSD = 0.07). In Figure 6.13, the significance level in the chi-square test is 0.952, which means the predicted distribution is in good agreement with the actual distribution. Figure 6.14 presents a foam with constrained surfaces. The corresponding test results for this work and de Vries' are 0.955 and 0.133 respectively. This comparison demonstrates that this work has a better performance than de Vries' method.

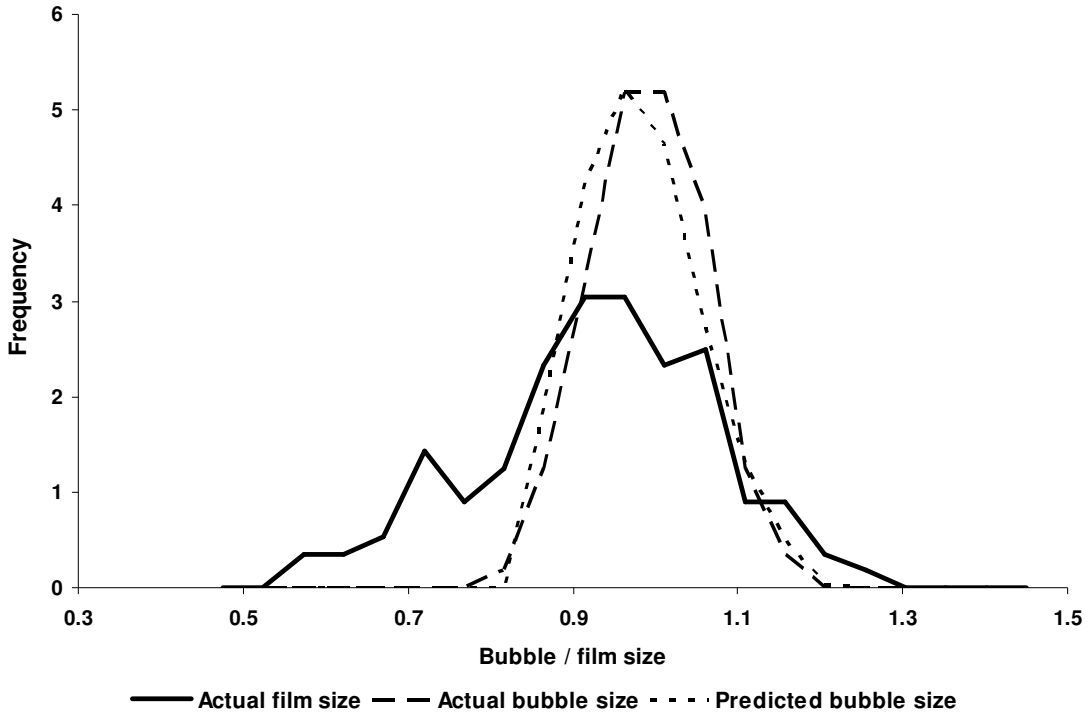

Figure 6.13: The predicted and the actual surface bubble size distributions of a slightly polydisperse foam with unconstrained surfaces (NSD = 0.07, bin width = 0.05).

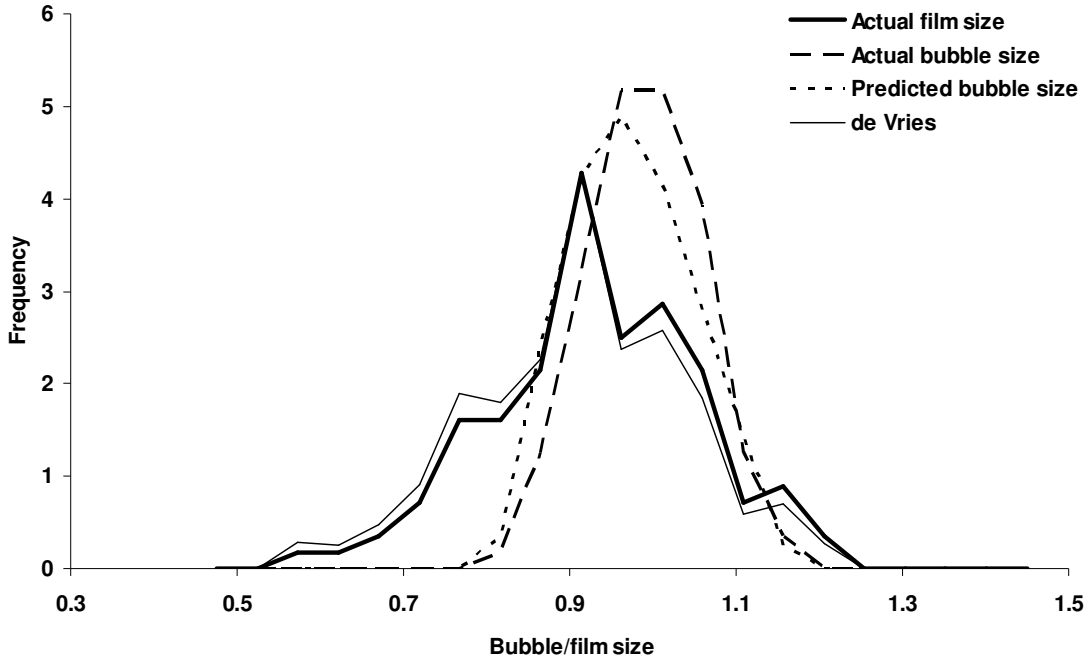

Figure 6.14: The comparison between the predicted bulk distribution of this work and that corrected by de Vries' method. The surface of foam is constrained (NSD = 0.07, bin width = 0.05).

Figure 6.15 and 6.16 shows the application to highly polydisperse foams with unconstrained and constrained surfaces respectively. For the unconstrained foam (NSD=0.30), the significance is as high as 0.998 which indicates an excellent reconstruction of the bulk distribution. In the constrained case (NSD=0.30), although the performance of de Vries' method is acceptable ($\alpha = 0.914$), this work ($\alpha = 0.994$) still outperforms it.

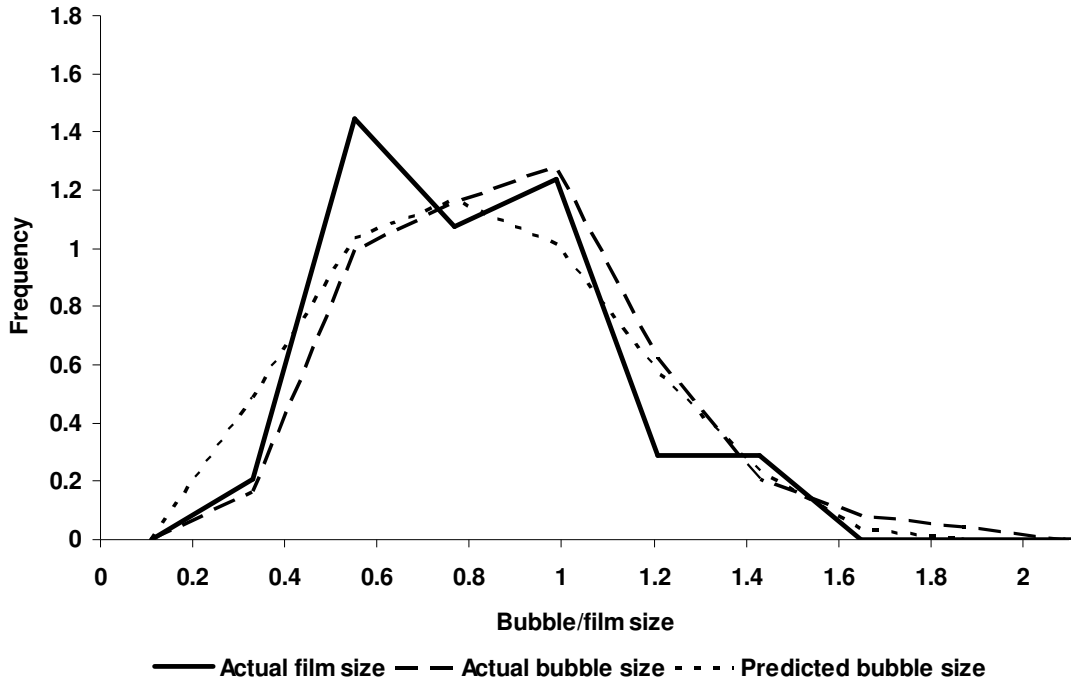

Figure 6.15: The predicted and the actual surface bubble size distributions of a highly polydisperse foam with unconstrained surfaces (NSD = 0.30, bin width = 0.22).

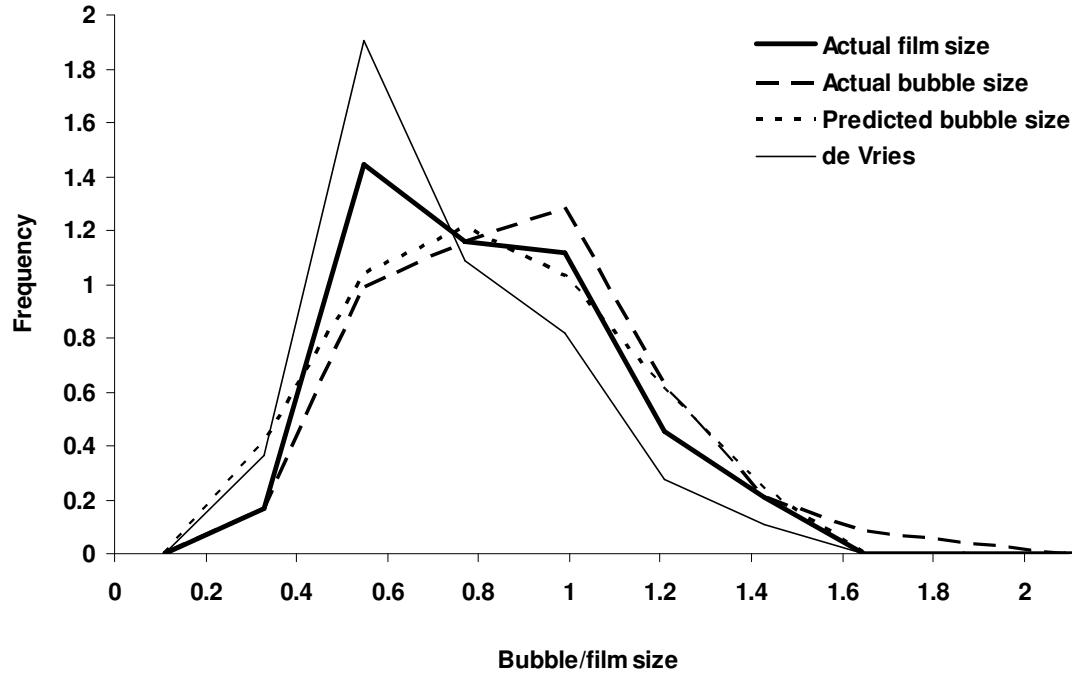

Figure 6.16: The comparison between the predicted bulk distribution of this work and that corrected by de Vries' method. The surface of foam is constrained (NSD = 0.30, bin width = 0.22).

Table 6.2 presents the results of the chi-square test which evaluates the agreement between the predicted (or corrected) bubble size distributions and the actual distributions.

NSD		Degrees of freedom, υ	χ^2	Corresponding significance level, α
Bi-disp (uncons)		**1**	**0.760**	**0.383**
Bi-disp (cons)	**This work**	**1**	**1.456**	**0.228**
	de Vries	**1**	**8.758**	**0.003**
0.07 (uncons)		**7**	**2.143**	**0.952**
0.07 (cons)	**This work**	**6**	**1.562**	**0.955**
	de Vries	**7**	**11.139**	**0.133**
0.30 (uncons)		**6**	**0.705**	**0.998**
0.30 (cons)	**This work**	**5**	**0.452**	**0.994**
	de Vries	**5**	**1.360**	**0.914**

Table 6.2: A comparison of the chi-square test for the predicted distributions in this work and the corrected distributions by de Vries' method.

In the previous examples, the model developed in this work shows a much better reconstruction of the bulk distributions than the method developed by de Vries. Based on these results, we can be reasonably confident that the inverse prediction model developed in this work exhibits excellent applicability and accuracy in reconstructing the 3D bubble size distribution from a given 2D surface film size distribution.

The results also show that the level of agreement between the corrected distributions

by de Vries' method and the actual distributions is low (less than 0.92 in all the cases). His universal method is not very successful in reconstructing the bulk distribution because it only takes the general sampling bias in the planimetric measurement of small bubbles into account, without incorporating the structural information of foam.

An obvious strength of the model developed in this work, compared to de Vries' method, is that it is based on the distribution of the rate of exposure of surface bubbles, which results from bubble size, bubble distortion, the pattern of packing and, possibly, bubble segregation on the surface. Thus it incorporates more information of foam structure into the 'distribution reconstructing' process.

The impact of foam structure to the surface film size distribution was qualitatively demonstrated by the experimental study by Cheng and Lemlich (1983), which studied the difference between surface film size distributions and internal bubble size distributions. Cheng and Lemlich pointed out that at least two other important factors may distort the bulk distribution on foam surface: bubble distortion and bubble segregation. Bubble distortion is an important source of errors in uniformly sized or very slightly dispersed foams. This has been ascertained by the simulation results of monodisperse foam where a range of film sizes is found on the surface of a uniformly sized foam. The bubble segregation effect is another important factor. In polydisperse foams, small bubbles tend to 'wedge out' large bubbles on the bounding surface or viewing plane. The mean surface film size is consequently less than the mean of the bubble size. In their study, for polydisperse foams, a 10%-15% difference between the mean of the film size and the mean of the bulk size was reported. In this work, in polydisperse foams, the mean of the surface film size is approximately 6%-14% less than the corresponding mean of the surface bubble size. Unfortunately, they did not present sufficient technical details about the foams that they produced, for example the number of bubbles and the bubble size distribution, which makes it impossible to replicate their experiment by simulation.

6.3 Surface structure and internal structure

In the previous sections, the surface film size distribution has been successfully related with the surface bulk distribution by Equation 6.1 (or 6.4). However, that link doest not provide direct information on the internal bubble size distribution, thus the internal structure. Exploring the connection between the 3D surface distribution and the 3D internal distribution becomes the last unit to connect the measured surface film size distribution and the internal bubble size distribution. This logic chain is shown in Figure 6.15.

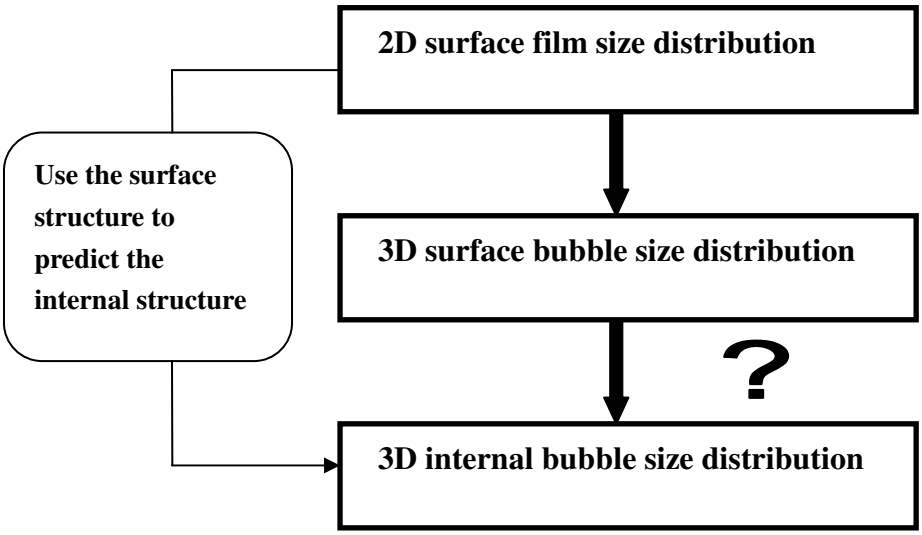

Figure 6.17: The logic chain followed in this work.

Therefore, it is necessary and important to examine how well the underlying distribution is approximated by the surface distribution over a variety of foams.

We assume that the surface bubble size distribution is the observed distribution and the internal bubble size distribution is the expected distribution. The null hypothesis states that these two distributions are the same. The significance level is 0.99, which is a very strict criteria on the agreement between the two distributions.

In Table 6.3, all the χ^2 are less than $\chi^2_{critical}$ for the given α and υ. The null hypothesis is accepted without exception. This means that the surface bubble size distribution is statistically the same at 0.99 level with the internal bubble size distribution. The surface bulk distribution is therefore a reliable good representative of the internal bulk distribution. No significant difference between the two distributions has been found in this work.

NSD	χ^2	$\chi^2_{critical}$ (α=0.99)
Mono	0	
0.07 (uncons)	0.767	1.647 ($\upsilon=8$)
0.07 (cons)	0.750	1.647 ($\upsilon=8$)
0.14 (uncons)	0.896	1.647 ($\upsilon=8$)
0.14 (cons)	0.901	1.647 ($\upsilon=8$)
0.20 (uncons)	0.451	1.239 ($\upsilon=7$)
0.20 (cons)	0.442	1.239 ($\upsilon=7$)
0.30 (uncons)	0.216	1.239 ($\upsilon=7$)
0.30 (cons)	0.210	1.239 ($\upsilon=7$)

Table 6.3: The chi-square test for the agreement between the surface bubble size distribution and the internal bubble size distribution. (uncons = unconstrained surface; cons = constrained surface.)

Based on this conclusion, the 2D surface film size distribution can be logically connected with the 3D internal bubble size distribution, and, therefore, the relationship between the two is established.

Conclusion

In this chapter, the functional form of the relationship between the surface film size and the size of the bubble to which it is attached is applied to predict both the surface film size distribution and the internal bubble size distribution in a variety of foams. The goodness of fit of the predicted distribution to the actual distribution has been proven to be excellent by applying the chi-square test. The inverse prediction model is also compared with the method proposed by de Vries (1957) which corrects the statistical bias in planimetric measurement of bubble sizes. In all of the cases, the model developed in this work outdoes de Vries' universal method. This is because the model developed in this work gauges the overall results of bubble size, bubble distortion and bubble segregation effects, which takes more structural information into account.

All the simulation results and the chi-square tests point out that the functional relationship is both valid and robust at least within the range of polydispersity studied in this work.

CHAPTER VII

CONCLUSIONS AND FUTURE WORK

7.1 Conclusions

This thesis reports novel simulation approaches to explore the relationship between the 2D surface structure and the 3D internal structure over a wide variety of dry foams. This is of importance because the direct measurement of the internal structure of foam is impractical due to the opaque nature of many foam systems. The internal structure of the foam must therefore typically be inferred from the surface structure. For instance, in mineral flotation, the surface of the froth is routinely recorded for image analysis and one of the objectives of this work is to demonstrate that a systematic bias exists between the film size distribution and the bulk distribution in image analysis.

3D Voronoi tessellation, based on constrained random placement or Monte Carlo method, is employed as the starting point to produce realistic 3D foam structures. The validity and accuracy of this method was ascertained by the comparison with the experimental results reported by Matzke (1946) who meticulously studied the 3D structure of uniformly sized foam. The distributions of the number of faces per bubble and the number of edges per face are statistically the same (at 0.99 level in the chi-square test) with the experimental results reported by Matzke. In addition, the excellent conformity with Kraynik's work (at 0.99 level in the chi-square test) also gives us great confidence in our simulation method. All of these evidences

demonstrate that the simulation of random foams based on Voronoi tessellation is successful in reproducing real foam structure and topology. Foams with both unconstrained and constrained surfaces are able to be effectively produced.

The topology of bubbles generated by this simulation method is in close agreement with the real random foam made by Matzke. The number of faces per bubble of the surface and underlying bubbles of monodisperse foam is 13.7 ± 0.1 and 11.0 ± 0.1 respectively, very close to Matzke's 13.7 and 11.0. The distribution of the number of faces per bubble, for both the internal and surface bubbles, broadens with the increase of polydispersity. Pentagonal faces are found to be the most common type for foams over all levels of polydispersity. The number of edges per face of the internal bubbles is found to be approximately independent of the bubble size distribution. While, for the surface films, a marked increase in the variability of the number of edges per face has been observed when the polydispersity increases.

In this work, bubble size distribution is used to characterize the foam structure. It has been demonstrated that the relationship between the size distribution of the films visible at the foam surface and the underlying bubble size distribution is complex, with a range of film sizes observed for a given surface bubble size. Even for foams with a uniform bubble size, a range of film sizes can be observed on the surface. This difference exists in all kinds of foams, from the monodisperse to the highly polydisperse. The systematic bias identified in this research supports our challenge to the commonly believed assumption used in industry: the 2D surface film size distribution obtained by image analysis is approximately identical to the 3D internal bubble size distribution.

A statistical approach was applied to quantitatively relate the surface film size distribution with the underlying bubble size distribution. It has been shown that, when the surface film size is divided by the size of the bubble to which it is attached, the distribution of this ratio collapses to a single curve that is independent of the internal

structure of foam. A functional form for this frequency distribution has been proposed and the coefficients have been obtained through non-linear regression method. The coefficient of determination for both of the empirical formula is above 0.99, which means an excellent fit to the simulation data. Using this functional form, the surface film size distribution based on a known underlying bubble size distribution is successfully predicted. The predicted distribution is statistically the same (at 0.99 level in the chi-square test) with the actual distribution. In the 'backward prediction'-predict the internal bubble size distribution based on a known surface film size distribution, all the predicted distributions, except for the bi-disperse foams, are statistically similar to the actual distributions at 0.95 level or above. It has also been demonstrated that the model developed in this work outperforms de Vries' method which applies a purely statistical approach to correcting the surface film size distribution.

All the results and statistical tests presented in this work lead to the conclusion that the simulation method and the model developed in this work are both valid and robust. They show considerable general applicability in both reproducing 3D foam structures with a wide range of bubble sizes and predicting the internal bubble size distribution based on a given surface film size distribution.

7.2 Future work

The foam model developed in this project works very well in static dry foams. While, in a large number of cases, bubbles move constantly within foams, accompanied by coarsening and bursting. Therefore, it is reasonable to incorporate these behaviors into the simulation in order to further study the impact of foam structure to foam behaviors and functionalities.

Another field may need much future work is further validation by experiments. Although the validity of the model has been ascertained by Matzke's experiment on monodisperse foam, it still needs to be examined in more complicated cases. Due to the opaque nature of most of the foams or froth, X-ray tomography can be an effective method to obtain detailed information from the internal structure. Further comparison with the experimental results from X-ray tomography may provide more insights to the study of 3D foam simulation.

REFERENCES

Aldrich, C., Moolman, D.W., Bunkell, S.J., Harris, M.C. and Theron, D.A. Relationship between surface froth features and process conditions in the batch flotation of a sulphide ore. Minerals Engineering, Vol.10, No.11, pp 1207-1218 (1997).

Bisperink, C.G.J., Ronteltap, A.D., Prins, A. Bubble size distributions in foams. Advances in Colloid and Interface Science, 38, 13-32 (1992).

Brakke, K.A. The surface evolver and the stability of liquid surfaces. Philos. Trans.: Math., Phys. Eng. Sci. 354:1715, 2143-2157 (1996).

Cheng, H. C. and Lemlich. R. Errors in the measurement of bubble size distribution in foams. Ind. Eng. Chem. Fundam. 22, 105-109 (1983).

Cox, S.J. and Whittick, E.L. Shear modulus of two dimensional foams: The effect of area dispersity and disorder. The European Physical Journal E, 21, 49-56 (2006).

De Vries, A. J. Foam stability, Rubber-Stichting, Delft (1957).

De Vries, A.J. Adsorptive bubble segregation techniques, Lemlich, R., Academic Press, New York (1972).

Di Meglio, J.M. and Baglioni., P. Local dynamics of foam drainage investigated by ESR. J. Phys.: Condens. Matter. 6, A375-A380 (1994).

Durian, D. J. Bubble-scale model of foam mechanics: Melting, nonlinear behaviour,

and avalanches. Physical Review E 55 (2): 1739-1751 (1996).

Grau, R.A. and Heiskanen, K. Bubble size distribution in laboratory scale flotation cells. Minerals Engineering 18 1164-1172 (2005).

Hadler K., Barbian N., Cilliers J.J. The relationship between froth stability and flotation performance down a bank of cells. In: Proceedings of XXIII International Mineral Processing Congress, Istanbul, Turkey (2006).

Hepworth, N. J., Hammond, J. R. M. and Varley, J. Novel application of computer vision to determine bubble size distributions in beer. Journal of food engineering 61, 119-124 (2004).

Hilgenfeldt, S., Kraynik, A. M., Reinelt, D. A. and Sullivan, J. M. The structure of foam cells: Isotropic Plateau polyhedra. Europhysics Letters., 67 (3), pp. 484-490 (2004).

Jiang, Y. and Glazier, J. A. Extended large-Q Potts model simulation of foam drainage. Philosophical Magazine Letters. Vol. 74, No. 2, 119-128 (1996).

Jiang, Y., Swart, P. J., Saxena, A., Asipauskas, M. and Glazier, J. A. Hysteresis and avalanches in two-dimensional foam rheology simulations. Physical review E. Vol.59, No. 5 (1999).

Kaplan, I.G. Intermolecular Interactions: Physical Picture, Computational Methods and Model Potentials. Wiley. Hoboken, New Jersy (2006).

Kawasaki, K. and Fuchizaki, K. Time evolution of three dimensional cellular systems: Computer modelling based on vertex-type models. Physica A. 221, 202-215 (1995).

Kose, K. 3D NMR imaging of foam structures. Journal of Magnetic Resonance, Series A 118, 195-201 (1996).

Kraynik, A. M., Reinelt, D. A. and Swol, F. V. Structure of random monodisperse foam. Physical Review E 67, 031403 (2003).

Kraynik, A. M., Reinelt, D. A. and Swol, F. V. Structure of random foam. Physical Review Letters, Vol. 93, No. 20 (2004).

Kraynik, A. M., Reinelt, D. A. and Swol, F. V. Structure of random bi-disperse foam. Colloids and Surfaces A: Physicalchem. Eng. Aspects 263 11-17 (2005).

Kuhn, U. Local calculations of Voronoi diagram. Information Processing Letters 68. 307-312 (1998).

Lambert, J., Cantat, I., Delannay, R., Renault, A., Graner, F., Glazier, J.A., Veretennikov, I. and Cloetens, P. Extraction of relevant physical parameters from 3D images of foams obtained by X-ray tomography. Colloids and Surfaces A: Physicochem. Eng. Aspects 263, 295–302 (2005).

Landau, D.P. and Binder, K. A guide to Monte Carlo simulations in statistical physics. Cambridge University Press, New York (2005).

Lennard-Jones, J. E. On the Determination of Molecular Fields. II. From the Equation of State of a Gas. Proceedings of the Royal Society of London. Series A, 106, 463-477 (1924).

Matzke, E. B. The three dimensional shape of bubbles in foam – An analysis of the role of surface forces in three dimensional cell shape determination. American Journal of Botany, 33, No.1, 58-80 (1946).

Monnereau, C. and Vignes-Adler, M. Optical tomography of real three-dimensional foams. Journal of colloid and interface science 202, 45-53 (1998).

Montoro, J. C. G and Abascal, J. L. F. The Voronoi Polyhedra as tools for structure determination in simple disordered systems. Journal of Phys. Chem. 97, 4211-4215 (1993).

Nakashima, K. and Nagai, T. and Kawasaki, K. Scaling behaviour of two-dimensional domain growth: computer simulation of vertex models. Journal of statistical physics. Vol. 57, Nos, 3/4 (1989).

Neethling, S.J. Private communication (2004).

Neethling, S.J., Lee, H.T., and Cilliers, J.J. Simple relationships for predicting the recovery of liquid from flowing foams and froths. Minerals Engineering. 16, 1123-1130 (2003).

Okamoto, Y. Generalized-ensemble algorithms: enhanced sampling techniques for Monte Carlo and molecular dynamics simulations. Journal of Molecular Graphics 22, 425-439 (2004).

Ozbayoglu, E. M., Akin, S. and Eren, T. Image processing techniques in foam characterization. Energy Sources, Part A, 29: 1175-1185 (2007).

Phelan, R., Weaire, D. and Brakke, K. Computation of equilibrium foam structures using the surface evolver. Experimental Mathematics, Vol.4, No.3 (1995).

Proussevitch, A. A., Sahagian, D. L. and Tsentalovich, E. P. Statistical analysis of bubble and crystal size distributions: Formulation and procedures. Journal of Volcanology and Geothermal Research, 164, 95-11 (2007).

Sadoc, J. F. and Rivier, N. Foams and Emulsions. Kluwer Academic Publishers, Dordrecht/ Boston/ London (1999).

Scott, D.W. On optimal and data-based histograms. Biometrika, Vol. 66, No. 3, 605-610 (1979).

Stone, H.A., Koehler, S.A., Higenfeldt, S. and Durand, M. Perspectives on foam drainage and the influence of interfacial rheology. J. Phys.: Condens. Matter 15 S283-S290 (2003).

Sugihara, K. A simple method for avoiding numerical errors and degeneracy in Voronoi diagram construction. IEICE Transactions on Fundamentals of electronics communications and computer sciences, 75: 468 (1992).

Valleau, J.P. Temperature-and-density-scaling Monte Carlo: methodology and the canonical thermodynamics of Lennard-Jonesium. Molecular Simulation, Vol.31, No.4, 223-253 (2005).

Vasconcelos, I. F., Cantat, I. and Glazier, J.A. Dynamics and topological aspects of a reconstructed two-dimensional foam time series using Potts model in a pinned lattice. Journal of Computational Physics, 192, 1-20 (2003)

Vazquez, A., Sanchez, R. M., Salinas-Rodriguez, E., Soria, A. and Mannasseh, R. A look at three measurement techniques for bubble size determination. Experimental Thermal and Fluid Science 30, 49-57 (2005).

Vera, M.U. and Durian, D.J. Enhanced drainage and coarsening in aqueous foams. Physical Review Letters. Vol. 88, No.8 (2002).

Wang, Y. and Neethling, S.J. Simulating realistic froth surfaces. Minerals Engineering

19, 1069-1076 (2006).

Weaire, D. and Hutzler, S. The physics of foam. Oxford University Press, New York (1999).

Xie, W., Neethling, S. J. and Cilliers, J. J. A novel approach for estimating the average bubble size for foams flowing in vertical columns. Colloids and Surfaces A: Physicochem. Eng. Aspects 263, 295–302 (2005).

Xu, T. and Li, M. Topological and statistical properties of a constrained Voronoi tessellation. Philosophical Magzine. Vol.89, No.4, 349-374 (2009).

Yang, R. Y. Zou, R. P. and Yu, A. B. Voronoi tessellation of the packing of fine uniform spheres. Physical Review E, Vol. 65, 041302 (2002).

APPENDIX I - publications

Two refereed publications have been produced that are related to this work.

1. “Simulating realistic froth surfaces”.

2. “The structure of flotation froth surfaces: the relationship between the surface film and bubble sizes”.

Available online at www.sciencedirect.com
ScienceDirect
Minerals Engineering 19 (2006) 1069–1076
MINERALS ENGINEERING
This article is also available online at: www.elsevier.com/locate/mineng

Simulating realistic froth surfaces

Y. Wang [a], S.J. Neethling [b,*]

[a] School of Chemical Engineering, University of Manchester, P.O. Box 88, Manchester, UK
[b] Earth Science and Engineering, Imperial College London, South Kensington Campus, London SW7 2AZ, UK

Received 21 December 2005; accepted 10 March 2006
Available online 19 May 2006

Abstract

Image analysis as a tool for monitoring and controlling flotation froths has become quite widely used in the minerals industry. One of the challenges is to be able to use the image analysis data to predict the performance of a flotation cell. One of the key parameters to be predicted is the water recovery from the froth, since this is intimately related to the gangue recovery and thus the grade. Recent theoretical developments have allowed for the calculation of this water recovery based on the air rate, froth stability and the bubble size distribution. The problem is that all that can be seen of a froth is the bubble films at the top surface. This paper uses physics based simulations of the froth structure to show that the relationship between the size distribution of the films seen at the top surface and the underlying bubble size distribution is a complex one. The paper presents some preliminary results on the statistical relationship between these distributions.

Keywords: Froth flotation; Flotation froths; Modelling

1. Introduction

In recent years image, analysis has become an increasingly widespread technology on flotation plants. It is usually used as an additional indicator in order to aid the operators in their control of the plant, though recently some attempts have been made to stabilise the froth behaviour by controlling the air rate in order to give a steady flux of froth out of the cell.

One of the biggest challenges is to use the image analysis data to predict the cell performance. Empirical approaches to this challenge have been presented in the literature (e.g. Aldrich et al., 1995; Hargrave and Hall, 1997), but the predictive ability is often not very good and the results tend to be cell and ore specific. In order to get generic relationships for the performance of flotation froths, the behaviour of the froth needs to be understood from a fundamental level. Since image analysis provides information on the surface structure (as well as surface motion) of the froth, it is the relationship between this surface structure and the underlying structure that is the main focus of this work.

2. Using image analysis information

This paper will use the prediction of water recovery as an example, since the theory relating the recovery of water to the flow rate of gas and structure of the foam has already been produced (Neethling et al., 2003a,b).

Typically, the average size of the bubble films on the top surface and the horizontal velocity are returned by image analysis software. This paper will demonstrate that in order to obtain accurate water recovery predictions not only is the correct average internal bubble size required, but also the bubble size distribution.

The water flow rate into the concentrate, Q_l, can be predicted using the following formula based on fundamental foam drainage theory (Neethling et al., 2003a), where Q_{air} is the volumetric flow rate of air into the cell, A_{Column} is the cross-sectional area of the cell at the froth surface, ρ and μ

* Corresponding author. Tel.: +44 2075949341.
E-mail address: s.neethling@imperial.ac.uk (S.J. Neethling).

0892-6875/$ - see front matter © 2006 Elsevier Ltd. All rights reserved.
doi:10.1016/j.mineng.2006.03.007

are the viscosity and density of the slurry within the froth and C_{PB} is the dimensionless Plateau border drag coefficient, which has a value of approximately 50 for immobile interfaces:

$$\text{if } \alpha < \frac{1}{2}: \quad Q_l = \frac{Q_{air}^2 \lambda}{k_1 A_{Column}} (1-\alpha)\alpha \tag{1}$$

$$\text{if } \alpha \geqslant \frac{1}{2}: \quad Q_l = \frac{Q_{air}^2 \lambda}{k_1 A_{Column}} \frac{1}{4} \tag{2}$$

where $k_1 = \frac{\rho g}{3 C_{PB} \mu}$, α is the air recovery from the cell (the fraction of air that flows over the lip of the cell as unburst bubbles). α can be predicted by image analysis using the velocity of the froth at the surface as it flows over the cell lip, v_{froth}, as well as the length of the cell lip, l_{lip}, and the average height of the froth above the lip, h_{lip}:

$$\alpha = \frac{v_{froth} h_{lip} l_{lip}}{Q_{air}} \tag{3}$$

The main structural parameter of interest is going to be one of the main focuses of this paper and that is λ, the length of Plateau borders per volume of foam. As a first level approximation, this parameter is proportional to the inverse of the bubble diameter squared, but in a typical flotation froth there is a wide range of bubble sizes, which introduces the problem of what is the most appropriate average bubble size to use and how is this influenced by the bubble size distribution. Secondly, how is the distribution of bubble sizes within the froth related to the bubble size distribution at the froth surface.

Due to the opaque and ephemeral nature of foams it is extremely difficult to obtain these relationships experimentally and so the approach used for this work is to use computers to generate physically realistic foam models on which theory can be based. The following section outlines the procedure by means of which these structures are produced.

3. Generating realistic froth structures

The method used in this paper is to simulate realistic foam/froth structure and examine the effect of changing the bubble size distribution. The reason why simulated foams/froths were used, rather than making use of the experimental data is due to the ephemeral and opaque nature of most foams/froths, which makes accurate measurements of the structure very difficult.

In order to produce a starting topology for these simulations a Voronoi tessellation was used (see Fig. 1). The tessellation points were generated by random placement, but restricting how close a new point could be to existing points. By changing the allowed spacing of these initial points, the degree of poly-dispersity of the foam could be adjusted. These initial structures are triply periodic and are thus equivalent to an infinitely large space filling foam.

The foams are simulated by producing minimum surface area structures. By using minimum surface area structures,

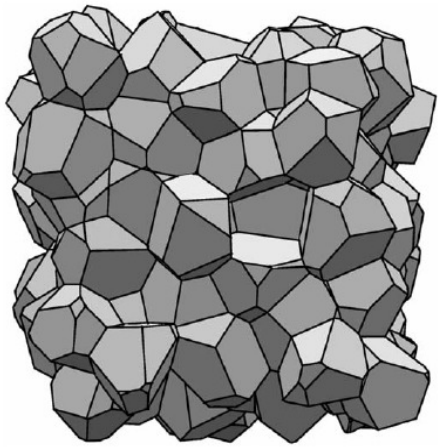

Fig. 1. An example of a period 3-dimensional Voronoi tessellation used as a starting structure.

it is assumed that the surface tension is constant with respect to position. In static, non-draining froth or foam, surface tension gradients will disappear as a result of the Marangoni effect. This effect is the result of surfactant being drawn from regions of high concentration towards those of lower concentration due to surface tension gradients.

If liquid drainage is occurring, surface tension gradients can be induced by surfactant on the interfaces being dragged along by the liquid. The attached surfactant cannot travel far, though (unless it desorbs), since the film interfaces are discontinuous (each bubble has its own interface). This means that most of the gradients will be at the scale of the individual bubbles. The Marangoni effect counteracts these gradients.

Since changes in the surface tension are typically proportional to the log of the change in the surfactant concentration, large changes in the surfactant concentration are usually required for even modest changes in surface tension. This means that this effect will typically only have a minor impact on foam structure and since it would be very complex to model without significantly influencing the results, it will not be included.

A potentially more important effect in flotation froths is that the system might not be at equilibrium, since the foams are quite rapidly stretching and deforming as they flow. This effect will not be included in this study, but is worthy of future study.

The generation of the minimum surface area structure based on this initial structure was accomplished using the Surface Evolver software (Brakke, 1996). It is not feasible to have the random placing of points result in a mono-dispersed foam and so when mono-dispersity was desired, all the bubble volumes were set to the same value, since the Surface Evolver software can adjust the structure in order to accommodate volume changes. During the minimisation procedure topological rearrangements were carried out as

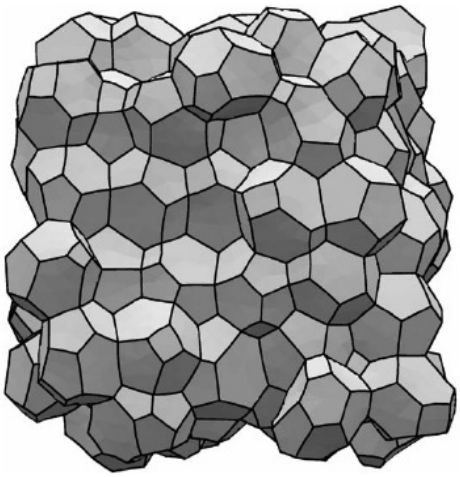

Fig. 2. A mono-dispersed random foam structure produced from the Voronoi tessellation in Fig. 1 using Surface Evolver.

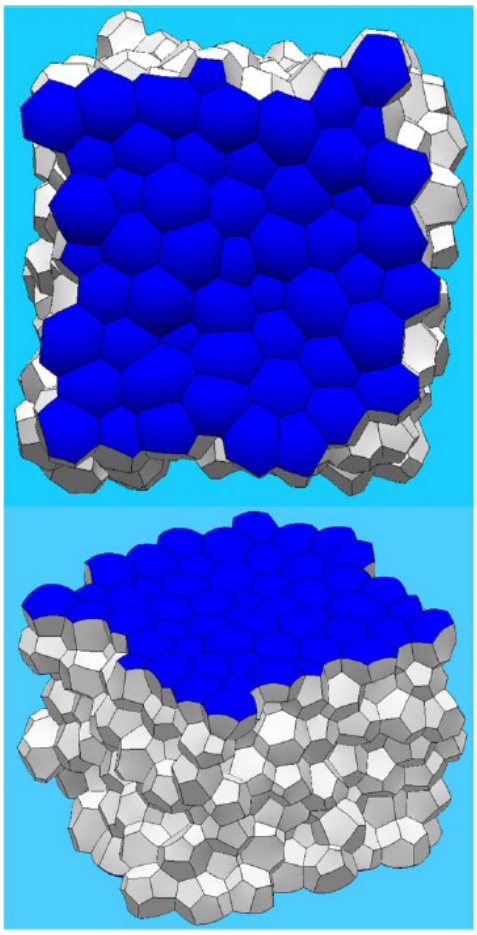

Fig. 3. A simulation of a random mono-dispersed foam with a free surface.

appropriate when film areas or plateau border lengths shrunk towards zero.

In order to ensure that the foam structure did not represent a relatively high energy local minima, a procedure similar to that employed by Kraynik et al. (2003) was employed. This consisted of annealing the structure by applying small compressional strains in each principal axis in turn. Fig. 2 shows a typical initial foam structure obtained from this process.

In order to investigate the relationship between the top surface of a foam and the internal structure, a fully period foam is not appropriate. In order to generate a surface, the foam is sliced through one of the periods. This produces what is in effect an infinitely large slab of foam with a free surface at the top and bottom. Since gravity is not considered when the structure is determined, having two free surfaces simply increases the accuracy of the statistics by doubling the number of surface bubbles. Once the structure has been sliced it is relaxed to a new minimum energy structure (see Fig. 3).

If the froth surface was only the exposed interface of a slice through an otherwise unchanged foam, then the statistics of the film sizes at the surface would be relatively easy to calculate, since it would be analogous to the stereological problem when slicing through ore samples, but with the simplification that the bubbles are quite regular in shape. The problem in this case is that the films are influenced by the fact that they are at an interface. The bubbles rearrange themselves and the films change size and shape in order to minimise the surface area.

4. The froth surface

Fig. 3 illustrates the problem with using the size of the bubble films on the top surface of the froth directly. In this figure, all the bubbles are identical in size, but it can be seen that there is quite a wide distribution of sizes for the films at the top surface. In general, there is not a one to one correlation between the size of the films at the froth surface and the size of the bubbles to which they are attached.

In Figs. 4 and 5, the underlying bubble size distributions are wider (characterised by the coefficient of variation, which is the standard deviation divided by the mean). While the sizes of the films at the top surface do change, the difference is not as distinct as the change in the underlying bubble sizes.

This is especially noticeable if the size distribution for the internal bubbles and the surface films are compared. In Figs. 6 and 7, the internal bubble sizes are reported as the equivalent spherical radii of the volumes, while the surface film sizes are reported as the equivalent circular radii of the projected areas. In Fig. 6, there is a clear distinction between the size distributions of the underlying bubbles for each of the simulations shown in Figs. 3–5 and the shapes of the distributions are close to Gaussian.

Fig. 7 shows the distribution of the sizes of the surfaces films. For these distributions there is far less distinction

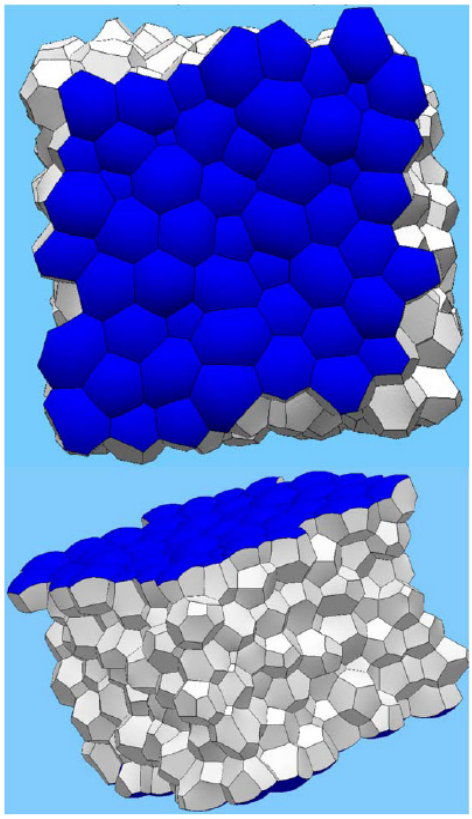

Fig. 4. A simulation of a random slightly poly-dispersed foam with a free surface (coefficient of variation: 0.047).

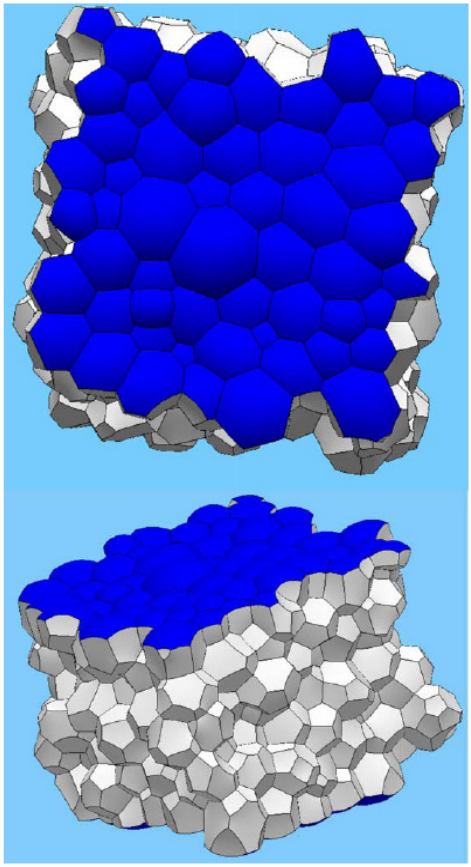

Fig. 5. A simulation of a random moderately poly-dispersed foam with a free surface (coefficient of variation: 0.136).

between the simulations. This is especially true for the half of the distribution corresponding to the smaller film sizes. The distributions are also not close to Gaussian and for the mono-dispersed and slightly poly-dispersed simulations are quite strongly skewed.

Fig. 8 illustrates part of the problem; at low levels of poly-dispersity there is no correlation between the film size and the size of the bubbles to which they are attached. Even as the poly-dispersity increases, the correlation remains quite weak. What is noticeable, though, is that there are films that have radii up to 5 times smaller than the bubble to which they are attached, but in these simulations no bubble has a film larger than about 1.16 times the radius of the bubble to which it is attached. This shows that large bubbles can have small films attached to the surface, but there is a limit to size of the film that can be attached to a bubble of a particular size.

5. The properties of the bubble size distributions

In order to understand the relationship between the size of the internal bubbles and the surface films, a large number of simulations have been carried out. This is an ongoing project, with only the low to moderately poly-dispersed end of the spectrum having been investigated thus far.

While the ultimate aim of this project will be to produce a correlation function linking the bubble size distribution and the film size distribution, this paper will illustrate some of the statistical relationships that have been obtained thus far.

The starting point for this discussion will be the key structural parameter for drainage, namely the length of Plateau borders per volume of foam, λ. This parameter is closely related to bubble size; if the shape of the distribution does not change, then λ is proportional to the inverse of the bubble diameter squared. Kraynik et al. (2003) used fully periodic foam simulations to derive the following relationship between λ and two different average bubble sizes, r_0, the effective radius of the average volume and r_{32}, the Sauter or area weighted mean (n is the number of bubbles in the sample):

$$r_0 = \sqrt[3]{\frac{\sum_{i=1}^{n} r_i^3}{n}} \tag{4}$$

$$r_{32} = \frac{\sum_{i=1}^{n} r_i^3}{\sum_{i=1}^{n} r_i^2} \tag{5}$$

Kraynik's formula for λ based on these two radii is as follows:

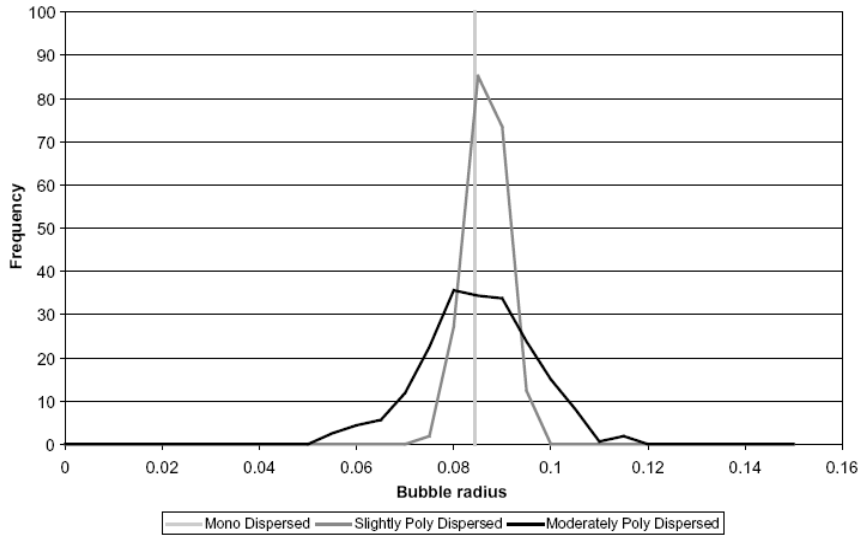

Fig. 6. Size distribution of the radii of all the bubbles from Figs. 3–5.

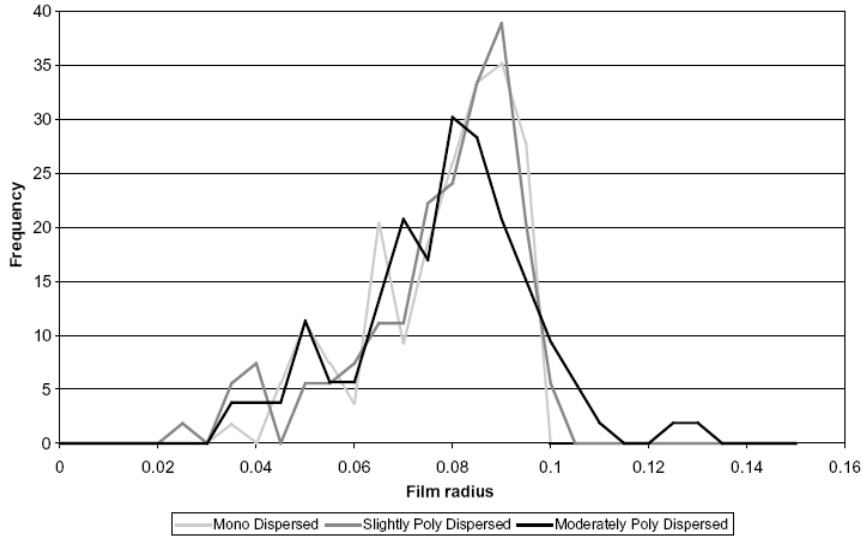

Fig. 7. Size distribution of the radii of the surface films from Figs. 3–5.

$$\lambda \approx \frac{1}{r_0^2}\left(0.423\frac{r_0}{r_{32}} + 0.024\right) \tag{6}$$

The ratio of r_0 to r_{32} is a dimensionless indication of the poly-dispersity of the bubbles. If only the internal bubbles are considered, then there is a 1 to 1 relationship between the r_0/r_{32} ratio and the standard deviation normalised by the arithmetic mean of the bubble size (coefficient of variation). This can be seen in Fig. 9. The actual relationship between the coefficient of variation and r_0/r_{32} will depend on the shape of the distribution, but all these simulations have essentially the same shape of bubble size distribution.

What this implies is that if we knew the standard deviation of the internal bubbles and the r_0 value we would be able to calculate the length of Plateau borders per volume of foam and thus an accurate value for the water recovery. Fig. 10 gives the relationship between the standard deviation of the radii of the internal bubbles and that of the surface films. The problem is that at low standard deviations, the poly-dispersity of the internal bubbles varies with little impact on the standard deviation of the surface films. Since it is the surface films for which information is known, this gives a large uncertainty for the calculated value for the underlying variability.

Fig. 7 indicates that while the standard deviation hardly varies, the shape of the distribution does vary. This means that an analysis of the entire shape of the distribution might hold a clue as to the underlying size distribution even

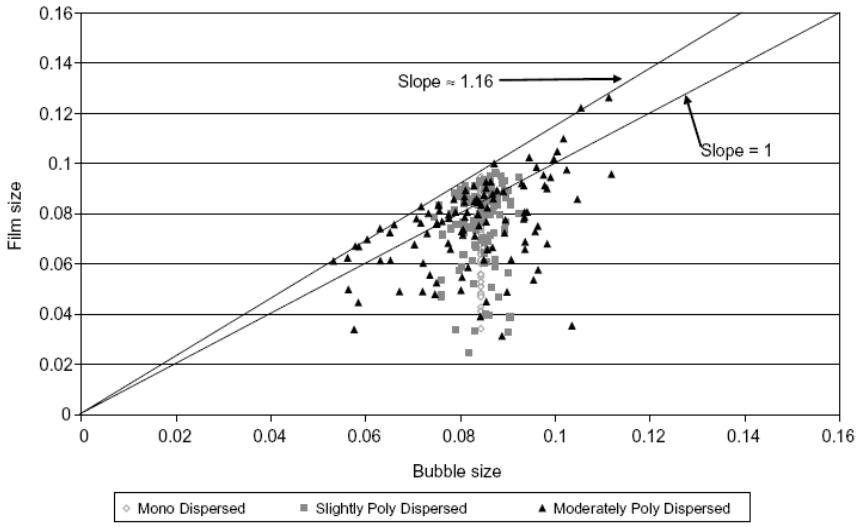

Fig. 8. Correlation between the surface film size and the size of the bubble to which they are attached.

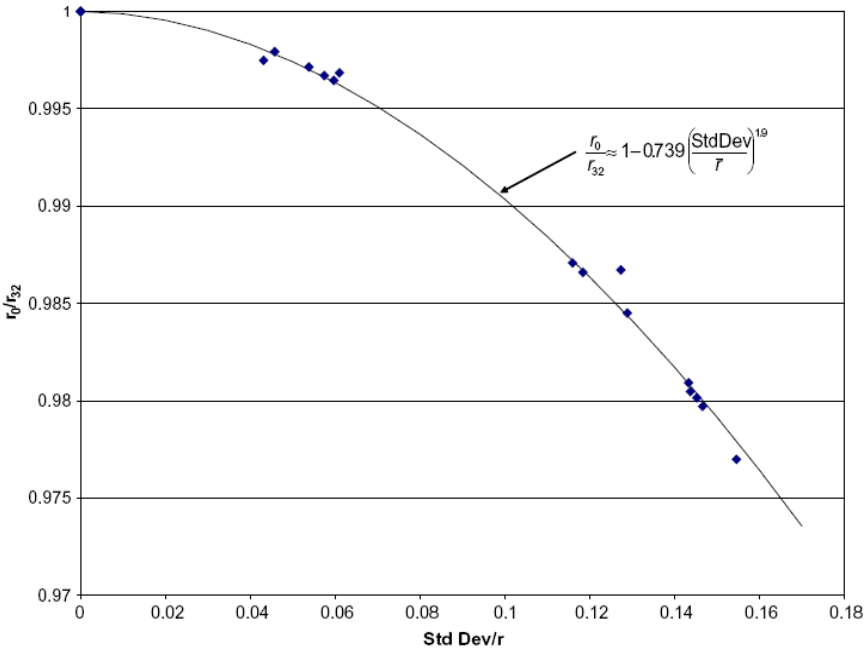

Fig. 9. The relationship between the ratio r_0/r_{32} and the coefficient of variation for the internal bubbles.

if there is little difference in the single value characterisation of the distribution that is the standard deviation, though this will require further work.

The second and probably more important relationship in calculating the water recovery is the relationship between the r_0 for the surface films and that of the internal bubbles. The reason why this relationship is critical is because it is inverse squared and thus strong. Fig. 11 shows the ratio of the surface to the internal r_0 as a function of the surface film ratio of r_0 to r_{32}. This graph seems to indicate that the discrepancy between the surface and internal r_0 values grow as the poly-dispersity increases (increasing poly-dispersity results in a decrease in r_0/r_{32}). While more simulations are required at higher poly-dispersities, these results indicate that the effect of poly-dispersity on the prediction of water recovery based on image analysis of the surface bubbles is not a trivial problem.

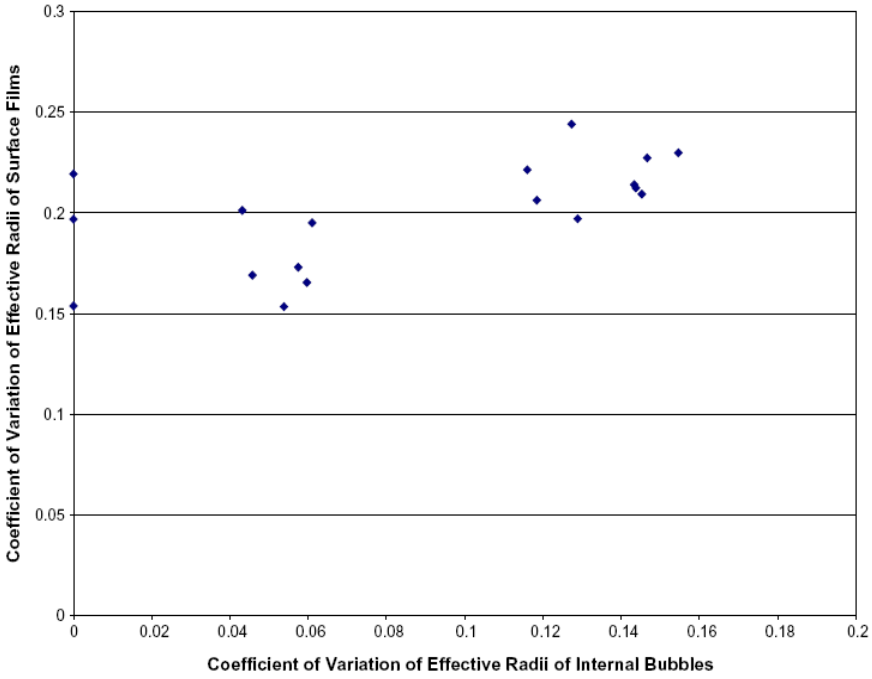

Fig. 10. The relationship between the variability of the size of the surface films and the internal bubbles.

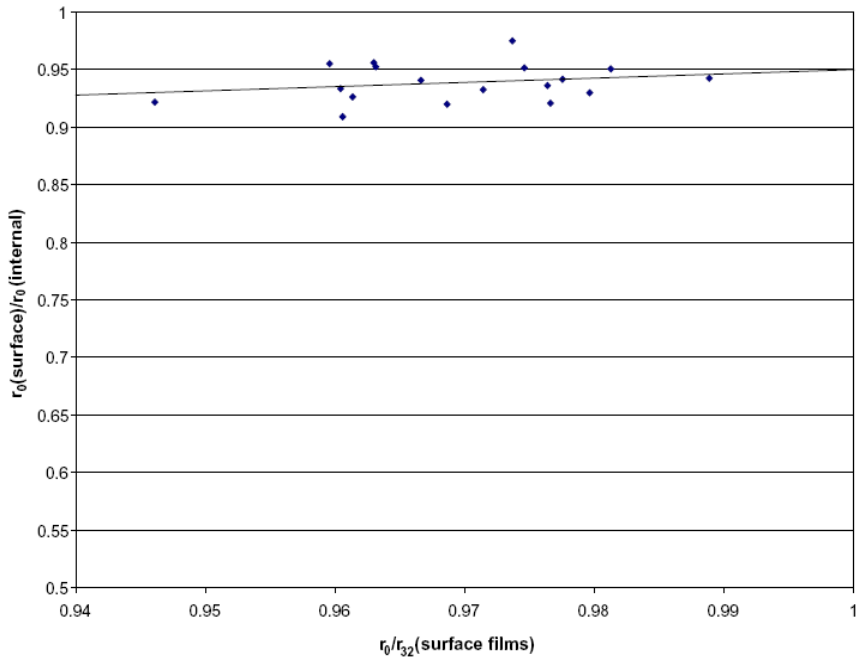

Fig. 11. The relationship between poly-dispersity (as represented by r_0/r_{32}) and the discrepancy between the surface and internal values of r_0.

6. Conclusions

This paper has demonstrated that the relationship between the structure of a froth surface and the underlying structure is a complex one. It has shown that even mono-dispersed foams have a reasonably wide distribution of film sizes at the froth surface.

Relationships between values of the two different mean bubble radii required for calculating the liquid drainage as calculated based on the surface films and the actual

internal bubble values are given, though the preliminary nature of this work means that the range of poly-dispersity used is limited, being restricted to relatively low poly-dispersity foams.

References

Aldrich, C., Moolman, D.W., Eksteen, J.J., Van Deventer, J.S.J., 1995. Characterization of flotation processes with self-organizing neural nets. Chemical Engineering Communication 139, 25–39.

Brakke, K.A., 1996. The surface evolver and the stability of liquid surfaces. Philosophical Transactions of The Royal Society of London – A 354 (1715), 2143–2157.

Hargrave, J.M., Hall, S.T., 1997. Diagnosis of concentrate grade and mass flowrate in tin flotation from colour and surface texture analysis. Minerals Engineering 10 (6), 613–621.

Kraynik, A.M., Reinelt, D.A., van Swol, F., 2003. Structure of random monodisperse foam. Physical Review E 6 (3), 031403.

Neethling, S.J., Lee, H.T., Cilliers, J.J., 2003a. Simple relationships for predicting the recovery of liquid from flowing foams and froths. Minerals Engineering 16 (11), 1123–1130.

Neethling, S.J., Lee, H.T., Cilliers, J.J., 2003b. The recovery of liquid from flowing foams. Journal of Physics – Condensed Matter 15, 1563–1576.

Colloids and Surfaces A: Physicochemical and Engineering Aspects: Volume 339, Issues 1-3, 1 May 2009, Pages 73-81

The Structure of Flotation Froth Surfaces: The Relationship between Surface Film and Bubble Size

Y. Wang and S.J. Neethling

Abstract

Image analysis is becoming more widely used in the monitoring of froth flotation cells. At present, the size distribution of the films visible at the froth surface are used directly as a proxy for the underlying bubble size distribution. This has been shown to be problematic, with big discrepancies between the film and bubble size distributions. In this paper, structural simulations of froth surfaces are used to address this problem. In order to have confidence in these simulated structures their topologies where compared to those found experimentally, with very good agreement. From these simulations, it was found that the distribution of possible film sizes relative to the size of the bubble to which it is attached is independent of the underlying bubble size distribution. This distribution of possible film sizes for a given bubble size was then used as the basis for an algorithm for determining the surface bubble size distribution based on the surface film size distribution obtainable by image analysis.

Introduction

The image analysis of froth surfaces is becoming routine in a number of flotation operations. Both the bubble size distribution and the velocity of the froth are typically measured. At present, though, these values are usually simply used as another indicator of plant behaviour to be used by the operators, rather than being used to predict plant performance.

Attempts have been made to link these measured froth parameters to flotation performance, but these have typically been very empirical and system specific (e.g. Aldrich *et al.*, 1995 and Kaartinen *et al.*, 2006). In order to produce useful performance indicators that can easily be applied to new flotation circuits with large amounts of experimentation on the specific systems, a theoretical understanding of froth behaviour is required. An example of this is a theoretical model for the recovery of water to the concentrate (Neethling *et al.*, 2003a). In this model, measurements of the gas rate into

the cell, the velocity of the froth over the overflow lip, the depth of the froth over the lip and, very importantly, the bubble size, can be combined to predict the amount of water being recovered to the concentrate. Water recovery is the most important factor in gangue recovery and thus an important factor in predicting the grade of the concentrate.

In laboratory studies with a mono-dispersed bubble size, this model was found to accurately predict the amount of water recovered (Neethling *et al.*, 2003b). When applied to industrial flotation data, there was found to be far more variability between the predicted and measured water recovery. When the model was rearranged to allow the bubble size to be predicted based on the measured water recovery, it was found that the data all collapsed onto a single curve (see figure 1), though not a straight line through the origin.

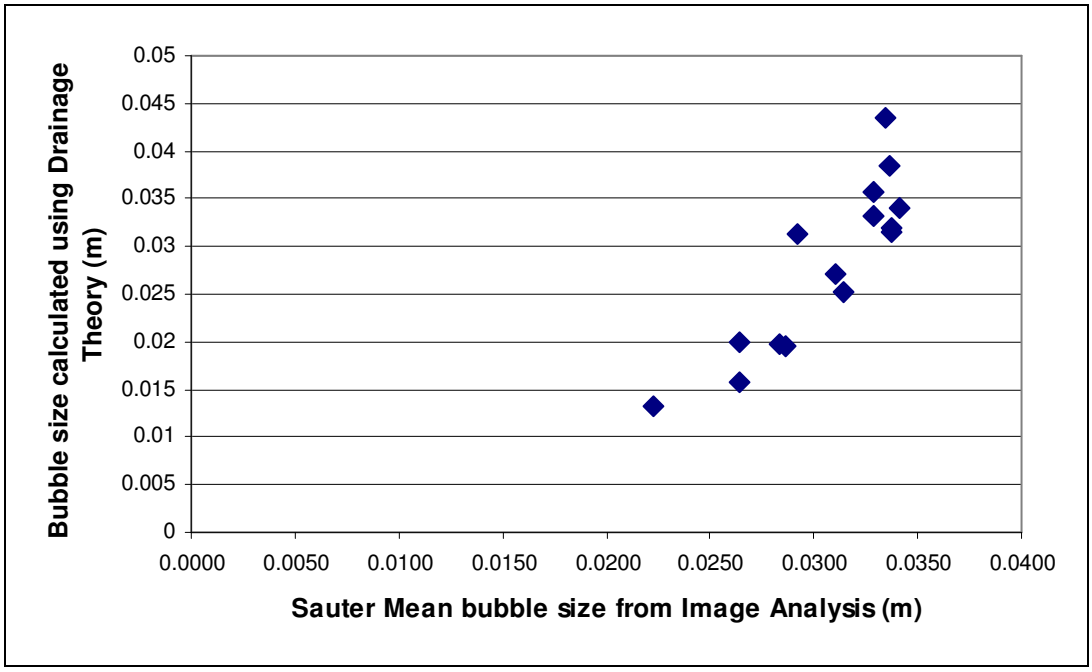

Figure 3: Bubble sizes calculated from drainage theory vs Sauter mean diameter from image analysis (Neethling *et al.*, 2003b).

From this figure it can be seen that while the bubble size predicted based on theory and the measured water rate and that obtained from image analysis all fall on the same curve, the range of values obtained by image analysis is narrower than that predicted from the theory, indicating that the image analysis is either under-reporting the large or the small bubbles (or a combination of the two). In order to accurately predict the water recovery, it is important that the image analysis give quantitatively accurate results and trends.

There are a number of reasons why the bubble size distributions obtained from image analysis might differ from that actually flowing over the cell lip. The first is that the image analysis algorithm might not be accurately segmenting the image. Watershed

algorithms, which are the most commonly used ones for this task (e.g. Sweet *et al.*, 2000), have the tendency to either over-segment large bubbles or under-segment small bubbles if their parameters are not accurately tuned. This is a technical issue, rather than a problem associated with froth behaviour, which is being overcome with improved hardware and software. The second potential problem is that the bubbles being measured are not necessarily representative of those flowing over the lip. Image analysis can only examine the surface bubbles, whereas there can be a few layers of bubbles in the froth flowing over the lip. This is especially true of some froths in which large bubbles are present on the surface layer, obscuring the large number of small bubbles that form the bulk of the froth flowing over the lip. Correcting for this problem is a complex issue that will require a more detailed understanding of froth stability and bubble coalescence than is currently available and is therefore beyond the scope of this paper.

It is the third potential problem with using image analysis that will be the main focus of this paper. Cameras mounted above the froth do not actually measure the size distribution of the surface bubbles, what it is actually measuring is the size distribution of the surface films/lamellae. In a previous paper (Wang and Neethling, 2006), we have already shown that the relationship between the surface film and the surface bubble size distribution is a complex one. In this paper, a method for predicting the surface bubble size distribution based on the surface film size distribution will be presented. The problem is a similar one to that encountered when obtaining data from polished sections through minerals, such when carrying out MLA studies, where the size distribution of the mineral grains needs to be predicted based on the size distribution of the sections through the grains (e.g. King, 1984). The same corrections cannot be used, though, seeing that there are some important differences; firstly, particles due not change their structure due to the proximity of a surface, whereas the structure of the froth is quite markedly influenced by the presence of a surface. Secondly, the polished sections pass through the original grains, whereas the image analysis is viewing a single film of the bubble, with all the rest of bubble lying below the surface.

In order to produce these relationships between surface film and bubble size distributions, a large number of froth structures in which both the surface film and internal bubble size distribution are known need to be studied. The opaque and transient nature of these systems make the direct experimental measurement of these distributions very problematic. Instead, a simulated froth structure will be used. Details of the method for producing realistic froth structures was given in a previous paper (Wang and Neethling, 2006) and therefore only a brief outline of the method will be given here.

Producing Realistic Froth Structures

The basis for these simulations is a Voronoi tessellation. The reason for using a Voronoi tessellation as the starting structure is because it is topologically similar to

froths and foams, with three faces meeting at an edge (Plateau border) and four Plateau borders meeting at a vertex. In order to study the relationship between the surface films and the underlying structure, a free surfaces is required. In order to produce free surfaces, a plane is sliced through one of the periods and the bubbles intersected by the plane removed. Figure 2a. shows a typical Voronoi tessellation with a free surface generated in this manner.

Where Voronoi tessellations differs from a froth or foam in structure is that it is not a minimum surface area structure, consisting of only flat faces. In order to produce the minimum surface structures required to mimic a real froth, the Surface Evolver package was used (Brakke, 1996). Topological transformations are carried out as required. For example, as edges approach zero length, they are replaced by triangular faces and vice versa. Finally, the structure is annealed to ensure that it is not stuck in a local energy minimum. Figure 2b. gives an example of a simulated froth structure after this surface area minimisation procedure has been carried out.

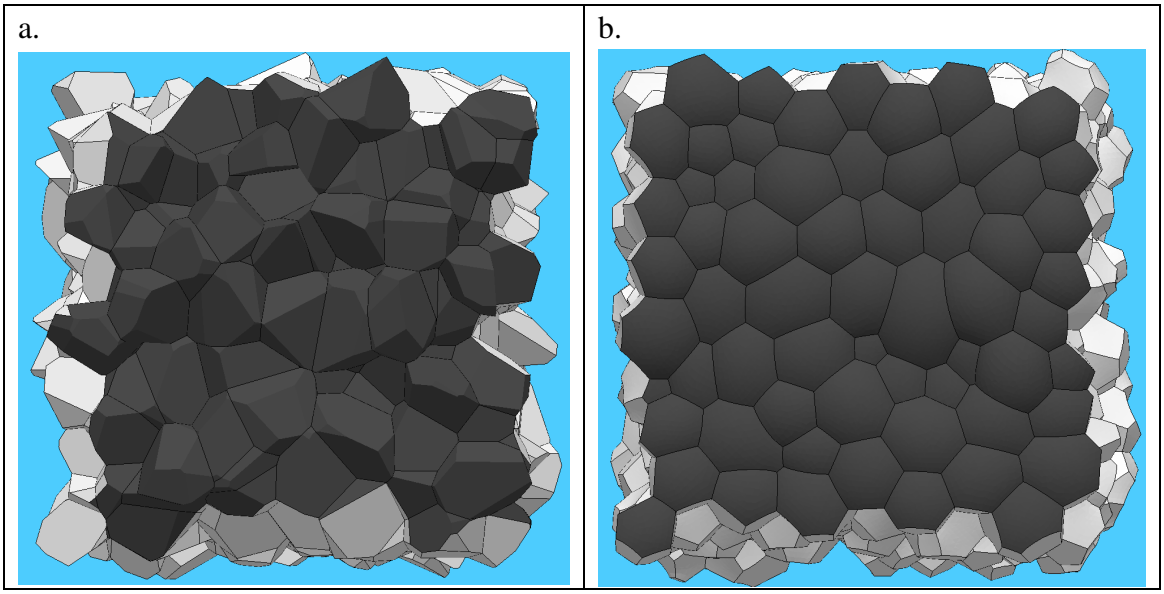

Figure 4: a) Voronoi Tessellation with a free surface. b) Resultant froth structure.

Experimental Verification of the Simulation Procedure

Due to the difficulties involved in making detailed measurements of foam structure, there is very little available experimental data which to verify the simulation procedure. One of the most comprehensive sets of data was produced by Matzke (1948), why created a mono-dispersed foam by blowing bubbles with a calibrated syringe and placing them individually into a beaker. He then used a dissecting microscope to manually count the number of faces on every bubble and the number of edges (Plateau borders) on every face. Due to the laborious nature of these experiments, they remain the best set of experimental data on the topology of foam.

Simulations of mono-dispersed foams were carried out, each containing 420 bubbles. The simulations were repeated 3 times with the average number of faces per bubble shows approximately 1% variation, demonstrating good repeatability between simulation runs. The simulated foams have an average of 11.1 faces per surface bubble, only slightly higher than Mazke's 11.0. The internal bubbles have 13.7 faces per bubble, which matches Mazke's, 13.7. In addition, Kraynik et al (2003) reported 13.7 to 13.9 faces per bubble for internal bubbles in simulated fully periodic mono-dispersed foam. Figure 3 shows the majority of the internal bubbles have 12 to 16 faces, with a distribution that is in close agreement with both Mazke's experiments and Kraynik's simulations. For the surface bubbles (Figure 4), 8 to 13 faces are the most common types, with good agreement between the experimental and simulated distributions. The reason for the slightly bigger discrepancy between the distributions for the surface bubbles compared to that of the internal bubbles is probably due to the smaller sample size available for the surface bubbles in both the simulated and experimental work.

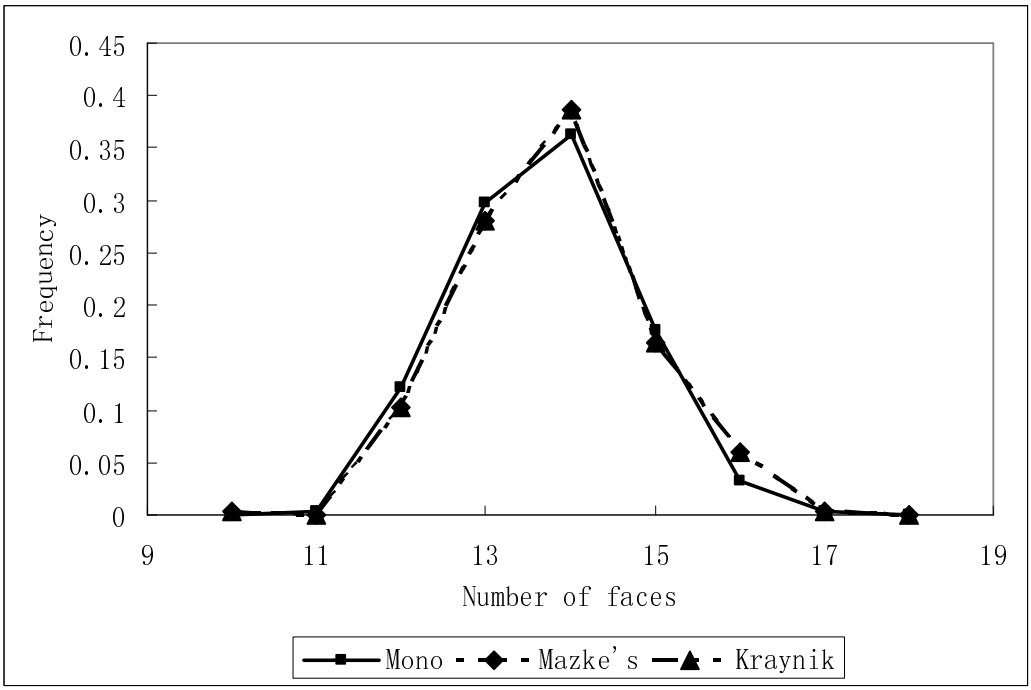

Figure 5: The number of faces per internal bubble in the simulated monodipsered foam, Mazke's (1948) and Kraynik's (Kraynik *et al.*, 2003) work.

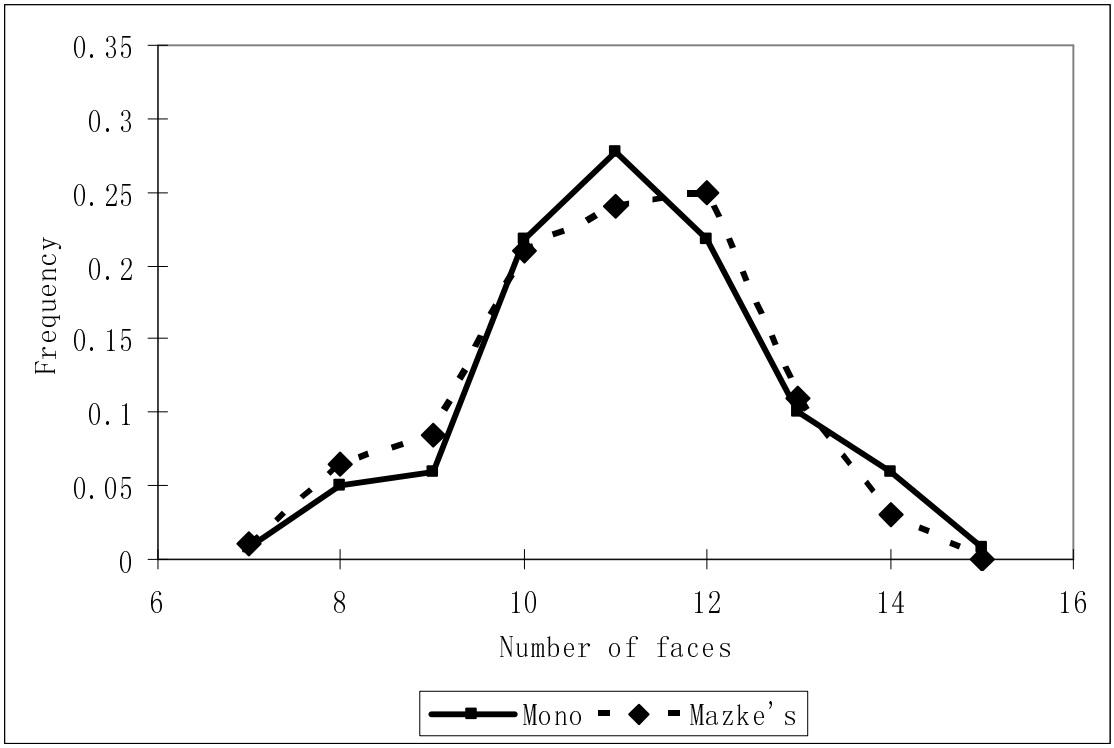

Figure 6: The number of faces per surface bubble in the simulated mono-dispersed foam and Mazke's (1948) work.

The close agreement between these experimental results and the structures of the simulated mono-dispersed foams gives confidence in the ability of these simulations to accurately represent real foams and froths.

The Relationship between Surface Bubbles and Films

In the previous paper on the structure of froth surfaces, it was shown that there was a marked difference between the size distribution of the surface bubbles and that of the surface films, though no method for correcting for this discrepancy was proposed. Figure 5 shows a similar set of simulated data, where it can be quite clearly seen that there is a marked difference between the bubble and surface film size distributions, with far less variation between the film sizes than seen in the bubble size distributions.

In this paper, the surface film size is represented by the equivalent circular radius of the vertically projected film area, while the bubble size is represented by the equivalent spherical radius of the bubble volume. The reason for using the vertically projected area of the surface films, rather than their actual area is because this is the area seen by vertically mounted cameras and thus typically used for image analysis.

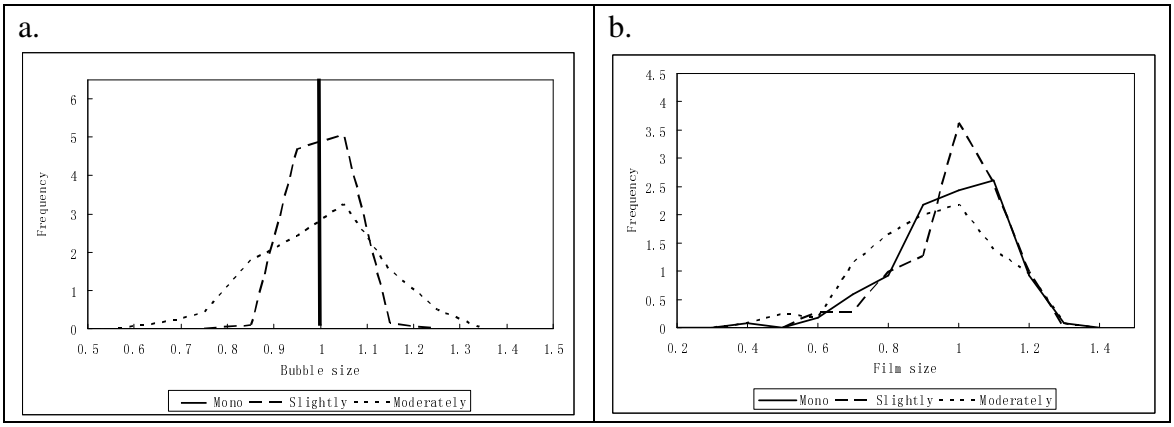

Figure 7: a) Surface bubble size distribution b) Surface film size distribution

For each bubble size there is a range of possible sizes for the surface film. This can be seen in figure 6, where the film size is plotted against the size of the bubble to which it is attached. It can be quite clearly seen that for each bubble size there is a range of possible surface film sizes. While there are a large number of films smaller than the bubble to which they are attached, there are few that are larger than the bubble.

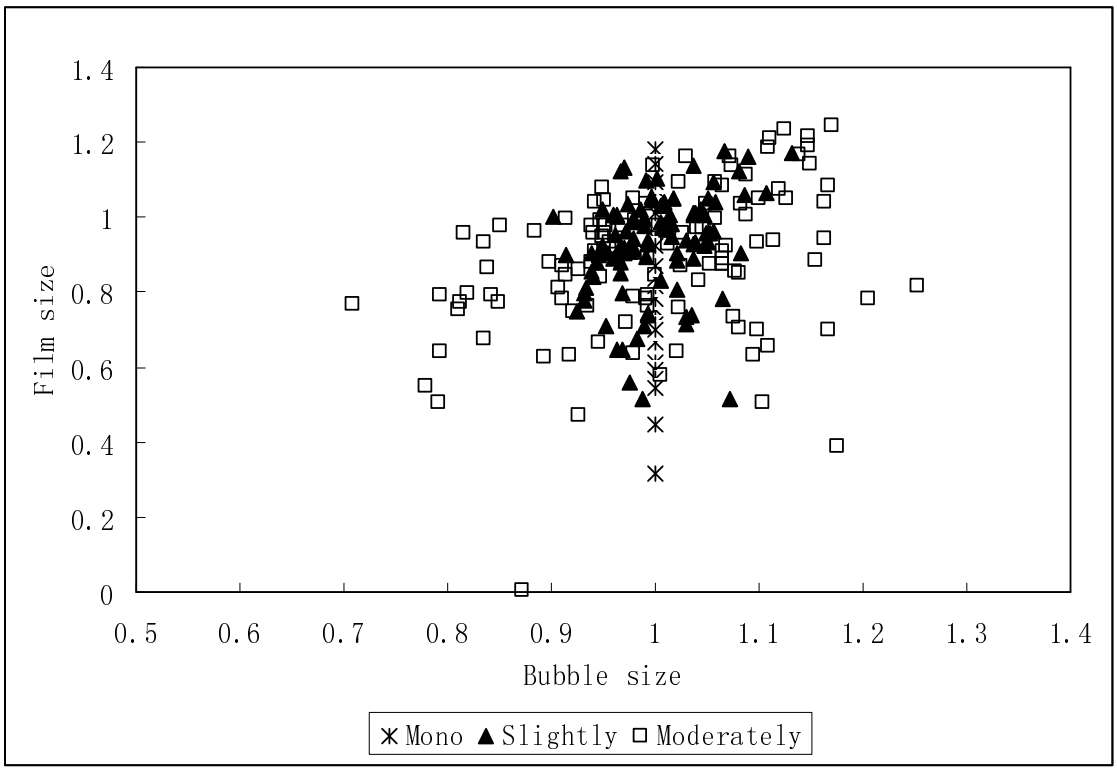

Figure 8: The size of the surface film versus the size of the bubble to which it is attached

In figure 7, the film size is divided by the radius of the bubble to which it is attached and plotted as a frequency distribution. It can be seen from this figure that the shape of this distribution does not depend on the poly-dispersity of the underlying bubbles. This

mean that the range of sizes that a film can adopt relative to its bubble size does not depend on the bubble size distribution, at least for the range of poly-dispersities studied in this work.

In figure 8 the data from the moderately poly-dispersed simulations is divided into relatively narrow bubble size intervals. Again the frequency distribution for the ratio of the surface film size to the size of the bubble to which the film is attached is plotted. While the small sample sizes involved in some of these bubble size intervals mean that there is quite a bit of variability in the data, all the trends are similar, with no systematic change in the shape of the distribution with the size of the bubble relative to the mean. This implies that the distribution of relative sizes that a film can adopt is relatively independent of the size of the bubble involved relative to the neighbouring bubbles.

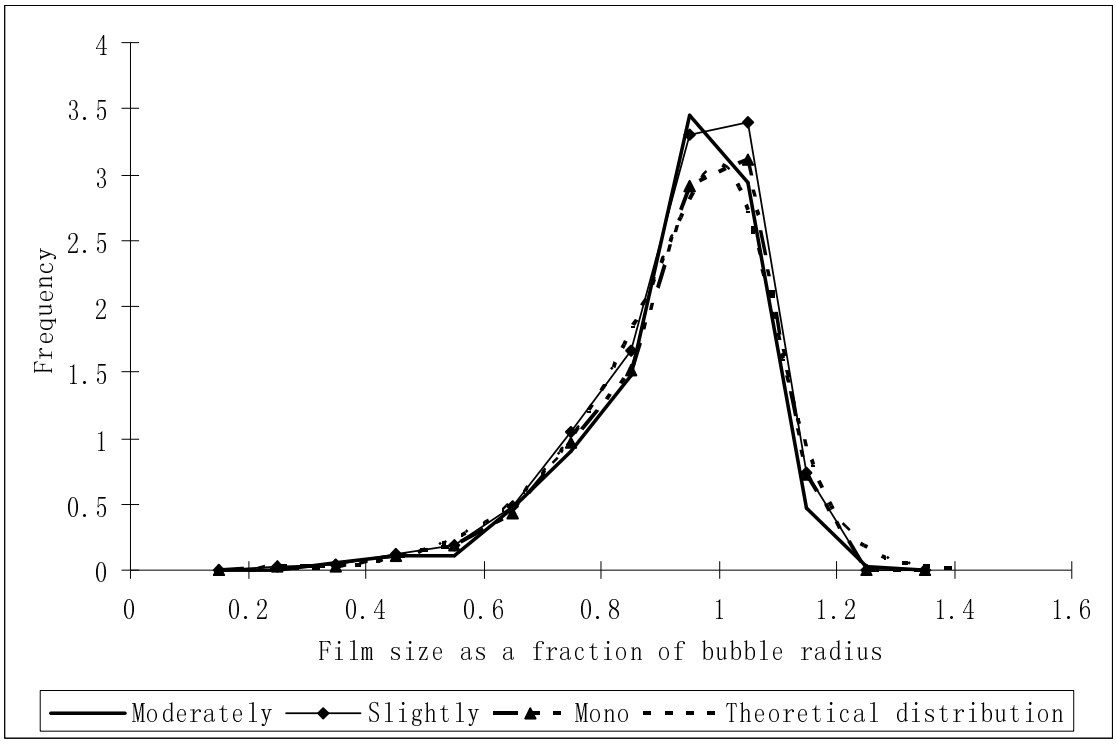

Figure 9: The cumulative frequency distributions for the ratio of the film size to the size of the bubble to which it is attached for mono-dispersed, slightly, moderately polydispersed foams. The theoretical distribution is based on equation 3.

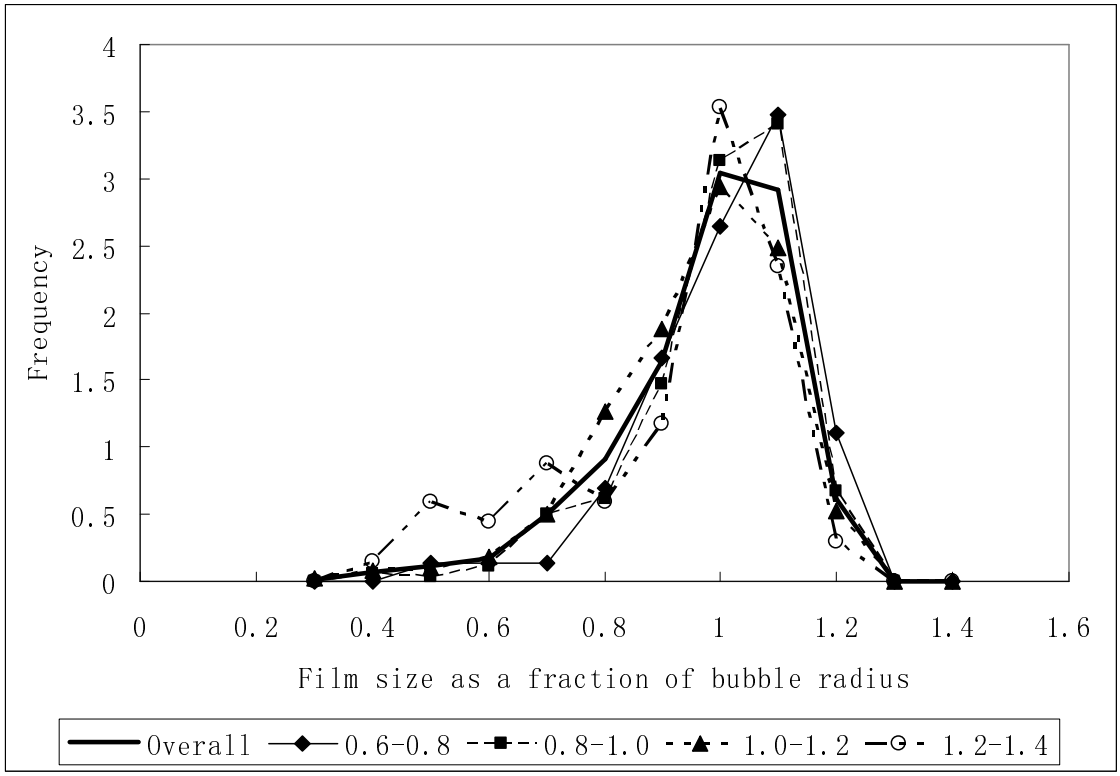

Figure 10: Frequency distribution for the ratio of film size to the size of the bubble to which it is attached for a number of narrow bubble size intervals

In order to make use of this distribution it must be fitted to a suitable functional form. When figure 7 is plotted on log-log axes (see figure 9), there is a straight line relationship between the frequency and the ratio of film size to bubble size for ratios less than one (films smaller than the bubble to which they are attached) indicating a power law relationship in this range. For films larger than the bubble to which they are attached, there is a very rapid drop off in frequency of occurrence. Equation 1 is an empirical form that meets both these conditions:

$$f\left(\frac{r_S}{r}\right) = K \frac{\left(\frac{r_S}{r}\right)^n}{1 + \exp\left(C\left(\frac{r_S}{r} - l\right)\right)} \qquad (1.)$$

(1)

Where: r_S = the surface film radius;

r = the surface bubble radius;

K, l, n and *C* are fitting parameters

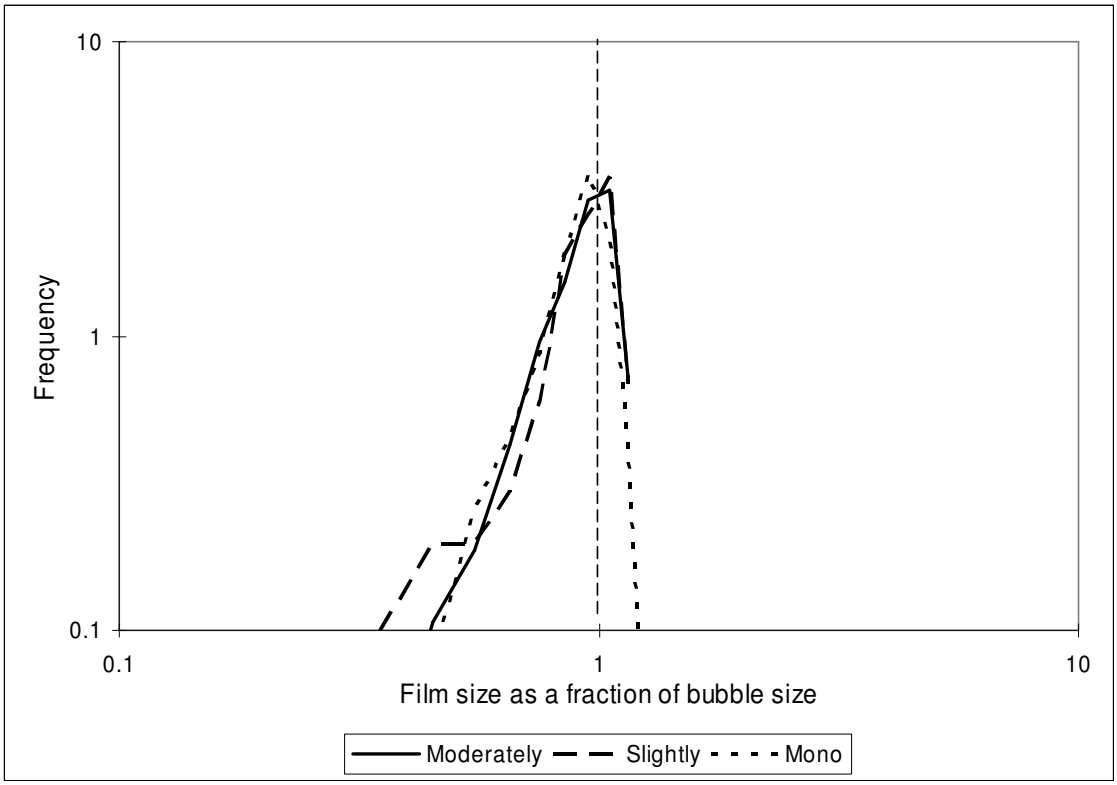

Figure 11: The frequency distributions from figure 7 plotted on logarithmic axes.

As equation 1 is a frequency distribution, the area under the curve must be 1:

$$\int_0^\infty f\left(\frac{r_S}{r}\right) d\left(\frac{r_S}{r}\right) = 1 \qquad (2.)$$

By adjusting the 4 fitting parameters in equation 1 subject to the constraint of equation 2, the following least squares fit is obtained:

$$f\left(\frac{r_S}{r}\right) = \frac{3.90\left(\frac{r_S}{r}\right)^{4.70}}{1 + \exp\left(21.9\left(\frac{r_S}{r} - 1.05\right)\right)} \qquad (3.)$$

Equation 3 is plotted on figure 7 as the "Theoretical distribution" and gives a good fit to the data.

Predicting Surface Film Sizes based on a known Bubble Size Distribution

The surface film size distribution, *T*, can be written as a function of the surface bubble size distribution, *S*, and the distribution from equation 3:

$$T(r_S) = \int_{r=0}^{\infty} f\left(\frac{r_S}{r}\right) S(r) dr \qquad (4.)$$

This is the inverse of what we actually wish to achieve, namely calculating the bubble size distribution based on the film size distribution, but it is a necessary intermediate step. Equation 4 requires the bubble size distribution as a continuous function. As the distributions will typically come from image analysis, they will usually consist of discrete size intervals. For this reason, a discrete approximation of equation 4 is desirable:

$$T(r_{S\,i}) \approx \sum_{r=0}^{r_{Max}} f\left(\frac{r_{S\,i}}{r_i}\right) S(r_i) \Delta r \qquad (5.)$$

Which can be written in matrix form as follows:

$$T(r_S) = A \cdot S(r), \qquad A_{i,j} = \Delta r \; f\left(\frac{i\Delta r_S + r_{S,\min}}{j\Delta r + r_{\min}}\right) \quad (6.)$$

Where: A = the coefficient matrix of the equation group.

$A_{i,j}$ = the entries in matrix A

The ability of equation 6 to be used in conjunction with equation 3 to predict the surface film size distribution based on a known bubble size distribution will be demonstrated using a simulated bi-dispersed froth. The reason for using a bi-dispersed foam for this demonstration is because the shape of bubble size distribution is markedly different to those used to generated the data on which equation 3 is based.

This bi-dispersed distribution also further illustrates the problem with using the film size distribution as a proxy for the bubble size distribution. Figure 10 shows the surface of a simulated froth in which there are two different sized bubbles, the larger ones having approximately twice the volume of the smaller ones. There are also approximately equal numbers of each size of bubble. Examining figure 10 it is far from obvious that there are only two different bubble sizes within the system.

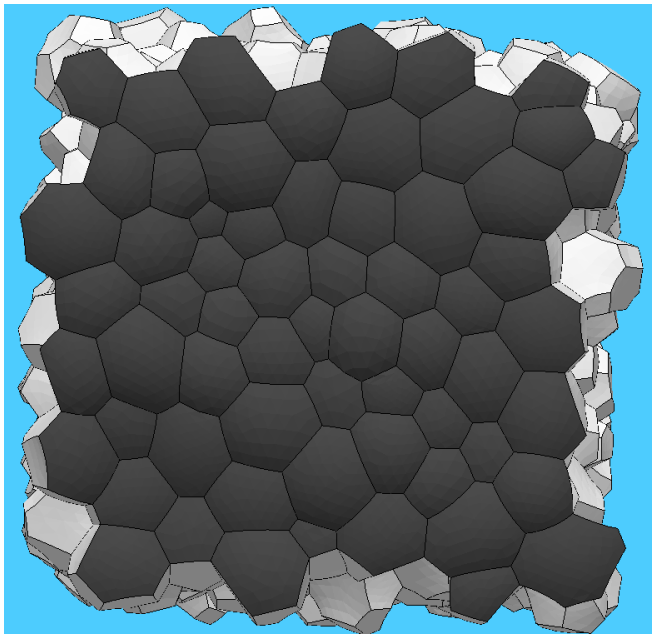

Figure 12: Surface of simulated bi-dispersed foam

Even when the surface bubble size distribution is examined (see “Actual Surface Distribution” in figure 11), the bi-dispersed nature of this system is not apparent. A combination of equations 3 and 6 is able to quite accurately predict the shape of this distribution, though (see “Predicted Surface Distribution” in figure 11). Figure 12 shows similar results for another simulated bi-dispersed foam, this one with the largest bubbles having 3 times the volume of the smallest.

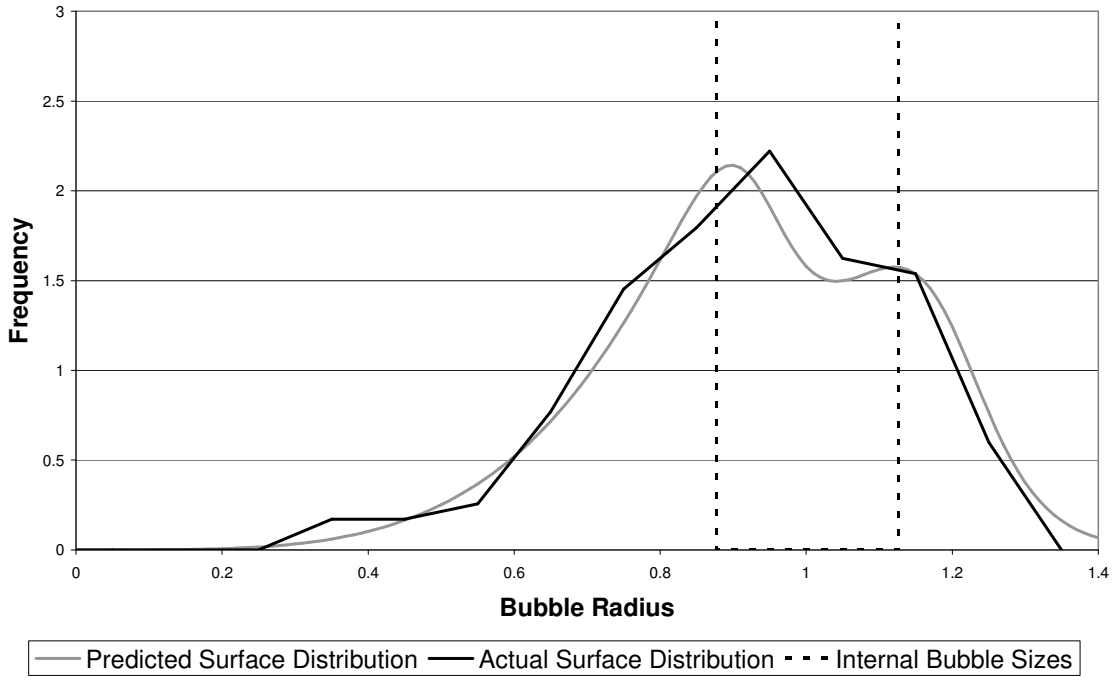

Figure 13: Predicted and simulated surface film size distributions for a bi-dispersed foam with the larger bubbles approximately twice the volume of the smaller bubbles.

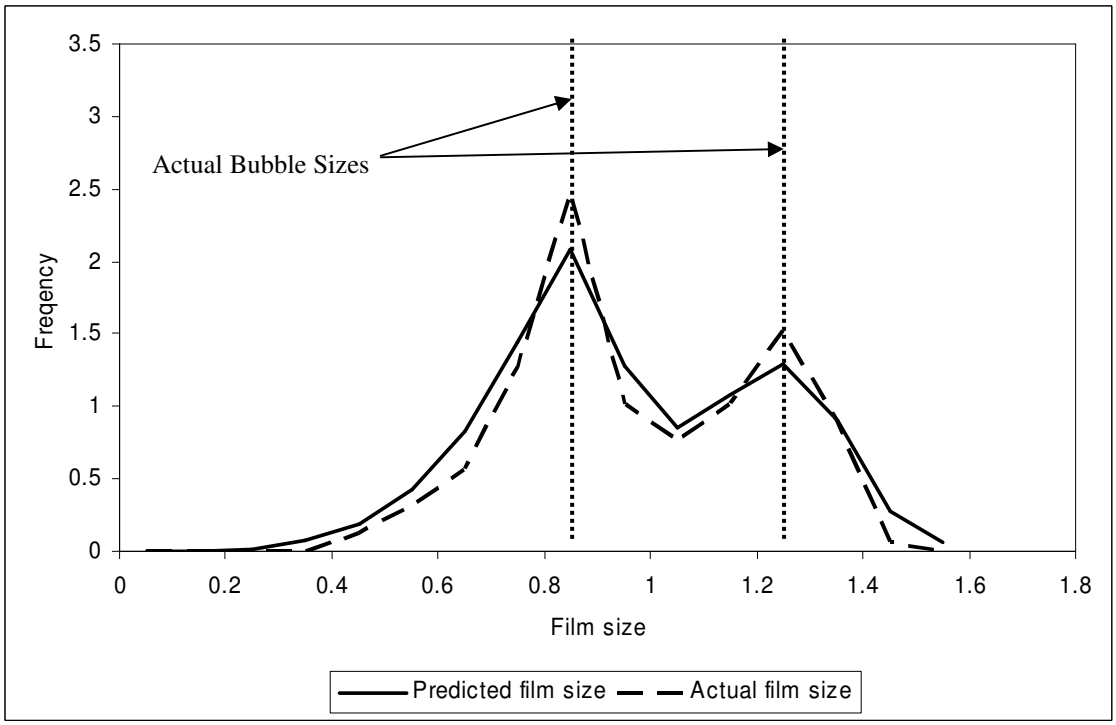

Figure 14: Predicted and simulated surface film size distributions for a bi-dispersed foam with the larger bubbles approximately three times the volume of the smaller bubbles

Calculating the Bubble Size Distribution using the Film Size Distribution

Thus far we have succeeded in solving the forward problem; that is predicting the film size distribution from a known bubble size distribution. Our aim, though, is to solve the inverse of this problem: predicting the surface bubble size distribution based on a known film size distribution as it is the film size distribution that can be measured using image analysis. The first approach attempted was to simply invert the matrix in equation 6. The problem with this method was that it was very sensitive to noise in the data, with all but the smoothest data giving some negative frequencies, with answers that fluctuated wildly around zero near regions of noisy data.

To overcome this problem a numerical approach was adopted. The estimated bubble size distribution is iteratively updated, subject to the constraint that no negative frequencies are allowed, in order to minimise the square of the discrepancy between the known and calculated surface film size distribution.

Figures 13 to 15 demonstrate the ability of this model to accurately predict surface bubble size distributions based on the film size distributions. In all these cases, the shape of the bubble size distributions are markedly different to those for the films, though the predicted and simulated distributions are quite close to one another. Since the simulations have been demonstrated to quite accurately model the structure of real froths, it is reasonable to assume that this model can accurately calculate the size distribution of surface bubbles based on the surface film size distributions.

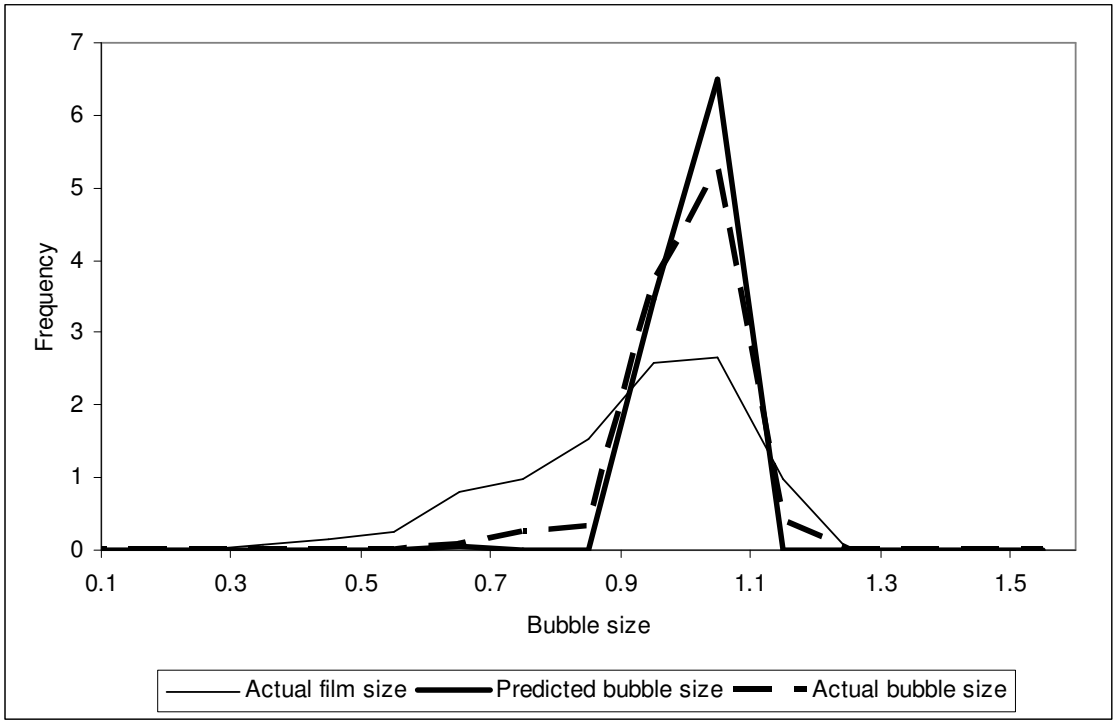

Figure 15: The calculated and the actual surface bubble size distributions for a poly-dispersed froth.

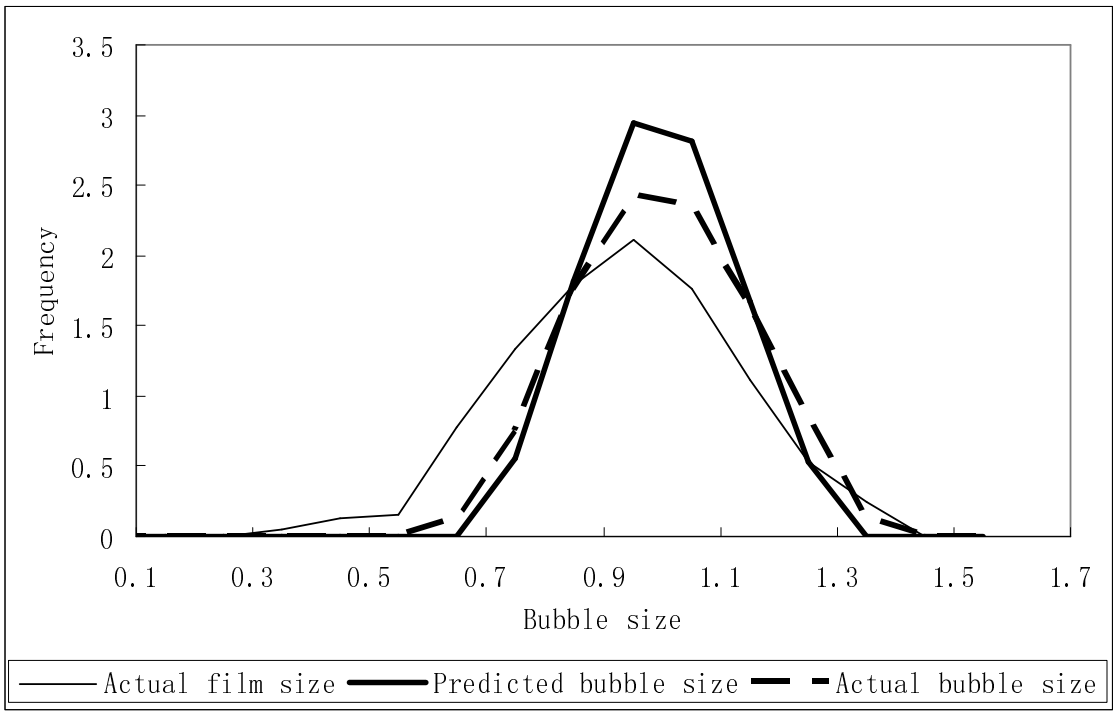

Figure 16: The calculated and the actual surface bubble size distributions for a more poly-dispersed froth.

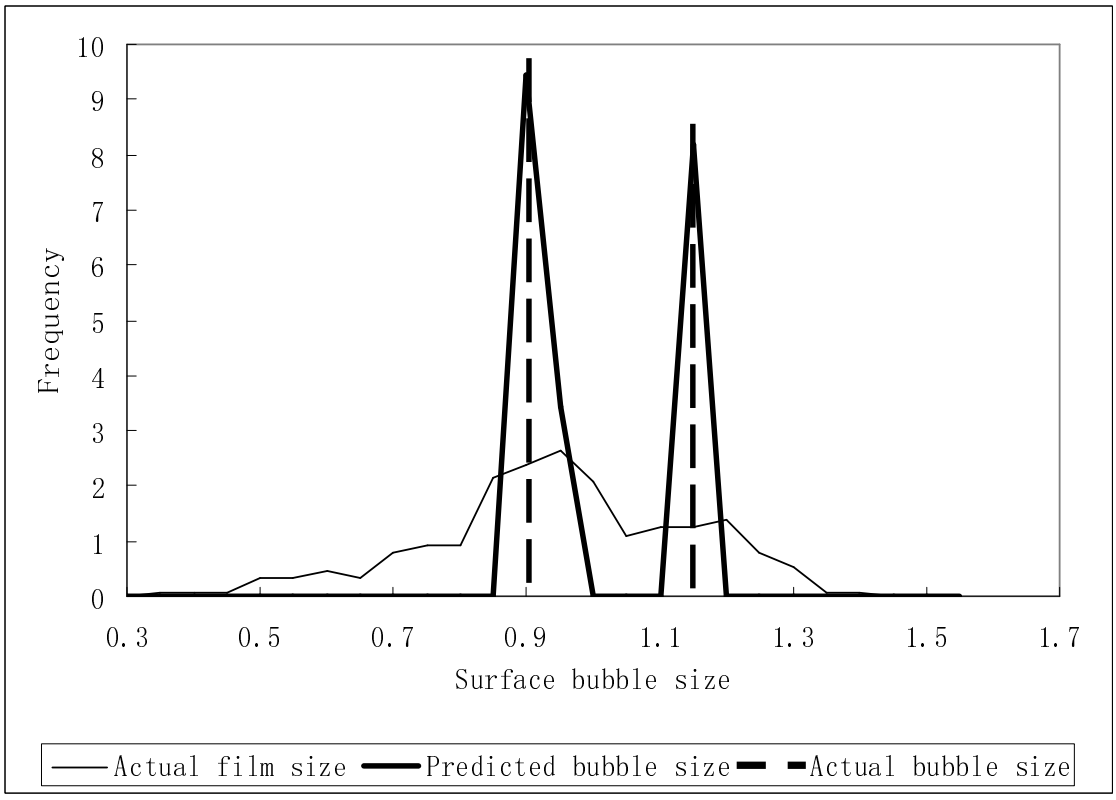

Figure 17: The calculated and the actual surface bubble size distributions of the bi-dispersed froth.

Future Work

This model is the first part of a two part process for predicting the size distribution of the bubbles reporting to the concentrate based on image analysis of the froth surface. It is able to predict the size distribution of the surface bubbles based on the size distribution of the surface films. The second step is to predict the size distribution of the internal bubbles based on that of the surface bubbles.

The big challenge in carrying this out is that the relationship depends on how the surface was created. Simple relationshipw have been proposed in which it is assumed that the distribution of bubbles at the surface is that which you would expect from putting a plane through the bulk of the froth, assuming that the bubbles are spherical (Cheng and Lemlich, 1983). This is exactly the same corrections as would be used for spherical particles in the stereological correction for polished mineral sections. This correction is too simplistic for a number of reasons; firstly, the bubbles at the surface are not intersecting a viewing plane, they are below the viewing plane, secondly, the structure and location of the bubbles are influenced by the proximity of the surface and, most importantly, the surface is not created by slicing the froth, but rather by the bursting of the previously overlying bubbles.

This means that the relationship between the surface bubble size distribution and that of the underlying bubbles is likely to depend on the bursting properties of the froth. For instance, if larger films are less likely to burst than smaller films, then the surface bubble sizes will smaller than expected and vice versa. This is therefore a complex problem that requires further study.

Conclusions

This paper demonstrates a method for carrying structural simulations of froth surfaces and demonstrates that these structures are topologically the same as those obtained experimentally.

It is then shown that the distribution of sizes that films can have relative to the size of the bubbles to which they are attached is independent of the overall size distribution of the bubbles or the size of the bubble involved relative to the other bubbles. This distribution was then shown to be able to accurately predict both the film size distribution from a known bubble size distribution, as well as the inverse of this.

References

Aldrich, C., Moolman, D.W., Eksteen, J.J. and Van Deventer, J.S.J., 1995. Characterization of flotation processes with self-organizing neural nets. *Chem. Eng. Comm.* **139**, 25–39.

Brakke, K.A., 1996. The surface evolver and the stability of liquid surfaces. *Philosophical Transactions Of The Royal Society Of London – A*, **354**, 2143-2157

Cheng, H.C. and Lemlich, R., 1983. Errors in the measurement of bubble size distribution in foam. *Ind. Eng. Chem. Fundam.*, 22, 105-109.

Kaartinen, J., Hatonen, J., Hyotyniemi, H. and Miettunen, J., 2006. Machine-vision-based control of zinc flotation-A case study, *Control Engineering Practice*, **14**, 1455-1466.

King, R. P., 1984. Measurement of particle size distribution by image analyser, *Powder Technology*, **39**, 279-289.

Kraynik, A.M., Reinelt, D.A. and van Swol, F., 2003. Structure of random monodisperse foam, *Physical Review E*, **67**, 031403

Mazke, E.B., 1946. The three dimensional shape of bubbles in Foam. *American Journal of Botany*, **33**, 58-80.

Neethling, S.J., Lee, H.T. and Cilliers, J.J., 2003a. The Recovery of Liquid from Flowing Foams. *J Phys. Condensed Matter*, **15**, 1563-1576

Neethling, S.J., Lee, H.T. and Cilliers, J.J., 2003b. Simple Relationships for Predicting the Recovery of Liquid from Flowing Foams and Froths. *Minerals Engineering,* **16**, 1123-1130

Sweet C.G., Bradshaw D.J., Cillers J.J.L., Wright B.A., De Jager G., Francis J.J., 2000. The extraction of valuable minerals from mined ore. "Smartfroth" *Adams & Adams Patent Attorneys Pretoria A&A*, REF: v13676 (1-11)

Wang, Y. and Neethling, S.J. , 2006. Simulating realistic froth surfaces, *Minerals Engineering*, **19**, 1069-1076

APPENDIX II – the source codes of the main Surface Evolver subroutines

Some of the important source codes produced by the command language of Surface Evolver are listed below. It includes the following parts:

1. Subroutine for calculating and outputting the list of the number of faces per bubble (NFPB) and the average value of NFPB for both surface bubbles and internal bubbles.
2. Subroutine for calculating and outputting the list of the number of edges per face (NEPF) and the average value of NEPF for both surface bubbles and internal bubbles.
3. Subroutine for calculating and outputting the equivalent circular radius of the projected areas and its distribution.
4. The subroutines to produce bi/tri-dispersed foams.
5. Subroutine for topological transformations. This subroutine is used to delete redundant edges and faces and implement topological transformations. It deletes edges and faces in such a way as not to violate Plateau's topological rules. It removes the need to use 'pop' commands in the simulation, which results in a better evolution in a topological transition.

1. Number of faces per bubble:

mark_surface : = (Marking the surface bubbles)

```
{
        foreach body bb do bb.surface:=0;
        foreach facet ff where ff.frontbody= =0 do body[ff.backbody].surface:=1;
        foreach facet ff where ff.backbody= =0 do body[ff.frontbody].surface:=1;
};
```

facecnt : = (count the surface bubbles)

```
{
        foreach body bb do
        {
                bb.num_faces:=0;
                if (bb.surface) then bb.num_faces:=1;
                foreach body bn do bn.cnted:=0;
                 bb.cnted:=1;
                 foreach bb.facets ff do
                 {
                        foreach ff.bodies bn do
                        {
                              if (bn.cnted= =0) then
                              {
                                    bn.cnted:=1;
                                    bb.num_faces+=1;
                              };
                        };
                };
        };
};
```

ffperbb:= (calculate the list of the number of faces per bubble and the corresponding average value for both the surface bubble and internal bubbles)

```
{
      mark_surface;
      facecnt;
      s_total:=0;
      s_num:=0;
      i_total:=0;
```

```
	i_num:=0;
	define sf INTEGER[27];
	define isf INTEGER[27];
	for (ii:=1;ii<=27;i+=1)
	{
		sf[ii]:=0;
		isf[ii]:=0;
	};

	foreach body bb do
	{
		if (bb.surface) then
		{
			s_total+=bb.num_faces;
			s_num+=1;
			sf[bb.num_faces]+ =1;

		}
		else
		{
			i_total+=bb.num_faces;
			i_num+=1;
			isf[bb.num_faces]+ =1;
		  };
	};
	for(ii:=3;ii<27;ii+=1) printf "sf%g %f	\n",ii, sf[ii];
	for(ii:=3;ii<27;ii+=1) printf "isf%g %f	\n",ii, isf[ii];

	printf "The average number of faces on a surface bubble: %f\n",s_total/s_num;
	printf "The average number of faces on an internal bubble: %f\n",i_total/i_num;
};

(Output command)
out_ffperbb2:=
{
   ffperbb2 | "ffperbb2.txt"
};
```

2. Number of edges per face:

eeperff:=

```
{
    define facenum INTEGER[25];
    define edgenum INTEGER[25];
    define surfacenum INTEGER[25];
    define intfacenum INTEGER[25];
    mark_surface;
    mark_face;
    foreach facet ff do ff.ffcnt:=0;
    for (ii:=1;ii<26;ii+=1)
    {
        facenum[ii]:=0;
        edgenum[ii]:=0;
        surfacenum[ii]:=0;
        intfacenum[ii]:=0;
    };
    foreach body bb do
    {
          foreach body[bb.id].facets ff do    /* available facets*/
          {
                if (ff.ffcnt<2) then
         {
           jj:=0;
           if (ff.sur==1) then
           {
              foreach body[bb.id].facets ff2 do
              {
                  if (ff2.sur==1) then
                  {
                      facet[ff2.id].ffcnt:=2;      /*deactivated for counting*/
                      foreach facet[ff2.id].edges ee do
                      {
                          foreach edge[ee.id].facets fff do
                          {
                              if (fff.sur==1) then
                              {
                                 if ((fff.frontbody==0) && (fff.backbody!=bb.id)) then
                                 {
                                     newedge:=1;
                                     for (kk:=1;kk<jj+1;kk+=1)
```

```
        {
          if (fff.backbody==edgenum[kk]) then
          {
            newedge:=0;
          };
        };

        if (newedge==1) then
        {
          jj+=1;
          edgenum[jj]:=fff.backbody;
        };

    };
    if ((fff.backbody==0) && (fff.frontbody!=bb.id)) then
    {

        newedge:=1;
        for (kk:=1;kk<jj+1;kk+=1)
        {
          if (fff.frontbody==edgenum[kk]) then
          {
            newedge:=0;
          };
        };

        if (newedge==1) then
        {
          jj+=1;
          edgenum[jj]:=fff.frontbody;
        };

    };

}
else
{
    if (fff.frontbody!=bb.id) then
    {
        newedge:=1;
        for (kk:=1;kk<jj+1;kk+=1)
        {
          if (fff.frontbody==edgenum[kk]) then
          {newedge:=0;};
```

```
                    };
                    if (newedge==1) then
                    {
                        jj+=1;
                        edgenum[jj]:=fff.frontbody;
                    };
                };
                if (fff.backbody!=bb.id) then
                {
                    newedge:=1;
                    for (kk:=1;kk<jj+1;kk+=1)
                    {
                        if (fff.backbody==edgenum[kk]) then
                        {newedge:=0;};

                    };
                    if (newedge==1) then
                    {
                        jj+=1;
                        edgenum[jj]:=fff.backbody;
                    };
                };

            };
        };
    };
  }
 };
}
else
{
    if (facet[ff.id].frontbody==bb.id) then
    {
        fid:=facet[ff.id].backbody;
    }
    else
    {
        fid:=facet[ff.id].frontbody
    };

    foreach body[bb.id].facets ff3 do
    {
        if ((ff3.frontbody==fid) ||(ff3.backbody==fid)) then
        {
```

```
ff3.ffcnt+=1;
foreach facet[ff3.id].edges ee do
{
    foreach edge[ee.id].facets ffff do
    {
        if (ffff.sur==1) then
        {
            if (ffff.frontbody==0) && (ffff.backbody!=bb.id) then
            {
                newedge:=1;
                for (kk:=1;kk<jj+1; kk+=1)
                {
                    if (ffff.backbody==edgenum[kk]) then
                    {newedge:=0};
                };
                if (newedge==1) then
                {
                    jj+=1;
                    edgenum[jj]:=ffff.backbody;
                };
            };
            if (ffff.backbody==0) && (ffff.frontbody!=bb.id) then
            {
                newedge:=1;
                for (kk:=1;kk<jj+1; kk+=1)
                {
                    if (ffff.backbody==edgenum[kk]) then
                    {newedge:=0};
                };
                if (newedge==1) then
                {
                    jj+=1;
                    edgenum[jj]:=ffff.frontbody;
                };
            };

        }
        else
        {
           if ((ffff.frontbody!=bb.id) && (ffff.backbody!=bb.id)) then
           {
               test1:=ffff.frontbody*10000+ffff.backbody;
               test2:=ffff.backbody*10000+ffff.frontbody;
               newedge:=1;
```

```
                                    for (kk:=1; kk<jj+1; kk+=1)
                                    {
                                        if ((test1==edgenum[kk]) || (test2==edgenum[kk])) then
                                        {newedge:=0;};
                                    };
                                    if (newedge==1) then
                                    {
                                        jj+=1;
                                        if (jj==8) then
                                        {printf "the bubble with 8 sides is: %g      \n",bb.id;};
                                        edgenum[jj]:=test1;
                                    };
                                };
                            };
                        };
                    };
                };
            };
            facenum[jj]+=1; /* count the number of edges per face of all the bubbles */

            if (body[bb.id].surface==1) then /*count surface and internal bubbles separately */
            {
                surfacenum[jj]+=1;
            }
            else
            {
                intfacenum[jj]+=1;
            };

        };    /*if ff.cnt <2*/


    };
};

for (ii:=3; ii<15; ii+=1)
{
    printf "The number of faces with %g edges for all bubbles is: %g \n\n",ii,facenum[ii];
};
printf "\n\n";
for (ii:=3; ii<15; ii+=1)
{
    printf "The number of faces with %g edges for surface bubbles is: %g
```

```
\n\n",ii,surfacenum[ii];
    };
    printf "\n\n";
    for (ii:=3; ii<15; ii+=1)
    {
        printf "The number of faces with %g edges for internal bubbles is: %g
\n\n",ii,intfacenum[ii];
    };
};
```

3. The actual and projected surface area of surface bubble:

function real Actual_Area (INTEGER b_id) /*direc: 1=x, 2=y 3=z*/ Calculate the actual surface area of the surface bubble)

```
{
    area_bub:=0.0;
    foreach body[b_id].facets ff where ff.frontbody==0 or ff.backbody==0 do
    {
        area_bub+=ff.area;
    };
    return(area_bub);
};
```

function real Surface_Area (INTEGER b_id, INTEGER direc) /*direc: 1=x, 2=y 3=z*/ (Calculate the projected surface area of the surface bubble)

```
{
     area_bub:=0.0;
     foreach body[b_id].facets ff where ff.frontbody==0 or ff.backbody==0 do
     {
          if (direc==1) then
          {
               a1:=torus_periods[2][2]/2.0;
               a2:=(vertex[ff.vertex[2].id].y-vertex[ff.vertex[1].id].y+3.0*torus_periods[2][2]/2.0)
               %torus_periods[2][2];
               a3:=(vertex[ff.vertex[3].id].y-vertex[ff.vertex[1].id].y+3.0*torus_periods[2][2]/2.0)
               %torus_periods[2][2];
               b1:=torus_periods[3][3]/2.0;
               b2:=(vertex[ff.vertex[2].id].z-vertex[ff.vertex[1].id].z+3.0*torus_periods[3][3]/2.0)
               %torus_periods[3][3];
               b3:=(vertex[ff.vertex[3].id].z-vertex[ff.vertex[1].id].z+3.0*torus_periods[3][3]/2.0)
               %torus_periods[3][3];
          }
          else if (direc==2) then
          {
               a1:=torus_periods[1][1]/2.0;
               a2:=(vertex[ff.vertex[2].id].x-vertex[ff.vertex[1].id].x+3.0*torus_periods[1][1]/2.0)
               %torus_periods[1][1];
               a3:=(vertex[ff.vertex[3].id].x-vertex[ff.vertex[1].id].x+3.0*torus_periods[1][1]/2.0)
               %torus_periods[1][1];
               b1:=torus_periods[3][3]/2.0;
               b2:=(vertex[ff.vertex[2].id].z-vertex[ff.vertex[1].id].z+3.0*torus_periods[3][3]/2.0)
```

```
            %torus_periods[3][3];
            b3:=(vertex[ff.vertex[3].id].z-vertex[ff.vertex[1].id].z+3.0*torus_periods[3][3]/2.0)
            %torus_periods[3][3];
        }
        else if (direc==3) then
        {
            a1:=torus_periods[2][2]/2.0;
            a2:=(vertex[ff.vertex[2].id].y-vertex[ff.vertex[1].id].y+3.0*torus_periods[2][2]/2.0)
            %torus_periods[2][2];
            a3:=(vertex[ff.vertex[3].id].y-vertex[ff.vertex[1].id].y+3.0*torus_periods[2][2]/2.0)
            %torus_periods[2][2];
            b1:=torus_periods[1][1]/2.0;
            b2:=(vertex[ff.vertex[2].id].x-vertex[ff.vertex[1].id].x+3.0*torus_periods[1][1]/2.0)
            %torus_periods[1][1];
            b3:=(vertex[ff.vertex[3].id].x-vertex[ff.vertex[1].id].x+3.0*torus_periods[1][1]/2.0)
            %torus_periods[1][1];
        };
        area_bub+=abs(a2*b1-a1*b2+a3*b2-a2*b3+a1*b3-a3*b1)/2.0;
    };
    return(area_bub);
};
```

4. The equivalent circular radius of the projected areas and its distribution:

image2:=

```
{
    define surcount real[3000];
    define proarea real[3000];
    define survol real[3000];
    medid:=0;
    medv:=0.0;
    num:=0;
    colourtop;
    foreach body bb do
    {
        onsurface:=0;
        foreach body[bb.id].facets ff do
        {
            if (ff.color==darkgray) then
            {
                onsurface:=1;
            };
        };
        if (onsurface==1) then
        {
            num+=1;
            surcount[num]:=bb.id;
        };
    };
    for (jjsu:=1; jjsu<num+1; jjsu+=1)
    {
        proarea[jjsu]:=Surface_Area(surcount[jjsu], 3);
        proarea[jjsu]:=sqrt(proarea[jjsu])*0.5642;
    };
    for (jj:=1; jj<num+1; jj+=1)
    {
        for (kk:=jj; kk<num+1; kk+=1)
        {
            if (proarea[kk]<proarea[jj]) then
            {
                medid:=surcount[kk];
                surcount[kk]:=surcount[jj];
```

```
                surcount[jj]:=medid;
                medv:=proarea[kk];
                proarea[kk]:=proarea[jj];
                proarea[jj]:=medv;
            };
        };
    };
    printf "The actual spherical equivalent radius of surface bubbles are:    \n";
    for (tt:=1; tt<num+1; tt+=1)
    {
        survol[tt]:=body[surcount[tt]].volume;
        survol[tt]:=0.6204*pow(survol[tt],0.33333333333);
        print survol[tt];
    };

    printf "The projected area of surface bubbles:    \n";
    for (jjsu:=1; jjsu<num+1; jjsu+=1)
    {
        print proarea[jjsu];
    };
};
```

out_image2:= (output the list of projected area of surface bubbles)

```
{
  image2 >>> "image2.xls";
};
```

5. The subroutines to produce bi/tri-dispersed foams.

make_bi_dispersed:= (produce bi-dispersed foam)

```
{
    totvol:=0.0;
    num:=0.0;
    foreach body vv do
    {
        totvol+=vv.volume;
        num+=1;
    };
    ave_size:=totvol/num;
    small_size:=totvol/num/bi_disp_ratio;
    num_small:=0.0;
    foreach body vv where vv.target<ave_size do
    {
        vv.target:=small_size;
        num_small+=1;
    };
    large_size:=(totvol-num_small*small_size)/(num-num_small);
    foreach body vv where vv.target>(ave_size+small_size)/2.0 do { vv.target:=large_size };
};
```

make_tri_dispersed:= (produce tri-dispersed foam)

```
{
    totvol:=0.0;
    num:=0.0;
    tri_min:=0.8;
    tri_max:=1.2;
    num_small:=0.0;
    num_large:=0.0;
    foreach body vv do
    {
        totvol+=vv.volume ;
        num+=1;
    };
    ave_size:=totvol/num;
    small_size:=ave_size*tri_min;
    large_size:=ave_size*tri_max;
    foreach body vv where vv.target<=small_size do
    {
```

```
        vv.target:=small_size;
        num_small+=1;
    };
    foreach body vv where vv.target>=large_size do
    {
        vv.target:=large_size;
        num_large+=1;
    };
    med_size:=(totvol-num_small*small_size-num_large*large_size)/(num-num_small-num_lar
    ge);
    num_med:=num-num_small-num_large;
    foreach body vv where (vv.target>small_size) and (vv.target<large_size) do
    {
        vv.target:=med_size;
    };
    printf "The number of small bubbles are:    %f      \n", num_small;
    printf "The number of medium bubbles are:    %f      \n", num_med;
    printf "The number of large bubbles are:    %f      \n",num_large;
};
```

6. The subroutine for implementing topological transition

Topstrans:= (Implement topological transformations)

```
{
    foreach edge e1 where e1.vertices[1].id==e1.vertices[2].id do
    {
        cnt+=1;
        If (valid_element(edge[e1.id])) then delete edge[e1.id];
        reset_counts;
    };
    edgedcnt:=0;
    facetdcnt:=0;
    quadquadcnt:=0;
    triedgecnt:=0;
    edgetricnt:=0;
    done:=0;
    foreach facet ff where ff.area<min_area do
    {
        if (!single) then done:=0;
        if (!done) and (valid_element(facet[ff.id])) and (ff.area<min_area/(top_fac*top_fac))
        and (no_quad==0) then
        pop_quad_to_quad facet[ff.id];
        if (pop_quad_to_quad_count>0) then
        {
            quadquadcnt+=1;
            done:=1;
            reset_counts;
            if (rclc) then recalc;
        };
        if (!done) and (valid_element(facet[ff.id])) and (ff.area<min_area/(top_fac*top_fac))
        then pop_tri_to_edge facet[ff.id];
        if (pop_tri_to_edge_count>0) then
        {
            triedgecnt+=1;
            done:=1;
            reset_counts;
            if (rclc) then recalc;
        };
        if (!done) and (valid_element(facet[ff.id])) then
        {
            del:=1;
            cnt2:=0;
```

```
foreach facet[ff.id].vertices vv do
{
    if (True_Valence(vv.id)>2) then cnt2+=1;
};
if cnt2>1 then del:=0;
if (cnt2==1) then
{
    del:=0;
    edgedcnt+=1;
    if facet[ff.id].edge[1].valence>=3 then
    {
        if valid_element(edge[facet[ff.id].edge[1].id]) then delete
        edge[facet[ff.id].edge[1].id];
        reset_counts;
        if (rclc) then recalc;
        done:=1;
    }
    else if facet[ff.id].edge[2].valence>=3 then
    {
        if valid_element(edge[facet[ff.id].edge[2].id]) then delete
        edge[facet[ff.id].edge[2].id];
        reset_counts;
        if (rclc) then recalc;
        done:=1;
    }
    else if facet[ff.id].edge[3].valence>=3 then
    {
        if valid_element(edge[facet[ff.id].edge[3].id]) then delete
        edge[facet[ff.id].edge[3].id];
        reset_counts;
        if (rclc) then recalc;
        done:=1;
    };
}
else if (cnt2==0) then foreach facet[ff.id].edges ee where (ee.valence==2) and
(!done) do
{
    if (!done) and (True_Valence(ee.vertex[1].id)>0) and
    (True_Valence(ee.vertex[2].id)>0) then
    {
        del:=0;
        foreach facet[ff.id].edges e1 where (!done) do
        {
```

```
                        if (True_Valence(e1.vertex[1].id)==0) or
                        (True_Valence(e1.vertex[2].id)==0) then
                        {
                            edgedcnt+=1;
                            if (valid_element(edge[e1.id])) and (!done) then delete
                            edge[e1.id];
                            reset_counts;
                            if (rclc) then recalc;
                            done:=1;
                            break 2;
                        };
                    };
                };
            };
            if (del) then
            {
                delete facet[ff.id];
                reset_counts;
                facetdcnt+=1;
                if (rclc) then recalc;
                done:=1;
            };
        };
};
foreach edge ee where (ee.length<crit_lent) and (ee.valence>2) do
{
    if (!single) then done:=0;
    if (!done) and (valid_element(edge[ee.id])) and (ee.length<crit_lent/top_fac) then
    {
        dopop:=1;
        foreach ee.facets ff do
        {
            valcnt:=0;
            foreach ff.edges e1 do
            {
                if e1.valence>3 then valcnt+=1;
            };
            if valcnt==3 then dopop:=0;
        };
        if (dopop) then pop_edge_to_tri edge[ee.id];
    };
    if (pop_edge_to_tri_count>0) then
    {
        edgetricnt+=1;
```

```
            done:=1;
            reset_counts;
            if (rclc) then recalc;
        };
        if (!done) and (valid_element(edge[ee.id])) then
        {
            del:=1;
            cnt2:=0;
            foreach edge[ee.id].vertices vv do
            {
                if (True_Valence(vv.id)>2) then cnt2+=1;
            };
            if cnt2==2 then del:=0;
            if (del) then
            {
                edgedcnt+=1;
                delete edge[ee.id];
                reset_counts;
                if (rclc) then recalc;
                done:=1;
            };
        };
};
foreach edge ee where (ee.valence==2) do
{
        smallcnt:=0;
        if (!single) then done:=0;
        foreach edge[ee.id].facet ff do
        {
            if ff.area<min_area then smallcnt+=1;
        };
        if (smallcnt==2) and (!done) then
        {
            if (True_Valence(ee.vertex[1].id)==0) or (True_Valence(ee.vertex[2].id)==0)then
            {
                edgedcnt+=1;
                if (valid_element(edge[ee.id])) then delete edge[ee.id];
                reset_counts;
                if (rclc) then recalc;
                done:=1;
            };
        };
};
```

```
    printf "Total number of edges deleted: %g\n",edgedcnt;
    printf "Total number of facets deleted: %g\n",facetdcnt;
    printf "Total quad to quad: %g\n",quadquadcnt;
    printf "Total edge to tri: %g\n",edgetricnt;
    printf "Total tri to edge: %g\n",triedgecnt;
};
```

Function INTEGER True_Valence(INTEGER vv) (**Calculate valence of a given vertex**)

```
{
  foreach edge ee do ee.mark:=0;
  cnts:=0;
  outsidedone:=0;
  foreach vertex[vv].edges ee do
  {
    if (ee.valence>2) and (!ee.mark) then
    {
      cnts+=1;
      ee.mark:=1;
    };
  };
  return cnts;
};
```